

Printed degradable piezoelectric microsystems: From ink formulation to device fabrication and characterization

Présentée le 5 octobre 2023

Faculté des sciences et techniques de l'ingénieur
Laboratoire des Microsystèmes Souples
Programme doctoral en microsystèmes et microélectronique

pour l'obtention du grade de Docteur ès Sciences

par

Morgan Mc Kay MONROE

Acceptée sur proposition du jury

Prof. V. Subramanian, président du jury
Dr D. Briand, Prof. L. G. Villanueva Torrijo, directeurs de thèse
Prof. C. Jean-Mistral, rapporteuse
Prof. M. Kaltenbrunner, rapporteur
Dr Y. Leterrier, rapporteur

Small acts, when multiplied by millions of people, can transform the world.

— Howard Zinn

Acknowledgements

I would like to take this opportunity to express my deep gratitude and appreciation to all those who have supported and guided me throughout my doctoral journey. This thesis represents the culmination of years of dedicated effort, and I owe its completion to the contributions and encouragement of many individuals and organizations. As the old saying goes, it takes a village.

First and foremost, I am profoundly thankful to my academic advisors, Dr. Danick Briand and Prof. L. Guillermo Villanueva, whose unwavering guidance, expertise, and mentorship have been instrumental in shaping the direction of my research. Danick, for taking a chance on me and giving me the opportunity to dive into this strange world of green and printed electronics. Your keen eye for innovative approaches and enthusiastic scientific discussions have pushed me in directions I didn't know I needed to go. Guillermo, for your optimism, passion for all things piezoelectric, and perpetual support that has gotten me through so much along the way. Your invaluable insights, patience, and commitment to excellence have been a constant source of inspiration. Thank you both so much.

I extend my gratitude to the members of my thesis jury—Prof. Yves Leterrier, Prof. Claire Jean-Mistral, and Prof. Martin Kaltenbrunner for their efforts in reviewing this thesis, as well as Prof. Vivek Subramanien for serving as president of the jury. Their constructive feedback, rigorous examination of my work, and for the insightful discussions that have enriched the quality of this thesis. Thank you for your hard work.

Acknowledgements must also be given to the many people who helped with the experimental aspects of this work. Dr. Jaemin Kim and Mr. Nicolas Fumeaux of EPFL-LMTS for their assistance with device fabrication and process integration. Drs. Damien Maillard and Seniz Küçük as well as Mr. Daniel Moreno Garcia for their assistance with device design, fabrication, and characterization of resonating cantilever structures. Thanks as well to the Masters students who have worked with me on this project, Antoine Duret and Julien Hurni—their hard work, and enthusiasm are greatly appreciated.

Thanks must also be given to Prof. Dragan Damjanovic and Dr. Lukas Riemer for their support conducting ferroelectric and piezoelectric characterization, as well as for the many, many scientific discussions along the way. As well I extend my deep gratitude to Dr. Peter van der Waal, the unsung hero of EPFL's Neuchatel campus. Your support in all things scientific has gotten me through so many hard times, but it was your friendship this is truly invaluable.

This thesis could absolutely not have been completed without the support of my labmates in both LMTS and A-NEMS. LMTS has been my home and my second family all these long years and is truly the most unique lab I have ever worked in. An exceptional place full of interesting and talented people, LMTS is a great research environment. I am grateful for every coffee break, every lunchtime swim, every apero, and every moment in between with this remarkable group of people. Special thanks must be given to Myriam Poliero, the shadow queen that keeps this lab group functioning in every sense.

To my second family in the Advanced NEMS lab, especially Damien, Danny, Soumya, Yara, and Seniz. I was not around often, but was always welcomed with open arms and a friendly environment. Thank you for the support.

To the Hike Squad – Djen, Giulio, Florian, Mike, Robert, Erika, Fatemeh, Sabrina – words cannot express. You know how important you are to me. Thank you for everything.

Thanks for the support of both the Current Affairs squad and the Green team. To Ryan, Silvia, and Alessio for their support, their conversations, and their friendship even when we lost at pub quiz. To James, Jaemin, Claudio, and Nicolas – thank you for joining me on this eco-friendly journey. Our discussions on materials, methods, and unconventional

workarounds were invaluable scientifically, and your support during the hard times was invaluable emotionally. Nico, we started this together and we finished it that way, too, submitting and defending less than a week apart. Jaemin and James, I couldn't have asked for better officemates. All others will have to live up to your gold standard.

Thanks to all of my other colleagues and friends at Microcity. To all of my neighboring lab, LAFT, you are like a second lab to me, thank you for adopting me into your group.

To my friends and family, your emotional support provided the necessary encouragement to persevere through the challenges of this journey.

Eternal gratitude to my family and friends back home, far away but ever present, for the unwavering belief in me and never-ending patience during the hard times. Thank you to my family – my parents, Ryan, Nathan, Forest, Muching – I couldn't have done this without you. To Shelby, Chris, Jerica, Rosanna, Ziyang, Elaine, Davina, and the rest of the Californians, I thank you for your continued friendship. For the innumerable videocalls at weird hours to listen to me complain about my experiments, and for travelling from all over the world to meet up with me. With deep appreciation and affection, thanks to Dr. Kevin Hughes, not only for keeping my cat alive for an entire year as I moved across the world, but also for still being my friend and my support afterwards.

Finally, thanks to my kitty cat, Merlin, for whom I am eternally grateful. He may only have a few braincells, but all of them have shown me incredible love and companionship.

This thesis is the result of collective effort, and I am deeply grateful to each and every one of you who has played a part in this academic endeavor. Thank you all for being a part of this important chapter in my life.

Morgan McKay Monroe

Neuchâtel, 29 August 2023

Abstract

As the world moves further and further into the semiconductor era, the amount of waste generated from electronics (“e-waste”) is increasing rapidly and unsustainably. Of particular note, alternatives to lead-based piezoelectric materials must be established. However, addressing e-waste reduction requires the development of both sustainable materials and green fabrication techniques, especially for high-volume, short-life uses. With low material waste and high scalability, additive manufacturing offers a greener alternative to conventional processing, and thus printed green piezoelectrics emerge as promising candidates to replace Pb-based counterparts. Even so, their integration into completely degradable devices has been hindered by processing complexity and high temperatures— alternative approaches must be established to enable entirely green printed piezoelectric devices.

To that end, this thesis focuses on the development of degradable piezoelectric microsystems composed entirely of green materials and fabricated using eco-friendly printing technologies. We cover aspects from ink formulation to device fabrication and characterization, establishing a facile process for the low-temperature printing of KNbO_3 -based piezoelectrics and their integration into fully printed green devices.

We begin with a down-selection of device and ink components, assessing several biodegradable piezoelectric materials (RS, ADP, ZnO, HA, KNbO_3) in feasibility studies, and finally selecting non-toxic potassium niobate (KNbO_3) after successful proof-of-concept investigations validate low-temperature poling of screen-printed perovskite materials on biodegradable substrates.

Next a screen-printing process for KNbO_3 is developed and refined. Inks in a 58:8:34 wt% KN:EC:pentanol mixture are prepared and characterized by printing standardized designs on silicon with Au electrodes. We assess the influence of process and material parameters on print quality and device performance, with focusing on KNbO_3 preparation via milling and post-processing. We achieve a piezoelectric response as high as 12.4 pC/N in 6 μm thick screen-printed layers.

The low-temperature printing process is then transferred onto degradable paper substrates. Performance evaluations are conducted on devices fabricated using paper and Si substrates with evaporated gold electrodes, employing both circular capacitor and cantilever device configurations. By optimizing poling parameters, we achieve piezoelectric coefficients as high as 18.4 pC/N, and averaging 13.6 pC/N on paper.

In the final phase, printed zinc and carbon conductors are integrated into the process, leading to the successful fabrication of fully printed, green piezoelectric devices for the first time. The influence of electrode materials on device performance is studied, obtaining effective piezoelectric coefficients as high as 4.6 and 5.1 pC/N for printed devices on paper with C and Zn electrodes, respectively.

The culmination of this research is the development of fully printed green demonstrator devices, including a paper-based force sensor array and an acoustic actuator integrated into entirely degradable headphones. These devices demonstrate the technological potential for practical applications.

The research presented in this thesis contributes to the development of sustainable and eco-friendly printed electronic devices, paving the way for the reduction of environmentally harmful e-waste on a global scale.

Keywords

Additive manufacturing, biodegradable electronics, degradable electrodes, ferroelectric, paper electronics, piezoelectric, printed electronics, screen printing, sustainable, transient electronics

Résumé

Alors que le monde avance de plus en plus vers l'ère des semi-conducteurs, la quantité de déchets électroniques générée augmente rapidement et de manière insoutenable. Il est particulièrement important d'établir des alternatives aux matériaux piézoélectriques à base de plomb. Cependant, la réduction des déchets électroniques nécessite le développement à la fois de matériaux durables qui peuvent être structurés par des techniques de fabrication respectueuses de l'environnement, notamment pour des dispositifs à courte durée de vie qui sont produits à grande échelle. Avec une faible production de résidus et une grande adaptabilité, la fabrication additive offre une alternative plus écologique aux procédés conventionnels. L'application de ce procédé aux matériaux piézoélectriques respectueux de l'environnement en fait des candidats prometteurs pour remplacer leurs homologues à base de plomb.

Néanmoins, leur intégration dans des systèmes entièrement dégradables a été entravée par la complexité des procédés et les températures élevées de mise en œuvre. Il est donc nécessaire de mettre en place des approches alternatives pour permettre la réalisation de dispositifs écologiques par impression.

Dans cette optique, cette thèse se concentre sur le développement de microsystèmes piézoélectriques plus respectueux de l'environnement composés de matériaux dégradables et fabriqués par impression. Elle couvre différents aspects, de la formulation de l'encre à la fabrication et à la caractérisation de ces dispositifs, en établissant un procédé simple pour l'impression à basse température de matériaux piézoélectriques à base de Le niobate de potassium (KNbO_3) et leur intégration dans des dispositifs entièrement imprimés.

Nous commençons par une sélection d'encres et de composants avec une évaluation lors d'études de faisabilité de plusieurs matériaux piézoélectriques dégradables (RS, ADP, ZnO, HA, KNbO_3). Le KNbO_3 est finalement sélectionné suite à une validation de la polarisation à basse température de matériaux pérovskite imprimés par sérigraphie sur des substrats dégradables.

Ensuite, un procédé de sérigraphie pour le KNbO_3 est développé et affiné. Des encres à base d'un mélange de 58:8:34 wt% KN:EC:pentanol sont préparées et caractérisées en imprimant des structures standards avec des électrodes en or sur du silicium. Nous évaluons l'influence des différents paramètres impliqués sur la qualité d'impression et les performances des composants avec un accent mis sur la préparation du KNbO_3 par broyage et son post-traitement. Nous obtenons une réponse piézoélectrique allant jusqu'à 12,4 pC/N pour des couches imprimées par sérigraphie de 6 μm d'épaisseur.

Le procédé d'impression à basse température est ensuite transféré sur des substrats en papier dégradable. Des évaluations de performances sont effectuées sur des échantillons fabriqués sur des substrats en papier et en silicium avec des électrodes en or évaporé, intégrant à la fois des structures de condensateur circulaire et de poutre en porte-à-faux. En optimisant les paramètres de polarisation, nous obtenons des coefficients piézoélectriques sur papier aussi élevés que 18,4 pC/N, avec une moyenne de 13,6 pC/N.

Dans la dernière phase, des conducteurs en zinc et en carbone sont intégrés au procédé, conduisant, pour la première fois, à la fabrication de dispositifs piézoélectriques entièrement imprimés et respectueux de l'environnement. L'influence du type d'électrode sur les performances des composants imprimés sur papier est étudiée, avec des coefficients piézoélectriques effectifs obtenus atteignant 4,6 et 5,1 pC/N pour des électrodes respectivement en carbone et en zinc.

Le résultat de cette recherche est le développement de démonstrateurs entièrement imprimés, comprenant un réseau de capteurs de force sur papier et un actionneur acoustique intégré dans des écouteurs dégradables. Ces dispositifs démontrent le potentiel de la technologie pour des applications pratiques.

La recherche présentée dans cette thèse contribue au développement d'appareils électroniques imprimés plus durables et respectueux de l'environnement, ouvrant la voie à la réduction à grande échelle des déchets électroniques nocifs pour l'environnement.

Mots-clés

Fabrication additive, électronique biodégradable, électrodes dégradables, ferroélectrique, électronique sur papier, piézoélectrique, électronique imprimée, sérigraphie, durable, électronique transitoire

Contents

Acknowledgements	i
Abstract	iv
Keywords	iv
Résumé	v
Mots-clés	vi
Contents	vii
List of figures	xi
List of tables	xiii
List of equations	xiv
Chapter 1 Introduction	1
1.1 Background and motivation.....	1
1.2 Objectives and challenges.....	2
1.3 Contributions and thesis outline.....	3
Chapter 2 Printed degradable piezoelectric microsystems: Fundamentals and technology	5
2.1 Overview of green materials	5
2.1.1 Defining “Green”	5
2.1.2 Green substrate materials.....	7
2.1.3 Green conductive materials	8
2.1.4 Green piezoelectric materials.....	9
2.2 Introduction to piezoelectrics	11
2.2.1 Piezoelectric working principle	11
2.2.2 Key characteristics of piezoelectric devices	11
2.2.3 Constraints of conventional piezoelectrics.....	12
2.3 Overview of printing technologies and ink development considerations	13
2.3.1 Introduction to printing technologies.....	13
2.3.2 Printing figures of merit and ink formulation considerations	14
2.3.3 Piezoelectric ink development	16
2.3.4 Printed piezoelectric microsystems.....	17
2.3.5 Techniques for dipole orientation in printed piezoelectrics.....	18
2.4 State of the art on degradable and printed piezoelectric microsystems	19
2.4.1 Degradable piezoelectric microsystems	19
2.4.2 Printed degradable piezoelectric microsystems.....	21
2.5 Challenges and conclusions.....	22
Chapter 3 Materials selection and process development towards low-temperature printed piezoelectrics	25
3.1 Printing processes, component materials, and device considerations	25
3.1.1 Device components: Substrate and electrode materials	25
3.1.2 Printing processes	27

3.1.3 Ink components: Solvents and binding agents.....	27
3.2 Initial materials down-selection for green piezoelectric microsystems	28
3.2.1 Piezoelectric material evaluation and down-selection.....	29
3.2.2 Conclusions from feasibility studies on degradable piezoelectric materials.....	33
3.3 Process validation using ceramic piezoelectric powders	33
3.3.1 Validation of low-temperature processes using screen printed BaTiO ₃ on paper substrates	34
3.3.2 Potassium niobate validation studies	37
3.4 Summary and conclusions	39
Chapter 4 Development and optimization of a low-temperature piezoelectric KNbO₃ printing process	40
4.1 KN ink preparation and device fabrication	41
4.1.1 KNbO ₃ powder preparation.....	41
4.1.2 Ink preparation	42
4.1.3 Device architecture and fabrication.....	43
4.1.4 Validation of piezoelectric response in KN printed devices	45
4.2 Process factors affecting print quality.....	45
4.2.1 KN particle size.....	46
4.2.2 Printing method.....	48
4.2.3 Binder content	49
4.3 Process factors affecting device performance.....	49
4.3.1 Film drying temperature	50
4.3.2 Electrode coverage, material, and processing techniques.....	50
4.4 Material factors affecting device performance	51
4.4.1 KN particle crystallinity.....	52
4.4.2 KN source powder and material purity.....	53
4.4.3 Grinding media.....	54
4.4.4 KN particle size and grinding process variance	55
4.5 Summary and conclusions	56
Chapter 5 Low-temperature processing of screen-printed piezoelectric KNbO₃ with integration onto biodegradable paper substrates	59
5.1 Methods	59
5.1.1 Powder processing and ink preparation.....	61
5.1.2 Device design	62
5.1.3 Fabrication	65
5.2 Results and Discussion.....	66
5.2.1 Ink and printed layer properties	66
5.2.2 Dielectric properties	67
5.2.3 Poling optimization and piezoelectric properties	68
5.3 Summary and conclusions	70

Chapter 6 Integration of screen-printed KNbO₃ with degradable printed electrodes and integration into demonstrator devices.....	71
6.1 Materials, methods, and manufacturing.....	71
6.1.1 Fabrication process overview.....	72
6.1.2 Sintering of printed zinc films	73
6.1.3 Materials and methods	74
6.2 Influence of electrode material on device properties.....	75
6.2.1 Physical characteristics	75
6.2.2 Dielectric and piezoelectric characteristics.....	78
6.3 Degradation Studies.....	79
6.4 Sensing Demonstration: Force Sensor.....	81
6.5 Actuating Demonstration: Acoustic Speaker.....	83
6.6 Summary and conclusions	87
Chapter 7 Conclusions and outlook.....	89
7.1 Summary and conclusions	89
7.1.1 Materials selection.....	89
7.1.2 Printing process development and performance improvement.....	90
7.1.3 Low temperature processes on degradable substrates	91
7.1.4 Integration of screen-printed KNbO ₃ with printed degradable electrodes and integration into demonstrator devices.....	91
7.2 Outlook.....	92
7.3 Closing remarks.....	93
Chapter 8 Appendix.....	94
8.1 Appendix A: Library of Green Materials	94
8.2 Appendix B: Characterization methods	98
8.2.1 Piezoelectric characterization: Berlincourt method.....	98
8.2.2 Cantilever characterization via Laser Doppler vibrometry.....	99
8.2.3 Particle size analysis.....	101
8.3 Appendix C: Expanded literature review on commonly printed piezoelectric materials	102
8.3.1 Literature review on printing of common piezoelectric materials.....	102
8.3.2 Literature review on solution processed or printed ZnO.....	103
8.4 Appendix D: Expanded details on materials down-selection studies	105
8.4.1 Initial studies concerning Rochelle salt and ADP.....	105
8.4.2 Initial studies concerning ZnO.....	105
8.4.3 Initial studies concerning hydroxyapatite.....	108
8.4.4 Process validation with barium titanate.....	111
8.4.5 Initial studies concerning potassium niobate.....	112
8.5 Appendix E: Dielectric leakage studies	114
8.5.1 Electrode coverage and material.....	114

8.5.2 Humidity sensitivity of printed KN films.....	114
References	116
Curriculum Vitae	129

List of figures

Figure 2.1	Visualization of the three fields relevant to this work.....	5
Figure 2.2	Distinctions between relevant "green" material terms.....	6
Figure 2.3	Thermal limits of common substrates.....	7
Figure 2.4	Schematic description of common printing techniques.....	13
Figure 2.5	Printing considerations and interplay.....	15
Figure 2.6	Schematic showing the concept of dielectrophoresis.....	18
Figure 2.7	Poling mechanism schematics.....	19
Figure 2.8	Examples of piezoelectric devices utilizing green materials.....	20
Figure 2.9	Thesis challenges associated with specific device components.....	22
Figure 3.1	Preparation of RS and ADP films.....	30
Figure 3.2	Screen printed ZnO film on glass substrate.....	31
Figure 3.3	Room temperature ZnO NF synthesis using shape-directing agents.....	32
Figure 3.4	Stencil printed HA on paper with sputtered Au electrodes.....	33
Figure 3.5	Fabrication of BT capacitor devices on paper substrates.....	35
Figure 3.6	Physical Analysis of printed BT devices on paper substrates.....	35
Figure 3.7	Poling process for screen printed barium titanate.....	36
Figure 3.8	Initial results of BT poling investigations.....	36
Figure 3.9	Examples of stencil printed KN layers during recipe down-selection.....	37
Figure 3.10	Diffraction spectra of KN powder.....	38
Figure 4.1	KN ink preparation process.....	42
Figure 4.2	Process flow and device design for ink development investigations.....	43
Figure 4.3	Details of the poling process for printed devices.....	44
Figure 4.4	Physical and electrical characteristics of validation samples.....	45
Figure 4.5	Particle size analysis of KN powders.....	47
Figure 4.6	Influence of grinding solvent ratio on printing quality.....	47
Figure 4.7	Influence of processing factors on printed KN film thickness.....	48
Figure 4.8	Printing quality variance resulting from increased ethyl cellulose binder content in ink.....	49
Figure 4.9	Cross-sectional SEM image of printed layer on a silicon substrate.....	50
Figure 4.10	Influence of surface treatment on dielectric behavior of KN capacitive devices.....	51
Figure 4.11	Influence of KN powder annealing on device characteristics.....	52
Figure 4.12	Study of device performance based on KN source material.....	54
Figure 4.13	Influence of grinding media on particle size and piezoelectric response.....	55
Figure 4.14	Piezoelectric response variance resulting from changes in grinding conditions.....	56
Figure 5.1	Overview of progress for printed KN on paper substrates.....	60
Figure 5.2	Ink and film characteristics.....	61
Figure 5.3	Predicted resonance frequency of the cantilevers.....	64
Figure 5.4	Full process flow diagram for piezoelectric device fabrication.....	65
Figure 5.5	Top-down view of cantilever device designs.....	66
Figure 5.6	Characterization of ink and printed layer properties.....	67
Figure 5.7	Dielectric characteristics of capacitor devices.....	68

Figure 5.8	Optimization of the poling parameters for piezoelectric coefficients.....	69
Figure 5.9	Characterization of cantilever devices	70
Figure 6.1	Overview of work on fully printed piezoelectric devices.....	72
Figure 6.2	Zinc post-printing process.....	73
Figure 6.3	Zinc post-printing sintering process development.....	73
Figure 6.4	Physical characteristics of the fabricated devices.....	76
Figure 6.5	Optical images of each device type in cross-section	77
Figure 6.6	SEM images showing the KN-electrode interfaces	77
Figure 6.7	Electrical behavior of piezoelectric devices	78
Figure 6.8	Degradation studies showing sample degradation under three different conditions.....	80
Figure 6.9	Fabrication and characterization of a fully printed degradable force sensor grid.....	82
Figure 6.10	Example data showing details of the force sensor measurements	83
Figure 6.11	Fully degradable headphones demonstration	84
Figure 6.12	Assembly of degradable piezoelectric buzzers.....	85
Figure 6.13	Assembly of degradable headphones	86
Figure 6.14	Displacement of a speaker membranes as measured using Laser Doppler Vibrometry	87
Figure 8.1	Visualization of the as-used Berlincourt meter	99
Figure 8.2	Annotated photograph of LDV setup.	99
Figure 8.3	Schematic of LDV signal processing	100
Figure 8.4	Particle size distribution analysis method	101
Figure 8.5	Schematic of a possible <i>in situ</i> texturing method.....	107
Figure 8.6	Quality improvement of screen-printed HA films.....	108
Figure 8.7	Simplified Process flow for HA device fabrication on glass substrate.....	109
Figure 8.8	Thickness measurement for screen printed hydroxyapatite layers	110
Figure 8.9	Powder diffraction spectra for two samples of hydroxyapatite	110
Figure 8.10	Initial Stencil printed BT device details.....	111
Figure 8.11	Evaluation of the influence of top electrode material on ferroelectric device performance.	114
Figure 8.12	influence of ambient humidity on KN device capacitance.....	115

List of tables

Table 2.1	Abbreviated list of green electronic materials known to be printable.....	6
Table 2.2	Summary of potential piezoelectric materials.....	10
Table 2.3	Comparison of printing technique characteristics.....	14
Table 2.4	State of the art on low-temperature printed piezoelectrics.....	17
Table 3.1	Comparison of relevant characteristics for printed electronics substrates	26
Table 3.2	Short-listed degradable binding agents.....	28
Table 3.3	Comparison of some known green piezoelectric materials.....	29
Table 4.1	Comparison of device parameters based on KN source material.....	53
Table 5.1	Material properties associated with resonance frequency model Equations (5.1) and (5.2). ...	63
Table 5.2	Cantilever properties associated with resonance frequency model Equations (5.1) and (5.2). ...	63
Table 5.3	Variables associated with the material property approximation model	64
Table 5.4	Target dimension values for all components in the cantilever devices.	64
Table 5.5	Key parameters of printed piezoelectric devices relative to reference values.....	66
Table 6.1	Comparison of piezoelectric device characteristics based on electrode material.....	77
Table 8.1	Summary table of green materials	94
Table 8.2	Variables used in derivation of Berlincourt method piezoelectric coefficient	98
Table 8.3	Equipment used for the in-house Berlincourt measurement	99
Table 8.4	Variables used in derivation of LDV method piezoelectric coefficient $d_{31,eff}$ calculation.....	101
Table 8.5	Expanded state of the art on 2D printed piezoelectrics.....	102
Table 8.6	Expanded state of the art regarding solution processed zinc oxide.....	103
Table 8.7	Tested ink formulations for green RS and ADP screen printing inks	105
Table 8.8	Tested ink formulations for green ZnO screen printing inks.	106
Table 8.9	Tested ink formulations for hydroxyapatite-based screen-printing inks.	108
Table 8.10	Ink compositions tested for potassium niobate-based screen-printing inks.	112

List of equations

(2.1)	11
(2.2)	11
(2.3)	11
(5.1)	62
(5.2)	62
(5.3)	63
(5.4)	63
(5.5)	63
(5.6)	63
(5.7)	64
(6.1)	82
(8.1)	98
(8.2)	98
(8.3)	98
(8.4)	98
(8.5)	98
(8.6)	98
(8.7)	98
(8.8)	98
(8.9)	98
(8.10)	98
(8.11)	100
(8.12)	100
(8.13)	100
(8.14)	100

Chapter 1 Introduction

1.1 Background and motivation

As we move further and further into the Digital Era, the amount of waste generated from electronics (“e-waste”) is increasing rapidly. It is estimated that the world collectively produces approximately *50 million megatons of e-waste annually*, corresponding to about 7 kg of e-waste per person, of which only about 20% is documented to be collected and recycled.^{1,2} Unfortunately, many of these electronics are heavily engineered, making them very difficult to recycle, if recyclable at all, and contain components known to be environmentally toxic.³ This is of particular concern for high production volume, short lifetime device applications such as wearable electronics, remote or environmental sensors, and healthcare monitoring.

More than just the physical quantity of e-waste, the microfabrication processes used in electronics production can themselves be harmful to the environment. Cleanrooms require vast amounts of energy to sustain, generate large amounts of material waste, and utilize hazardous and often non-renewable chemicals in many of the processes.⁴⁻⁶ It is thus imperative that we develop alternative forms of electronics using greener, more sustainable materials and processes in order to reduce these negative impacts on our world.

One method of reducing e-waste is by using green (i.e., non-toxic, degradable, or renewable)[†] resources. Many degradable materials with useful electrical properties have been identified, and a huge push is underway to make these materials processable.⁷⁻⁹ In another direction, printed electronics are gaining popularity. Printing offers an eco-friendly alternative to cleanroom processes as a highly scalable, low-material waste, and more energy efficient fabrication method.

Combining these technologies to produce printable degradable electronics offers a more sustainable solution to conventional processes. Towards this, excellent progress in simple printed systems utilizing transient conductors, insulators, and semiconducting degradable materials. But to manufacture more complex green devices, such as sensors or actuators, more specialized materials and processing methods are required. Green printing processes for transducing materials must be developed.

Piezoelectric materials, in particular, are a critical component of many MEMS devices—acting as speakers, microphones, accelerometers, sensors, and more. Their ability to convert between electrical and mechanical energy make them ubiquitous in many commercial MEMS devices. Yet in many applications, the piezoelectric material is lead zirconate titanate ($\text{Pb}(\text{Zr},\text{Ti})\text{O}_3$, “PZT”), a perovskite material which has a large piezoelectric response but is environmentally toxic due to the presence of lead. As a result, effort has been made in recent years to identify and develop lead-free piezoelectrics with excellent properties in order to replace PZT in electronic systems. Some newer devices are instead utilizing lead-free aluminum nitride, AlN, which can produce high quality resonating devices, but is very challenging to process outside of microfabrication techniques, or alternative perovskite materials such as barium titanate (BaTiO_3 , “BT”) or lithium niobate (LiNbO_3), whose materials pose their own environmental concerns. Other developments of green piezoelectrics are hindered by the low piezoelectric performance of biological piezomaterials and their inherent fragility.

As an additional challenge in the realization of green printed piezoelectrics, even the most robust degradable substrates—such as cellulose or silk fibroin, for example—thermally decompose at temperatures around 200 °C. This constrains the processing methods that can be utilized for full device realization with eco-friendly components. To enable greener

[†] A more detailed definition of “green” materials for the purposes of this work is provided in the beginning of the following chapter (Section 2.1.1).

technologies, printable piezoelectrics must be developed that can be integrated with other degradable components, for which more sustainable processes must be established.

Yet to date, there has been minimal work done on the development of piezoelectric devices that are both degradable and printable. This void must be filled in order to fully realize a world of green electronics and mitigate the issues of e-waste threatening our world. We propose herein an extended study to evaluate the current state of degradable electronics with a special emphasis on printed and piezoelectric microsystems, and develop methods to realize fully printed piezoelectric devices entirely from green components for future use in various applications such as environmental sensors, smart packaging, consumer electronics, and healthcare.

1.2 Objectives and challenges

This thesis addresses the objective of developing more sustainable piezoelectric microsystems by implementing renewable or degradable materials via additive manufacturing or printing processes. Since the field of printable green piezoelectric materials and applications is sparse, the main objective of this thesis is to refine a robust method of printing degradable or non-toxic piezoelectric materials, and integrate that process with other green components to make entirely printed, piezoelectric devices applicable to the real world. In this project, the necessary manufacturing techniques and protocols to realize these goals will be developed.

Printing of degradable piezoelectric materials and subsequent device integration is still quite premature and thus there is much room for research and development. In relation to this, certain scientific questions must be answered, including:

- What printing or other processing methods can be used to deposit films of eco-friendly piezoelectric materials such that a piezoelectric response is produced? What must be done to achieve this behavior reproducibly?
- What factors influence piezoelectric performance from such printed films? Can this response be tuned through adjustments to processing techniques or ink formulations?
- What sort of considerations must be made for integrating the piezoelectric with other device components such as degradable substrates and conductive traces? What methods or processes can be used to realize this integration?
- What sort of piezoelectric properties can be achieved with fully printed eco-friendly piezoelectric materials, when integrated into green devices using low-temperature processes?

To focus the project, in order to achieve the main objective certain sub-objectives are chosen to be addressed during the project. They are as follows:

- Down-selection of eco-friendly candidate materials for substrates, conductors, piezoelectrics, and ink components, including identification of any materials limitations that may inhibit full process integration
- Development of the piezoelectric ink and the associated printing processes
 - Development of a stable piezoelectric ink including final material selection for degradable or non-toxic piezoelectric materials, solvents, binders, and any other ink components
 - Optimization of printing processes for such an ink, with focus on printing quality and reproducibility
 - Development of procedures for achieving consistent piezoresponse in the printed material by domain orientation via advanced printing and/or poling techniques
 - Adaptation of any processes, as necessary, to low temperatures enabling compatibility with degradable substrates
 - Characterization of the printed piezoelectric layers, including development and validation of measurement techniques for quantifying the effective device piezoresponse
- Progressive integration of the developed process with other green device components
 - Selection or development of a printable degradable conductive material compatible with the processing techniques utilized for the piezoelectric layer, and integration with the developed printing process
 - Integration of piezoelectric and degradable conductive inks with each other and with a degradable substrate
 - Validation of piezoelectric response in fully printed devices on degradable substrates

- Design and realization of piezoelectric demonstrator devices using the developed additive manufacturing processes, including demonstrations of both sensing and actuating functionalities.
 - Utilization of demonstrated piezoelectric response to align with an appropriate end application and direct advanced device design.
 - Manufacture of demonstrations and quantitative evaluation of performance characteristics applicable to the intended device type.

The challenges for this work come predominantly in the form of material processing and manufacturing—the development of low temperature printing processes to print functional materials, and the integration of those materials with each other.

The primary and most critical challenge to overcome is the development of a printable ink that exhibits piezoelectric properties. Piezoelectric materials and their performance are critically linked to the presence of a net dipole moment in the material layer. In microfabrication, this is usually achieved through epitaxial deposition of monocrystalline layers, attaining a dipole through highly oriented crystallinity. However, in printed layers, the attainment of a net dipole is nontrivial, and the method in which the piezoelectric property is achieved must be considered from the onset of ink and process development.

The second major challenge is associated with materials integration. It is critical that all steps of the printing process are compatible with the materials in the other components of the devices. In the simplest form, a printed piezoelectric device is composed of a substrate, two conductive electrodes, and the piezoelectric layer between them. Thus, all processing steps for the piezoelectric material must not compromise the substrate or electrodes, and similarly, the processing of the electrodes and substrate must not compromise the piezoelectric layer. Herein lies a key challenge of this work, as the thermal constraints of degradable substrates (≤ 200 °C) are incompatible with many of the conventional techniques that would otherwise be used. Hence, any processing step developed for the printed conductive and piezoelectric components must be adapted so as to not exceed the thermal limits of the selected substrate material.

By addressing these challenges, this thesis intends to develop printed piezoelectric devices entirely using green components and environmentally friendly additive manufacturing processes for the first time.

1.3 Contributions and thesis outline

This work has established the first ever process for low temperature (< 200 °C) printing of green piezoelectrics through the development and optimization of a screen printable potassium niobate ink. The piezoelectric behavior of this ink on silicon substrates is demonstrated, the process is then transitioned to degradable substrates, achieving effective piezoelectric coefficients as high as 18.4 pC/N on paper substrates. In doing so, this thesis generated knowledge regarding the influence of processing parameters on device performance, validating the ferroelectric poling process and optimizing poling parameters to maximize piezoelectric response while reducing process duration. The first ever fully printed, green piezoelectric devices are manufactured by integrating the KNbO_3 piezoelectric ink with printed electrodes composed of zinc- as well as carbon-based materials. This involved process optimization for the sintering process of screen-printed zinc electrodes compatible with degradable paper substrates. Piezoelectric coefficients as high as 4.6 and 5.1 pC/N were achieved for devices on paper substrates with carbon and zinc electrodes respectively, demonstrating the versatility of the printed piezoelectric with a range of degradable electrode materials. Finally, two types of demonstrator devices are realized, in the form of a paper-based force sensor array and an acoustic micro-speaker, the latter implemented in entirely degradable headphones, using the methods developed in this work.

The thesis structure begins with a review of relevant scientific and technological fundamentals, followed by a discussion of green materials selection. The succeeding chapters describe benchmarks in the process development as the system increases in complexity. Starting with the development of a low-temperature printable piezoelectric ink, then the fabrication and characterization of screen-printed piezoelectric devices with conventional substrates and electrodes. In the next phase, the process is transferred to degradable substrates, and study the influence of substrate material on device performance. In the last phase, degradable screen-printed electrodes are integrated into the system in place of more

conventional evaporated electrodes, and a comparison of device performance is conducted. The work concludes with the exhibition of piezoelectric device functionality through the fabrication of entirely printed degradable sensing and actuating demonstrator devices.

Chapter 2 aims at providing a general introduction to the scientific and technological fundamentals related to this work. First, the concept of “green” materials is described from a broad perspective, including some definitions and considerations for green electronics, and options for potential device materials. Following this, piezoelectric materials are introduced, the relevant theory regarding their working principle, and the general requirements for proper device operation and characterization. Next, an overview of printing technologies is given, including printing methods, ink development, and a brief state of the art on printed piezoelectric materials. The chapter concludes by reviewing the state of the art specifically focused on green printed piezoelectrics, before summarizing the key challenges of this work.

Chapter 3 focuses on initial down-selection of ink components for printed piezoelectrics as well as process validation. To start, target electrode and substrate materials for end goal devices are discussed, as the properties of these components are crucial considerations for further process development of the piezoelectric component. Afterwards, some potential ink component materials are identified, focusing on sustainable or eco-friendly material options. This is followed by piezoelectric material evaluation and feasibility studies of degradable piezoelectrics Rochelle salt, Ammonium dihydrogen phosphate, hydroxyapatite, and zinc oxide. The focus then turns to non-toxic perovskite piezoelectric materials, first conducting process validation with a known material, barium titanate, for both printing integration on degradable substrates and for poling process efficacy at room temperature. With this complete, the chapter ends with initial work on the down-selected piezoelectric material, potassium niobate (KNbO_3 , “KN”), by confirming its printability and ferroelectric nature.

Chapter 4 focuses on the development of a low temperature printing process for a piezoelectric KNbO_3 -based ink. This begins with an overview of the primary fabrication steps (KN powder preparation, ink mixing, and device fabrication) followed by verification of a piezoelectric response in printed KN and the establishment of baseline device characteristics for use as a reference in further process development. Using that procedure, process parameters influencing printed layer quality and device yield (including KN particle size and grinding process parameters, printing methodology, and ink component proportions) are studied. Next, parameters influencing dielectric behavior of devices are assessed, such as printed layer drying conditions and electrode material properties and processing. Finally, parameters affecting piezoelectric performance are studied, with a focus on the source material used in ink preparation, looking into the influence of KN source material, powder crystallinity, and grinding parameters on device response. The discussion concludes with a finalized process appropriate for further integration with degradable substrates.

Chapter 5 concerns the process transfer and steps necessary to print the KNbO_3 ink on green substrates. To this end, devices are designed in the form of circular capacitors and cantilever structures to evaluate the performance of the piezoelectric ink on paper substrates as compared to ideal silicon substrates. Next, the specific fabrication process for these two device architectures on both substrates is detailed. After fabrication, the physical, dielectric, and piezoelectric characteristics of devices fabricated on paper and silicon substrates are evaluated and compared. This study demonstrates a printed KN piezoelectric device manufactured on degradable substrates for the first time.

Chapter 6 focuses on the final phase of this work, wherein green printed conductors are integrated into the printing process to produce entirely printed green piezoelectric devices. The process changes necessary for this integration are detailed for devices made with either carbon or zinc-based screen-printed electrodes. The devices made with the printed electrodes are then compared with thermally evaporated gold electrode devices as used previously, assessing physical, dielectric, and piezoelectric characteristics. Next, a preliminary degradation study is reported on for these devices, showing promising results in a variety of degradation conditions. The study ends by developing two types of demonstrator devices for practical applications. First, the sensing capabilities of this technology platform are demonstrated as a grid of force sensing touch pads entirely printed on paper. In the second, piezoelectric actuation is exhibited by fabricating printed acoustic actuators that are then integrated into a fully green pair of headphones. Both demonstrators are then characterized to confirm their functionality in the intended use case.

Chapter 7 presents a summary of this thesis, including some concluding remarks and future perspectives related to this work and the results achieved herein.

Chapter 2 Printed degradable piezoelectric microsystems: Fundamentals and technology

This chapter introduces the fundamental concepts and discusses the current state-of-the-art with regards to the key topics that are explored throughout this thesis. As this work lies at the intersection of three major research fields (green technologies, printed electronics, and piezoelectrics), we briefly overview each of these topics and the state of their intersections (Figure 2.1). We start with a short discussion of “green” concepts and considerations relevant to this thesis and follow-up with an abbreviated down-selection of component materials for substrates and conductive elements before finishing the section with a brief discussion of green piezoelectric materials. In the next part, we introduce the piezoelectric effect and discuss key figures of merit and processing considerations applicable to device development. The third section overviews printing technologies, with a special focus on challenges and considerations for the additive manufacturing of piezoelectric materials. The last section of this chapter provides an overview of the current state-of-the-art regarding green or printed piezoelectric devices, with particular attention to any works reporting on piezoelectric devices that are both printed and green. We conclude by revisiting the motivations and challenges related to this thesis, and how they connect to this state-of-the-art review.

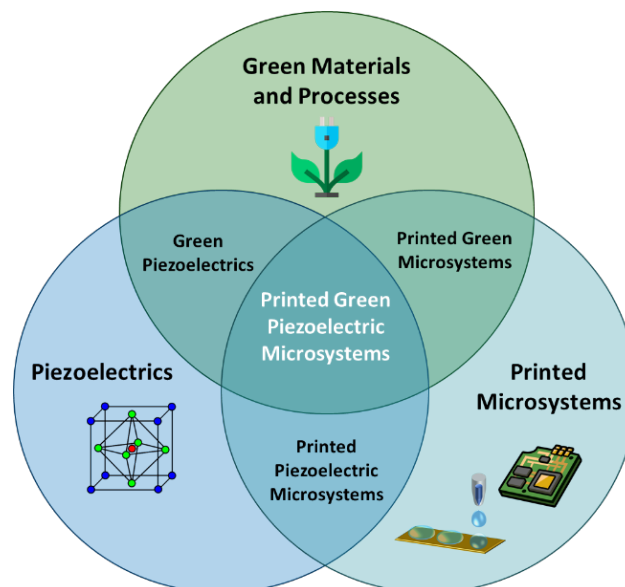


Figure 2.1 Visualization of the three fields relevant to this work: Green materials and technologies, piezoelectric devices, and printed electronics.

2.1 Overview of green materials

2.1.1 Defining “Green”

The Oxford dictionary defines “green” in an environmental context as “being not harmful to the environment”.¹⁰ Yet this term is quite vague when used in the realm of eco-friendly electronics, and makes discussing the field of printed green electronics a challenge. Even so, the body of work concerning green electronics has already been reviewed several times,

notably by Irimia-Vladu, Tan, and Chen (though minimal work has been reported on degradable piezoelectric microsystems, particularly in terms of green manufacturing processes, as will be discussed later in this chapter).^{11–17} Many of these reviews overlap between systems that are (bio)degradable, biocompatible, bioresorbable, or transient. The nuances between these terms are important for future materials selection and are described simply in Figure 2.2. In particular, “transient” can have several interpretations, but generally indicates that the device or material is temporary and has a finite useful lifetime. Thus, it serves as an umbrella term covering both degradable and bioresorbable materials, but not necessarily biocompatible materials.


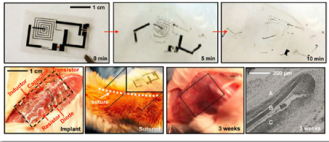

Transient		Intransient
(Bio)degradable	Bioresorbable	Biocompatible
Breaks down in the environment into nontoxic and/or inert components	Safely implantable in humans <i>and</i> disappears after a period of time	Safely implantable in humans without causing them any long-term harm, but remains in place
 Huang2014	 Hwang2012	 Lei2017

Figure 2.2 Distinctions between relevant “green” material terms.

Henceforth, the word “green” is used specifically to describe degradable or environmentally friendly systems unless stated otherwise, not referring to human-compatible systems as that is not the focus of this work. Even so, these terms do not always have consistent definitions based on the authoritative body defining them. *For the purposes of this work, green or degradable electronics are defined as those which can be broken down into constituent parts over the course of several months, such that the base parts are inert and cause no harm to the environment.* This standard is based off the EU standard for compostable bioplastics, which expects that within 6 months, over 90% of the material has degraded into components that cause no harm to the environment (EN13432:2000).¹⁸ For the purposes of this thesis, the primary focus is on the end-of-life aspects of materials, but it is worth noting that mining and manufacturing of source materials have a significant and complex impact on the environment, however such studies are out of the scope of this work.

Table 2.1 Abbreviated list of green electronic materials known to be printable.

	Insulators	Conductors	Semiconductors
Inorganic	Si ₃ N ₄	Au	Ge
	SiO ₂	Fe	Si
	Al ₂ O ₃	Mg	ZnO
	ZrO ₂	Mo	
		W	
		Zn	
Organic	Caffeine	Polyaniline	
	DNA	Carbon	
	Gelatin		
	PCL		
	PLA		
	PLGA		
	PVP		
	Silk		

This EU standard was selected as a framework for this thesis and not as a singular definition due to the complexity of degradation mechanisms involved in electronic systems. Conventional biodegradation involves the breakdown of organic components into simpler compounds (ex: H_2O , CO_2 , CH_4 , etc.), in the presence of microorganisms (typically bacteria or fungi). Other forms of degradation can be chemical degradation (ex: dissolution of soluble ions into water), photodegradation (ex: chemical breakdown in the presence of UV light), or biochemical (ex: enzymatic degradation of fats with lipase).^{19–23}

As we build a technology platform for printed green piezoelectric devices, we must thus take into consideration the materials used for all components of the devices, not solely the piezoelectric, and evaluate the mechanisms of degradation for each when assessing their suitability for the targeted system. It may well be that the device need not fully disintegrate so long as the resulting sub-components are found to be environmentally benign. Morsada, Yu, Ashammakhi, and Cenci all discuss degradation mechanisms for components commonly used in transient electronics.^{17,24–26}

Efforts to improve green processes for degradable microsystems have already yielded success regarding the development of printed insulators, conductors, and semiconductors.^{13,14,27} The full scope of this field is broad and will not be heavily reviewed here. Instead, we highlight in the following sections a small selection of printable degradable materials (with a summary in Table 2.1), and provide an *extensively* expanded list of degradable materials in Section 8.1 of the Appendix for further reference.

2.1.2 Green substrate materials

Proportionally comprising the majority of an electronic device when compared to the functional materials, substrate selection is critical for further process development. Ideal substrates must provide mechanical support for the printed layers, yet minimally affect device performance (along with, of course, being degradable). Furthermore, substrate materials must withstand all processes utilized for all steps in device fabrication—being inert to ink component chemicals and robust to any post-printing curing steps. This may pose a challenge for full process integration.

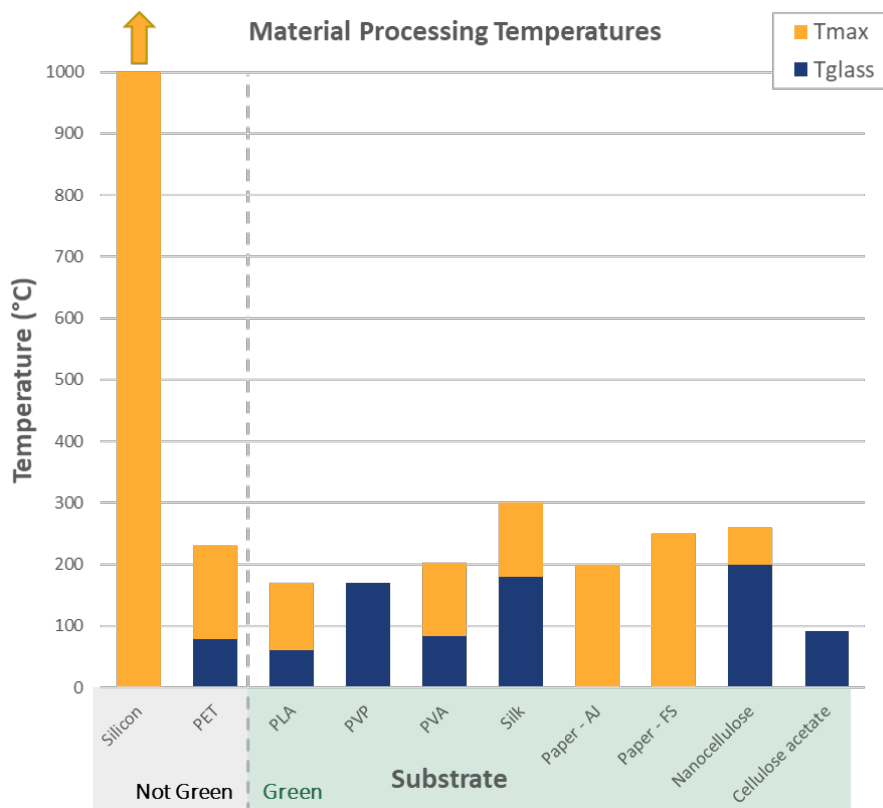


Figure 2.3 Thermal limits of common substrates used for conventional (Silicon, PET) and degradable (others) printed electronics.

With regards to degradability, popular options for substrate material include paper, silk, and PLA. While these materials are readily available, they have a low temperature range in which they can be used and can be challenging to work with. In fact, essentially all degradable substrates used in current research have a thermal limit of 200 °C or below (Figure 2.3). This results from the fundamental limits of certain organic compounds, which destabilize or chemically decompose in the range of a few hundreds of degrees.^{21,28} In fact, the development of high thermal stability degradable substrates as substitutes for PCBs is a major target for green electronics, yet no alternative has become commercially available to date.²⁹

Developing printing processes that are compatible with the low temperature threshold for degradable substrates will be a core challenge in this research. Towards the selection of substrate materials for this work, silk, paper, and other cellulose derivatives exhibit the highest thermal stability.^{30,31} While silk has a larger thermal range of operation, its high solubility in water makes robust device fabrication difficult due to substrate performance variance with changing ambient humidity. Further, the lack of commercial silk products in a form factor suitable for printing processes serves as an unnecessary added challenge. Thus, silk was dismissed as a potential substrate material at the present time. Instead, paper was selected as the focus material due to its renewability, high thermal stability, and commercial availability.

2.1.3 Green conductive materials

Conductive materials are a critical component in any electronic device and must be critically assessed for use in fully printed green piezoelectric systems as electrode materials. While conventionally printed conductors are based on metals, for degradable electronics, some organics such as carbon or polyaniline can be utilized instead, with a tradeoff between processability and conductivity. Due to its green nature, carbon has been a standard material for printed degradable electronics despite its conductivity limitations, with numerous carbon inks commercially available for 3D, inkjet, and screen-printing applications.

In 2014, Yin studied the dissolution mechanisms of metals for transient electronics applications and identified only a small selection of degradable metals: Mg, Mo, W, Zn, and Fe.³² While their reactivity makes certain metals degradable, it also poses a significant challenge with regards to processability and reliability over the lifetime of the device, as these metals oxidize readily into insulating metal oxide compounds and degrade through dissolution in water. Degradable electronic devices produced with foundry processes have deposited these metals (particularly Mg and Zn) generally using electrodeposition or sputtering, but techniques for additive manufacturing of degradable metallic conductors have only recently been reported.

Conventional printable conductors are typically[‡] processed by printing an ink composed of metal particles with a binder, either relying on a high loading of metallic particles to produce a network of conductive traces or, alternatively, consolidating the metallic particulate in post-processing via melting or sintering into more robust cohesive conductive traces.^{33–39} The high temperature melting and sintering methods used for more conventionally used printed conductors (Ag, Cu, etc.) are incompatible with degradable substrates and will need to be addressed if a fully degradable printed device is to be realized. For degradable metals, the metal particles in the inks quickly develop native oxide shells around the metallic core, producing an insulating layer upon printing. Because the metallic cores cannot contact one another, simply relying on a high particulate loading in the ink for conductivity is ineffective and further post-printing steps must be taken to reduce this oxide shell for the desired conductive properties, then sinter the metallic layers into a bulk trace prior to re-oxidation. Such chemical reduction of oxide shells was first shown with (readily oxidizing, but not degradable) copper inks, and was later adapted for use with other metallic systems.^{40,41}

As a structural support, 3D printing of Mg alloys has been studied for several years, utilizing a range of oxide reduction and sintering techniques, however applicability to 2D printing is limited due to high oxidation rates of magnesium films.^{42,43} Karunakaran and Telang both discuss additive manufacturing of Mg in depth. Both Mahajan and Li have developed new techniques for printing conductive Zn traces utilizing sintering techniques compatible with low temperature limited substrates, utilizing photonic curing and anhydride-assisted reactions, respectively.^{33,34} Laser

[‡]Raut provides a nice summary table of metal printing techniques and reported material parameters.

sintering of ZnO has also been investigated to this end.^{36,44} Recently, work at EPFL-LMTS has developed a hybrid electrochemical plus photonic process providing high conductivity and and better stability than the individual processes.⁴⁵

In selecting green printable conductors, both the conductivity of the layer as well as the method of printing must be taken into consideration to ensure that the printing process is compatible with both the piezoelectric and substrate material while also producing a layer with the desired electric properties. To this end, carbon-, magnesium-, and zinc-based inks show the most promise for printed green applications.

2.1.4 Green piezoelectric materials

The recent legislative push to reduce the hazardous material content in electronic goods (RoHS) has resulted in a scientific push to research and develop green piezoelectric materials suitable as replacements for PZT and its derivatives. As a result, the field of “Pb-free piezoelectrics” has surged in popularity, with thousands of research articles published in the last two decades. Reviews on Pb-free piezoelectrics have been conducted by Banerjee, Priya, Aksel, He, Wei, Shibata, Safari, Zhang, Rödel, and Panda, and thus will not be exhaustively discussed here.^{46–57} Within that category, perovskites barium titanate (BaTiO_3 , “BT”) and potassium sodium niobate ($(\text{K},\text{Na})\text{NbO}_3$, “KNN”) along with their many derivatives have dominated the research field as potential replacements for PZT.

Yet while the ferroelectric community is content to consider all things Pb-free as “green”, not all these materials can necessarily be considered harmless to the environment. Bismuth titanate (BiTiO_3), for example, is generally considered toxic to humans due to bismuth leaching over time. Due to the comparatively high stability of perovskite ceramics, the degradation properties of such materials have been poorly studied when compared to organic materials which break down more readily. Chorsi claims such lead-free perovskites are biocompatible as a result of this high stability but does not provide a reference for this information.⁵⁸ Some information can be gleaned from studying those inorganic piezoelectric materials which occur naturally in the environment (ex: quartz, CaTiO_3 , MgSiO_3) or are composed of non-toxic base components (ex: KNN, KN, GaN), but more controlled studies have not been reported to date.

A list of green piezoelectric materials is shown in Table 2.2 below, with indications of what degradation mechanisms have been identified for these materials, their notable piezoelectric coefficients, and which, if any, printing methods have been used to process these materials. This list can be broadly split into categories of inorganic and organic materials. Of the inorganic materials, few have been established as degradable or non-toxic, and fewer still have been implemented thus far in printing processes. The non-perovskite ceramics present remarkable challenges with regards to printing as most of those identified thus far are non-ferroelectric, the complexity of which will be elaborated upon in the following sections. Of the inorganic non-perovskites, only ZnO shows promise for development towards the goals of this thesis based on the precedent for printing of this material.

From the inorganic perovskites, naturally occurring minerals CaTiO_3 and MgSiO_3 are of interest, but minimal work has been conducted to study their properties neither in printing nor in piezoelectric applications. The “sister” materials KNN and KN show great promise based on their ferroelectric nature and (for KNN) printing precedent, with bulk piezoelectric coefficients >400 pC/N for KNN, and >100 pC/N for KN. The lack of commercial utilization of such materials means full degradation studies have yet to be conducted, but first principles and toxicity studies have established both as non-toxic and predominantly inert.⁵⁹ Commercial unavailability of high purity KNN poses a secondary challenge to process development using this material, but is not a limitation with KN.

The selection of degradable organic materials exhibiting piezoelectric behavior is more extensive than for inorganic materials. Many of these materials have been utilized in 3D printing, but in most cases the main focus has been on the fabrication of biological scaffolding, not piezoelectric applications. Furthermore, many of the biological piezoelectric materials exhibit small piezoelectric response, not ideal for practical applications. In order to obtain reproducible piezoelectric properties, most of these organic materials would require the development of new processing protocol, including printing, curing and dipole orientation methods. Only Rochelle salt, ADP, and hydroxyapatite stand out for potential use in the intended application. Rochelle salt and ADP for their large piezoelectric response and solubility in water, and hydroxyapatite based on the extensive literature precedence for printing applications.

The results of this review show a number of eco-friendly piezoelectric materials, but the potentially viable candidates for printing applications are slim: ZnO, KN, Rochelle salt, ADP, and hydroxyapatite. In the following sections, we will discuss the fundamentals, technologies, and challenges relevant to developing one of these materials into a printed piezoelectric device.

Table 2.2 Summary of potential piezoelectric materials, with focus on degradable or printed options. Empty fields indicate that the property is unknown.

	Material	Degradable	Degradation mechanism(s)	Printing precedent	Ferro-electric	d_{ij} (pC/N)	Ref.
<i>Inorganics</i>	GaN	Nontoxic		N	N	2 – 4 [d ₃₃] 1.5 [d ₃₁]	58,60
	AlN	N	n/a	N	N	3 – 6 [d ₃₃] 2 [d ₃₁]	58,61–63
	ZnO	Y	Hydrolysis	SP, IJP, AJP, EHD	N	6 – 13 [d ₃₃] 5 [d ₃₁]	58,64–67
	Quartz	Y	Hydrolysis	N	N	2.3 [d ₁₁] 0.67 [d ₁₄]	58,68
	Topaz (Al ₂ SiO ₄ (F,OH) ₂)	Y		N	N		68
	Tourmaline (CaAl ₃ Mn ₆ (BO ₃) ₃ (SiO ₃) ₆ (OH) ₄)	Y		N	N	1.83 [d ₃₃] 0.34 [d ₃₁] 3.63 [d ₁₅]	68
<i>Perovskites</i>	KNN ((K,Na)NbO ₃)	Conflicting reports		SP	Y	120 – 700 [d ₃₃] 93 [d ₃₁]	53,55,58,61,6 2,69–71
	KN (KNbO ₃)	Untested but nontoxic		N	Y	57 – 109 [d ₃₃]	55,72
	CaTiO ₃	Y		3D	Y		73
	MgSiO ₃	Y		N	Y		73
	LiNbO ₃	N	n/a	N	Y	11 – 23 [d ₃₃] 1 [d ₃₁] 68 [d ₁₅]	49,58,74
	BaTiO ₃	N	n/a	SP, IJP, 3D	Y	190 [d ₃₃] 78 [d ₃₁]	58,70,71,75
	(Pb(Zr,Ti)O ₃)	N	n/a	SP, IJP, 3D	Y	200 – 600 [d ₃₃] 274 [d ₃₁]	58,61,62,76,7 7
<i>Organics</i>	Amino acids (alanine, β-glycine)	Y	Enzymatic, Hydrolysis	IJP		10.4 [d ₃₃] 178* [d ₁₆] 6 – 20 [d _{ij}]	23,52,58,78
	Peptide NTs	Y	Enzymatic	IJP		17.9 [d ₃₃] 60 [d ₁₅]	23,52,58,78
	DNA	Y	Enzymatic, Hydrolysis	IJP		0.07 [d ₁₄]	68,79,80
	Sucrose	Y	Enzymatic	3D			68,81–83
	Cellulose	Y	Enzymatic	3D		19.3 [d ₃₃] 0.1 – 0.2 [d ₁₄] 2.1 [d ₂₅]	23,49,83–85
	Silk-II Fibroin	Y	Enzymatic	3D	N	1.5 [d ₁₄]	58,86
	Starch (amylose)	Y	Enzymatic	3D		2 [d ₁₄]	83,87
	Chitosan	Y	Enzymatic	IJP, 3D		18.4 [d ₃₃]	83,84
	Collagen (bone, tendon)	Y	Enzymatic	3D		2.64 [d ₃₃] 0.2 – 12 [d ₁₄] 2 [d ₁₅]	23,58,68,83,8 4,88,89
	Proteins (fibrin, chitin, elastin)	Y	Enzymatic, Hydrolysis	3D		0 – 9.5 [d ₃₃] 0.1 – 2 [d ₁₄]	52,84,90
	Keratin (hair, nails, hooves)	Y	Enzymatic	3D		0.1 – 1.8 [d ₁₄]	58,83
	Gelatin	Y	Enzymatic, Hydrolysis	3D	Y	20 – 24 [d ₃₃]	52,83,91
	M13 Bacteriophage	Y	Enzymatic	N		0.3 – 12.2 [d ₃₃]	23,92
	PLLA, PLDA	Y	Hydrolysis	3D		6 – 12 [d ₁₄]	23,58,93–96
	PHB	Y	Enzymatic, Hydrolysis	3D		2.9 [d ₃₃] 1.6 – 2 [d ₁₄]	84,95,97–100
	PA-11 (Nylon)	Y	Hydrolysis	3D	N	2 – 7.2 [d ₃₃]	49,95,101
	PVDF	N	n/a	SP, IJP, 3D	Y	33 [d ₃₃] 23, 6.7 [d ₃₁]	49,58,102,103
	P(VDF-TrFE)	N	n/a	SP, IJP, 3D	Y	38 [d ₃₃]	58,95,104,105
	Rochelle Salt (NaKC ₄ H ₄ O ₆ ·4H ₂ O)	Y	Hydrolysis	SP	Y	2300 [d ₁₄]	74,106,107
ADP (NH ₄ PO ₄)	Y	Hydrolysis	N	N	11.7 [d ₁₄]	108	
Hydroxyapatites	Y		SP, IJP	Y	1 – 16 [d ₃₃]	68,89	

2.2 Introduction to piezoelectrics

Piezoelectricity is a fundamental phenomenon in materials science, which describes the ability of certain materials to generate electric charges in response to applied mechanical stress or deformation, and vice versa, to deform when subjected to an electric field. Piezoelectrics are attractive for use in transducing applications due to their relatively large power density and simplicity compared to other mechanisms. They are widely used in commercial applications such as sensors, actuators, energy harvesters, and more, with implementations in MEMS micropositioners, industrial monitors, medical imaging systems, and acoustic devices. The unique properties of piezoelectric materials make them an indispensable component of modern electronics technologies.

2.2.1 Piezoelectric working principle

Piezoelectricity arises from the asymmetry of the crystal lattice structure in these materials, resulting in the displacement of positive and negative charges, creating an electric potential across the material. Such piezoelectric materials exhibit a direct piezoelectric effect when converting mechanical energy into electrical energy, and an inverse piezoelectric effect when converting electrical energy into mechanical motion.

The constitutive equations (in strain-charge notation) to describe the piezoelectric effect in a material are detailed in equations (2.1) and (2.2).

$$\mathbf{S} = \mathbf{s}^E \mathbf{T} + \mathbf{d}^T \mathbf{E} \quad (2.1)$$

$$\mathbf{D} = \mathbf{d} \mathbf{T} + \boldsymbol{\varepsilon}^T \mathbf{E} \quad (2.2)$$

Where \mathbf{S} is the strain vector, \mathbf{s}^E is the elastic compliance matrix, \mathbf{T} is the stress vector, \mathbf{D} is the electric displacement field, \mathbf{d} is the piezoelectric matrix, \mathbf{E} is the electric field, and $\boldsymbol{\varepsilon}^T$ is the material permittivity. For further details on the fundamentals of piezoelectrics, refer to Tichy et al.¹⁰⁹ In simplified tensor notation, the x , y , and z -axes are denoted as 1, 2, and 3 and the more complex shear forms of piezoelectric response in y - z , z - x , and x - y planes as 4, 5, and 6 respectively.

2.2.2 Key characteristics of piezoelectric devices

The performance of piezoelectric materials is characterized with several key figures of merit. For the purposes of this work, focus will be limited to a few core metrics: Curie temperature, piezoelectric coefficient, and relative permittivity. These metrics are essential for understanding and comparing the performance of different piezoelectric materials. However, it is important to note that there are additional factors and parameters that can influence the overall performance and suitability of piezoelectric materials to specific applications, such as mechanical strength, temperature stability, frequency response, and environmental durability. Consideration of these factors is necessary to ensure optimal performance and reliability in practical applications.

2.2.2.1 Curie temperature

When a piezoelectric material undergoes a phase transition, the piezoelectric properties are generally lost. The Curie temperature (T_c) represents the temperature at which this phase transition occurs. The Curie temperature is an important factor in determining the operating temperature range for a particular material and application. This characteristic value will thus be relevant in the materials down-selection process.

2.2.2.2 Relative permittivity

The relative permittivity of the material, ε_r , represents the material's ability to store electrical energy when an electric field is applied. A higher relative permittivity implies a higher charge storage capacity, which is beneficial for applications such as energy storage, capacitors, and dielectric sensors. This value can be determined using impedance spectroscopy with some known geometric parameters. If samples are fabricated with known geometry in a parallel plate construction, the relative permittivity can be calculated following the parallel plate capacitor equation (2.3).

$$C = \varepsilon_0 \varepsilon_r \left(\frac{A}{h_{piezo}} \right) \quad (2.3)$$

Where C is the measured device capacitance in Farads, ϵ_0 is the vacuum constant ($\epsilon_0 = 8.854 \text{ pF/m}$), ϵ_r is the relative permittivity, A is the effective device area, and h_{piezo} is the thickness of the piezoelectric layer.

2.2.2.3 Piezoelectric coefficient

Of primary importance is the piezoelectric coefficient, d , which provides a measure of the materials ability to convert between mechanical and electrical responses. It quantifies the relationship between the applied mechanical stress or strain and the resulting electrical charge or voltage. It is typically reported in two forms, depending on how the value was determined, in picocoulombs per newton (pC/N) when calculated using the direct piezoelectric effect, or in picometers per volt (pm/V) when determined using the indirect effect. Higher values of the piezoelectric coefficients indicate a stronger piezoelectric response and are desirable for applications requiring high sensitivity and efficiency.

As mentioned previously, the piezoelectric coefficient is a tensor quantity related to the geometry of the crystal structure of the material. For the purposes of this work, evaluating and characterizing the entire tensor for each material system was deemed impractical. As such, the focus will be on the specific coefficients most conventionally used in practical device implementations. Commercial piezoelectric devices primarily make use of either the longitudinal or transverse effect.¹¹⁰ In conventional piezoelectric notation, this is represented by piezoelectric coefficients d_{33} and d_{31} , indicating that the resulting charge produced when the material is stressed is either in plane with or normal to the applied stress.

For material down-selection, we will also note degradable materials with significant contributions in shear piezoelectricity, in the form of d_{14} or d_{15} , as will be discussed in the following sections.

The effective longitudinal piezoelectric coefficient, $d_{33,eff}$, can be determined readily using the Berlincourt method, in which a force is applied simultaneously to both the test material and a reference piezoelectric of known characteristics. A relationship between the resulting voltage output is used to calculate the effective coefficient of the sample under test. This method is described further in Section 8.2.1 of the Appendix.

The transverse piezoelectric coefficient, $d_{31,eff}$, can be calculated through the resonance characteristics of a piezoelectric cantilever. By measuring the beam properties around resonance, the quality factor (Q) and $d_{31,eff}$ can be measured at a known actuating voltage. This is detailed further in Section 8.2.2 of the Appendix.

The effective piezoelectric coefficients are heavily influenced by how the material has been processed as well as the geometry of the resulting device, as adjacent materials have the potential to mechanically clamp the piezoelectric and reduce its apparent performance.

2.2.3 Constraints of conventional piezoelectrics

While piezoelectric materials possess unique and valuable properties, they also have certain drawbacks that should be considered. Though the library of materials exhibiting some form of piezoelectric response is large, the subset of those exhibiting strong enough properties for practical applications is fairly limited. This subset is dominated by brittle ceramics (ZnO, AlN, and such perovskites as lead zirconate titanate or barium titanate), which are relatively fragile and prone to mechanical failure, limiting their implementation to low strain conditions. Further challenges arise from the high temperatures required to process these materials, which are commonly sintered at temperatures of 600 °C or above. Though more mechanically robust, piezopolymers generally have lower piezoelectric coefficients compared to ceramics, which can impact their sensitivity and efficiency. They may also exhibit temperature-dependent behavior and lower operating temperature ranges compared to ceramics.

From an environmental standpoint, the dominance of lead-containing PZT and its derivatives is cause for concern. As a toxic heavy metal, care must be taken for proper disposal of PZT-containing devices. Further legislation (Including the EU RoHS 1 Directive) are limiting the use of hazardous materials, including lead, in electronics, providing extra incentive to develop lead-free piezoelectrics.¹¹¹

Finally, as will be briefly discussed in the following section, piezoelectric materials require complex processing techniques to exhibit reproducible piezoelectric performance. This complexity is amplified when the piezoelectric material is additively manufactured as opposed to manufactured with conventional methods.

2.3 Overview of printing technologies and ink development considerations

After a review of green technologies and piezoelectrics, the third technology relevant to this thesis work is the development of additive manufacturing techniques for the green piezoelectric. First, we briefly overview some of the common printing technologies (visually summarized in Figure 2.4), evaluating their advantages and disadvantages such that a specific technique most appropriate for this work can be identified. We then discuss the considerations for ink development towards a printable piezoelectric material, identifying the challenges that will arise therein. We end this section doing a brief state-of-the-art review of printed piezoelectric devices, with a focus on green printed piezoelectrics.

2.3.1 Introduction to printing technologies

In the field of printed electronics, several printing and manufacturing methods are commonly employed. These can be subdivided into conventional and digital printing techniques, with the most common methods summarized in Table 2.3. Conventional techniques are cheaper and faster, but the requirement for a pre-fabricated transfer plate means they lack adaptability to new designs, whereas digital techniques can be re-programmed for new designs quickly, but at the tradeoff of speed. Other solution processing techniques such as dip or spin coating can provide useful insight for the development of specific inks but will not be discussed here. Sreenilayam, Wu, and Aleeva all provide detailed overviews of this topic.^{112–114}

2.3.1.1 Conventional printing techniques

Conventional techniques include screen (or stencil) printing, flexographic, and gravure printing. These techniques tend to be more cost effective than digital techniques, with significantly higher printing speeds. They tend to use higher viscosity inks comprised of particles in dispersion which are comparatively stable compared to the inks used for such digital processes as inkjet or EHD printing. Their primary disadvantage comes in the lack of pattern adaptability, as the masks, meshes, and rolls must be fabricated in advance of printing (but can generally be reused many times).

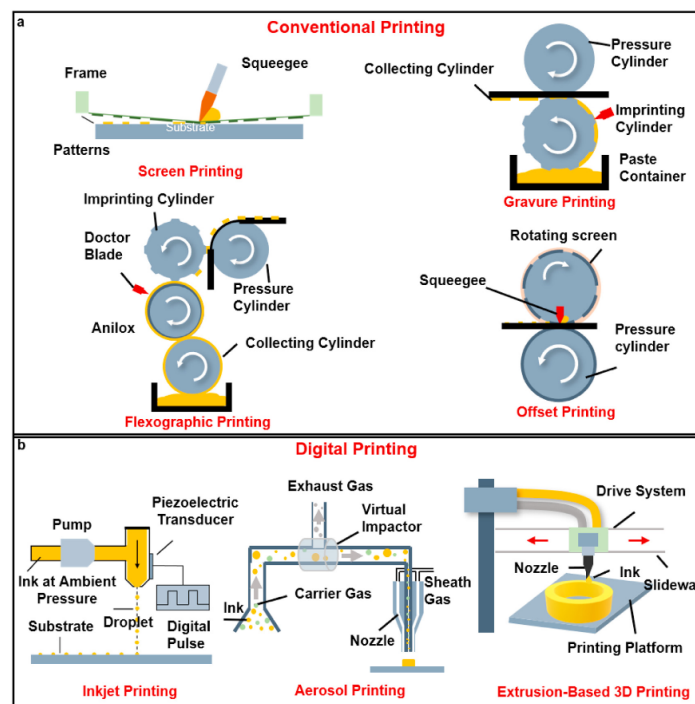


Figure 2.4 Schematic description of common printing techniques. Figure from Li.¹¹⁵

Screen printing is a well-established technique, where ink is pushed through a fine mesh screen onto the substrate, creating patterns matching the apertures in the mesh. Being very cost effective and fairly straightforward, it is ideal for large-scale production and can print a diverse range of inks and is one of the most commonly used techniques in printed electronics as a result. Screen printing inks are typically high viscosity particle dispersions and produce films in the range of a few

microns in thickness. Printing resolution is limited by the weave of the mesh and is usually limited to 50 μm or greater as a result.

Roll-to-roll processes including screen, flexographic, and gravure printing are frequently used for high-volume production in printed electronics. Using flexible relief plates and a rotary printing press (flexographic) or ink-filled patterns engraved into the cylinder (gravure), ink is quickly transferred onto the substrate. These processes are extremely high speed but require high levels of precision and ink development for consistent fabrication.

Table 2.3 Comparison of printing technique characteristics. Adapted from Li and Garlapati.^{115,116}

Type	Technique	Ink viscosity (cP)	Print resolution (μm)	Print thickness (μm)	Print speed (m/min)	Throughput (m^2/s)	Contacting
Conventional	Screen	500 – 5000	30 – 50	5 – 100	0.5 – 20	Med-High	Contact
	Flexographic	50 – 500	45 – 100	<1	5 – 180	Med-High	Contact
	Gravure	100 – 1000	10 – 50	<1	3 – 100	High	Contact
Digital	Inkjet	2 – 20	30 – 50	<1	0.02 – 500	Low-High	Non-contact
	Aerosol Jet	1 – 1000	<25	<1	0.01 – 0.06	Low	Non-contact
	EHD Jet	1 – 10^4	~ 1	<1	0.01 – 0.5	Low	Non-contact
	3D Printing	5 – 20	50	16 – 30	18 – 30	Med	Contact

2.3.1.2 Digital printing techniques

In comparison to the conventional techniques, digital printing techniques are a more recent development. Processes such as inkjet, aerosol jet, and extrusion printing (including Fused Deposition Modeling and Direct Ink Writing) do not require pre-fabricated designs, and instead can be adjusted digitally, to allow a greater flexibility in patterns and thus faster design iterations and customization.

Inkjet printing is widely used for printed electronics, allowing the precise deposition of conductive, semiconductive, or insulating inks onto a substrate using jetting nozzles. It offers high resolution and versatility, making it suitable for various materials. Inks for inkjet printing can be composed of either precursor solutions or particle dispersions and have much lower viscosities than the inks used by screen printing. The development of stable inkjet inks is non-trivial as a result, and the thin printed layers (sub-micron) deposited can be a drawback for some applications.

Aerosol jet printing is a non-contact technique that uses a high-velocity, directed gas stream to the deposit aerosolized droplets of the ink (typically a liquid-phase polymer or an ink dispersion containing nanoparticles of the functional material) onto the substrate, enabling precise printing of fine features. It is particularly suitable for printing onto complex and three-dimensional surfaces due to the programmable directionality of the printing nozzle and the fast-drying nature of the ink, but the establishment of reproducible printing parameters for novel inks can be a highly involved process.

Finally, 3D printing methods are increasingly being utilized for printed electronics. It allows the fabrication of complex three-dimensional structures with embedded electronics using techniques like Fused Deposition Modeling (FDM) and Stereolithography (SLA). These processes permit higher complexity devices with the addition of a vertical axis to the printing process.

2.3.2 Printing figures of merit and ink formulation considerations

2.3.2.1 Ink and printed layer figures of merit

To assist in ink development, certain figures of merit are taken into consideration. These include both properties of the ink itself as well as those of the resulting printed layers. Key properties of the ink itself include fluid rheology, volatility, and shelf life. For the printed layer, layer thickness, surface roughness, and adhesion to the substrate are critical properties, followed by more specialized performance properties depending on the purpose of the printed layer such as mechanical flexibility and environmental stability.

The ink's viscosity affects its printability and the resolution of the printed features. It should have an appropriate viscosity to allow for smooth printing while maintaining the desired feature dimensions. Ink viscosity must be adjusted appropriately for the intended printing technique and can be measured empirically using rheometry. Ideal inks should be

made of easily accessible and cheap materials and be shelf-stable over long time periods (months to years) without significant changes in its properties or performance, but this comes secondary to other factors for initial development.

For the printed layers, figures of merit are primarily associated with physical characteristics, though it is worth noting that the printing technique utilized also influences into these properties. Layer thickness and surface roughness can be empirically determined using profilometry or confocal microscopy. Film adhesion is critical for robust printed electronics, and is highly dependent on ink composition and interaction chemistry with the materials onto which the ink is printed. It can further be affected by printing techniques and curing conditions, as residual stresses in printed layers from fast curing or excessively thick films result in cracking and delamination. Layer adhesion can be determined using ASTM F1842–15.¹¹⁷

Finally, functional layers for printed electronics should exhibit high stability against environmental factors such as humidity, temperature, light exposure, and chemical exposure. They should be resistant to degradation or changes in electrical properties over time. This property poses a particular challenge for this work, where the intent is to develop devices that are degradable at End-of-Life. A careful balance must be maintained to achieve reproducible device performance from degradable and green materials.

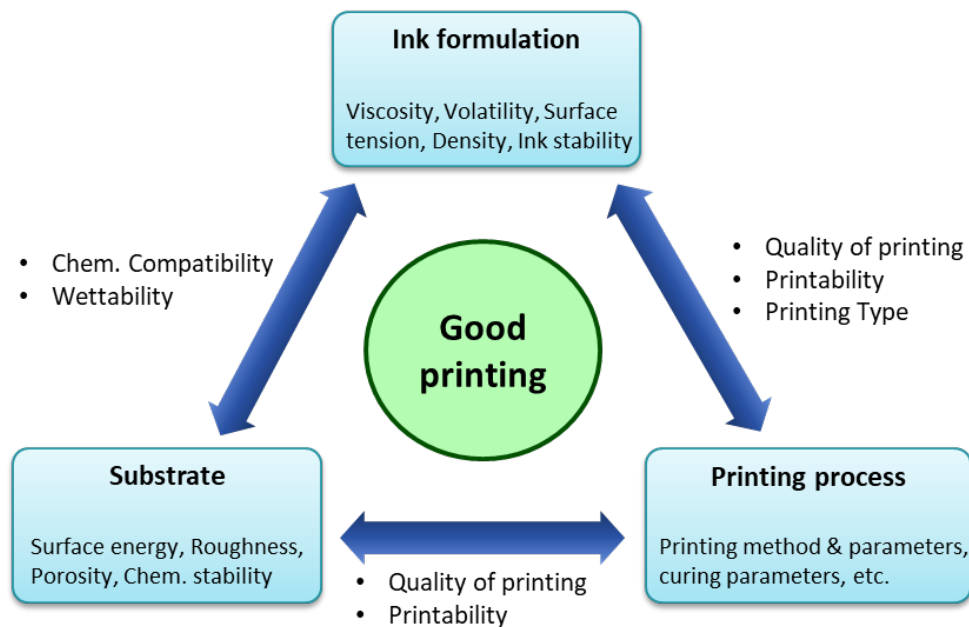


Figure 2.5 Printing considerations and interplay. Figure adapted from Mancinelli.¹¹⁸

2.3.2.2 Ink formulation considerations

Ink development for printed electronics requires a careful balance of ink formulation, substrate considerations, and printing processes. This balance must be maintained to ensure that the resulting layer is a continuous film with appropriate mechanical properties without compromising the electrical functionality of the film in the process. Some of the many considerations for this balance are detailed in this section (and summarized in Figure 2.5 above), though this discussion is not exhaustive.

Ink formulation may include selecting component materials (any functional materials, binders, or solvents) that result in a stable dispersion or solution but must also consider appropriate rheology appropriate for the intended printing process while ensuring that all components are compatible with the substrate material. Additionally, the surface chemistry of the substrate and its interaction with the deposited ink play an important role in film adhesion. Ink wettability on the substrate is also influenced by substrate surface properties (chemistry, roughness, porosity), which further influences printing resolution and film thickness.

The volatility of solvents used in ink formulation affects the drying rate of the printed layer. This should be sufficiently fast to reduce manufacturing time, but not so fast that the ink dries before the printing process is complete. This is especially relevant for processes that involve printing nozzles, where fast-drying inks result in nozzle clogging.

Meanwhile, printing parameters for film curing can influence solvent removal rate, for example with higher temperature curing steps accelerating evaporation. Too-fast solvent evaporation can result in residual stresses in the printed film that may lead to layer cracking and delamination, so printing parameters and ink formulation must be adapted to prevent this.

Ink viscosity must be low enough to allow for printing, but if the ink is not viscous enough, the printed layers may not form a continuous film. Meanwhile, an overly thick ink can present challenges with certain types of printing. Viscosity of the ink can be influenced by the ratio of components in the formulation in addition to their properties. Larger particle sizes for components result in more viscous inks but may prove too large for nozzle or mesh apertures. Similarly, increasing binder content can increase viscosity, but if too high, will also result in residual stresses in the printed film.

As mentioned above, these are but a few of the considerations required when developing a novel ink formulation. In the following chapters, we will discuss specific parameters in more depth as we work towards the development of a novel piezoelectric ink formulation.

2.3.3 Piezoelectric ink development

Inks for printed piezoelectrics generally come in one of two forms;[§] either as a dispersion of particles in a carrier fluid that is printed directly or as a solution of precursor chemicals that are reacted to form the target material post-printing. We provide some brief considerations here of the challenges associated with each method, and direct the reader to works by Derby, Zhang, and Zavanelli (among numerous others) for further details.^{112,119–123}

2.3.3.1 Particle dispersion printing

Inks of this form consist of three primary components: a carrier fluid^{**}, the active ingredient, and a binding agent. Depending on the interaction of these components, further additives may also be included to stabilize the dispersion. This type of ink is more commonly used with stencil, screen, and inkjet printing than other forms of printing.

A key challenge in developing such inks is to produce an ink in the correct viscosity range for the designated printing application that is also a stable dispersion of particles. Depending on the interaction chemistry of the particles with the fluid and with each other, particles can agglomerate and then sediment in the ink. Particle agglomeration poses a particular challenge for polarized particles (such as piezoelectric materials), and commercial inks compensate for this through the use of dispersants and stabilizers that neutralize surface charges in the particular to improve dispersion in the carrier fluid. These components can be burned out of the resulting layer after printing in a baking step, which is a necessary step for processes in which the neutralization of surface charges is undesirable for layer functionality. Yet most commercial dispersants generally specify burnout temperatures above 300 °C to ensure full volatilization of organic constituents, making not suitable for use in the low-temperature processes we currently target.^{124–126} No viable dispersant or surfactant has been identified in the literature that has both a burn-out temperature below 150 °C and was environmentally friendly.^{††}

The particle size of solid components can further affect ink stability, with larger particles more likely to sediment than smaller ones. It may be necessary to modify the material either during synthesis or using milling processes to reduce particle size and achieve a stable dispersion. Further, printing processes require that ink particulate is significantly smaller than the aperture through which it is being printed, in order to prevent clogging. For example, inkjet printing conventions recommend particulate of diameter that is 1% the diameter of the printhead nozzle. Conventional inks for screen printing require particulate to be <10 μm in diameter.

Of note, inks can be dried, cured, or sintered in a number of different ways depending on the binding agent material(s) in use, with solvent evaporation as the simplest, but including chemical, thermal, or UV curing.^{124,127} As many of these processes are not compatible with the processing limitations of degradable electronics, the more facile solvent evaporation binders are preferred for this work.

[§] A third category for printing polymeric piezoelectrics such as PVDF and PLLA will not be discussed here.

^{**} The terms “Carrier fluid” and “solvent” are referred to interchangeably with regards to ink components throughout this work.

^{††} One surfactant, Triton X-100, has a burn-out temperature in the appropriate range, but is banned in the EU due to environmental toxicity.

2.3.3.2 Precursor or sol-gel printing

Generally speaking, the alternative to dispersion-based inks is liquid phase inks. This can come in the form of polymers dispersed in a solvent (e.g., PVDF), or involve inks containing dissolved precursor agents that are reacted post-printing to synthesize the desired active material, often taking advantage of sol-gel chemistries for ink formulation (e.g., PZT).¹²⁸ With an ink formulation that is entirely liquid phase, such inks are well suited to high precision processes such as inkjet or aerosol jet printing where nozzle clogging from solid particulate is a known challenge, but is also applicable to other printing methods. Further, this ink form permits the printing of thinner active layers that are not limited by the source ingredient powder size. Drawbacks for such inks include issues with the solution chemistry to achieve the desired material without compromising ink rheology or stability. Further challenges arise from the post-printing steps, which can require high temperatures or long processing times.¹²⁹

2.3.4 Printed piezoelectric microsystems

Some precedent for the development of a printed green piezoelectric device can be gleaned from the techniques used to print other piezoelectric materials. A huge amount of effort has been made in the printing of piezoelectric materials thus far, with a strong focus on PZT, ZnO, PVDF, and BaTiO₃. Sol-gel processes have been heavily used to inkjet or screen print piezoelectric materials, including PZT and PZT-type compounds, BiFeO₃, BaTiO₃, BNT-BT, BZT-BCT, BNKT, KNN, KNN:Mn, AlN, and ZnO (nanowires, nanoribbons, nanorods, etc.).^{61,62,130–136} PVDF and PVDF-TrFE have also been screen and inkjet printed in recent years. PVDF, which is biocompatible but not degradable, has had significant focus for wearable electronics applications.^{104,106,134,137,138}

Even focusing the review to solely Pb-free printed piezoelectrics, minimal work has been conducted to develop low temperature (<200 °C) processes, as would be necessary for use with degradable paper substrates. Processes for perovskites (BT, KNN, etc) require sintering well above this thermal limit.^{48,52,152,153} Standard ceramics printing technologies utilize inks with very low binder content, producing a loosely assembled green body that requires a post-printing sintering step at temperatures of 800–1200 °C. Even the most advanced “low-temperature” processes for ceramics still sinter above 600 °C.

Table 2.4 State of the art on low-temperature printed piezoelectrics showing studies with the lowest reported maximum processing temperature for several commonly utilized piezoelectric materials. Abbreviations for printing methods include screen printing (SP), inkjet printing (IJP), and electrohydrodynamic jetting (EHD).

Piezoelectric Material	Printing Method	Substrate (s)	Electrode (s)	T _{Max,Bulk} (°C)	T _{Max,Work} (°C)	d _{33,Bulk} (pC/N)	d _{33,Work} (pC/N)	P _{r,Work} (μC/cm ²)	E _{c,Work} (kV/cm)	Ref.
(K,Na)NbO ₃	SP	Al ₂ O ₃	Pt	1060 – 1105	850	100 – 300	88	5 – 10	57.3	139–142
PZT	SP	Si	Pt, Ag	900 – 1200	750	593	101	—	—	61,143,144
BaTiO ₃	IJP	ZrO ₂	Pt	1100 – 1230	600	190	—	3.1	1.1	145–147
BaTiO ₃ -PUA Composite	SP	Steel	Ag	—	150	—	1.31	—	—	148
PVDF-TrFE	IJP	PI, PET	Ag	140	140	32	—	—	—	104,149
ZnO	EHD	Si, PET	ITO	1100 – 1300	25	6 – 13	23.7 ^(PFM)	—	—	58,150,151

A compromise can be made by instead producing a polymer-ceramic composite, which can be fabricated at lower temperatures, but at the cost of a significant reduction in piezoelectric response. Towards the development of Pb-free piezoelectrics, several groups have reported on ceramics composited with PVDF or PDMS, with barium titanate and KNN both commonly used as the ceramic component.¹⁵⁴ Table 2.4 summarizes some common piezoelectric materials, their conventional properties (maximum process temperature, piezoelectric coefficients), and the properties measured when printed at the lowest reported processing temperature. An expanded table reviewing works reporting printed piezoelectrics can be found in Section 8.3 of the Appendix.

2.3.5 Techniques for dipole orientation in printed piezoelectrics

The fundamental nature of piezoelectricity lies in the asymmetry of the material on a crystalline level resulting in a net dipole moment across the structure. This can present itself in organic polymer materials based on the orientation of the constituent components, or in inorganic materials from a molecular level.⁵⁸ A subset of piezoelectric materials includes ferroelectric materials, for which the polarization of the structure can be changed through the application of a sufficiently large external electric field.

Typical printing processes result in the random deposition of particulate onto the substrate, with no concern for orientation. This stochastic positioning of particulate is unsuitable for piezoelectric applications, as the random alignment results in a net zero dipole moment across the bulk of the material and thus no observable piezoelectric effect. A diverse range of techniques have been established in recent decades to produce this net dipole in printed piezoelectric materials, either during the material fabrication process, or in a post-processing polarization step if the material is ferroelectric in nature.

For non-ferroelectric piezoelectric materials, the active material *must* be oriented during the deposition process. The directional deposition methods used in conventional microfabrication (ex: atomic layer deposition, chemical vapor deposition, or similar techniques), are not suitable for solution-based processes and thus cannot be used.^{155–158} Instead, sol-gel methods are regularly used to synthesize the material layer, either directly onto a crystalline substrate or in a solution mixed with seed crystals that aid crystal growth in the preferred direction.^{132,159–161} Techniques using blade-casted sol-gel solutions impregnated with high-aspect ratio seed crystals have been shown to produce well-oriented grains in the resulting piezoelectric material layers.^{85,162}

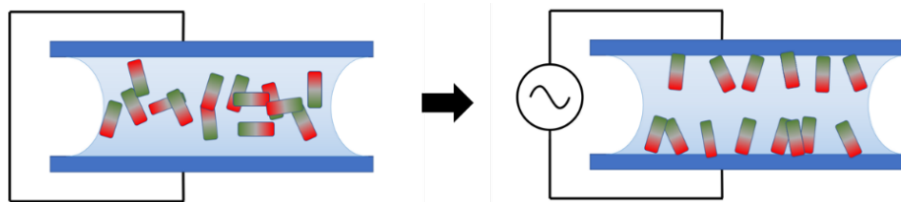


Figure 2.6 Schematic showing the concept of dielectrophoresis.

As an alternative, recent work has focused on particulate orientation using dielectrophoresis.^{163–165} Herein, an external field is applied to the ink immediately following deposition, acting on the dispersed piezoelectric material particulate prior while it is still mobile in the carrier fluid (Figure 2.6). This promotes the orientation of the individual particles along the electric field, which then is maintained once the ink is dry. While this option shows promise, process parameters (applied field strength, frequency, duration, etc) must be defined uniquely for each ink composition, which can be a challenge. Additionally, the process requires the introduction of electrodes prior to ink drying, which increases the complexity of the manufacturing process.

The above-mentioned methods are commonly used for printed ferroelectrics, but the material response can be further enhanced through electric poling. There are several common poling methods used for ferroelectric materials to induce and control their polarization, however the primary methods are direct field poling and corona discharge poling.

As the most widely used method for poling ferroelectric materials, direct poling it involves applying a strong electric field to the material, typically above its coercive field, to reorient the domains and induce a desired polarization direction (see Figure 2.7(a)).^{166–170} The material is usually heated above its Curie temperature to enhance domain mobility during poling. The material is then cooled while maintaining the applied electric field, thereby "freezing" the polarized state. This method has several drawbacks, including increased likelihood of dielectric breakdown as the material is in direct contact with the electrodes, and the necessity to uniformly heat the material, which is typically done in a bath of silicone oil and thus is not practical for printing applications.

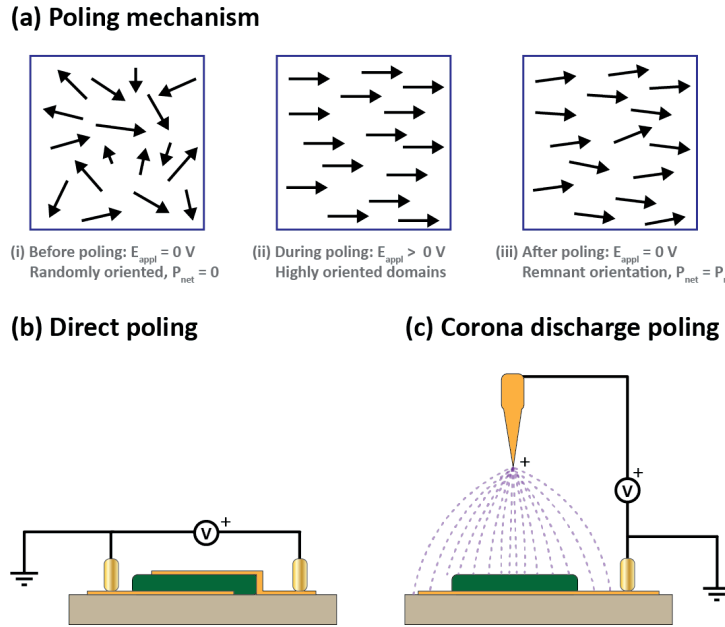


Figure 2.7 Poling mechanism schematics showing (a) general poling mechanism steps, as well as (b) direct and (c) corona discharge poling configurations.

Corona discharge poling is an alternative to direct poling whereby charge is “sprayed” from a needle onto a material sitting on a grounded backplate, but whose surface that has no electrode, thus generating a field across the sample surfaces.¹⁷⁰ This non-contact method prevents breakdown at weak points in the material, and permits a wider range of electrode configurations and larger device areas. The tradeoff lies in the challenge of establishing robust parameters (voltage, duration, gap distance, etc.) for reproducible processes.

2.4 State of the art on degradable and printed piezoelectric microsystems

In this section, we provide a complete overview of the available literature regarding degradable piezoelectric microsystems, reviewing both non-printed and printed instances. We find that while the materials and technologies to realize fully printed, fully green piezoelectric devices have been demonstrated, the full realization of such devices are yet to be seen, as there are still great challenges to overcome to that end. Direct comparison of degradable device piezoelectric performance in literature is made difficult by the lack of standardized parameter reporting, but is provided when available.

2.4.1 Degradable piezoelectric microsystems

Demonstrations of fully degradable piezoelectric devices are scarce in the current field of research. Essentially all examples of green piezoelectric devices have been published within the last ten years, with one of the earliest works was Gullapalli’s ZnO NW-paper composite strain sensor in 2010.¹⁷¹ Chorsi’s notable 2019 review concisely overviews the majority of advances in degradable piezoelectrics through the the early developments, including implemetaions in cell characterization, energy harvesting, biochemical sensing, pressure sensing, and healthcare monitoring.⁵⁸ Paper impregnation with nanostructures continues to be a common method of piezo device fabrication, with several works devoted to ZnO NP-paper devices (as exemplified by Wang’s accelerometer in Figure 2.8(a)).^{172–177}

ZnO NW energy harvesters have been the focus of much research for applications in transient implantable devices. Zhu used cleanroom techniques to deposit aligned ZnO NWs in a flexible energy harvester.¹⁷⁸ Dagdeviren demonstrated a fully bioresorbable harvester utilizing piezoelectric ZnO with Mg contacts, with fabrication based on cleanroom techniques (e.g., sputtering, evaporation), but does not provide an empirical piezoelectric coefficient (depicted in Figure 2.8(b)).¹⁷⁹

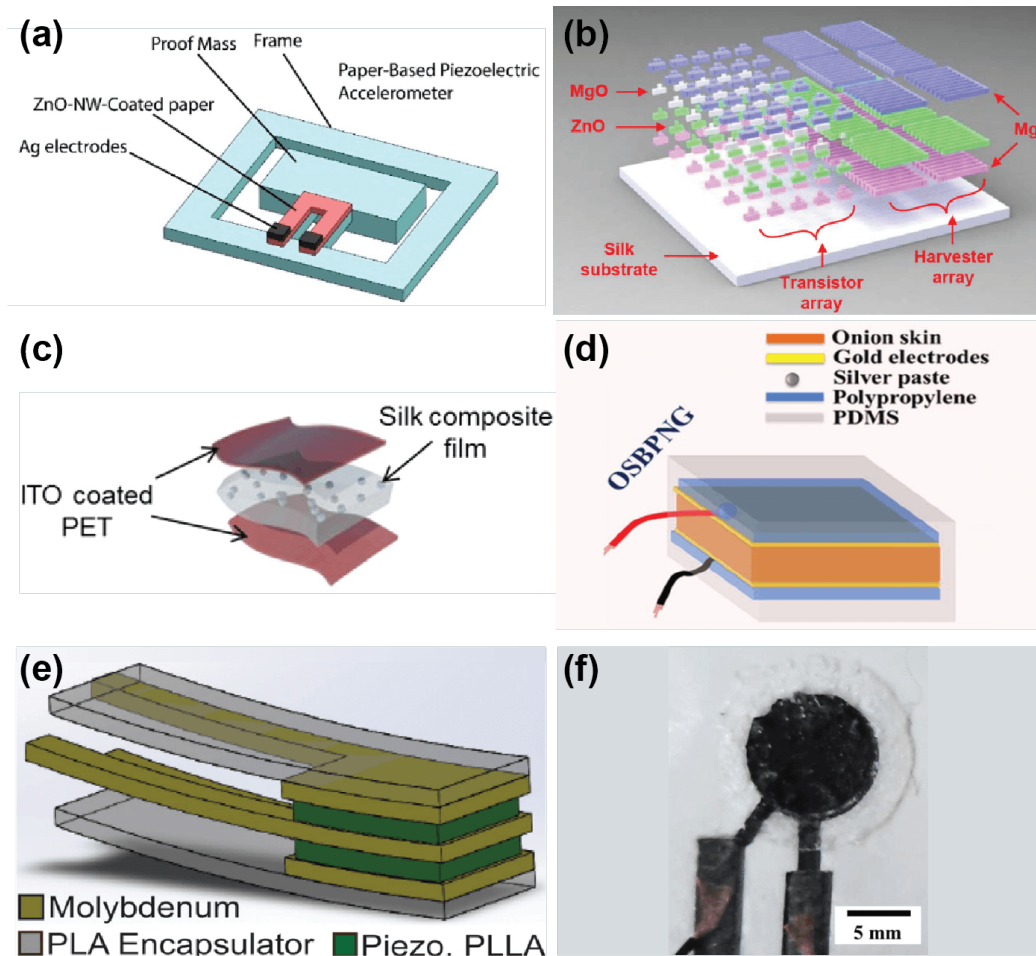


Figure 2.8 Examples of piezoelectric devices utilizing green materials for some or all of the device components. (a) Piezoelectric accelerometer fabricated using ZnO-impregnated paper.¹⁷⁵ (b) Energy harvester microfabricated using all green components, with ZnO thin films as the piezoelectric material.¹⁷⁹ (c) Silk-fibroin based nanogenerators utilizing Pb-free ferroelectric materials dispersed in a fibroin matrix.¹⁸⁰ (d) Nanogenerator utilizing onion skin as the piezoelectric component.¹⁸¹ (e) Force sensor comprised of all green components, fabricated from laminated layers.¹⁸² (f) Fully printed transducer utilizing Rochelle Salt as the piezoelectric and carbon for electrode materials on paper substrates.¹⁸³ Images reproduced from Wang, Dagdeviren, Kim, Maiti, Curry, and Lemaire respectively.

Piezoelectric biopolymers including silk, cellulose, and collagen have been composited with ferroelectric materials (including PZT and hydroxyapatite), then cast into films and implemented into pressure sensing and energy harvesting devices (Kim's silk-perovskite compsite is depicted in Figure 2.9(c)).^{88,180} Lemaire developed Rochelle salt-impregnated paper for degradable piezoelectric applications through a facile room temperature solution based impregnation process, using non-degradable copper electrodes and later screen-printed Ag electrodes, from which a piezoelectric coefficient of 3–25 pC/N was measured.^{184,185} In another work, Lemaire developed fully degradable devices by transferring Rochelle salt monocrystals onto paper substrates with screen-printed carbon electrodes.¹⁸³ By using natural wood scaffolding, Lemaire manufactured self-oriented Rochelle salt composites, with printed carbon electrodes, reporting a piezoelectric response (d_{33}) of 11 pC/N.¹⁸⁶

Recent work has focused on methods for orienting cellulose fibers for use in piezoelectric applications, with success found using cellulose micro- and nanofibrils and utilizing strong external fields during film casting to achieve alignment.^{187–190} Kim also developed an electro-active paper piezo-actuator via the mechanical alignment of wet cellulose fibers, demonstrating acoustic performance of devices with thermally evaporated Au electrodes, with a maximum piezoelectric response (d_{31}) of 5.2 pC/N.¹⁸⁷ Kim^{††} utilized chitin films obtained from biological sources to manufacture audio transducers using Ag NW electrodes.¹⁹¹

^{††} Different Kim.

Maiti and Karan have made progress in recent years into the development of high energy density piezoelectric energy generators from bio-waste materials such as onion, fish scales, chicken feathers, and spider silk (see Figure 2.8(d)).^{181,192-194} Their current methods used for fabrication focus on the development of a piezoelectric films with sputtered or painted electrodes, yet none of their works have demonstrated fully degradable devices thus far. Biological piezomaterials including M13 bacteriophage, diphenylalanine peptide nanotubes, and semi-crystalline amino acids have been implemented into energy harvesters by several groups for potential use in implantable devices, overcoming the processing challenges of biological components through self-assembly strategies to achieve oriented layers.^{195,196}

Poly-L-lactic acid (PLLA) has shown great promise for degradable and biomedical piezoelectric applications, having been utilized for a variety of cell and tissue actuators, with Tajitsu developing biocompatible PLLA piezoelectric tweezers for thrombosis treatment.⁵⁸ Curry developed the first fully degradable piezo force sensor in 2019 using PLLA foil sandwiched between sheets of molybdenum ($d_{14} \approx 11$ pC/N), and later improved upon this design with electrospun PLLA, in one of the few continuing works to demonstrate the full degradation of a piezoelectric sensor (Figure 2.8(e)).^{197,198}

2.4.2 Printed degradable piezoelectric microsystems

With regards to materials that are both degradable and piezoelectric, only a small number have been fabricated using printing technologies, and of those, reports focused on printing specifically for piezoelectric applications is even less common. Cellulose, collagen, silk, PLLA, and even DNA have been 3D printed for structural applications, but none have been reportedly printed for piezoelectric uses.¹⁹⁹⁻²⁰³

On another front, sol-gel synthesized hydroxyapatite was spin-coated on silicon with reported piezoelectric coefficients as high as 8 pC/N as measured with piezoforce microscopy (PFM).²⁰⁴ Markham followed this work, reporting a piezoelectric coefficient (d_{31}) of 0.02 pC/N for with screen printed hydroxyapatite films on ITO substrates.^{205,206}

Printing of ZnO is particularly well developed due to its semiconducting properties, with over 30 different publications describing methods of screen or inkjet printing of the material.^{66,207-219} Despite this enormous body of work, none of these reports focus on the printing of ZnO specifically for *piezoelectric* applications, save one. Garcia-Farrera reported in 2019 on near-field electrohydrodynamic jetting of ZnO thin films on Si and PET, with a piezoelectric coefficient of 23.2 pm/V as measured by PFM.¹⁵¹ Their work noted the necessity of a large local electric field and ionization of the feedstock solution for successful ZnO particle orientation. If this material is to be used, new manufacturing techniques must be developed to allow for the oriented deposition of ZnO for good piezoelectric properties. Of the literature reporting ZnO printing for non-piezoelectric applications, one of the most common methods involves printing a Zinc hydrate precursor followed by thermal reduction and annealing at temperatures above 500 °C. While this method is readily reproducible and prevents common nozzle clogging issues, the high temperature post-processing limits the substrates with which it can be used; indeed, nearly all works demonstrating this method have done so on glass or silicon substrates. Utilizing this method would require overcoming this processing temperature constraint in addition to developing a method for dipole orientation in the resulting ZnO layer (this has been demonstrated recently for other sol-gel based indium oxides using Deep-UV curing, but has yet to be reported for piezoelectric ZnO).¹¹⁸

Finally, Lemaire has been developing methods of processing Rochelle salt into biodegradable devices, first developing impregnation and transfer methods as mentioned previously. Lemaire then presented preliminary results on inkjet and screen printing processes for Rochelle salt films on paper substrates (depicted in Figure 2.8(f)).^{183,185,186,220} Thus far, Lemaire has not published any fully printed green piezoelectric device, continuing to utilize non-degradable electrodes. Despite this, Lemaire's work is the only known system integrating printing techniques with degradable piezoelectric materials onto green substrates for full device realization.

2.5 Challenges and conclusions

We wish to develop processes for a printable and environmentally friendly piezoelectric device. Since the field of printable green piezoelectric materials and applications is sparse, **the main objective of this thesis is to develop more sustainable piezoelectric microsystems via printing, including the development of a novel ink formulation, establishment of a process for achieving a piezoelectric response, and integrating this process with sustainable materials into fully printed piezoelectric devices applicable to the real world.**

In this chapter, we have reviewed some of the fundamental concepts relevant to green materials, piezoelectricity, and printing technologies. We have also reviewed where current research has made progress at the intersections of these three fields, looking into printed piezoelectrics, green piezoelectrics, and finally printed green piezoelectrics. We used this review to identify some promising materials and techniques for the fabrication of fully green, fully printed devices, as well as identifying the challenges with achieving the goal.

Our review found that minimal work has been done on developing printing methods for green piezoelectric materials specifically for piezoelectric properties. Even further, none have yet integrated additively manufactured piezoelectrics intentionally with degradable electrodes and substrates to achieve fully green, fully printed piezoelectric devices.

While many green piezoelectric materials have been identified, the piezoelectric response of most of these materials is prohibitively low for practical applications, making down-selection of piezoelectric material a non-trivial process. The conventional methods of processing piezoelectric materials (e.g., sputtering, sol-gel, etc) are in opposition with the thermal limitations of degradable substrate materials, so one major challenge will be developing processes for both piezoelectric and conductive materials that occur entirely below 200 °C for compatibility with degradable substrates.

Both screen and inkjet printing show promise for piezoelectric applications, but screen printing is preferred for initial development due to the simpler ink formulation. Though viable screen-printing ink formulations have been made for non-degradable piezoelectric materials, the development of a stable piezoelectric ink with reproducible properties is challenging. The thermal constraints of degradable substrates will limit what processes can be utilized during material deposition and treatment and process development towards proper dipole orientation is a particular challenge for printed piezoelectrics. Finally, developing processes to integrate the conductive and piezoelectric layers onto green substrates without compromising material properties will require finesse and careful advanced planning for success. Figure 2.9 summarizes some of these key challenges associated with the primary components of a piezoelectric device (substrate, conductive elements, and piezoelectric elements).

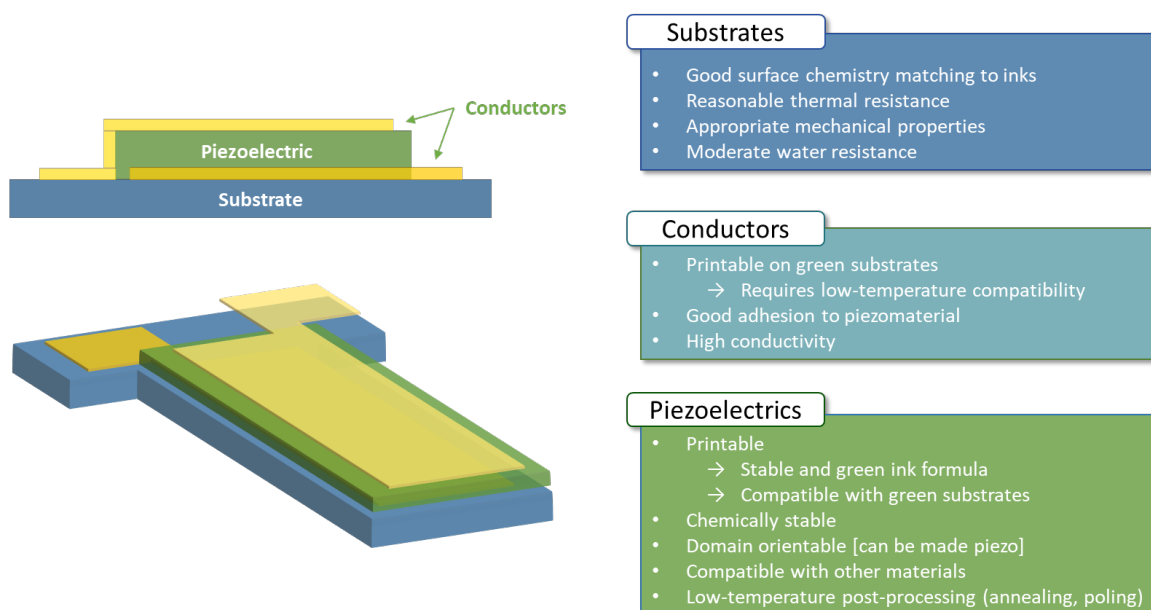


Figure 2.9 Thesis challenges associated with specific device components.

By addressing these challenges, we intend to develop printed piezoelectric devices using entirely green components and environmentally friendly additive manufacturing processes. In doing so, we hope to develop a technology platform and a toolkit onto which further work can be conducted towards the implementation of entirely green electronics and thus the worldwide reduction of electronic waste.

We aim to achieve this goal in a series of development steps of increasing complexity. First, we aim to evaluate and down-select materials for the piezoelectric active material. We then will develop a printable ink using this material and fabricate devices from it using standard substrate and electrode materials (Si, Au). We then will assess the devices for piezoelectric performance. Next, we will transfer the printing process to degradable paper substrates and perform a comparison of device behavior on the two substrates. Finally, we will transition to fully printed degradable electrodes for the piezoelectric devices and utilize the fully printed devices to develop demonstrators of piezoelectric device functionality.

Chapter 3 Materials selection and process development towards low-temperature printed piezoelectrics

This chapter aims to describe the process development taken for the fabrication of a low-temperature processable, screen-printable piezoelectric ink. We first evaluate potential materials and processes for use in devices and ink formulations (substrate and electrode materials, printing technique, binding agent and solvent materials). We select materials known to be green and sustainable and evaluate their potential for use in such an application. We then address the more difficult challenge: down-selection of a green piezoelectric material. We briefly summarize the tests conducted during initial evaluation of degradable or non-toxic candidate materials (Rochelle salt, ammonium dihydrogen phosphate, zinc oxide, hydroxyapatite, and potassium niobate), as well as their outcomes. With the degradable materials (RS, ADP, ZnO, and HA) all exhibiting major manufacturing challenges, we next assess the non-toxic KN. We begin by validating processes for low-temperature printing and poling of perovskite materials using barium titanate as a proxy material, achieving a piezoelectric response ($d_{33,eff}$) for BT films printed on paper substrates at room temperature as high as 1.8 pC/N. Following this, a preliminary KN ink is developed, and capacitive devices are fabricated to confirm the material can be screen printed. With a final study of KN crystalline structure confirming its piezoelectric nature, we end the chapter by choosing potassium niobate as the piezoelectric material for use in further work.

3.1 Printing processes, component materials, and device considerations

3.1.1 Device components: Substrate and electrode materials

In Section 2.1, we conducted an initial evaluation of green materials with potential for integration into printed green piezoelectric devices. We now look to identify target materials for the final devices. As previously discussed, one of the core challenges to this work is establishing manufacturing methods for piezoelectric layers that are compatible with the other components of the system. We established key concerns regarding thermal limitations and chemical compatibilities of the piezoelectric processes with the other two fundamental device components: the substrate and the electrodes. Hence, in order for this work to be successful, target materials for these other components must be identified at an early stage so that proper accommodations can be made for their limitations during piezoelectric ink development.

3.1.1.1 Substrates

In identifying options for green substrates, we previously noted the challenges associated with the low thermal limitations of such degradable materials that must be compensated for when adapting the processing methods used for conventional piezoelectrics. For printing purposes, we consider thermal limitations from the perspective of processability, which includes both the maximum temperature prior to melting or decomposition, but also the glass transition temperature at which mechanical properties are compromised. In addition to temperature limitations, other relevant material properties include the printing surface roughness, the substrate's water resistance (both directly and in the form of humidity sensitivity), and to a lesser extent, commercial accessibility. Table 3.1 shows a comparison of these properties for both a selection of promising green substrate materials and some more common non-degradable substrates (Si, PET, PI). The polymeric degradable substrates (PCL, PLA, PVA) under consideration exhibit low glass transition temperatures and high responsiveness to water, while cellulose acetate has a maximum processing temperature of just 90 °C. As a result, paper

and silk are the most promising candidates for substrate materials, with high thermal limits and established precedent as printing substrates. We must now evaluate these materials and assess their advantages and drawbacks.

Silk films have been found to exhibit thermal resistances >200 °C and can have very low surface roughness, though compatibility with developed inks and processes has yet to be verified. The solubility of silk fibroin films in water is of concern for integration with aqueous inks or processes, and the lack of commercially available substrate products introduces the challenge of in-house substrate fabrication and the lowered material quality inherently associated with this.

Table 3.1 Comparison of relevant characteristics for printed electronics substrates, for both common non-degradable and degradable substrate materials.

Class	Material	T _{glass} (°C)	T _{max.} (°C)	Water solubility	Surface roughness	Rel. perm., ϵ_{rr} (-)	Ref.
Non-degradable	Silicon		>1400	Slightly soluble	Very smooth	11 – 12	16,221
	PET	74 – 79	230 – 265	Insoluble	Smooth	3 – 4	221,222
	PI	>300	>400	Insoluble	Smooth	2.8 – 3.5	223,224
Degradable	Paper	–	150 – 250	Insoluble, swells	Rough	~2	7,225
	Silk	178	>250	Soluble	Smooth	2.5 – 3.5	27,31,86,226
	PCL	-65 – -60	57 – 63	Degrades	Smooth		15,17,98,227
	PLA	45 – 65	160	Insoluble, degrades	Smooth	2.7	15,17,98,99,228
	PVA	83	200	Soluble	Smooth	~3	17,229,230
	Cellulose Acetate		90	Insoluble	Smooth	2.5 – 2.7	231,232

Commercial paper products designed for printed electronics applications can also demonstrate thermal limits over 200 °C with low to moderate surface roughness (<20 nm for the highest quality paper products, but generally in the range of 1–5 μ m). As composite films composed primarily of cellulose fibers, paper substrates have comparatively high surface roughness and a high internal porosity, which must be compensated for during process development. The surface roughness limits the minimum layer thicknesses that can be achieved for printed device components and, at the same time, it will have an effect on printed device yield. The effects of film porosity are multifaceted. High porosity may result in discontinuous layers if the ink utilized is too thin (a frequent concern for inkjet printing applications), but may aid in film adhesion for thicker inks such as those used for screen printing. Meanwhile, paper film porosity influences printed device performance with changes in ambient humidity causing water absorption. These challenges can be partially overcome through the use of products specifically designed for printed electronics applications (ex: ArjoWiggins HD series, FelixSchoeller pe:smart series), but need to be evaluated as the development process progresses.

Despite these challenges, paper was selected as the most promising substrate material for device applications due to its thermal robustness, established degradability, and, of course, commercial availability. In initial ink and process development, however, alternative substrates (PET, glass, silicon) are used instead. In Chapter 5, we will discuss the transfer of the developed printing process onto paper substrates.

3.1.1.2 Electrodes

In Section 2.1.3 we overviewed some conductive materials with potential for use in this work, briefly discussing some considerations for materials selection. Of those materials, carbon- and zinc-based inks show the most promise. For any electrode material, considerations need to be made to ensure that no part of the piezoelectric printing compromises the performance of these conductive layers. Carbon inks, while generally less conductive than metallic conductors, are well established for printing processes and can be printed in ambient conditions (without further post-processing) to produce conductive layers. Alternatively, zinc-based degradable inks are actively being developed by Fumeaux at EPFL-LMTS, in a two-step sintering method that is compatible with degradable substrates while still showing high electrical conductivity.⁴⁵ This process has shown potential for integration with printed piezoelectrics as a result. Both the carbon- and the zinc-based inks in consideration are water-soluble, care will be taken to select piezoelectric ink ingredients that are compatible with printing on top of such layers without compromising their functionality.

For initial process development, thermally evaporated or sputtered gold electrodes are used as electrodes instead, first on silicon substrates (Chapter 4), and later on paper substrates (Chapter 5). In Chapter 6, we discuss the integration of the developed piezoelectric printing process with printed carbon- or zinc-based electrodes.

3.1.2 Printing processes

At this point, it becomes relevant to identify a printing method to target printing development. In Section 2.3, we gave an overview of commonly used printing processes, including their advantages and limitations. Now a specific method or methods must be chosen such that ink development and material selection can be tuned to the constraints of the process.

For this selection, we take into consideration the limits of the processes, the complexity of ink development, and the intended goal of this work. In Chapter 1, we set a goal of developing printed green piezoelectrics, with intended use in applications with high production volume and short lifetime. For large production volumes, we target printing processes with medium or high printing throughput. This includes screen, gravure, flexographic, inkjet, and 3D printing methods, but excludes EHD and aerosol-jet printing (refer to Table 2.3). 3D printing is not, however, practical for the targeted applications at this time (though it has potential to be developed in the future). In terms of ink development and process complexity, gravure and flexographic printing are not ideal, due to the complexity of establishing multi-layer roll-to-roll systems, and poor adaptability to process changes.

From this, we are left with screen- (or stencil-) and inkjet printing as candidates for process development—each with their own challenges. A digital process, device designs can be readily re-configured using inkjet printing processes, while screen printing requires the manufacture of a printing mask or mesh, slowing down interaction speed. Ink development is generally more straightforward for screen printing than inkjet inks. Stable formulations of inkjet inks for particle dispersion-type inks can be complex and involve specialized additives to ensure proper dispersion of functional materials, and particulate used in inkjet inks must be small enough to prevent nozzle clogging. As a result, inkjet printing inks are usually less viscous and deposit thinner films than screen printing inks.

For initial evaluation of degradable piezoelectric materials, we keep both screen and inkjet printing options available, working first to establish if achieving a piezoelectric response is achievable using either method. This is mostly demonstrated in the variety of ink compositions and ingredients evaluated as we cover the range of potential ink formulations for stability and printing quality. In many of these initial studies, stencil printing is used in place of screen or inkjet printing as ink quality was not sufficient for implementation into either of the intended methods.

In the final down-selection, we select screen printing as the printing technique of choice for further ink optimization.* This decision is based on the comparative simplicity of realizing stable ink formulations for screen printing, the established precedent for screen printable perovskite inks, and the thicker films which prove beneficial for printing on paper substrates (the thickness compensates for the roughness of the substrate, and thus improves device yield in later development phases).

3.1.3 Ink components: Solvents and binding agents

Functionality of the printed layer depends heavily on the nature of the piezoelectric material, but ink development is dependent also on the other ink ingredients, and on their proportional content in the ink recipe. As discussed in Section 2.3.2.2, quality printing depends on the careful balance of these ingredients, taking material chemistry and interactions into account. Before we assess material potential for printing applications, we must identify some candidate ink ingredients for use as solvents and binding agents (sometimes “binders”) that can be used for ink development during those feasibility studies. We focus on selecting sustainable and degradable materials for these components when possible, recalling the goal of this thesis to develop green printed systems. We begin by identifying promising materials from literature, down-select based on known material compatibilities, and further down-select based on empirical evidence. We note that this discussion is targeted towards the development of inks containing solids dispersed or dissolved in a fluid, and is not necessarily universally applicable to all forms of inks used in additive manufacturing.

3.1.3.1 Solvents

Solvents (sometimes “carrier fluids”) considered a selection of non-polar and polar solvents, including water, isopropanol, acetone, ethanol, pentanol, and DEGMBE (diethylene glycol monobutyl ether). Early studies found that the high volatility of acetone, isopropanol, and ethanol made the quality of printing low for all test materials, and they were eliminated.

*Spoilers.

DEGMBE was used for some HA process validation, but as it is not known to be a sustainable solvent, was discarded from further development. Finally, water and pentanol were selected as target solvents for ink development. Later investigations (discussed briefly in the following sections, but further elaborated in 8.4 of the Appendix) found water to be unsuitable as a carrier fluid for two reasons. When used for particle dispersion type inks, the strongly polar water resulted in particle agglomeration and eventual sedimentation of all ink recipes investigated.[†] Tseng has reported on a sustainable method of pentanol production from *e. coli*, and its lower volatility and rheological properties make it a good choice as a carrier fluid.[‡] Thus, the finalized recipe we will report in the coming chapters uses pentanol as the solvent.[‡]

Table 3.2 Short-listed degradable binding agents

Class	Material	H ₂ O-soluble	Alcohol-soluble
Polymer	Polyvinyl alcohol (PVA)	Y	Y
	Polyvinylpyrrolidone (PVP)	Y	Y
Cellulose-Derivative	Carboxymethyl cellulose (CMC)	Y	Some
	Ethyl cellulose (EC)	N	Y
Polysaccharide	Sucrose	Y	N
	Amylose (Starch)	N*	Y
	Gum arabic	Y	
	Gum tragacanth	Y	
	Guar gum	Y	N (most)
	Xanthan gum	Y	
Protein	Albumin	Y	
	Chitosan	Y	
	Gelatin	Y	N

3.1.3.2 Binding agents

For binding agent selection, we identified a range of materials from literature, with synthetic polymers, cellulose derivatives, polysaccharides, and proteins as the four primary classes of binders used in green technologies (see Table 3.2). As binding agents vary in solubility, not all combinations of solvents and binders are possible for evaluation. Initial tests were predominantly conducted with polyvinyl alcohol (PVA), polyvinylpyrrolidone (PVP), ethyl cellulose (EC), and gum tragacanth. Further evaluation identified PVP and ethyl cellulose as the most promising candidates for ink formulation, as ink viscosity could be adapted easily with these two synthetic polymers by varying both the loading and the molecular weight of the binder. Based on their solubility in different carrier fluids, PVP is most applicable to aqueous inks, while ethyl cellulose which is insoluble in water is the better suited for non-polar solvents.

The degradability of PVP is widely accepted, yet there remains some debate with regards to the degradability of ethyl cellulose. This comes primarily due to its insolubility in water and concerns regarding future EC accumulation in bodies of water. However, as a cellulose derivative, microbiological and thermal degradation of ethyl cellulose has been reported as early as the 1950s.^{234,234} It has been approved as a food additive in the by the USFDA and, in a 2020 study conducted by the European Food Safety Authority, was deemed safe for all animal species and safe for the environment.²³⁵ So for the purposes of this thesis, where we have defined “green” to mean materials that are non-toxic and cause no harm to the environment, EC is considered to be degradable.

3.2 Initial materials down-selection for green piezoelectric microsystems

The purpose of this preliminary work was to assess the feasibility of developing a printable green piezoelectric material. This involves identification of the other device component materials (substrates, electrodes) and down-selection of ink ingredients (solvents, binders) prior to the critical evaluation of potential piezoelectric active materials.

[†] This could potentially be compensated for using stabilizing additives, but no degradable stabilizers were identified in literature, and such material development is outside the scope of this work.

[‡] Spoilers.

3.2.1 Piezoelectric material evaluation and down-selection

Based on the literature review conducted in Section 2.1.4, six potential piezoelectric materials are selected for screening, separated into two categories: degradable materials, and non-toxic materials. In Table 3.3, we make a comparison of the candidate materials to more commonly used piezoelectric materials including PZT, AIN, and PVDF. In the degradable category, the four candidate materials include sodium potassium tartrate “Rochelle salt” ($\text{KNaC}_4\text{H}_4\text{O}_6 \cdot 4\text{H}_2\text{O}$, “RS”), ammonium dihydrogen phosphate ($\text{NH}_4\text{H}_2\text{PO}_4$, “ADP”), zinc oxide (ZnO), and hydroxyapatite ($\text{Ca}_5(\text{OH})(\text{PO}_4)_3$, “HA”). Though these materials are proven to be degradable, they pose a greater challenge for integration with printing processes.

Two other degradable piezoelectric polymer materials were initially considered—PLLA and chitosan—but dismissed due to challenges with dipole orientation. These materials must be oriented during manufacturing to generate a net polarization, and no literature precedent has reported a method of achieving this with printing processes. Thus, these materials were not studied, though they show promise for future development.

In the non-toxic materials category is sister compounds potassium sodium niobate ($(\text{K},\text{Na})\text{NbO}_3$, “KNN”) and potassium niobate (KNbO_3 , “KN”). Perovskites such as these have more established printing methods and larger piezoelectric responses, making successful printing process development more likely. However, due to a lack of commercial application, only initial toxicological studies have been conducted on these materials, confirming their non-toxic nature. Full degradation studies have yet to be conducted on these materials so no conclusions can be made as of yet regarding full degradation. As a result, we chose to perform an initial feasibility studies and down-selection analyses of the known degradable materials first, before assessing the non-toxic materials as an alternative.

Table 3.3 Comparison of some known green piezoelectric materials with commonly used piezoelectric materials, including properties and known relevant values. A blank space indicates that a quantity could not be found in literature.

	Degradable Green Mat'ls				Non-toxic Green Mat'ls		Non-degradable Mat'ls			
	RS	ADP	ZnO	HA	KNN	KN	BT	PZT-4	AIN	PVDF
	$\text{KNaC}_4\text{H}_4\text{O}_6 \cdot 4\text{H}_2\text{O}$	$\text{NH}_4\text{H}_2\text{PO}_4$	ZnO	$\text{Ca}_5(\text{OH})(\text{PO}_4)_3$	$(\text{K},\text{Na})\text{NbO}_3$	KNbO_3	BaTiO_3	$\text{Pb}(\text{Zr},\text{Ti})\text{O}_3$	AIN	$-(\text{C}_2\text{H}_2\text{F}_2)_n-$
Printing precedent	Y	Y	Y	Y	Y	N	Y	Y	N	Y
Ferroelectric?	Y	Y	N	Y [§]	Y	Y	Y	Y	N	Y
Curie temp., T_c (°C)	24.9	45	n/a	? [§]	400–420	435 (225)	120–130	328	n/a	100–150
Domain orientability	Medium	Medium	Difficult	Medium	Easy	Easy	Easy	Easy	Difficult	Medium
Piezo coefficient (bulk), d_{ij} (pC/N)	2300 [d_{14}]	11.7 [d_{14}]	12 [d_{33}]	0.5–16 [d_{33}]	200–650 [d_{33}]	109 [d_{33}]	190 [d_{33}]	289 [d_{33}]	5 [d_{33}]	15 [d_{33}]
	12 [d_{36}]	51 [d_{36}]	5.2 [d_{31}]	<0.1 [d_{31}]	32–49 [d_{31}]	51.7 [d_{31}]	78 [d_{31}]	123 [d_{31}]	2–2.65 [d_{31}]	16.5–23 [d_{31}]
Melting point, T_m (°C)	76	190	1975	>800	1050	1060	1650	1533	2200	177
Density, ρ (kg/m ³)	1770	1800	5680	3160	4300	4360	5700	7500	3260	1780
Young's mod., Y (GPa)	10–18		110	6		245	67	63	340	2
Coupling coeff., k_{33} (–)	0.3	0.28	0.41			0.49–0.66	0.5	0.7	0.39	0.16
Rel. perm., ϵ_r (–)	9–1100	14–57.6	9.26–11	4.96–8.73	500	394–500	500–5000	1730	8.5	9
Ref.	106,107,236–239	108,240–243	58,65,67,159,244	89,205,206,245	142,246–248	72,141,142,249–251	75,147,154,252	57,77,125,253	61–63,254,255	49,58,102,103

Both KN and KNN are polarizable ferroelectric materials that with large piezoelectric responses (more than 100 pC/N in bulk ceramics for both). While printing processes for KNN have been established, current processes require sintering at temperatures exceeding 1000 °C, and thus have yet to integrate with degradable substrates or conductive elements. Further challenges arise from material quality control—the KNN powder must be synthesized in-house—adding a significant degree of complexity and variability to the manufacturing process.^{139,252,256–258} Meanwhile, KN has no printing precedent,

[§] Ferroelectric nature of hydroxyapatite contested.

but is available in powder form in purities $\geq 99.9\%$. As the two materials are highly similar in composition and structure, the ink formulations previously developed for printed KNN can be adapted for use with KN as a starting point for low-temperature process development. Another perovskite material, barium titanate (BaTiO_3 , “BT”), has been heavily developed in printing applications, but its toxicity (attributed to Ba^+ dissolution) disqualifies it as a candidate for this work.^{259–261} As a result, we will use BT for process validation, as will be discussed further in Section 3.3.1, but not continue to develop it after validation is complete.

The final down-selection criterion for choosing a material from this test group was based off the following characteristics: ink stability, printability, printing reproducibility, verified piezoelectric nature (in printed material), and tunability of piezoresponse via additional processing techniques such as poling or directed material orientation where applicable.

3.2.1.1 Rochelle salt and ADP

The first two materials investigated for use as printable degradable piezoelectric materials were Rochelle salt and ammonium dihydrogen phosphate. Initial work by Lemaire at EPFL-LMTS served as a jumping off point for producing RS and ADP inks.^{184,185,262} As water soluble crystals, basic processing of these materials is straightforward: saturated solutions of dissolved material are drop-cast onto substrates, and solid crystals precipitate upon evaporation of water to form a layer in the shape of the deposited droplet. To begin, ink development focused on solutions containing RS (CAS 6381-59-5, $\geq 99\%$, Merck) or ADP (CAS 7722-76-1, Reagent grade, Merck) in deionized water with no further additives. The ADP or RS source crystals were dissolved in DI H_2O at 50°C to produce supersaturated solutions upon cooling to ambient conditions. These were then dropcast onto a variety of substrates through mold or stencil patterns and allowed to dry over 0.5–3 hours to precipitate the crystal layers. Figure 3.1(a) depicts this schematically. These first deposition tests were implemented directly onto substrate materials (i.e., without electrodes) until a reproducible printing process could be established.

Immediate results indicated that solutions containing ADP crystallized at such a fast rate that the resulting layers were inhomogeneous and unreproducible. Reduction to 90% saturation of ADP in H_2O (at 24°C) did not provide sufficient decrease in crystallization rate to make ADP viable. Such high crystallization rates resulted in clogging issues even with nozzle apertures as large as $1\text{ mm}\varnothing$, and thus are expected to cause similar manufacturing issues with the smaller nozzles or mesh apertures targeted for later printing processes. Further attempts to slow the crystallization process were unsuccessful, and thus ADP was discarded from further investigation.

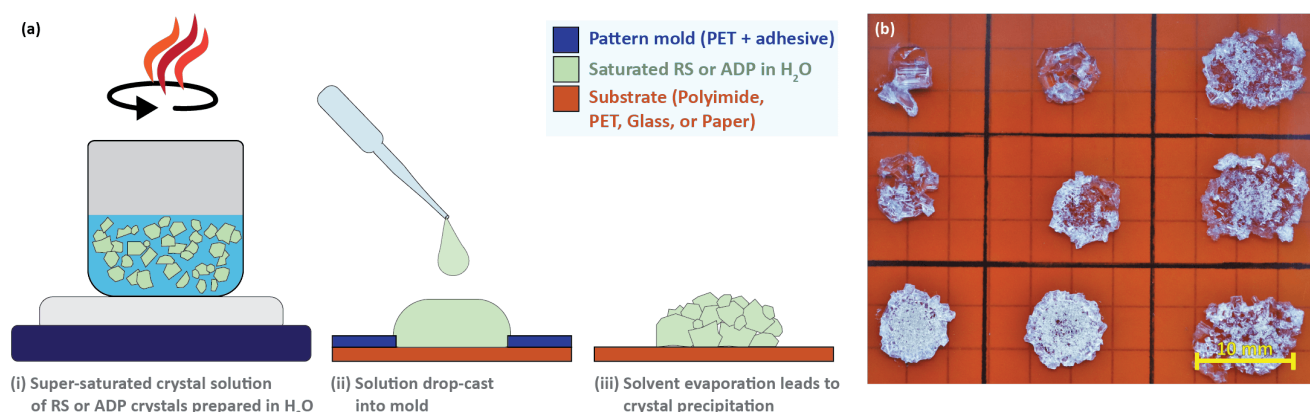


Figure 3.1 Preparation of RS and ADP films including (a) Initial process for RS and ADP printing including (i) preparation of a supersaturated solution of RS or ADP in DI H_2O , (ii) drop-casting of solution ($30\ \mu\text{L}$ aliquots) onto substrate within a stencil or mold, (iii) evaporation of H_2O resulting in crystal precipitation into a film. (b) Example of inconsistent crystallization with an RS ink as drop-cast on PI with large variations in crystal orientation and grain size upon drying despite no variance in process parameters.

The results of studies on Rochelle salt indicated that RS can be solution deposited in a facile manner but has several serious drawbacks for device integration concerning stability and reliability. The brittle nature of the crystals caused layer failure due to cracking and delamination, while the precipitation of consistent and oriented crystals on degradable substrates proved to be an immense challenge (Figure 3.1(b)).

To improve RS layer adhesion, green binding agents were evaluated to the solution to improve layer mechanical properties. As binder integration in supersaturated solutions proved unsuccessful, 90% saturated RS solutions were used for these tests, with the binding agent content introduced in quantities of 0.5–7 wt% (relative to RS content). Tested binders included a PVA (CAS 9002-89-5, Mowiol 4-88, Merck), PVP (CAS 9003-39-8, K90 or K360, Merck), gum tragacanth (CAS 9000-65-1, Merck), and egg albumin (CAS 9006-59-1, $\geq 98\%$, Merck), with a full range of test parameters is detailed further in Section 8.4.1 of the Appendix. Regardless of binder material or content, no tested ink was found to produce well adhered layers with consistent crystallization on any substrate. Further attempts to develop devices using these films resulted in failure due to mechanical issues and device shorting through non-continuous RS layers.

As an alternative method of reproducible crystallization, RS crystals were annealed post-deposition, however the material was found to decompose into insoluble constituents at 36 °C, making crystal annealing infeasible. Furthermore, the low Curie temperature (25 °C) and highly hygroscopic nature of RS limit the practical applications for this material in a commercial setting. It may provide a viable path forward, but would be extremely limited in application scope, with great hurdles to overcome in the development of reproducible processes. As such, this material was also dismissed from further study at this point.

3.2.1.2 Zinc oxide

Zinc oxide has been the focus of much work in photovoltaic and piezoelectric applications, and there is an enormous body of work on the printing of ZnO, with multiple inkjet printing inks commercially available for photovoltaic applications. Appendix Table 8.6 includes a summary of prior works involving or developing methods for printed zinc oxide. This feasibility study involved two major areas of investigation. First, assessing the printability of ZnO inks made with fully green components. Second, assessing methods of ZnO orientation onto substrates compatible with the chemical and thermal limitations of degradable substrates. While we provide a summary here, Section 8.4.2 of the appendix further elaborates on the feasibility studies conducted for ZnO for green piezoelectric applications.

Initial screening showed that ZnO-based screen printable inks can be successfully developed using entirely degradable components. To start, aqueous dispersions of ZnO nanoparticles (NPs) (CAS 1314-13-2, 20 wt% in H₂O, 50–80 nm ϕ , 99.99%, Nanoshel-UK Ltd.) was mixed with PVA or PVP binders such that binder content was 2–10 wt% relative to ZnO content, which was 10–15 wt% of the total ink mass. It was found that inks with 10 wt% ZnO and 5–10 wt% PVP produced high quality films, with a layer thickness of 12 ± 2 μm when stencil printed through 27 μm thick PET stencils and dried at room temperature. Inks were stable for up to 3 weeks before particle agglomeration caused significant change in print quality. These inks can be printed onto glass, polyimide, and paper substrates with reasonable adhesion (Figure 3.2). However, the as-printed inks were not oriented and thus exhibited no piezoelectric response.

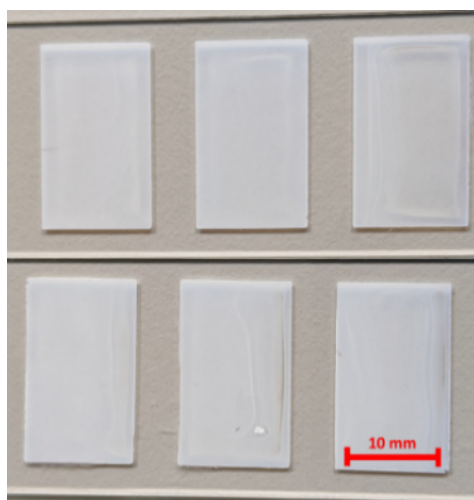


Figure 3.2 Screen printed ZnO film on glass substrate.

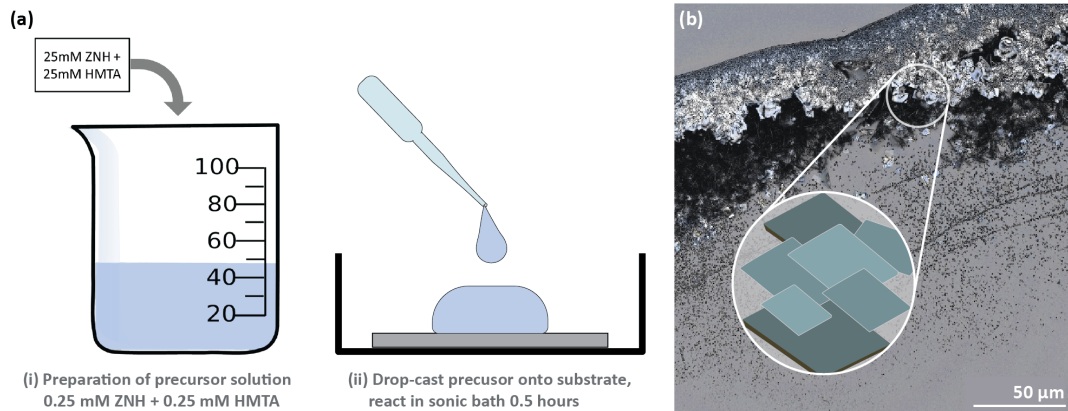


Figure 3.3 Room temperature ZnO NF synthesis using shape-directing agents. (a) Simplified process steps. (b) "Coffee Ring" of ZnO nanoflakes synthesized using a modified sonochemical method adapted from Vabbina.^{263,264}

As a follow-up, two feasibility studies were conducted to assess whether ZnO could be printed into an oriented layer. In one method, orientation can potentially be achieved using ZnO particles with plate or flake-like geometries that preferentially orient with the large surface parallel to the substrate upon drying. To this end, an ink containing a ZnO precursor and a shape directing agent must first be printed onto the substrate before conversion to ZnO nanoflakes (NFs). Towards this, 25 mM zinc nitrate hexahydrate ($\text{Zn}(\text{NO}_3)_2 \cdot 6\text{H}_2\text{O}$, CAS 10196-18-6, 98%, Merck) and 25 mM shape-directing hexamethylenetetramine (HMTA, CAS 100-97-0, Merck) were dissolved in DI H_2O . This solution was then drop-cast (10 μL aliquots) onto a glass substrate and ultrasonically reacted to produce ZnO NFs at room temperature (Figure 3.3(a)). This method was developed using a modified sonochemical method adapted from Vabbina.^{263,264} While flakes were successfully synthesized in a room temperature process, as depicted in Figure 3.3(b), the yield of nanoflakes was deemed too low to reliably produce viable devices for practical applications.

In the second feasibility study, dielectrophoresis was utilized to attempt layer orientation of a ZnO particle dispersion (further detailed in Appendix section 8.4.2.2). The investigation showed some minor particle alignment, but the process was deemed impractical for the high-volume device applications for which this thesis is targeting. With both feasibility studies showing potential, but great challenges for developing methods of domain orientation in printed ZnO, it was concluded that ZnO was not an ideal candidate for further study, but could potentially be revisited if studies on all other candidate materials proved unsuccessful.

3.2.1.3 Hydroxyapatite

Hydroxyapatite ($\text{Ca}_5(\text{PO}_4)_3(\text{OH})$, HA) has been reported by multiple groups to present piezoelectric properties, and its biodegradable and sustainable nature make it a promising material for printed electronics applications. Through successive iterations, inks were developed for stencil printing of HA layers compatible with both glass and paper substrates. The selected ink for further testing contained 25 wt% HA (CAS 12167-74-7, stoichiometric HA, CamBioceramics) in DI H_2O with 15 wt% 360K PVP relative to HA content. Films were stencil printed on glass or paper substrates using 27 μm thick PET stencils and dried at room temperature, resulting in 5–10 μm thick HA films (Figure 3.4). Capacitive devices were fabricated in a parallel plate architecture using sputtered gold electrodes on glass substrates, then electrically poled before piezoelectric evaluation with a Berlincourt meter.

No piezoelectric response was measured from any of the experimental samples. Later work replicating prior studies from Lang and Markham reporting on the phenomenon yielded no piezoelectric response in fabricated devices, bringing the piezoelectric nature of the material into question.^{89,205}

To assess this, powder diffraction of source HA material was used to determine its crystal phase, with an expectation of a noncentrosymmetric monoclinic $\text{P}2_1$ structure reported by Lang. This study found that the stoichiometric source powder was a centrosymmetric hexagonal crystal system, $\text{P}6_3/\text{m}$, and thus could not be piezoelectric. This, combined with observed incompatibilities with most degradable conductor candidates in consideration indicates that this material was not an ideal candidate for further study. See Appendix Section 8.4.3 for further details on the preliminary investigations conducted for HA.

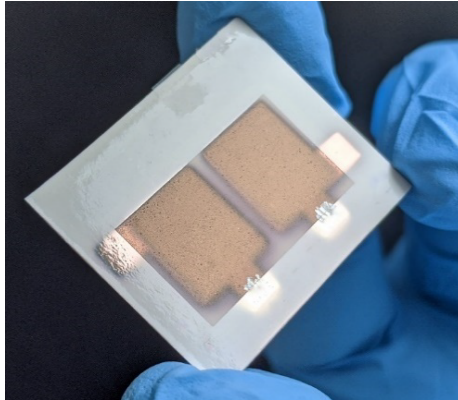


Figure 3.4 Stencil printed HA on paper with sputtered Au electrodes.

3.2.2 Conclusions from feasibility studies on degradable piezoelectric materials

With feasibility studies on degradable piezoelectric material candidates concluded, we find that each of the tested materials has significant challenges to overcome before printed piezoelectric devices can be realized. We find extreme processing challenges with both ADP and RS that limit their printability, as well as material limitations of temperature and hygroscopicity limiting their potential device applications. We determined that zinc oxide can be printed in a green manner, but material orientation remains difficult. While dipole orientation methods show some potential, following this route would introduce large amounts of risk into the study. Finally, we find that hydroxyapatite, despite numerous reports to the contrary, does not have a noncentrosymmetric crystalline structure necessary for piezoelectricity and cannot be used for this application.

Before continuing with further process development of the highly challenging hurdles for these materials, we instead look to the second class of candidate materials identified earlier: the non-toxic perovskite materials. Though not yet proven to be degradable,** their non-toxic nature is still a step in the correct direction for green piezoelectric devices and would still serve as proof that such processes can be achieved for printed piezoelectric materials and act as a foundation upon which future research can build.

3.3 Process validation using ceramic piezoelectric powders

In this second phase of feasibility studies, we look to evaluate the potential of non-toxic perovskites for printed applications as an alternative to the degradable materials assessed initially. In Section 3.2.1, we selected potassium niobate as the material of interest over the generally preferable KNN due to reasons of practicality, with the expectation that process transfer to KNN in the future would be straightforward.

Before finalizing the selection of this material, several issues must be addressed. First, validation that perovskites printed at low temperatures can demonstrate a piezoelectric response. Second, verification that KN can be printed. Finally, confirmation of the ferroelectric nature of KN. By assessing these areas of risk, we intend to gain confidence that low temperature printed KN can be realized for such applications.

First, we look to confirm that perovskite materials can exhibit a piezoelectric response when processed entirely at low temperature. This challenge is two-fold, as we must confirm both the manufacturing procedure as well as the poling process. Printed perovskites reported in literature generally are sintered post-printing, with temperatures well above the 200 °C constraint of paper substrates (as discussed in Section 2.3.4). Alternatively, perovskites can be processed at low temperatures, through compositing in a polymer matrix (usually PVDF or PDMS, among others), but with a significant reduction in piezoelectric response when compared to the bulk perovskite or the sintered printed perovskites. We choose

** As mentioned previously, no full degradation studies have yet been reported for KN or KNN, only toxicological assessment. Thus, degradability cannot be claimed one way or another at this time.

not to take the composite approach, and instead adapt the ink composition to compensate for the reduced structural integrity that comes with skipping the sintering step. Ink formulations for perovskites that are to be sintered generally minimize the binder content in the film, as its primary function is to maintain the green body shape until sintering, where it decomposes and leaves undesirable pores in the film. Without sintering, this binder content is too low to maintain film integrity, so we intend to compensate by increasing the ink binder content. For validation studies, we care only that the film can be printed and produce a piezoelectric response, but later we will assess the influence of varying binder content on device performance (Section 4.2.3).

For this first evaluation, we choose to assess processing with a more established perovskite material, barium titanate, as a proxy for KN. With the 2003 implementation of RoHS directives, barium titanate has increased in popularity as the pre-eminent lead-free perovskite, resulting in more established printing processes for BT. Even so, no full degradation studies have been reported in the literature for barium titanate. Preliminary studies by Polonini and Ahamed have reported bio- and cytotoxicity of BT, attributed to toxic Ba^{+} leaching from the material into the environment.^{259–261} This toxicity eliminates it from the candidate pool for the purposes of this thesis, but established BT ink formulations will serve as a basis for testing the adapted ink composition during low-temperature printing process validation.

Barium titanate is also a good proxy material for testing the intended poling process, based on its low Curie temperature of approximately 130 °C. This enables poling verification for samples on paper substrates using both the standard direct poling methods (i.e., poling at the Curie temperature) as well as the modified room temperature process. For these two reasons—established printing precedent and low Curie temperature—we chose BT for low-temperature validation of printing and piezoelectric response.

The second and third challenges will follow only after low-temperature process validation with BT is complete, and return the focus to KN. In this, we look to assess if an ink can be developed for printing KN such that capacitive devices can be realized. We will use ink compositions used previously for BT and KNN screen printable inks as a jumping-off point for this preliminary ink development. Finally, with that verification complete, we assess the crystalline structure of the printed KN to confirm its piezoelectric nature.

3.3.1 Validation of low-temperature processes using screen printed $BaTiO_3$ on paper substrates

3.3.1.1 Ink preparation and device fabrication

The recipe for BT inks was prepared using a recipe based on inks established by Stojanovic for screen-printed BT thick films, containing approximately 70:30 wt% BT:pentanol, with <1 wt% binding agents.²⁵² As discussed, this recipe was altered to increase the binder content, resulting in a recipe containing 70:10:20 wt% BT:EC:pentanol. Ingredients included barium titanate powder (CAS 12047-27-7, <3 μm , 99%, Merck), ethyl cellulose (CAS 9004-57-3, Merck, viscosity 10 cP, 5% in toluene/ethanol 80:20 (lit.), extent of labelling: 48% ethoxyl), and pentanol (CAS 71-41-0, Merck, ReagentPlus, $\geq 99\%$). Iterative development of the recipe was conducted to improve print quality, during which time the process transferred from stencil printing to screen printing as recommended by Stojanovic. The details of this initial BT ink and process development are elaborated in Section 8.4.4 of the Appendix. The new recipe was 64:8:28 wt% BT:EC:pentanol, mixed in a planetary mixer at 500 rpm for a total duration of 3 hours, in 30 min intervals. A polymer mesh (PME 120-30Y) fabricated by Serilith AG (Balwil, CH) was used for screen printing.

With ink preparation complete, thermally evaporated electrodes composed of 10/100 nm Cr/Au were deposited on paper substrates through a stainless steel shadowmask. Next, the BT ink was screen printed onto the substrate and dried at room temperature for 30 min after each of two BT layers. Finally, top electrodes were deposited using the same thermal evaporation parameters as those used for bottom electrodes. Figure 3.5 depicts schematically the fabrication process for such devices as well as photographs of the devices post-fabrication. Devices were fabricated in batches with patterns arranged to match a conventional 100 mm ϕ wafer. Each wafer contained 84 devices with functional capacitor surface areas of 1, 5, 10, and 20 mm² with between 10 and 28 copies of each size on the same wafer (Figure 3.5(b)). The fabrication process was replicated to produce between one and three wafers for each set of fabrication parameters to ensure reproducibility across the wafer as well as between wafers.

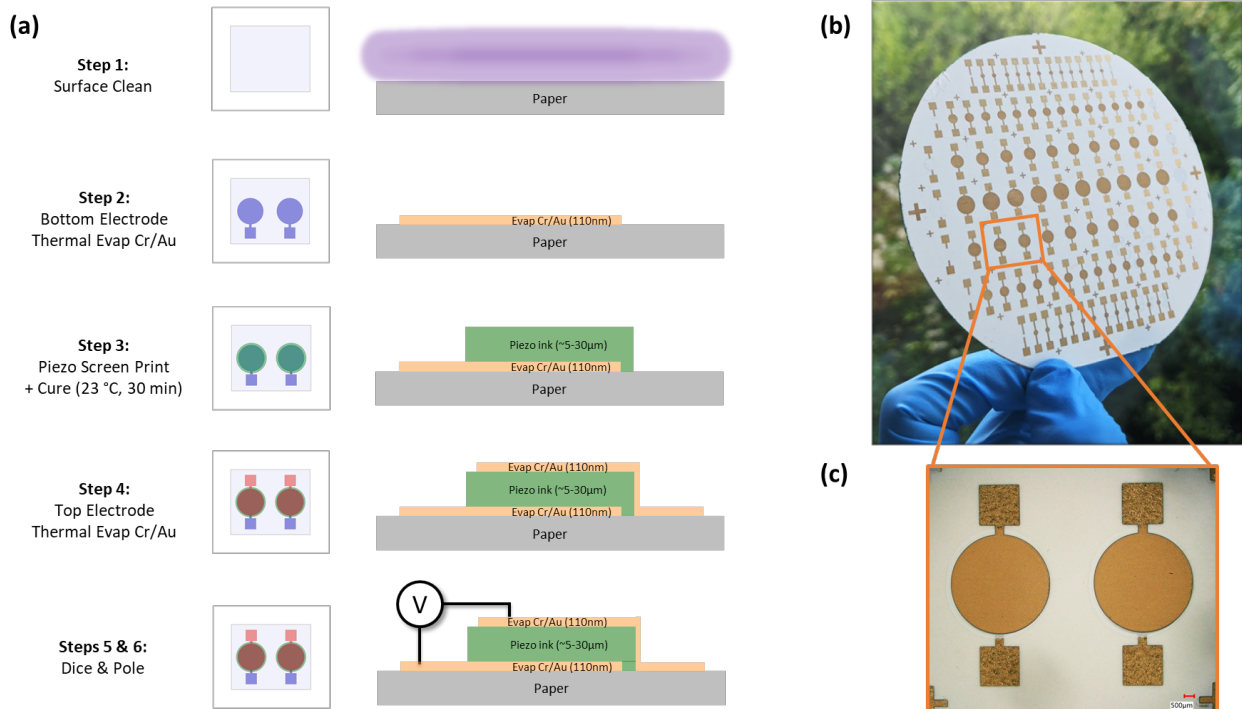


Figure 3.5 Fabrication of BT capacitor devices on paper substrates showing (a) details of process steps, (b) full size wafer as-fabricated, and (c) closeup image of capacitor devices.

The thinner layers resulting from screen printing (as opposed to stencil printing), resulted in more reproducible device characteristics as compared to previous fabrication methods. Printing linewidth was as low as 150 µm with individual BT layers approximately 5 µm thick. Due to the roughness of the paper substrate, two layers of BT were required to achieve high yields of unshorted devices, resulting in devices with BT films of approximately 10 µm and an average surface roughness of 2 µm (see Figure 3.6). This new process ensured device yields >80%, sufficient for further testing.

3.3.1.2 Piezoelectric response in BaTiO₃ screen printed films

The direct poling method was used to pole the printed BT devices, first heating the sample to the Curie temperature (130 °C), then ramping the voltage applied across the electrodes in 10 V increments until the applied field reached the set value of 2.5, 5, or 7.5 V/µm. The field was then held for a soak period of 30 min before the sample was allowed to cool passively to ambient conditions (approximately 45 min) with the electric field continually applied. Once the sample temperature was below 40 °C, the applied field was removed in a single step, completing the poling process. This procedure is depicted schematically in Figure 3.7. Something worth noting at this point is the inconsistent poling parameters commonly reported in literature for printed ferroelectrics, even when discussing the same ferroelectric material, with poling fields ranging from 0.1–10 V/µm and poling durations ranging from 1 min to as much as 24 hours. As optimum poling parameters are unique to each material and system, literature poling parameters can only serve as a starting point upon which further poling optimization studies must be conducted. For this system, we evaluate the influence of poling temperature, duration, and applied field on piezoelectric response, repeating each set of parameters on a minimum of three printed BT devices.

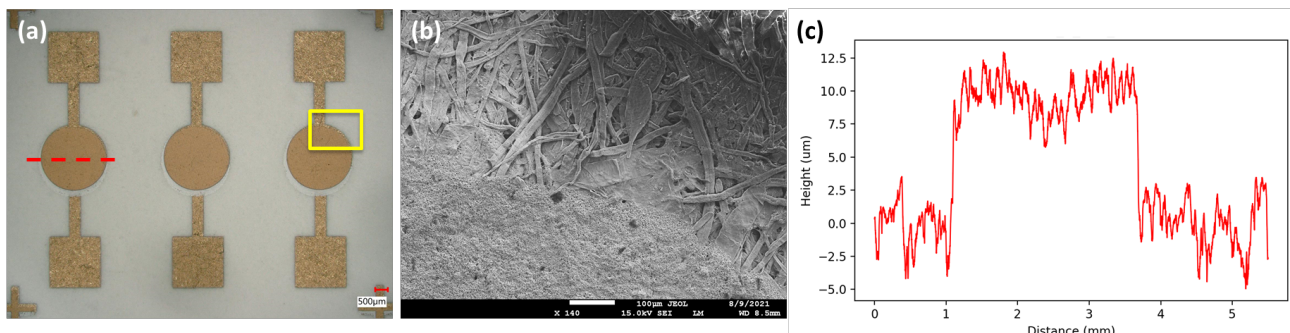


Figure 3.6 Physical Analysis of printed BT devices on paper substrates showing (a) device photography, (b) top-down SEM image of the BT-paper interface, and (c) surface profilometry of the BT layer.

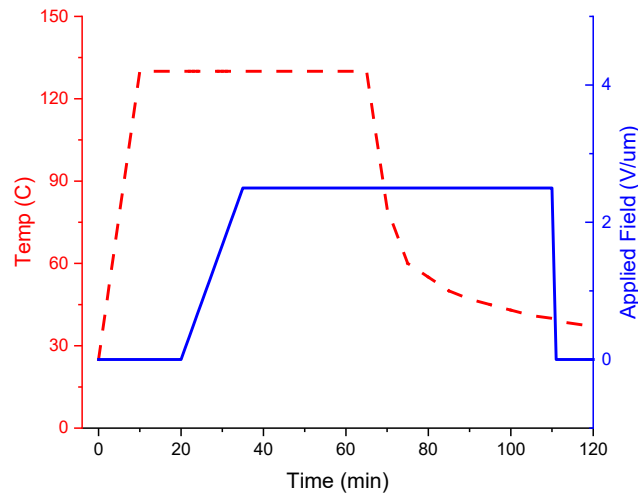


Figure 3.7 Poling process for screen printed barium titanate, showing the temperature and applied electric field as a function of time.

After poling, it was found that printed BT devices on paper showed a piezoresponse after poling at both the Curie temperature and in ambient conditions. This was confirmed with both Laser Doppler vibrometry (Figure 3.8(a,b)) as well as Berlincourt measurements (Figure 3.8(c)). The piezoelectric response was notably lower for the samples poled at ambient conditions, with Berlincourt measurements of the effective piezoelectric response, $d_{33,eff}$, of 4.4 pC/N when poled at 130 °C and 1.0 pC/N when poled at 24 °C at the same applied field and duration. Initial studies of poling optimization (Figure 3.8(c,d,e)) for BT printed samples on paper showed a strong dependence on poling temperature, but less on poling field and poling duration as studied for samples poled at the Curie temperature. In studying the influence of poling field and duration when implemented at 135 °C, coefficients ($d_{33,eff}$) as high as 5.9 pC/N were measured. For room temperature poling, the highest measured coefficient was 1.8 pC/N. This preliminary result implies that the long poling durations reported in literature may be unnecessarily lengthy, and that studying poling process duration further may significantly reduce processing times and thus permit faster development cycles.

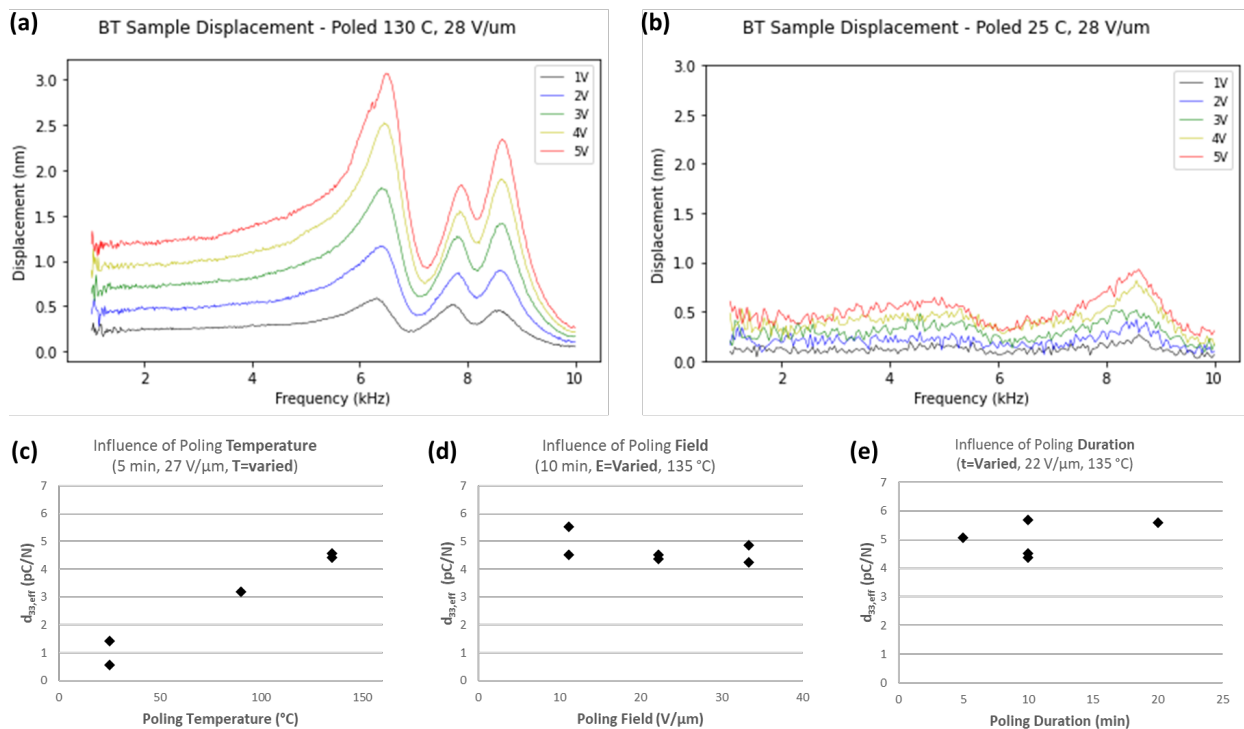


Figure 3.8 Initial results of BT poling investigations. Top row: LDV response for printed BT devices actuated under the same actuating conditions after poling at a field of 28 V/μm at (a) 130°C and (b) 25 °C. Bottom row: $d_{33,eff}$ measurement results (Berlincourt method) with varied (c) poling temperature, (d) poling field, and (e) poling duration.

Though Chen and Wang have both reported 3D printed BaTiO₃ with large piezoelectric responses of 146 and 190 pC/N respectively, these values were achieved after sintering the printed structures at 1300 °C.^{265,266} For low-temperature 2D printed BT, only Nguyen has reported a piezoelectric coefficient, when preparing a BT-PUA composite cured at 150 °C, for which a value of 1.3 pC/N was measured, matching reasonably well the measured printed BT values.¹⁴⁸

This feasibility study confirmed that (a) barium titanate devices can successfully be fabricated on paper substrates and (b) such devices can be poled at both the Curie temperature and at ambient conditions to result in a measurable piezoelectric response. It further supported the hypothesis that poling parameters can influence the net piezoelectric response attained, and should thus be further studied to improve the piezoelectric response of printed piezoelectric devices. With the conclusions of this study, we gain confidence that such processes for device fabrication and low temperature poling are possible with the less toxic perovskite material of interest, KN, and now look to confirm its printability and piezoelectric nature before finalizing it as the down-selected piezoelectric material for further development of this thesis work.

3.3.2 Potassium niobate validation studies

In this final set of validation studies, we aim to confirm the printability of KN as well as verify its piezoelectric nature prior to further printing process development, as will be discussed in Chapter 4.

3.3.2.1 Preliminary KNbO₃ ink development

As there was no published precedent in the literature for printing potassium niobate, initial studies were conducted to determine if a printable ink could be developed for KN. These inks were developed for screen printing KN over several iterations, focusing primarily on printed layer quality and viscosity, with ink compositions based off of work from Dulina and Li.^{257,258} High purity KNbO₃ source material (CAS 12030-85-2, 99.999%, Alfa Aesar) was used as the functional material. The ink compositions tested are detailed in the Appendix (Section 8.4.5), along with a more detailed description of this investigation. Solvents assessed included H₂O, IPA, EtOH, DEGMBE, and pentanol. In the initial round of development, inks contained 5–10 wt% KN. Binding agents tested were PVP, gum tragacanth, and ethyl cellulose, and were tested in the range from 2–20 wt%. In total, more than 20 potential ink recipes (varying combinations of solvents and binders in addition to KN and binder loading) were evaluated in this feasibility study.

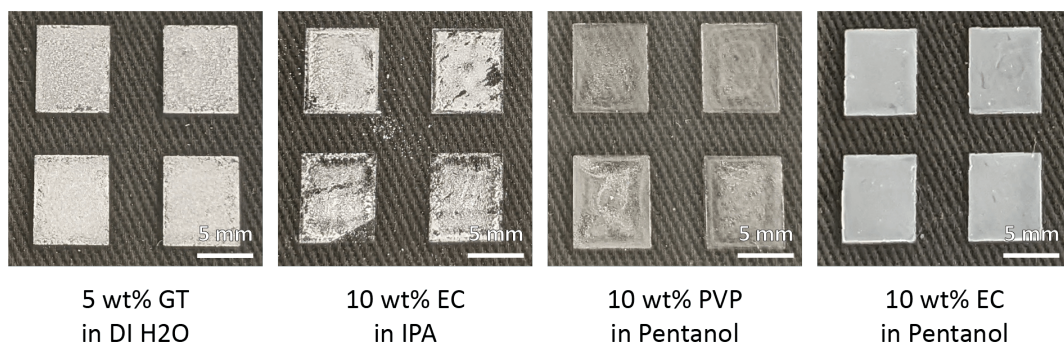


Figure 3.9 Examples of stencil printed KN layers during recipe down-selection. All inks displayed contain 10 wt% KN in addition to the annotated recipes and were printed under the same processing conditions.

For initial assessment, test ink compositions were stencil printed onto glass substrates through 27 and 125 μm thick PET stencils, allowed to dry for 30 min in ambient conditions, then evaluated for their structural properties. Examples of test inks are depicted in Figure 3.9, showing inks containing 10 wt% KN with a variety of binding agents, showing the influence of binding agent and solvent on printed film condition. Regardless of recipe, ink stability was very poor, with KN particulate observed to sediment within several hours of initial mixing. KN inks comprised of 10 wt% EC and 10 wt% KN in pentanol produced the most homogeneous printed layers of the material combinations evaluated with the slowest rate of sedimentation. The comparatively low volatility of pentanol and its corresponding influence on film drying time permits reduction of residual stresses and thus improved film quality as compared to IPA or EtOH-based inks of the same composition, while inks using EC as the binding agent proved the most homogeneous. Even this selection of solvent and binder, print quality was poor, with adhesion problems and high surface roughness. Further investigation attributed the ink sedimentation to large KN particle size in the source powder, also a likely cause of the high surface roughness

observed in printed layers. It was hypothesized that milling the source powder to reduce the average particle size of the KN material would therefore improve ink stability as well as reduce printed layer surface roughness.

Hence, ball milling was used to grind a small batch of KN powder following a procedure established by Birol (detailed further in Section 4.1.1.2) to test this hypothesis and found it to hold merit, as ink stability and layer roughness improved significantly with reduction in particle size.²⁴⁹ The resulting batch of ink (10 wt% ground KN with 10 wt% EC in pentanol) was used to fabricate preliminary parallel plate capacitor structures using 20 nm thick sputtered gold electrodes on glass substrates with device areas of 1, 4, and 9 mm². KN layers were stencil printed using 27 μm thick PET stencils to fabricate the devices depicted in the inset image of Figure 3.10, resulting in printed films of 5–15 μm thickness and an average roughness of 2–3 μm.^{††} Fabrication of such devices verified that capacitors could indeed be realized using the developed KN ink, though with a yield of working devices below 30%, significant improvements were deemed necessary as part of future work (as will be addressed in Chapter 4).

3.3.2.2 Piezoelectric nature of KNbO₃

The high purity KN powder used for ink development (>99.999%) is expected to be in the non-centrosymmetric orthorhombic phase at room temperature, but in the course of particle milling, it is possible that this might have changed. Thus, we elected to confirm the ferroelectric nature of the material used for printing prior to further advances in printing.

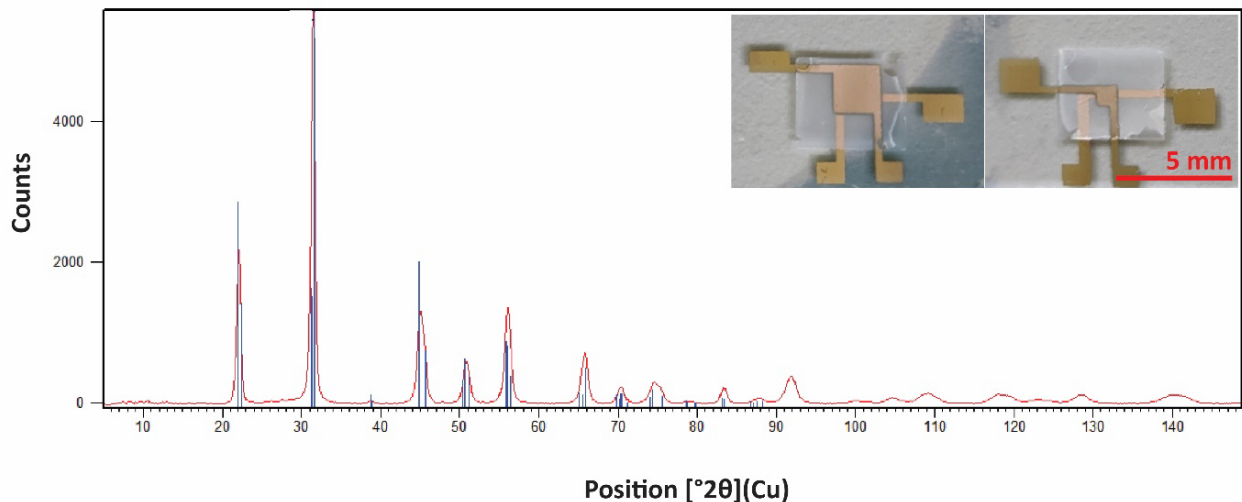


Figure 3.10 Diffraction spectra of KN powder, showing Amm2 orthorhombic crystal structure, with inset showing the as-fabricated initial devices utilizing this material.

It was hypothesized that the milling process utilized to reduce the particle size additionally compromised the crystal structure of the material, most likely through mechanically degrading the particulate to be less crystalline, or possibly through an unanticipated phase transition caused by introduced impurities. To test this hypothesis, powder diffraction was used to evaluate the crystal structure of the KN powder post-grinding, which was found to be in the orthorhombic (Amm2) phase. This is the expected phase for room temperature KNbO₃ and is a piezoelectric crystalline phase (resulting spectra depicted Figure 3.10). As a result, it was confirmed that the KN powder used in ink development was indeed a viable material for printed piezoelectric devices.

With low temperature printing and poling processes confirmed using barium titanate as a proxy, preliminary results showing a path towards printed KN, and confirmation of the crystalline nature of the KN material used, we conclude with the down-selection of non-toxic piezoelectric materials and identify potassium niobate as the choice for future process developments.

^{††} Stencil printing was used in this instance due to low ink viscosity, which was incompatible with screen printing. This is adjusted in the following chapter.

3.4 Summary and conclusions

In this chapter, the development process towards printed green piezoelectric devices is begun by evaluating and down-selecting functional materials. To start, key considerations of device and ink components are briefly reviewed, as is necessary to ensure full device compatibility towards the end goal of a fully printed green piezoelectric device. This is followed by selecting a printing method on which to focus development efforts.

For device components, paper was first identified as the target substrate for printing based on its comparatively high thermal resistance of approximately 150 °C. Zinc and carbon were selected as potential electrode materials, with zinc being the preferred choice based on its higher conductivity, but a riskier material for device integration due to its complex processing. Carbon electrodes are more established, with simpler processing, but the lower conductivity of carbon electrodes makes it less desirable than zinc depending on application. We elected to focus on screen printing as the printing method of choice, due to the simplified ink formulation and the thicker layers compensating for the paper surface roughness. This was followed by defining some considerations for ink components, with a focus on green binding agents and solvents, before an evaluation and down-selection of potential piezoelectric components was undertaken.

We first assessed four biodegradable piezoelectric candidate materials. Rochelle salt and ammonium dihydrogen phosphate were dismissed from further study based on the challenges associated with reproducible fabrication of oriented crystal layers in combination with their high sensitivity to changes in ambient humidity and temperature conditions. Zinc oxide-based inks were successfully formulated, but particle orientation proved to be a significant challenge. Though a viable material if none others were identified, ZnO was not continued for further study. Hydroxyapatite showed promise, with screen printable inks successfully formulated into capacitive devices, but no piezoelectric response was observed from the samples. Further crystallinity studies found HA to not be in a piezoelectric crystal phase and thus it was dismissed from the study.

Following the conclusion of those studies, we considered using non-toxic perovskite materials in their stead. To start, we used proxy material barium titanate to verify that perovskite materials could be processed at low temperatures and demonstrate a piezoelectric response. By modifying conventional BT inks, films were successfully printed onto paper substrates at room temperature, and BT capacitive devices were fabricated. Device poling was conducted at both the Curie temperature and at room temperature, with measurable piezoelectric response confirmed at both poling conditions. Coefficients as high as 5.9 pC/N were measured for devices poled at 135 °C and 1.8 pC/N when poled at 25 °C. This positively confirms that room temperature printed perovskites can exhibit a piezoelectric response after poling in ambient conditions.

As a continuation of the perovskite feasibility study, potassium niobate inks were developed using pentanol as a solvent and ethyl cellulose as a binding agent. After grinding of the KN particulate to produce higher stability inks, capacitive devices were fabricated from stencil-printed KN layers. Crystalline analysis via powder diffraction showed the material to be in a non-centrosymmetric crystalline phase and thus viable for piezoelectric behavior.

Thus, we demonstrated that KN could be developed into screen printable inks, and that it is in the correct crystalline phase to exhibit ferroelectric properties. This successful series of investigations permits the final confirmation of KN as the material of choice for future device development and optimization, as will be elaborated upon in the following chapters.

Chapter 4 Development and optimization of a low-temperature piezoelectric KNbO₃ printing process

In this chapter, we look to develop a manufacturing process for the fabrication of screen-printed KNbO₃ piezoelectric devices, and study factors that influence device performance and print quality.

In the previous chapter, we verified that ferroelectric materials processed at room temperature can demonstrate a measurable piezoelectric response through a feasibility study using barium titanate. We conducted preliminary work to develop a KN-based ink and fabricate simple capacitive structures with it. We then confirmed the ferroelectric nature of KN by powder diffraction.

We now look to further develop and improve this ink, aiming to define robust processes for fabricating printed piezoelectric devices with a KN-based active layer. This includes refining ink composition, printing parameters, and poling parameters to enhance piezoelectric performance. In optimizing an ink for device applications, improvements are not limited exclusively to piezoelectric characteristics, but must additionally consider the quality and reproducibility of the printing process—a compromise must be made between piezoelectric performance and manufacturability. We chose to do this first on more conventional (but non-degradable) glass and silicon substrates for this study to better study system before transitioning to degradable substrates in Chapter 5.

Yet before a detailed development cycle can be conducted, the piezoelectric response of printed KN films must be empirically demonstrated. To this end, we begin the discussion by describing the basic manufacturing steps utilized in this chapter: grinding the KN powder, preparing the piezoelectric ink, and fabricating printed capacitor devices on silicon and glass substrates. We additionally note those parameters which change through this development phase. The capacitor devices manufactured using the initial process parameters are then characterized for both physical and electric properties. In doing so, we experimentally substantiate piezoelectric response in such printed devices for the first time and establish a baseline against which further process developments can be compared.

Next, we assess factors affecting the print quality and device yield, both concerning the ink recipe (e.g., KN particle size, binder content) as well as processing (e.g., printing method). We evaluate factors influencing device dielectric and piezoelectric performance, focusing on studying how properties of the KN powder used in the ink affects piezoelectric performance (e.g., KN source and purity, grinding process parameters). These studies serve to identify those process parameters which result in the highest piezoelectric response without otherwise compromising device integrity when fabricated on non-degradable substrates.

This chapter concludes with a summary of the end process identified for further integration into green devices, as well as a brief discussion of future studies and prospects for this ink development. The content of this chapter serves as the process development work conducted towards the publication of a research article published in *Microsystems & Nanoengineering* in February 2023, the results of which are discussed in the following chapter (Chapter 5).²⁶⁷

4.1 KN ink preparation and device fabrication

This section describes the three primary phases of the manufacturing process. We begin with the KN powder preparation, including details of the grinding process. This is followed by the KNbO₃ ink recipe and mixing methodology, followed by the standard device fabrication process. We end the section by fabricating a set of samples for piezoelectric response validation, which serves as a benchmark for the process improvements discussed throughout the remainder of the chapter.

4.1.1 KNbO₃ powder preparation

4.1.1.1 Source material selection

For the purposes of this study, commercially available KNbO₃ (KN) source powders were selected to ensure high purity KN was utilized. Due to a lack of commercial applications, and materials scarcity resulting from the COVID-19 pandemic, the pool of available suppliers was limited, and just three source powders were acquired for study. The primary powder was supplied by Alfa Aesar (“AA”) with a reported purity of 99.999% (metal basis). This powder was utilized for the majority of the studies discussed further in this chapter. For comparison, two other powders were additionally studied, supplied by Stanford Research Materials (“SRM”), in purities of 99.9% and 99.999%. The particle size distribution and constituent impurities of all three powders were determined by proprietary processes of the manufacturers and thus were not controlled for in the course of this work.

4.1.1.2 Particle size reduction via ball milling

As mentioned previously in Section 3.3.2, particle size is a critical factor in the manufacture of a screen printable KN ink. Of primary concern, the initially evaluated KN inks (manufactured using the 99.999% purity AA ink) were found to be unstable over time due to sedimentation of the particulate, and those sufficiently stable produced printed layers of significant surface roughness. Further investigation determined that the particulate of KN utilized in the inks was several microns in diameter—significantly larger than ideal for screen printing applications. A proof-of-concept experiment confirmed that both ink stability and print quality could be improved through grinding* of the KN source powder to reduce particle size.

The initial experiment followed the procedure described by Birol, which was used as the basis for further studies regarding KN particle size reduction.²⁴⁹ This process is visualized in Figure 4.1 below. First, 7 g of KNbO₃ source powder (Alfa Aesar, 99.999% pure, metals basis) was mixed with 14 mL of isopropanol in a 125 mL stainless steel vessel. Stainless steel grinding media (200 g, 2 mmØ) was mixed into the vessel which was then sealed. The milling vessel was placed in a planetary ball mill (Retsch PM200) for 24 hours, with a directional switching period of 5 min and a jar rotational speed of 200 rpm. The solvent-to-powder grinding ratio of 2 mL isopropanol per 1 g of KN proved to be significant for successful grinding, as will be discussed in Sections 4.2.1 and 0.

Once complete, the jar was unsealed and the powder-solvent slurry was separated from the grinding media using a sieve (Teflon mesh, aperture 0.5 mm) and placed in a glass evaporation dish to allow for evaporative removal of the remaining IPA solvent at room temperature over approximately 72 hours (conducted in a fume hood). The powder was then collected and dried in an oven at 120 °C to ensure the removal of any adsorbed humidity before integration into an ink. Later process iterations improved this evaporation process by placing the evaporating dish on a hotplate at 80-120 °C for the duration of the separation, reducing the process step from 72 hours to approximately 12 hours, with no influence on the resulting powder. As will be discussed in Section 4.4.1, this process was later modified to include a post-grinding annealing step to improve the crystalline quality of the powder. Annealing was conducted in a muffle furnace at 625 °C for 4.5 hours and was followed by a passive cooling step of approximately 16 hours.

* The terms “grinding” and “milling” are used interchangeably throughout this discussion.

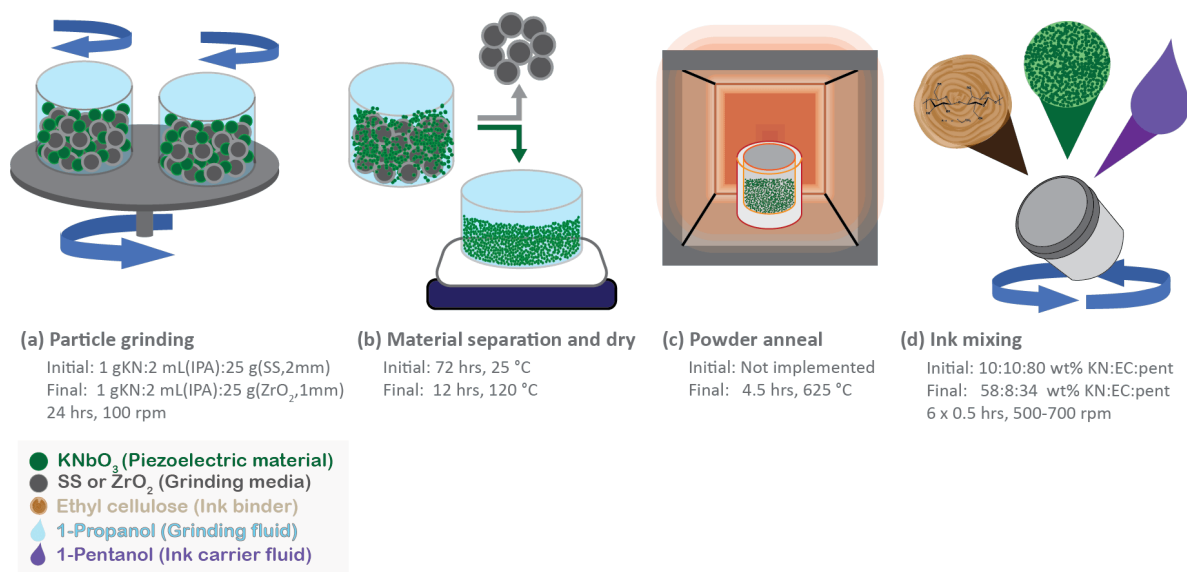


Figure 4.1 KN ink preparation process consisting of (a) grinding of KN particles, (b) separation of ground particles from grinding media and drying off of isopropanol grinding aid, (c) annealing of powder to improve particle crystallinity and (d) mixing of screen-printable KN ink.

Later work involved the transition from stainless steel grinding vessels and media to Teflon jars and ZrO₂ media (1 mmØ) to reduce potential contamination from jar materials into the ground KN powder. With this came the transition from a Retsch PM200 to a QM-SP2 planetary ball mill and minimally adjusted grinding parameters. This will be discussed in Section 4.3, along with some commentary on the influence of grinding parameters on device performance.

The 99.9% purity SRM source powder was found to have a significantly smaller average particle size than the 99.999% purity powders from either SRM or AA, and thus the grinding step was not necessary for inks developed with this source material.

4.1.2 Ink preparation

With KN powder processing complete, ink preparation is fairly straightforward. Ink components included the prepared KNbO₃ powder, ethyl cellulose (CAS 9004-57-3, Merck, viscosity 10 cP, 5% in toluene/ethanol 80:20 (lit.), extent of labelling: 48% ethoxyl) as the binding agent, and pentanol (CAS 71-41-0, Merck, ReagentPlus, ≥99%) as the solvent.

The three components were added to a mixing jar according to the recipe-defined mass ratios, and 5 g of Al₂O₃ mixing balls (6 mmØ) were added to the jar. A planetary ball mill was then used to mix the ink components (initially using a Retsch PM-200, later using a Thinky ARE-250) in a series of 30 min increments at 500-700 rpm, repeated 6 times with a 10 min pause between steps. This incremented mixing was implemented to reduce evaporative solvent losses from container heating during the high energy mixing steps. After mixing, the ink was sealed, then stored in a refrigerated environment when not in use.

The initial ink recipe developed during the materials down-selection process consistent of 10 wt% KN and 10 wt% EC in pentanol. While this ink was sufficient for proof-of-concept investigations, the poor ink stability and resulting low device yield made it non-desirable for further process development, even after particle size reduction, and incompatible with screen printing processes due to the too-low ink viscosity. It was deemed necessary to adapt the ink recipe for higher stability prior to further testing.

To this end, the KN ink recipe was first adjusted by significantly increasing the loading of KN particulate from 10 to nearly 60 wt% KN. This loading was selected based off of the BT ink used for validation testing (and additionally utilized by Sivanandan for PZT inks).²⁶⁸ The improved recipe contained approximately 58:8:34 wt% KN:EC:pentanol (still requiring the adjustment of KN particle size as mentioned in Section 3.3.2). The ink remained stable, with minimal sedimentation, over the course of several months—a remarkable improvement over the prior inks with 10 wt% KN—and improved rheology towards implementation in stencil and screen-printing applications. This improved recipe served as

the basis for all inks developed and investigated in this chapter. Section 4.2.1 overviews some of the printing improvements observed with this adjusted recipe.

4.1.3 Device architecture and fabrication

We elected to fix the basic device architecture and fabrication process for devices during this development phase so as to reduce the set of contributing factors related to device performance during analysis. All devices were fabricated in a parallel plate capacitor architecture on glass or silicon substrates using standard 100 mm \varnothing wafers, with the same device architectures utilized in the BaTiO₃ feasibility studies described previously in Section 3.3.1, with each wafer containing 84 devices with effective capacitor areas of 1, 5, 10, or 20 mm². Circular capacitor devices were designed such that there a 100–300 μm gap was present between the edge of the electrodes and the edge of the piezoelectric layer ($d_{KN} > d_{electrode}$). This extra distance in the piezoelectric film served multiple purposes. It compensated for mask misalignment between the multiple device layers, reducing device shorting caused by human error. Additionally, it served to reduce edge effects of the electrodes on dielectric analysis, while also significantly increasing the exposed surface pathlength between electrodes to reduce the chance of breakdown caused by surface flashover to permit device poling at higher fields that would otherwise be infeasible. For all parameters studied in this chapter, a minimum of 42 devices were fabricated (half of the designed wafer depicted in Figure 4.2 below), with at least 5 devices of each capacitive area, to ensure thorough analysis of device performance.

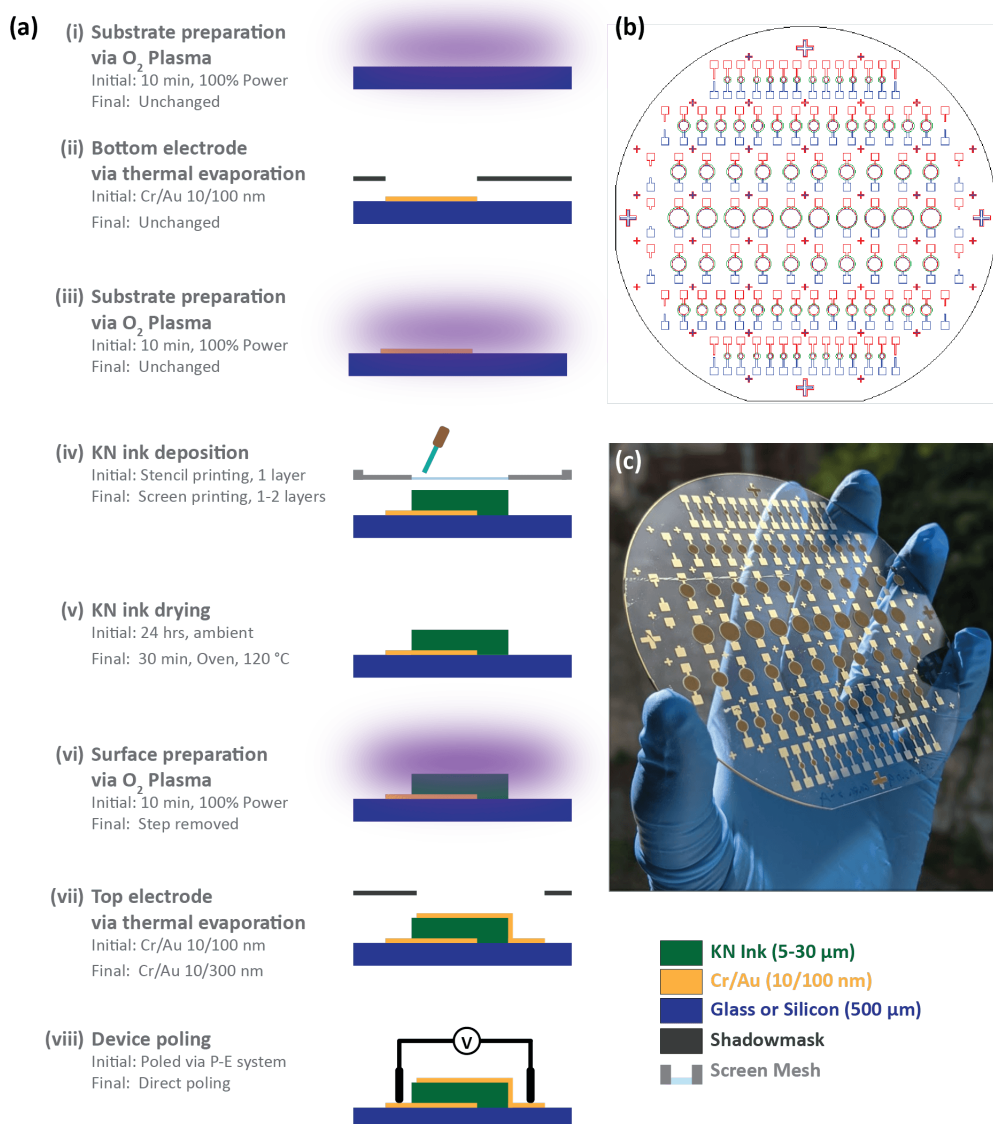


Figure 4.2 Process flow and device design for ink development investigations showing (a) process steps for capacitor device fabrication, (b) Top-down schematic of device layout showing 1, 5, 10, and 20 mm² devices, and (c) photograph of a completed set of printed capacitors.

The general fabrication process is described schematically in Figure 4.2(a) above, with seven basic steps. First, the glass or silicon substrate was pretreated using an O₂ plasma cleaner (Diener ATTO, 100% Power, 10 min). The bottom electrode (10/100 nm Cr/Au) was thermally evaporated using a Leybold L560 thermal evaporator onto the substrate through a stainless steel shadowmask. The substrate was then pre-treated once more with the O₂ plasma cleaner (parameters unchanged), to improve printed layer adhesion. Immediately following the plasma treatment, the KN ink was stencil printed onto the substrate. Stencil printing was conducted using single-use stencils made from electrostatically adhesive PET films of 27 or 95 μm thickness (Nexus HP05S(27um) or GP20), laser-cut in-house to the desired pattern using a Trotec Speedy-300 laser cutter. Following stencil printing, the stencil was removed from the substrate and the KN film was dried in ambient conditions for 12–24 hours.

Later process development transitioned from stencil- to screen-printing (discussed in Section 4.2.2). Screen printing was conducted using a manual screen printer (Charmhigh 3040 High Precision Manual Solder Paste Printer), with a maintained substrate–mesh gap of 2 mm. Mesh fabrication was provided by Serilith AG using a polymer mesh (PME 120-30Y) mesh material. With the thinner layers resulting from the transition to screen printing, printed layers could be dried at higher temperatures without the risk of residual stress-induced delamination and cracking (as was observed in stencil printed layers). These ink layers were dried in a Memmert UF110plus oven at 80 or 120 °C for 30 min after each layer. In Section 4.3.1, we discuss the influence of layer drying temperature on device performance.

In another deposition step (step vii), the top electrode was thermally evaporated onto the stack through a stainless steel shadowmask using the same deposition parameters as utilized for the bottom electrode. In Section 4.3.2, we briefly assess the influence of the thermally evaporated top electrode thickness, material, and processing conditions on the fabricated capacitors. Figure 4.2(b) depicts a top-down schematic of the wafer layout, showing seven rows of circular capacitor devices ranging from 1 to 20 mm². The design detailed in subfigure (b) is used to fabricate the wafer photographed in Figure 4.2(c) on a glass substrate using via stencil printing using the described process.

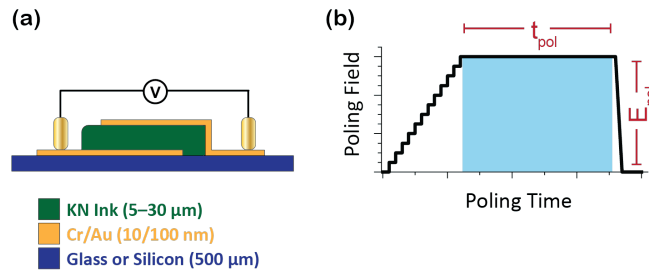


Figure 4.3 Details of the poling process for printed devices. (a) Schematic of a device being poled, showing the voltage being applied across the top and bottom printed electrodes. (b) Visualization of the poling process, showing the stepped increase in applied field up to the setpoint, E_{pol} , followed by a soak for a duration of t_{pol} , and finishing with an immediate full removal of the applied field.

To end the fabrication process, the printed devices are poled. In the initial validation test, this is done using a Sawyer-Tower circuit, but all later processes use a programmable high voltage power supply (HVPS, Peta-Pico-Voltron, developed in-house) instead. With the HVPS, printed devices are contacted across the top and bottom electrodes, using a method similar to that described previously during process validation with BT samples (and depicted here in Figure 4.3). Poling was performed at ambient conditions. The voltage was applied across the electrodes with a stepped ramp equivalent to 1 V/μm every 5 s until the applied field reached the target value. The target poling field, E_{pol} , was maintained for a set time period, t_{pol} ; where, upon completion of the soaking period, the voltage was dropped to 0 V/μm in a single step to complete the process. To start, poling processes were implemented with durations of 10–20 min and applied fields of 20–60 V/μm. In the next chapter (5.2.3), we conduct a more in-depth study evaluating these parameters and their impact on piezoelectric performance.

Prior to full device characterization, an analysis of device yield is conducted as a metric for the fabrication process as a whole. For this, the device resistance across the top and bottom electrodes is measured, and the device is considered functional if $R_{device} \geq 1 \text{ M}\Omega$ and shorted if the value does not meet this criterion. The percentage of the devices on a single wafer meeting this criterion is used to calculate the yield ($Batch \text{ Yield} = 100 * \frac{N(R_{device} \geq 1 \text{ M}\Omega)}{N_{total, batch}}$). In early analyses, device yield was also computed as a function of device area, as there is a correlation between higher functional area and higher rates of device failure, but improvements to printing processes quickly removed the necessity for such precision.

4.1.4 Validation of piezoelectric response in KN printed devices

Prior to extensive process improvement, the piezoelectric nature of the developed KN-based printed system must first be empirically confirmed. In fabricating these validation samples, potential process parameters requiring further study or improvement can be clearly identified. Furthermore, these devices will serve as a benchmark against which further processes and devices could be compared.

These devices were fabricated in the following manner: First, the KN powder (99.999% purity, AA) was ground using the standard 200 rpm for 24 hours protocol, with 2 mm ϕ stainless-steel (SS) grinding media in a SS vessel and a grinding ratio of 1 gKN:2 mL(IPA), before mixing into an ink using the standard recipe described above (58:8:34 wt% KN:EC:pentanol).

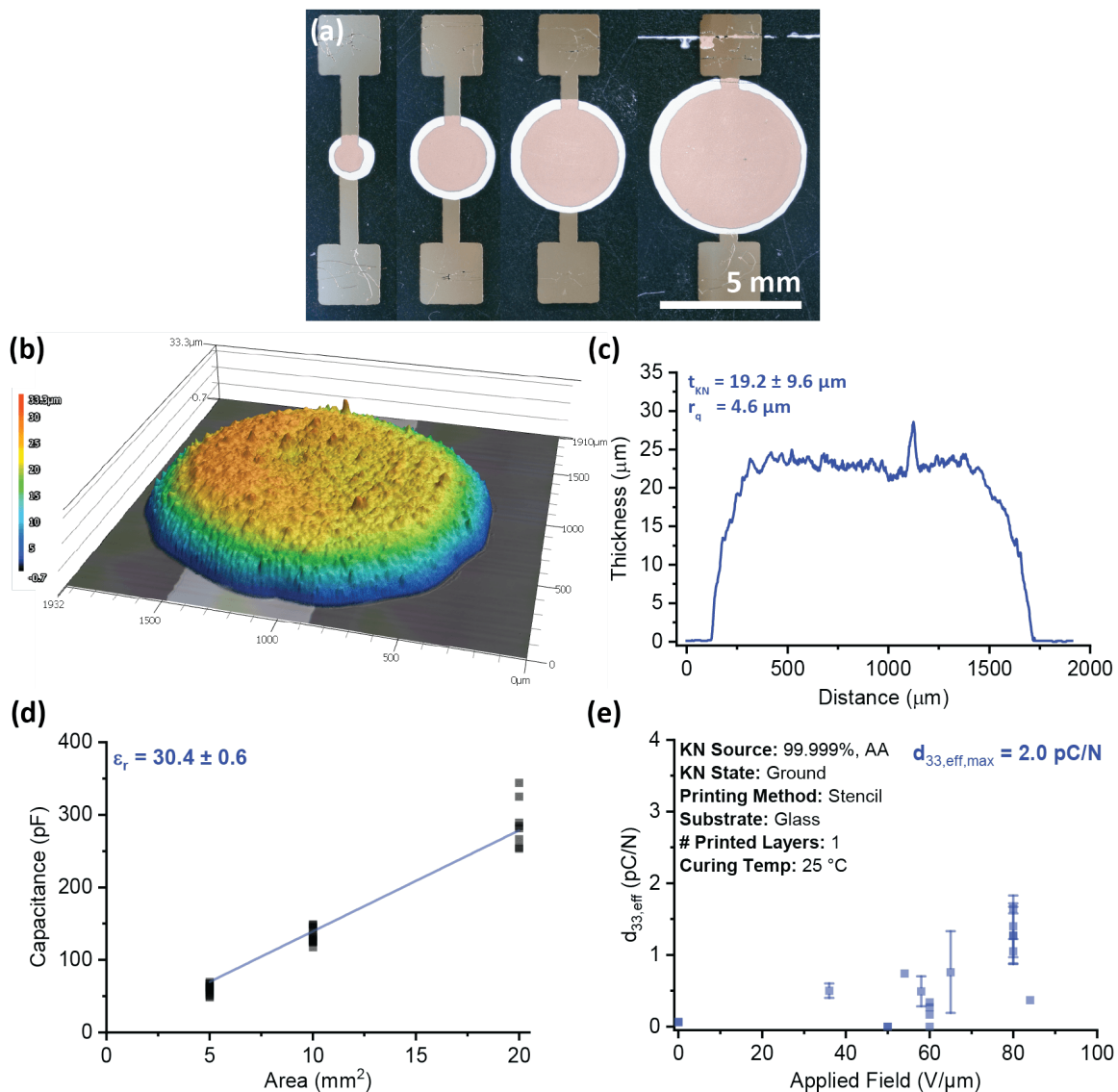


Figure 4.4 Physical and electrical characteristics of validation samples. Physical characteristics shown include (a) photograph of fabricated devices with effective surface areas of 1, 5, 10, and 20 mm², (b) confocal microscopy 3D scan showing the surface of a single device (vertical axis magnified 10x for visualization), and (c) line surface profile of printed layer. Electrical characteristics including (d) determination of layer relative permittivity and (e) measured effective piezoelectric coefficient, $d_{33,eff}$, as a function of maximum applied field.

With the standard 10/100 nm Cr/Au electrodes described above, a single layer of the prepared ink was stencil printed on glass substrates using laser-cut stencils of 27 μ m thickness and dried in ambient conditions for 24 hours prior to top electrode deposition via thermal evaporation.

The unshorted printed device yield was >95% for this process, and printed layers were on average $19.2 \pm 9.6 \mu\text{m}$ thick with an average surface roughness of $4.6 \mu\text{m}$ as calculated using confocal microscopy. Figure 4.4 shows some exemplary data of the physical characteristics of these early devices. Impedance analysis was conducted using an Agilent 4294A impedance analyzer, and the relative permittivity of the printed layer was calculated as 30.4 ± 0.6 (as measured in ambient conditions with a relative humidity of 30%), as plotted in Figure 4.4(d), within the expected permittivity range for a KN and EC composite material. Samples were then poled using a Tower-Sawyer circuit (conventionally used for ferroelectric P-E loop measurements) built and provided by D. Damjanovic of EPFL-IMX-DD, with applied electrical fields up to $85 \text{ V}/\mu\text{m}$ and a cycling rate of 50 Hz (making the soak time at $E_{\text{max}} = 0.02 \text{ s}$). Following the poling process, the effective longitudinal piezoelectric coefficient, $d_{33,\text{eff}}$, was measured using the Berlincourt method, the results of which are exhibited in Figure 4.4(e). The largest measured piezoelectric coefficient was approximately 2.0 pC/N and increased with increasing maximum applied poling field. This was the first known instance of a room-temperature printed piezoelectric device made of potassium niobate, even though the values were significantly lower than the bulk coefficient reported for KNbO₃.

This validation successfully verified the piezoelectric nature of devices fabricated from printed KN piezoelectric layers and serves as a reference against which the studies detailed in the rest of this chapter will compare.

4.2 Process factors affecting print quality

Before device performance can be studied, a process must be established to produce high quality printed layers in a reproducible manner. As mentioned in the previous chapter, the initially developed KN ink was sufficient for proof-of-concept experiments, but the low unshorted device yield (<15%) and poor layer quality (prone to cracking and delamination) limited the practicality of the system for use in large scale manufacturing—as is one of the specified goals of this work. To this end, several parameters were evaluated for their influence on print quality (e.g., layer thickness, surface roughness, adhesion to substrate) and device yield (percentage of devices exhibiting dielectric behavior $\geq 1 \text{ M}\Omega$ upon completion of the fabrication process). We now take some time to assess these parameters before continuing with the process development focused on device performance.

4.2.1 KN particle size

The as-acquired KN source powder used in initial investigations supplied by Alfa Aesar proved to be inadequate for printing applications due to the large average particle size, requiring the milling process described in Section 4.1.1. Particle size distribution analysis determined the average particle diameter of the unground powder to be $3.8 \pm 4.2 \mu\text{m}$, notably larger than what is desirable for printing applications where the particle size should be <10% of the targeted layer thickness (which is $<10 \mu\text{m}$ for this work). Using the initial milling parameters described above, inks prepared from the ground powder (58.6:7.5:33.9 wt% KN:EC:pentanol) exhibited a marked improvement in both print quality and device yield, with an improvement in device yield from <10% with the unground powder to >95% with the ground powder.

After further refinement of the milling process, the average particle diameter was reduced to just $160 \pm 80 \text{ nm}$ (milled with the finalized parameters noted in Figure 4.1). As depicted by the particle size distributions in Figure 4.5(a), the milling process not only reduced the average particle size, but also improved the homogeneity of the powder. This can be further inferred upon inspection of the unground and ground powders by scanning electron microscopy (SEM) as shown in Figure 4.5(b).

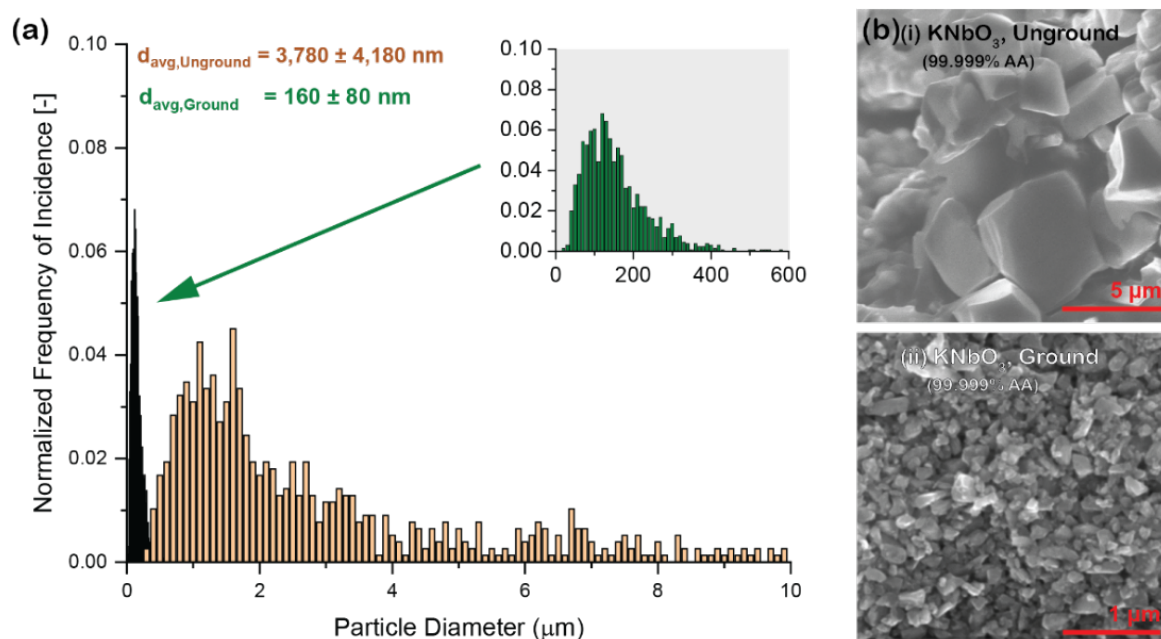


Figure 4.5 Particle size analysis of KN powders including (a) particle size distribution for both the unground and ground KN (99.999% purity, AA), and (b) SEM images of (i) unground and (ii) ground KN particles as used for particle size analysis.

In order to achieve this result, a short series of studies was conducted to assess the influence of grinding process parameters on print quality. A reduction in milling speed from 200 rpm to 100 rpm was found to have detrimental effects on layer quality. We believe this is because the energy imparted in the milling process scales with the square of the jar velocity, and thus a four-fold reduction with the speed halved. The resulting powder showed no significant change in particle size distribution as compared to the unground powder, and thus the print quality was effectively unchanged as well. Milling time was set to 24 hours in accordance with Birol's procedure. A study involving varied milling time found that milling times longer than 24 hours resulted in particulate that approached the nanomaterial range (defined by $d_{50} < 100$ nm). Though using smaller particulate is typically associated with improved print quality, it would negatively affect the potentially achievable piezoelectric response of the material, as has been established previously in several studies.^{269–272} Furthermore, nanoparticles have been recently established as potentially hazardous to biological organisms, and thus non-ideal for the intended application in degradable electronics.^{273–275}

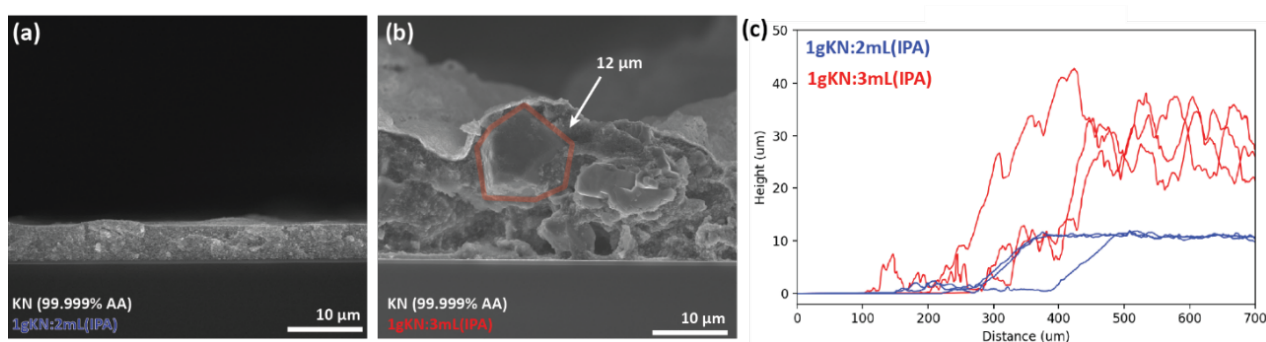


Figure 4.6 Influence of grinding solvent ratio on printing quality showing SEM cross-sections of samples with (a) 1:2 grinding ratio and (b) 1:3 grinding ratio, along with (c) surface profilometry of screen-printed films using KN powder processed with these two grinding conditions, each plotted in triplicate.

A final study was conducted evaluating the influence of the ratio of KN powder to IPA solvent during the grinding process. The standard ratio was established as 2 mL isopropanol per 1 g of KN source powder. Quantities below 1 gKN:2 mL(IPA) ratio could not be effectively realized and are not reported here. With a ratio of 1 gKN:3 mL(IPA) or greater, the resulting powder produced printed layers with remarkably large surface roughness not observed in layers fabricated with the 1:2 ratio. Particle size analysis showed a nonhomogeneous distribution of particles with the higher solvent ratio, as depicted in Figure 4.6(a,b), matching well with the high surface roughness determined by surface profilometry (Figure 4.6(c)). It was hypothesized that the more dilute slurry allowed sedimentation of the largest particulate in the milling jars

before the grinding process could commence. Despite this, device yield for devices printed with the higher ratio was still >90%, permitting further device characterization. In Section 0, we will revisit this parameter to assess the influence of grinding ratio on the piezoelectric response of printed devices.

4.2.2 Printing method

With the printing layer improvements resulting from the increased KN content in the ink and the effective particle size reduction after the grinding process, the manufacturing process methodology could be transferred from stencil to screen printing. Initial ink development had focused on stencil printing due to the rapid iterative nature of in-house fabricated stencils for adjusting device design. However, the stencil printing methods used thus far for fast iterative ink development were deemed nonideal for ongoing device work, as the thickness of the stencils used (27 or 95 μm) limited the thickness of the printed layer to >20 μm , and frequently resulted in layer cracking from residual stresses. In addition to limiting the thickness device that could be fabricated, the stencil method resulted in large thickness variance across the dimension of the layer dependent on printing direction. Thus, the manufacturing process was transferred to screen printing, where individual layers could be printed in the range of 1–10 μm (depending on ink properties).

The process transition focused on adapting an ink developed for stencil printing to use with screen printing processes. The ink used for this investigation used the standard recipe (58:8:34 wt% KN:EC:pentanol), with KN powder (99.999% purity, AA) ground using the ideal conditions discussed in the previous sections. Two sets of devices of the same design were fabricated under the same processing conditions with the exception of the printing method with the first printed using stencils (27 μm thickness), and the second screen printed using a polymer mesh (PME 120-30Y).

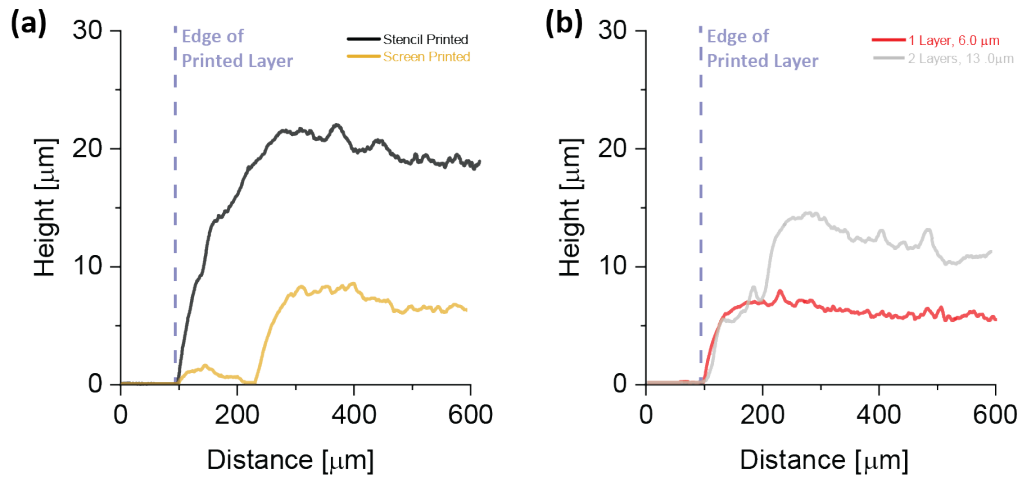


Figure 4.7 Influence of processing factors on printed KN film thickness, including (a) printing technique and (b) number of printed layers.

The capacitor devices fabricated with stencil printing achieved a yield of >90% viable devices, while those made with screen printing achieved a yield of 83%, defined by the percentage of unshorted devices ($R \geq 1 \text{ M}\Omega$). The reduced yield for screen printed devices was attributed to a combination of device shorting through the thinner KN layer and top electrode mask misalignment. Regardless, the yield was deemed sufficiently high for manufacturing purposes. Confocal microscopy and surface profilometry were utilized to evaluate the layer thickness and surface roughness of both sample types. Stencil printed devices had an average thickness of $18.3 \pm 0.4 \mu\text{m}$ while screen printed devices measured $6.0 \pm 0.3 \mu\text{m}$ in thickness. Examples of sample profiles are depicted in Figure 4.7(a) showing the significantly thicker stencil printed layer as compared to the screen-printed layer otherwise processed in the same conditions.

In a second experiment, the same manufacturing process using screen printing was conducted to evaluate the possibility to print multiple layers of KN to produce thicker films. Devices of one or two screen printed layers were fabricated and assessed for yield and device quality. Device yield was comparable between the two sample sets, with an 83% yield for devices with a single screen printed KN layer and 78% for those with two screen printed layers. It was hypothesized that, for samples printed in the same conditions, mask alignment and user technique were more significant factors influencing device yield as opposed to stochastic failures caused by pinhole shorting through the KN film. Surface profilometry confirmed the expected result: the two-layer device was approximately twice the thickness of the single layer screen

printed devices (6.0 and 13.0 μm for the single- and double-layer devices respectively). Figure 4.7(b) shows this result from profilometry scans. Film adhesion was evaluated using ASTM F1842–15 standard testing protocols and were rated at a 4B-5B level, showing excellent adhesion. This will be further discussed in Section 5.2.1 for the finalized ink and process.

With confirmation that device yield was not significantly affected by the transfer to screen printing, and the improved printing resolution resulting from thinner layers with the option for stacking multiple layers, the process transfer was considered successful. Thus, the following studies transitioned entirely to screen printing unless otherwise noted.

4.2.3 Binder content

As discussed in Section 3.3, high temperature sintering used in conventional ceramics processing is not feasible on degradable substrates. We compensate for this by using a higher-than-typical binder content to improve structural integrity in the printed layer (7–8 wt% as opposed to the more common 1–2 wt%). We now look to assess if device performance can be enhanced through increasing binder content further.

The basic ink recipe established in Section 4.1.2 above contains an ethyl cellulose content of 7.4 wt%, resulting in printed layers containing approximately 67:33 vol% KN:EC. For comparison, we prepare an ink containing 12.2 wt% EC to produce printed layers of 50:50 vol% KN:EC, while maintaining a fixed quantity of both KN (99.9% purity, SRM) and pentanol. The resulting ink delaminated from the substrate immediately upon drying, resulting in a device yield of 0%.

Further increases in solvent content—elongating film drying time to allow further dissipation of residual stresses—permitted printing of this ink without immediate delamination. We established a limit of approximately 11.0 wt% EC in the ink from which a capacitive device could be fabricated on silicon, with a yield of just 12%. Impedance analysis of these devices determined a relative permittivity of 19 ± 2 , as compared to the reference ink with a measured permittivity of 38 ± 2 . Evaluation of the resulting devices' piezoelectric performance was limited due to the low device yield. Of the samples measured, the effective piezoelectric coefficient was significantly reduced, with a maximum measured value of 1.7 pC/N compared to 7.3 pC/N for devices fabricated from the 7.4 wt% ink prepared in the same method.

This short-loop investigation emphasized the key trade-off between device performance and ink composition. Increased binder content has the potential to improve piezoelectric response, but also influences device yield based on layer delamination. Future work could be done to assess the influence of binder content on piezoelectric response more thoroughly and introduce parameters such as varying the molecular weight of the EC instead of varying the loading amount or introducing other binding agents with more desirable physical properties. As this is out of the scope of the current work, the binding agent content was fixed to be 7.4 wt% in the ink for all future studies.

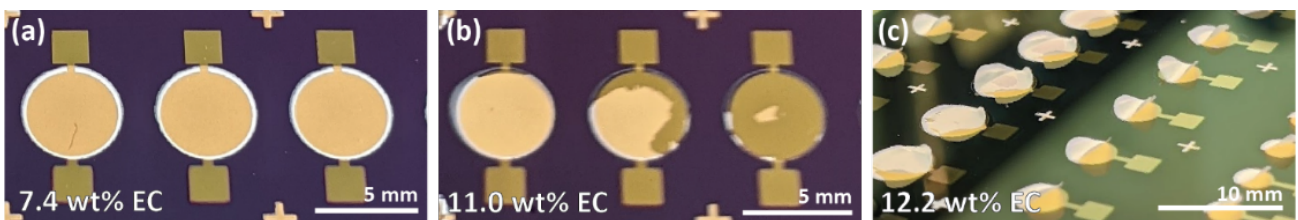


Figure 4.8 Printing quality variance resulting from increased ethyl cellulose binder content in ink from (a) 7.4 wt%, (b) 11.0 wt%, and (c) 12.2 wt%.

4.3 Process factors affecting device performance

In the development process, several variables were identified as potentially influencing dielectric performance of the printed KN capacitors. Of note, impedance analysis conducted on printed devices characterized in early development iterations exhibited unexpected levels of undesirable electrical leakage, indicating that the material was not acting purely as a capacitor but had a resistive component as well. By diagnosing and addressing the source(s) of this leakage, it was hypothesized that device performance could be improved. Here, we briefly discuss some of these investigations and any process changes that came about as a result (and detailed further in the Appendix Section 8.5).

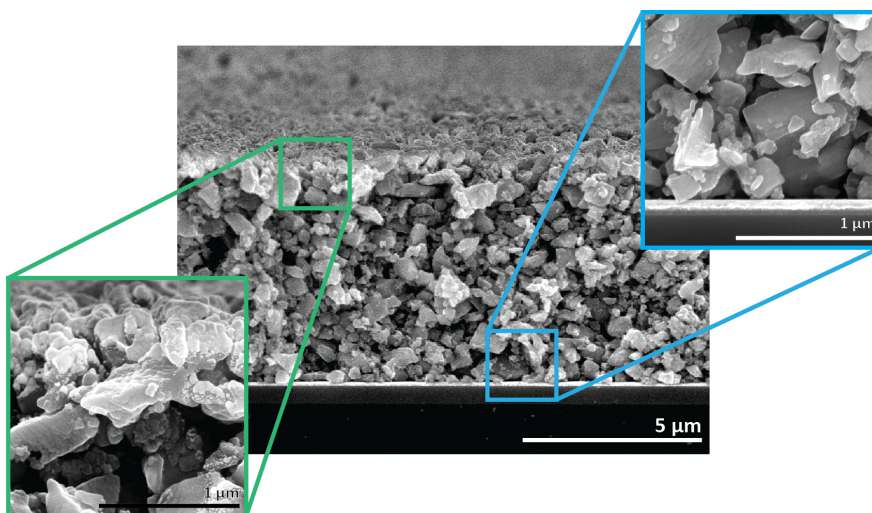


Figure 4.9 Cross-sectional SEM image of printed layer on a silicon substrate, with insets showing the potentially non-continuous thermally evaporated gold top electrode (green) and the porous nature of the KN printed layer at the interface with the bottom electrode (blue).

4.3.1 Film drying temperature

One proposed source of electrical leakage behavior stemmed from the possibility of pentanol solvent trapped in the printed layer, residually present due to the low fluidic conductance in the KN films even after 24 hours of drying in ambient conditions. Diagnostic inspection of the KN printed layer in cross-section (Figure 4.9) was conducted via scanning electron microscopy (SEM), which confirmed that the printed layer was highly porous, and thus solvent retention in the film is possible.

To study this effect, the layer drying temperature was increased from 24 °C to 80 or 120 °C (dramatically enhancing the rate of solvent volatilization and thus ensuring removal of residual pentanol) and any changes in dielectric behavior were studied. Stencil printed KN films in previous iterations were dried under ambient conditions based on film delamination observed when dried at higher temperatures—resulting from residual stresses in printed layers drying too quickly—and thus such an experiment was not feasible. However, the transition from stencil to screen printing came with a reduction in printed film thickness (from nearly 20 μm per layer to just 6 μm per layer when screen printed) that mitigates this concern, and thus the proposed hypothesis could be further investigated.

To test this hypothesis, a series of devices were screen printed according to the standard protocol described above (ink prepared using ground 99.999% AA KN), with the experimental variable as the drying conditions for the KN layer post-printing. Printed films were dried in a Memmert UF110plus oven for a period of 30 min at either 80 or 120 °C prior to top electrode deposition. Physical characterization of these samples found no significant change between drying conditions, with average film thicknesses of 5.9 and 6.0 μm for the 80 and 120 °C drying conditions respectively. Neither set of samples exhibited detrimental effects from the higher temperature curing conditions (e.g., no layer cracking or delamination was observed), as was a concern mentioned previously. Dielectric analysis found no significant difference in device characteristics dependent on film drying temperature, with the relative permittivity of the devices using 80 and 120 °C drying conditions respectively calculated as 24.2 and 23.9. This can be further compared to an equivalent device dried under ambient conditions with a relative permittivity of 25 ± 2 . With no major detrimental effects observed yet a significantly shortened fabrication time reduced from >12 hours to just 30 min per layer, further investigations implemented a 30 min drying step per layer at 120 °C for future investigations.

4.3.2 Electrode coverage, material, and processing techniques

Next, we assessed if the top electrode influences device performance. No change in device performance was observed when substituting the gold top electrode for thermally evaporated aluminum or platinum films, supporting the hypothesis that the material itself was likely not influencing device performance. To maintain consistency for the following experiments, gold was selected as the standard electrode material until process integration with printed conductive electrode materials is implemented (to be discussed in Chapter 6). The effect of electrode material on device performance

is revisited in that chapter, where the influence of carbon- or zinc-based printed electrodes is evaluated as compared to thermally evaporated gold electrodes.

In a separate study, we noted that KN capacitive structures were highly sensitive to changes in ambient humidity, with dielectric leakage increasing with increased humidity. Upon inspection of the top electrode via SEM (Figure 4.9 inset in green), we noted that the 100 nm top electrode was not fully continuous. It was hypothesized that this was either resulting in a smaller effective device area than that specified in the initial design due to the disconnected layer segments or was enabling ambient water to permeate the electrode layer. To study this, samples were fabricated with significantly thicker top electrodes (300–600 nm), and their dielectric behavior characterized. The thicker top electrodes showed no significant change in dielectric behavior as compared to equivalent devices with the standard 100 nm of gold top electrode tested under the same conditions. Hence, it was concluded that the effective device area was unchanged with the additional material and therefore the electrode was likely continuous across the device. A controlled study of device response to ambient humidity can be found in Appendix Section 8.5.2, where it was found that device architecture has a more significant impact on response than the material itself. Future work could study this behavior and work to mitigate it through device structure or the introduction of encapsulation layers.

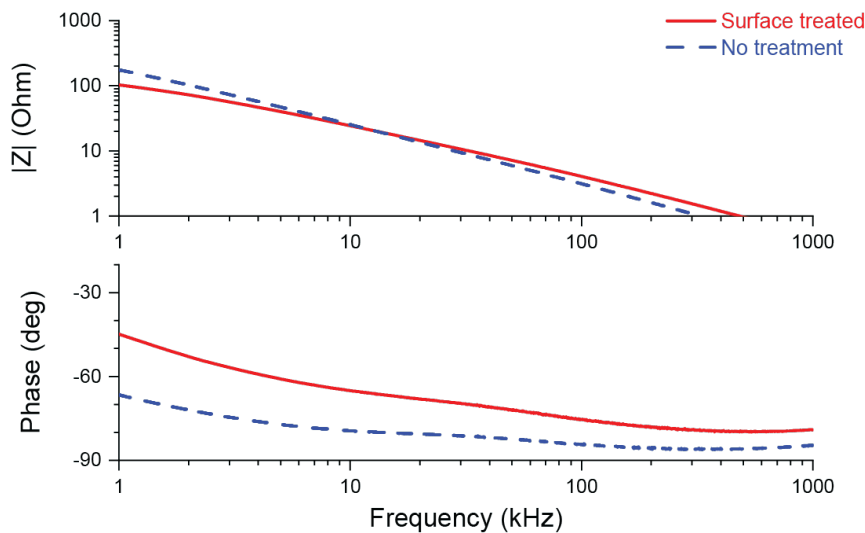


Figure 4.10 Influence of surface treatment on dielectric behavior of KN capacitive devices comparing those that did (red) with those devices that did not (blue) receive such treatment prior to top electrode deposition.

In a final study, we assessed the influence of surface treatment on device performance. Early development iterations included an oxygen plasma treatment step immediately before the top electrode was deposited via thermal evaporation (Figure 4.2(vi)). It was hypothesized that this treatment, incident on the porous printed KN layer, may be interacting with the material and resulting in non-ideal device behavior. Devices were thus fabricated with and without this final surface treatment step and dielectric behavior assessed. For all samples tested, it was found that devices receiving the final surface treatment exhibited less ideal behavior as compared to those which did not receive such a treatment (Figure 4.10), with a dielectric loss tangent, $\tan(\delta)$, at 100 kHz of 0.26 for samples treated with the plasma compared to 0.10 for samples without such treatment. Further, device behavior across samples was more consistent for samples without the surface treatment, and there was no change in the physical characteristics of the deposited electrode. Thus, the final plasma treatment step was deemed unnecessary and was removed from successive fabrication processes.

4.4 Material factors affecting device performance

The final section of this chapter concerns the evaluation of factors influencing piezoelectric device performance, with a focus on the KN powder source used in ink preparation.

4.4.1 KN particle crystallinity

Initial proof of concept experiments with KN particle size reduction conducted in the previous chapter predominantly followed the grinding procedure described by Birol and discussed in 4.1.1.2. It was later proposed that the grinding process can negatively impact the crystallinity of the powder particulate due to the mechanical nature of the ball milling method. As piezoelectric performance is linked to material crystallinity and interactions as grain interfaces, it was hypothesized that annealing the powder after grinding to improve crystallinity will correspondingly improve piezoresponse in the resultant printed devices.

To test this hypothesis, 10 g of 99.999% purity AA KNbO₃ powder were ground using SS media for 24 hours at 100 rpm. Following the separation and drying process, half of the ground powder was annealed in a Thermo Fischer Thermolyne F6020-33-80 Tabletop muffle furnace at 625 °C for 4.5 hours, followed by a passive cooling step of approximately 16 hours. A small sample of the two ground powder sets (both unannealed and annealed) were utilized for XRD evaluation, with the remainder mixed into inks from which devices were fabricated via stencil printing onto silicon substrates.

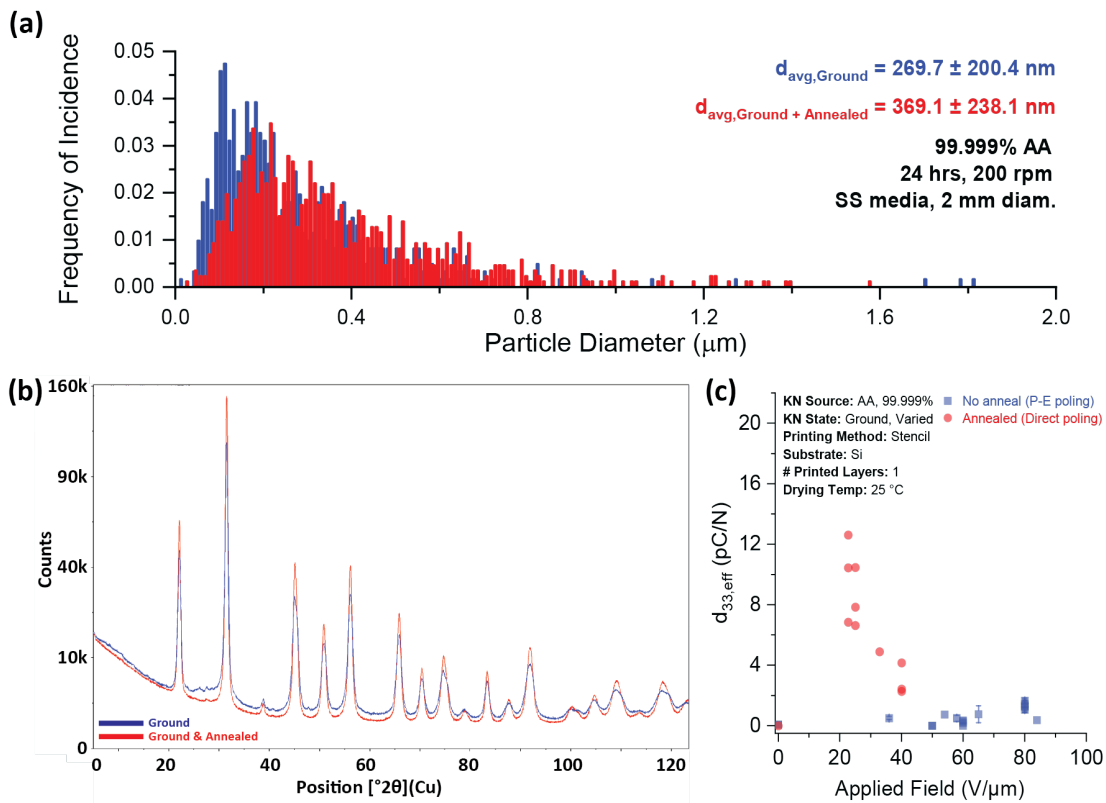


Figure 4.11 Influence of KN powder annealing on device characteristics including (a) Particle size distribution of both the unannealed and annealed KN powder post-grinding, (b) XRD spectra of two ground KN powders, with the annealed powder showing improved crystallinity compared to the not annealed powder, and (c) piezoelectric response of devices made with the annealed and not annealed KN powders, showing improved $d_{33,eff}$ in the sample with annealed powder used in the ink.

Particle size distribution analysis (Figure 4.11(a)) of both powders indicated a slight increase in average particle size in the annealed powder, from $270 \pm 200 \text{ nm}$ in the unannealed powder to $370 \pm 240 \text{ nm}$, but further studies are required to verify this with high confidence. Following this, crystallinity studies were conducted on both the annealed and unannealed powders using powder diffraction. The resulting spectra indicate that the two samples are in the same crystalline phase (Amm2), with the annealed powder exhibiting a higher degree of crystallinity than the unannealed powder, as inferred from the sharper peaks in the spectra depicted in Figure 4.11(b). This sufficiently confirms the hypothesis that annealing the powder post-grinding improves the crystallinity of the material, and does not exhibit any detrimental effects on crystalline structure when processed in this manner.

In a final experiment of this study, the samples fabricated with the annealed powder were poled using the direct poling technique (detailed in 4.1.3 and visualized in Figure 4.3) and evaluated for their piezoelectric response via Berlincourt method. These samples were fabricated in a method comparable to those characterized in the initial process validation

(Figure 4.4(e)), with the exception of poling method, as the direct poling system was unavailable during the initial validation experiment. Regardless, Figure 4.11(c) shows the piezoelectric response as a function of poling field for these two sample sets (For the annealed KN samples: $t_{\text{pol}} = 10$ min, $E_{\text{pol}} = 0\text{--}40$ V/ μm), showing a significant increase in $d_{33,\text{eff}}$, with the annealed powder, reaching a piezoelectric coefficient as high as 12.6 pC/N as compared to the 2.0 pC/N reported in the initial validation.

It was concluded that post-grinding annealing improves powder crystallinity, and devices fabricated from this annealed powder can exhibit improved piezoelectric performance. Thus, this annealing step was integrated into all further investigations in which particle size reduction via grinding was required.

4.4.2 KN source powder and material purity

In the realm of perovskite ferroelectrics, the introduction of impurities into the perovskite matrix has been well established to affect the ferroelectric performance of the material, with both benefits and detriments depending on the constituent materials.²⁷⁶ As material development is out of the scope of this body of work, the effect of impurities could not be studied in a well-controlled manner. In lieu of this, we elected to vary the source KN material, as it was assumed that different suppliers will have slightly different dopant concentrations in their material. By utilizing exclusively high purity source powders ($\geq 99.9\%$), we constrain the potential factors associated with these impurities and can get a sense for the magnitude of this influence before determining the necessity of more extensive studies.

We begin this study by developing printable inks from the three source powders discussed previously (Section 4.1.1.1), all with the same composition so as to exclusively vary the KN material used. This includes four inks: one made from the 99.9% pure SRM powder as supplied without any additional processing (the smaller initial particle size made grinding not critical for a printable ink with this powder), and three inks made from ground and annealed powders (99.9% pure SRM, 99.999% pure SRM, and 99.999% pure AA). The four powders were inspected by scanning electron microscopy for particle size analysis, as depicted in Figure 4.12(a). All samples were imaged under constant conditions using a JEOL JSM-7500TFE scanning electron microscope in secondary electron detection mode (magnification = 10,000x, accelerating voltage = 15.0 kV, WD = 8.6 mm). The particle size distribution is inconsistent, as expected, and must be individually determined for each powder and processing method. Developing methods to modify these materials to make such distributions more equivalent is a great challenge, and not part of the focus of this body of work. As such, the performance of devices will be evaluated with the powders as they are depicted herein, with an open door to future development in this area of investigation.

With the inks prepared using the standard recipe, devices were simultaneously fabricated with all four inks via screen printing onto silicon substrates, with two printed layers of KN ink per device. Device characterization in the form of impedance analysis (conducted at 45%RH, 23.3 °C) showed that the 99.999% pure AA powder exhibited the least amount of electrical leakage (Figure 4.12(b)). Piezoelectric characterization after poling was conducted using the Berlincourt method and is plotted in Figure 4.12(c). The 99.999% purity Alfa Aesar powder also resulted in devices with the highest piezoelectric response, with an average $d_{33,\text{eff}}$ of 7.9 ± 1.9 pC/N for samples poled at fields between 10 and 35 V/ μm , poling duration of 10 min, and a maximum measured value of 12.4 pC/N under these conditions. The key characteristics of the printed devices are summarized in Table 4.1.

Table 4.1 Comparison of device parameters based on KN source material.

Property	Variable	Units	99.9% SRM, Unground	99.9% SRM, Ground & Annealed	99.999% SRM, Ground & Annealed	99.999% AA, Ground & Annealed
Film thickness	h_{KN}	μm	14.9 ± 1.0	10.6 ± 0.8	10.9 ± 1.0	13.0 ± 1.3
Relative permittivity	ϵ_r	–	38 ± 2	42 ± 5	55 ± 4	43 ± 5
Dielectric Loss (at 100 kHz)	$\tan(\delta)$	–	0.24	0.18	0.32	0.11
Avg. Piezoelectric coeff.	$d_{33,\text{eff,avg}}$	pC/N	4.5 ± 1.4	5.4 ± 1.2	6.7 ± 2.4	7.9 ± 2
Max. Piezoelectric coeff.	$d_{33,\text{eff,max}}$	pC/N	7.3	7.0	9.9	12.4

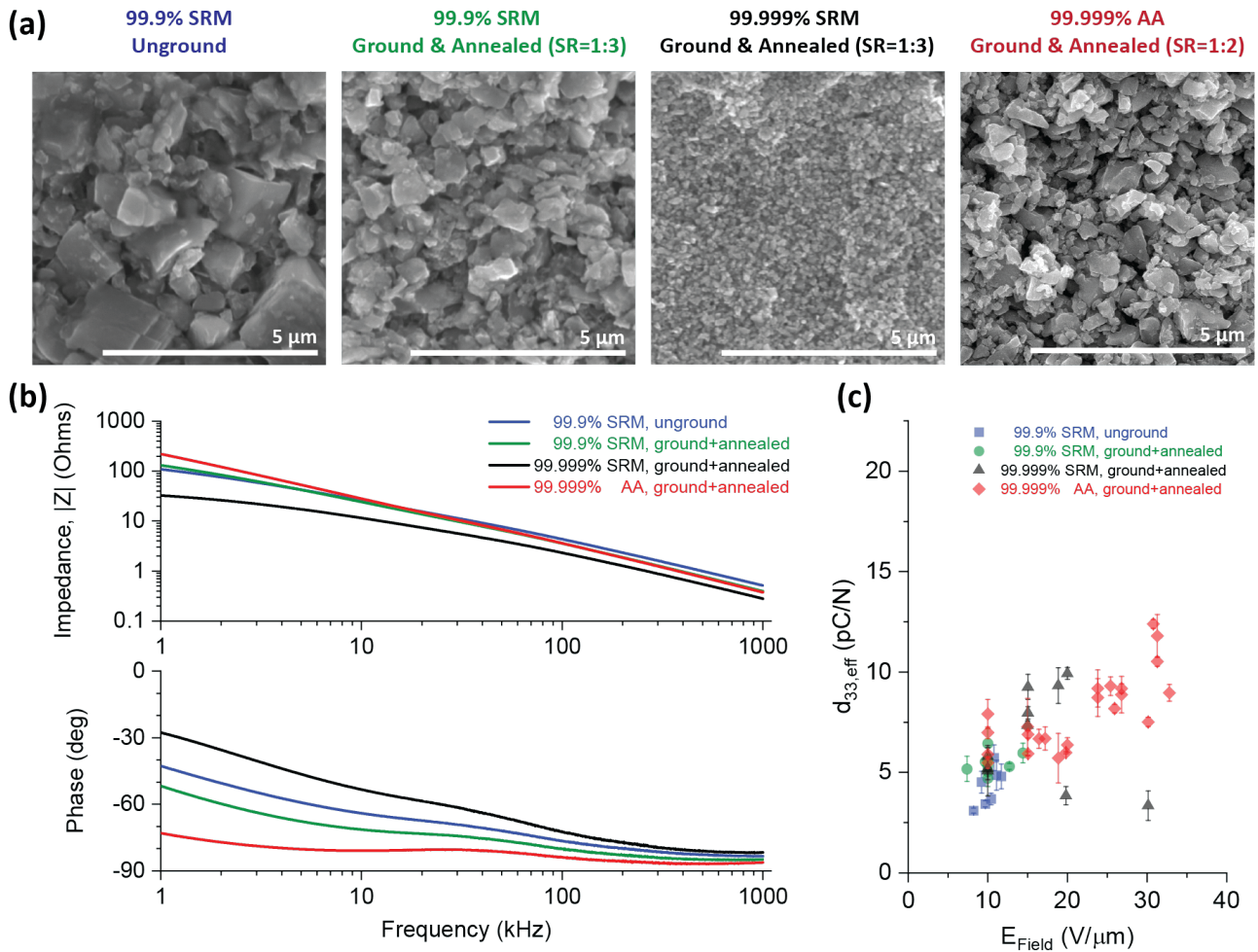


Figure 4.12 Study of device performance based on KN source material including (a) SEM images of the four source materials characterized in this investigation, showing the variance in particle size across materials. (b) impedance and phase spectra for devices fabricated from all four test powders, and (c) piezoelectric response as a function of applied poling field for each device type.

From this study, it was concluded that KN material source does indeed have an influence on printed device performance. The varied particle size distributions observed in the prepared KN powders generally corresponds to layer thickness in printed films, with larger particulate resulting in thicker films for inks of the same composition by mass ratio. Dielectric behavior is also influenced by source material, with the powders supplied by Stanford Materials exhibiting higher dielectric losses as compared to the Alfa Aesar sourced powder and as compared to each other. Finally, the piezoelectric performance of the devices is influenced by the source material, with the higher purity materials from both suppliers generally having a larger piezoelectric coefficient than the lower purity material.

We conclude this study with the observation that, for the purposes of this body of work, the 99.999% pure powder supplied by Alfa Aesar (after in-house particle size reduction) exhibited the best performance out of the four source materials studied. Thus, this material was selected as the source material for future studies.

4.4.3 Grinding media

Initial work on particle size reduction of KN particulate was identified to have a potential source of error related to the processing step: the material used as grinding media. In this initial work, the particle grinding was conducted using stainless steel grinding media in a stainless-steel grinding vessel which, having a lower hardness rating than the ceramic KN, was itself potentially ground and introduced into the KN powder used in ink preparation.

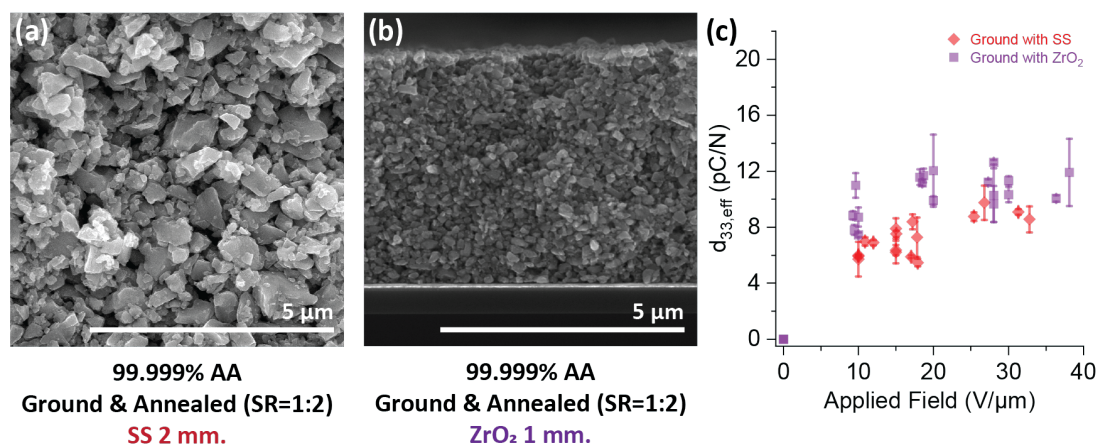


Figure 4.13 Influence of grinding media on particle size and piezoelectric response showing the resultant powder from grinding with (a) 2 mm \emptyset SS milling media or (b) 1 mm \emptyset ZrO₂ media, as well as (c) piezoelectric response as a function of poling field for devices made with the two resulting powders.

A study was thus conducted to evaluate the significance of grinding material on device performance. In this study, the grinding process was repeated with a fresh quantity of KN source material (99.999% purity, AA), but with ZrO₂ grinding media (1 mm \emptyset) in a Teflon milling vessel in place of the SS media (2 mm \emptyset) and vessel used initially, as these materials were not expected to negatively influence the KN powder. Capacitor devices were then fabricated from the resulting ink with the standard screen-printing fabrication process on silicon substrates. The piezoelectric coefficient, $d_{33,eff}$, was then measured via the Berlincourt method to compare device performance ($t_{pol} = 10$ min, $E_{pol} = 0-40$ V/ μ m). The results of this study are found in Figure 4.13 above. The average particle size of the powder ground with ZrO₂ media was reduced in comparison to that ground using SS media, 160 ± 80 nm as compared to 370 ± 240 nm. Additionally, the piezoelectric response was higher for material milled with ZrO₂ media, with an average $d_{33,eff}$ of 10.3 ± 2.0 pC/N as compared to 7.9 ± 1.9 pC/N for the SS milled powder. As a result, ZrO₂ media was used for all further investigations.

4.4.4 KN particle size and grinding process variance

In Section 4.2.1, we discussed the influence the solvent to KN ratio was for effective and homogeneous grinding and thus producing high quality, low roughness layers. It was determined that 2 mL(IPA) per gram of KN powder was preferable as compared to 3 mL(IPA) in this regard. However, further studies were conducted to assess if this change in particle size distribution showed a significant influence on piezoelectric response in printed devices. To this end, devices were fabricated using each type of powder, and poled using the direct poling method established previously ($t_{pol} = 10$ min, $E_{pol} = 0-70$ V/ μ m).

As shown in Figure 4.14, the samples manufactured with the standard 1:2 grinding ratio exhibited higher effective piezoelectric response as compared to samples manufactured using the 1:3 ratio. The highest measured $d_{33,eff}$ value for the 1:2 ratio samples was 13.3 ± 1.1 pC/N, while that for the 1:3 ratio samples was 7.6 ± 0.4 pC/N. Even so, the median value for the 1:3 sample set was 2.9 pC/N as compared to 10.0 pC/N for the 1:2 samples. It was further observed that, in general, the breakdown field of the samples with the higher grinding ratio was significantly reduced compared to the reference samples. The inhomogeneous nature of the ground particles resulted in films of high surface roughness (> 9 μ m) in films 25–30 μ m thick. It was hypothesized that breakdown was occurring in the thinner regions of this film, where the electric field was larger than was estimated based on average film thickness.

This study confirms that the more homogeneous ink resulting from the lower 1 gKN:2 mL(IPA) grinding ratio is preferable to that made using a higher solvent content during grinding. This is true both in terms of layer quality (homogeneous particulate, lowered surface roughness) as well as piezoelectric performance. As a result, the 1:3 ratio ink was discarded from further study in lieu of the 1:2 ratio ink. Further work is certainly required to further optimize particle size as a function of the grinding parameters, with the aim to achieve a highly homogeneous particle size distribution while maximizing piezoelectric response. Such work could assess grinding time, speed, and solvent ratio as well as factors not discussed herein such as milling media size and loading but would likely require specialized optimization for each source powder.

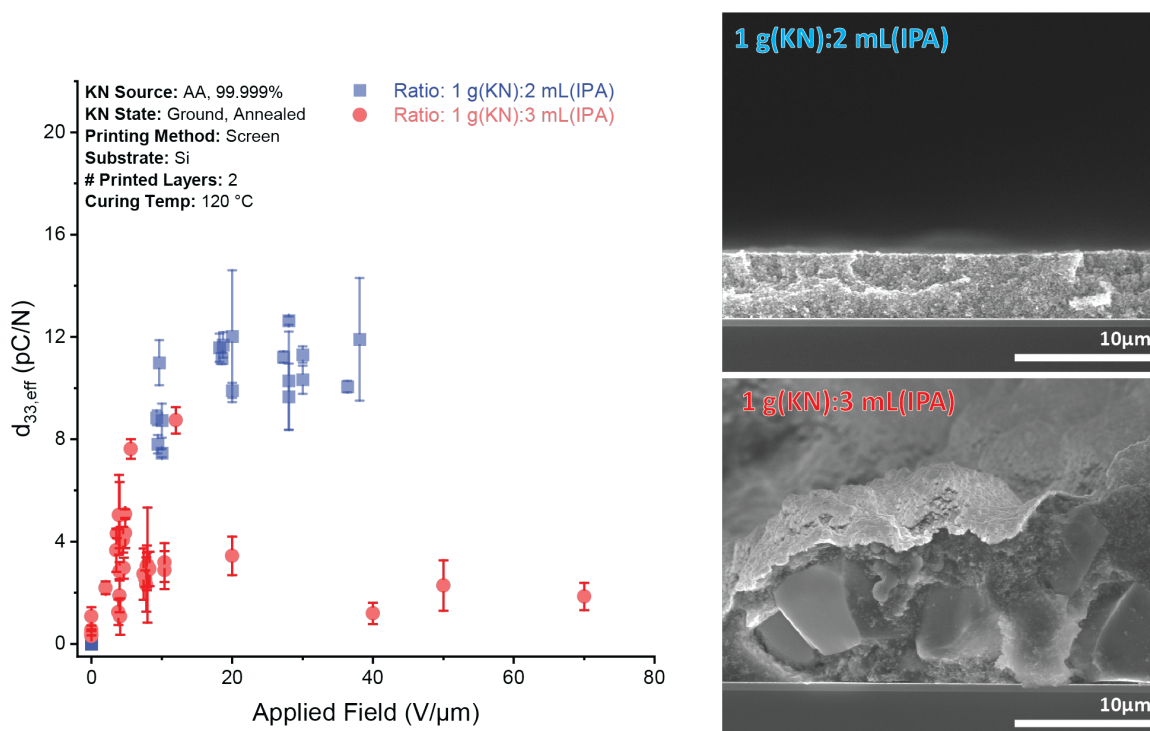


Figure 4.14 Piezoelectric response variance resulting from changes in grinding conditions.

4.5 Summary and conclusions

In this chapter, we made significant inroads into the development of a low-temperature printing process for KNbO₃ piezoelectrics. We first gave an overview of the primary fabrication steps (KN powder preparation, ink mixing, and device fabrication) as well as establishing a benchmark for printing quality and device performance.

We followed with a series of process development studies focusing on improving the physical properties of the printed layer, with significant improvements stemming from KN particle size reduction and a transition from stencil to screen printing techniques. As a result, the printed layer thickness was reduced to just 6 μ m and viable device yield was increased from <15% to consistently >90%, sufficient for progression onto device performance improvement studies.

Next, we studied the influence of several processing factors on the dielectric behavior of printed devices, using the process improvements implemented in the previous section. It was found that drying the screen-printed layers at higher temperatures slightly improves dielectric performance while dramatically reducing fabrication time (from 12 hours per layer to just 30 min). Studies of the influence of electrode material and thickness found that there was no significant performance difference with platinum as compared to gold electrodes, or with electrode thicknesses of 100 nm as compared to 300 nm. It was determined that the surface pre-treatment step prior to top electrode deposition was unnecessary and negatively impacted device performance, and thus was removed from the manufacturing procedure.

In the final section of this chapter, the focus changes to factors influencing piezoelectric response of printed devices. It was found that annealing the source powder post-grinding improved material crystallinity and piezoelectric response significantly. Following this was a study of how source material influences piezoelectric device performance, with observed variance depending on the material supplier and processing conditions. We down-select from the available material sources for 99.999% purity powder supplied by Alfa Aesar, which exhibited both the best dielectric characteristics as well as the higher piezoelectric response of the tested samples. Finally, we study the influence of grinding media and grind solvent-to-KN ratio on piezoelectric response, finding improvements with the transition from SS to ZrO₂ milling media and with a grinding ratio of 2 mL(IPA) per 1 gKN.

The final process results in highly reproducible devices printed on silicon substrates with a yield of >95%. Device thickness is tunable, as multiple layers of KN can be stacked on top of each other in 6 μm increments. Devices have demonstrated piezoelectric response ($d_{33,eff}$) as high as 13.3 pC/N, a major improvement when compared to the initial devices where the highest measured piezoelectric response was 2.0 pC/N.

With all of this, there is still significant room for potential improvement to both the fabrication methodology as well as the materials used to permit higher performance devices than those reported thus far. One potential area of future study is ink composition optimization, assessing the influence of binding agent and its properties on layer integrity and piezoelectric response. This could further assess the transition to alternative degradable binding agents or solvents. In another direction would be a focus on the KN source material, working to adjust particle size for the highest possible piezoelectric response, or evaluating the influence of material impurities and dopants on device performance. A third course of study would be to develop alternative methods of improving the structural integrity of the printed layer, through a novel low temperature sintering process or a more complex binding mechanism. Incorporating these advancements and addressing the aforementioned areas of study would further the development of eco-friendly printed piezoelectric devices, opening up exciting possibilities for a wide range of applications in the future.

At this point, however, it was determined that the printing process was sufficiently developed and the piezoelectric response of fabricated devices sufficiently large so as to permit transition onto degradable paper substrates. This will be the focus of the following chapter, as we work progressively on the development of fully printed degradable piezoelectric devices.

Chapter 5 Low-temperature processing of screen-printed piezoelectric KNbO_3 with integration onto biodegradable paper substrates

This chapter describes the process development taken for the fabrication of a low-temperature processable, screen-printable KNbO_3 ink, as well as the parameters evaluated for best performance. The content of this chapter is based off of a research article published in *Microsystems & Nanoengineering* in February 2023.²⁶⁷

The development of fully solution-processed, eco-friendly piezoelectrics is a critical step in the development of green electronics towards the worldwide reduction of harmful electronic waste. However, recent printing processes for piezoelectrics are hindered by the high sintering temperatures required for conventional perovskite fabrication techniques (discussed previously in Table 2.4 and expanded upon in Table 8.5 of the Appendix), which are unsuitable for use with degradable substrates. Thus, a process was developed to manufacture lead-free printed piezoelectric devices at low temperatures to enable integration with eco-friendly substrates and electrodes (Chapter 4). A printable ink was developed for screen printing potassium niobate (KNbO_3) piezoelectric layers in microns of thickness at a maximum processing temperature of 120 °C with high reproducibility.

This work shows the first successful fabrication of fully eco-friendly KNbO_3 -based printed piezoelectric devices on green substrates.^{55,59} Through careful material selection and the utilization of printing technologies, the core challenges associated with conventional high-temperature processed Pb-based piezoelectrics are overcome. Key challenges of ink development are addressed through the adjustment of particle size and ink component compositions to develop a high-quality screen-printable ink. This study comprises the novel development of a printable KNbO_3 ink along with the first instance of entirely low-temperature printed perovskite materials for piezoelectric applications. With a maximum processing temperature of 120 °C, this process permits the development of printed piezoelectric devices on biodegradable substrates, such as paper, for the first time. We demonstrate the versatility of this technology through the fabrication and characterization of transducer disks and resonating structures on both silicon and paper substrates. The printed layers were 10.7–11.2 μm thick, with acceptable surface roughness values in the range of 0.4–1.1 μm . The relative permittivity of the piezoelectric layer was 29.3. Through poling optimization, we attain an average piezoelectric response ($d_{33,eff}$) on paper substrates of 13.6 ± 2.8 pC/N, with maximum values reaching 18.4 pC/N. This work allows for the further development of printed green piezoelectric devices integrated with other biodegradable components.

5.1 Methods

The development of a facile, robust process for the low-temperature printing of sustainable KN inks consisted of three primary phases: powder processing and ink development, device design and fabrication, and characterization. We then look to evaluate the limits of printability, the dielectric behaviour, and most critically, the piezoelectric characteristics of the KN layer as implemented in different device structures with a focus on poling optimization. Additionally, we focus on the performance of this layer when printed on a biodegradable substrate (paper) relative to the

measured performance from same process on a more conventional substrate (silicon) and the theoretical values from bulk KN properties.

Two primary device architectures were fabricated, parallel plate capacitors and resonant cantilevers, each produced on both silicon and paper substrates. This combination facilitates a comparison of device behaviour on different substrates, a proof of concept for versatile printing capabilities, and a characterization of piezoelectric behaviour in both longitudinal and transverse modes. Figure 5.1 shows a summary of the device architectures, fabrication, scalability, and key piezoelectric response of the as-fabricated devices, all of which are discussed in further detail. Figure 5.1(a) shows a simplified fabrication process for these devices, with a cross-section of the finished device stack shown in Figure 5.1(b), including approximate layer dimensions. The finalized printed devices for both the parallel plate capacitor and cantilever structures are imaged in Figure 5.1(c).

Crucial to this process, all component materials selected for these devices are non-toxic: the ink (composed of KN particles, ethyl cellulose, and pentanol), the electrodes (composed predominantly of gold, which is an inert noble metal), and the paper substrate (primarily composed of cellulose).

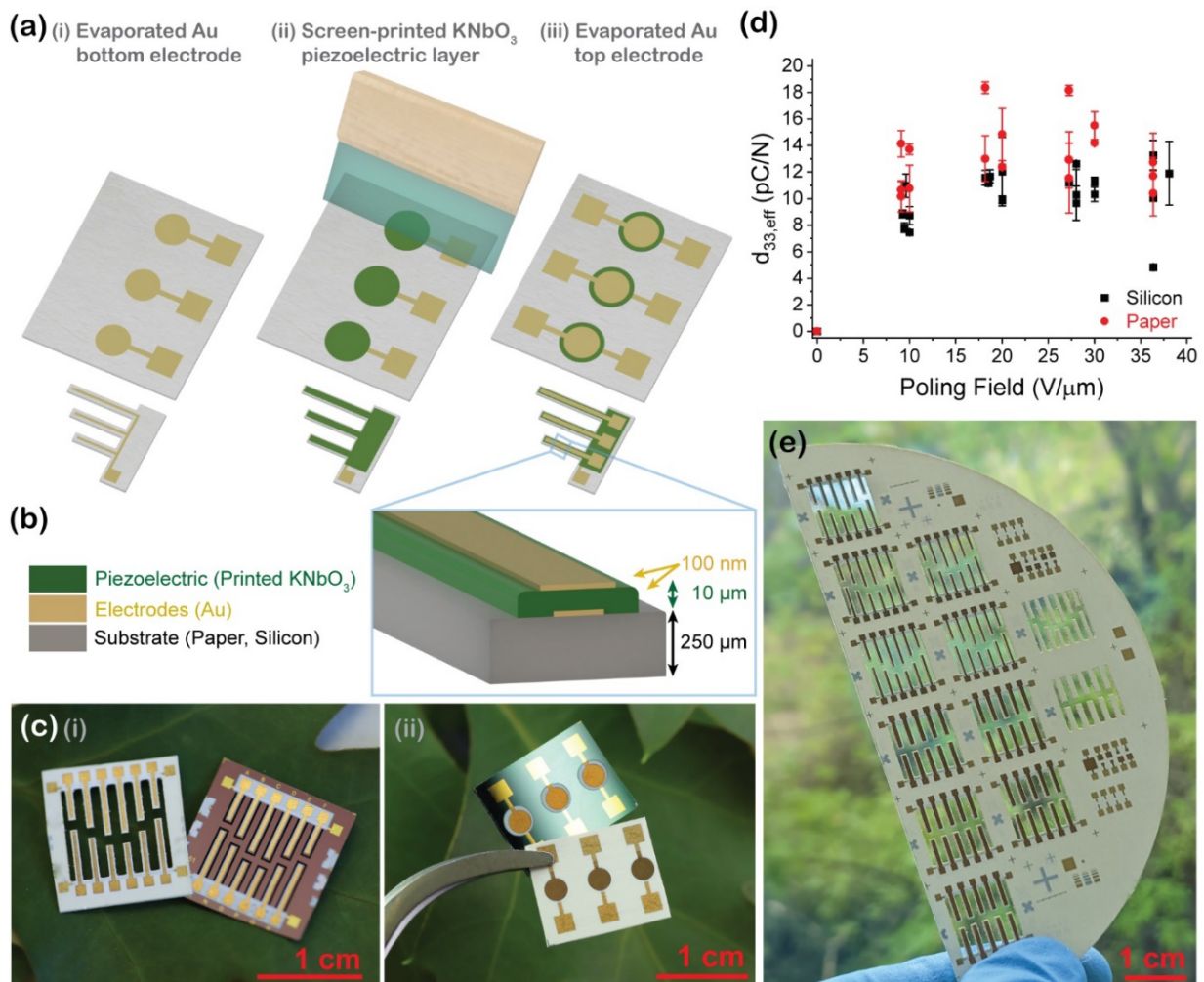


Figure 5.1 Overview of progress for printed KN on paper substrates including (a) simplified process flow for the fabrication of printed piezoelectric devices including (i) bottom electrode deposition via thermal evaporation, (ii) screen printing of the KNbO₃ piezoelectric layer, and (iii) top electrode deposition via thermal evaporation. (b) Cross-section of the printed device layers indicating layer thicknesses. (c) Images of the as-fabricated (i) cantilever and (ii) capacitor structures printed on both paper and silicon substrates. (d) Effective d_{33} response achieved as a function of the poling field for capacitor structures, measured via the Berlincourt method. (e) Cantilever devices printed at the wafer scale on paper substrates.

5.1.1 Powder processing and ink preparation

Ink preparation followed with the process refined in the previous chapter (Chapter 4). Schematics of the specific parameters used in powder milling and ink preparation are detailed in Figure 5.2(a), including steps of (i) grinding the KN particles in a planetary ball mill, (ii) separating the ground particles from the milling media and solvent, (iii) reannealing the particles to improve crystallinity, and (iv) mixing the ink.

To achieve a homogeneous distribution of particulate, 5 g of KNbO₃ powder (99.999% purity, Alfa Aesar) was mixed with 10 mL of isopropanol and 125 g of ZrO₂ grinding media (2 mm Ø, Retsch Product # 05.368.0089); the system was placed in a planetary ball mill (QM-3SP2) for 24 hours, with a directional switching period of 0.3 hours and a jar rotational speed of 200 rpm (Figure 5.2(a)i). Next, the powder-solvent slurry was separated from the grinding media and placed on a hotplate at 120 °C for 12 hours to evaporate the solvent, resulting in a dry, ground powder (Figure 5.2(a)ii). Finally, the resulting powder was annealed to improve particle crystallinity. Annealing was conducted in a Thermo Fischer Thermolyne F6020-33-80 Tabletop muffle furnace at 625 °C for 4.5 hours, and was followed by a passive cooling step of approximately 16 hours (Figure 5.2(a)iii).

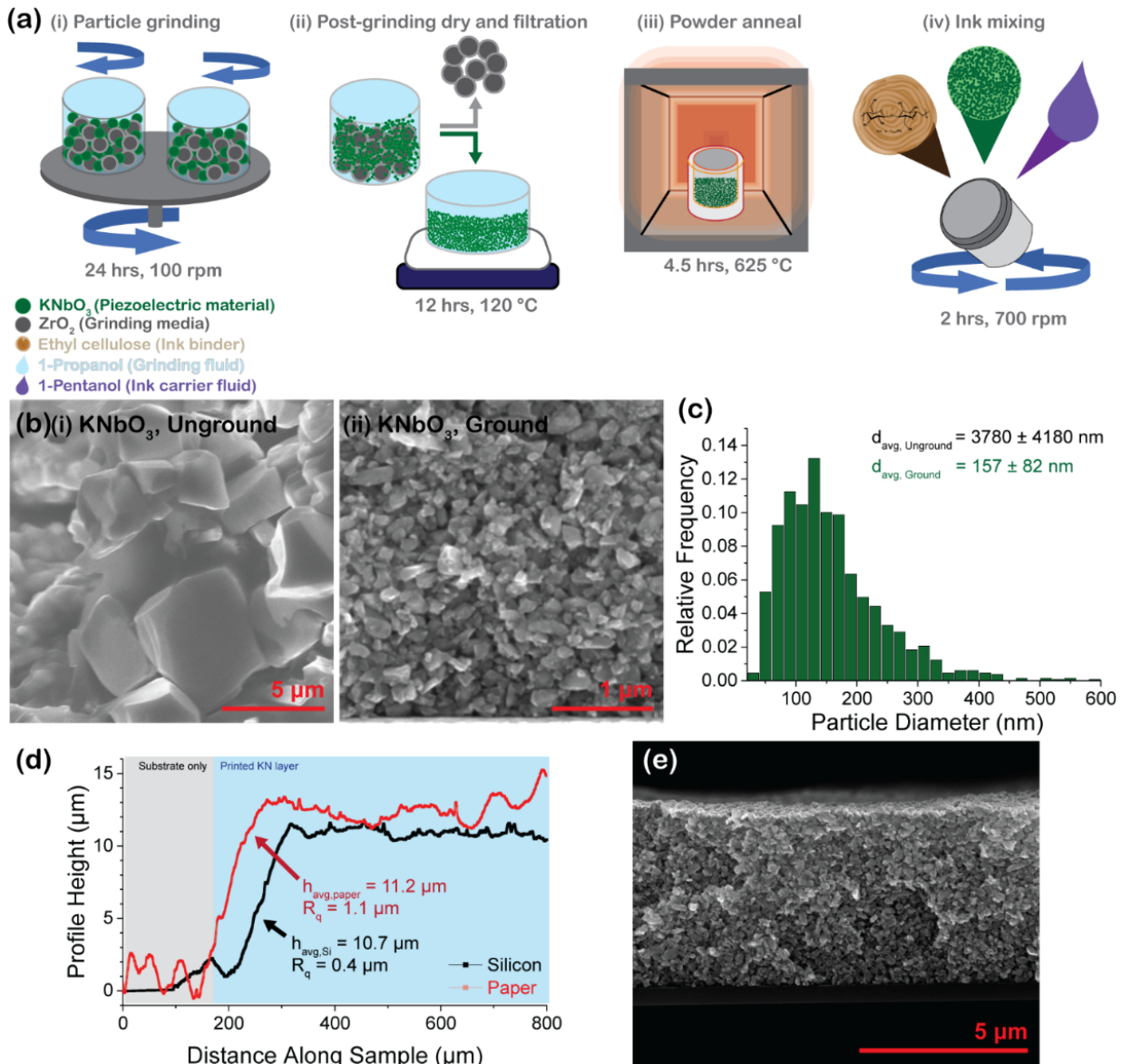


Figure 5.2 Ink and film characteristics including. (a) Powder process diagram including (i) grinding of KN particles, (ii) separation of ground particles from grinding media and drying off of isopropanol grinding aid, (iii) annealing of powder to improve particle crystallinity, and (iv) mixing of screen-printable KN ink. (b) SEM images of (i) unground and (ii) ground KN particles. (c) Particle size distribution of ground KN material, and (d) Edge surface profile of KN ink as-printed on paper and silicon substrates noting layer thickness and surface roughness. (e) SEM cross-sectional image of KN ink printed on silicon substrate.

The particle size distribution for ground KNbO₃ particles was determined via image analysis using scanning electron microscopy (JEOL JSM-7500TFE) and ImageJ image processing software. Image analysis showed a significant reduction in size from the initial, unground KN powder (Figure 5.2(b)i) to the finalized, ground KN powder (Figure 5.2(b)ii). The postgrinding particle size distribution is shown in Figure 5.2(c), showing a reduction in the average particle diameter of the KN particles from $3.78 \pm 4.18 \mu\text{m}$ in the unground powder to $160 \pm 80 \text{ nm}$ in the ground powder. Details of the particle size distribution analysis could be found in Section 8.2.3 of the Appendix.

The finalized ink was achieved by mixing the three components in a proportional ratio of 58:7.5:35 wt% KN:EC:pentanol (Figure 5.2(a)iv). The mixture was mixed in a planetary mixer (Thinky ARE-250) with 5 g of Al₂O₃ milling media (5 mmØ, Retsch Product # 05.368.0019) at 700 rpm for a total of 2 hours in 30 min intervals to reduce solvent evaporation due to system heating. Slight additions of pentanol were required to adjust for the mass lost to evaporation as needed to attain the targeted ink viscosity. Once mixed, ink was stored at 5 °C in a well-sealed container. This ink was highly stable and viable for printing after more than 6 months under these storage conditions.

Upon printing, the surface profilometry of the KN layers (Figure 5.2(d)) showed average thicknesses of 10.7 μm on silicon and 11.2 μm on paper. The surface roughness of the printed KN layers was greater when printed on paper relative to when printed on silicon; attributed to the initial roughness of the paper itself, with an RMS layer roughness of 0.4 μm on silicon substrates and 1.1 μm on paper substrates. However, this surface roughness was determined to be acceptable for device fabrication, confirmed by SEM imaging (Figure 5.2(e)).

5.1.2 Device design

Two architectures were selected to evaluate the printed KN material and demonstrate its applicability in piezoelectric devices. Both designs are based on a standard parallel plate capacitor construction, with a planar piezoelectric layer between the top and bottom electrodes.

5.1.2.1 Circular capacitor device design

The first design involves parallel plate capacitors with circular footprints of varied surface areas $A = 1, 5, 10, \text{ and } 20 \text{ mm}^2$. The direct piezoelectric effect could then be utilized to determine the effective longitudinal piezoelectric coefficient, $d_{33,eff}$, from these devices via the Berlincourt method. Additionally, this design permitted the determination of the printed piezoelectric layer relative permittivity on each substrate according to a parallel plate capacitor assumption as follows Equation (2.3).

5.1.2.2 Cantilever device design

To accompany the circular capacitor structures, a second design was proposed for the fabrication of piezoelectric cantilevers. By taking advantage of the indirect piezoelectric effect and analysing the characteristics of the piezoelectric cantilevers at resonance, the effective transverse piezoelectric coefficient, $d_{31,eff}$, could be determined. However, to enable direct comparison of samples on paper and silicon substrates, device geometries must be determined that (a) can be achieved on both substrate materials with different fabrication processes, (b) maintain the necessary assumptions for the approximations used in determining cantilever resonance, and (c) result in device resonance in the measurable range of available analysis instrumentation.

5.1.2.2.1 Bimorph cantilever resonance frequency model

With the assumption that the thermally evaporated metallic electrodes do not contribute significantly to the system, the cantilever could be approximated as a bimorph composed of a substrate and a piezoelectric layer such that the resonant frequency is predicted as follows Equations (5.1) and (5.2):

$$f_r = \frac{1.875^2}{2\pi L^2} \sqrt{\frac{\langle EI \rangle_{eq}}{\langle \rho A \rangle}} = \frac{1.875^2}{2\pi L^2} \sqrt{\frac{\langle EI \rangle_{eq}}{w_c(\rho_{sub}h_{sub} + \rho_{piezo}h_{piezo})}} \quad (5.1)$$

$$\langle EI \rangle_{eq} = \frac{w_c [E_{sub}^2 h_{sub}^4 + E_{piezo}^2 h_{piezo}^4 + E_{sub} E_{piezo} h_{sub} h_{piezo} (4h_{sub}^2 + 6h_{sub} h_{piezo} + 4h_{sub}^2)]}{12(E_{sub} h_{sub} + E_{piezo} h_{piezo})} \quad (5.2)$$

where f_r is the first resonance frequency of the cantilever, $\langle EI \rangle_{eq}$ is the flexural rigidity of the beam, and $\langle \rho A \rangle$ is the mass per unit length of the beam. A full list of variables is provided in Table 5.1 and Table 5.2.

This predictive model was used with known fabrication limitations and design constraints to identify physical device parameters that enable both reproducible fabrication and quality characterization of the resulting cantilevers. For the purposes of this design process, certain assumptions and constraints were enacted. The thickness of the thermally evaporated electrodes was assumed to be negligible compared to the thickness of the piezoelectric layer and substrate, permitting the assumption of a bimorph cantilever. The possible range of resonance frequencies was limited by the frequency range easily detectable by available equipment, and thus was constrained to the range of 1–20 kHz. The width of the piezoelectric film was limited by screen printing resolution, empirically determined to be approximately 100 μm .

Table 5.1 Material properties associated with resonance frequency model Equations (5.1) and (5.2).

Property	Variable	Units	Active layer* (Printed KNbO ₃)	Substrate (Silicon)	Substrate* (Paper)
Layer thickness	h_i	μm	10	247	200
Young's modulus	E_i	Pa	73*	150	1.9*
Density	$\rho_{\text{piezo,KN}}$	kg/m^3	2500*	2330	1025*

Several material properties for KN and paper were estimated for this model, due to their novelty for use in this application. In particular, the densities and Young's moduli of the paper substrate and KN printed layers were initially estimated. These values were updated accordingly as new information was gained empirically through successive development iterations. A comparison of this model to the built devices is discussed later (Figure 5.9), and the specific model parameters for this system are listed in Table 5.1 and Table 5.2.

Table 5.2 Cantilever properties associated with resonance frequency model Equations (5.1) and (5.2).

Property	Variable	Units	Values*
Resonance frequency (n=1)	f_r	kHz	1 – 20
Cantilever length	L	mm	$> 5 * w_c$
Cantilever width	w_c	mm	> 0.8
Cantilever thickness	h_{total}	μm	$h_{\text{piezo}} + h_{\text{sub}}$

Initial development cycles were conducted prior to the empirical evaluation of several material properties in this model that would provide concrete values for such parameters. Yet for first tests, these values had to be approximated. For the paper substrate, literature predictions were used at first to establish a range for density and Young's modulus values, which later were refined using FEM simulations. For the piezoelectric layer, a simplified composite approximation was used initially, with literature predictions to determine a numerical range for these values. This assumes that the final ink layer will contain all components of the ink recipe except the solvent, which is evaporated upon drying of the ink. This includes the KN powder and the ethyl cellulose binder. Equations (5.3)–(5.7) detail the approximations made, while Table 5.3 details the specific variables and values used in this approximation of ink properties.

$$f = \frac{V_{\text{binder}}}{V_{\text{binder}} + V_{\text{active}}} = \frac{\left(\frac{m_{\text{binder}}}{\rho_{\text{binder}}}\right)}{\left(\frac{m_{\text{binder}}}{\rho_{\text{binder}}} + \frac{m_{\text{active}}}{\rho_{\text{active}}}\right)} \quad (5.3)$$

$$E_{\text{ink,high}} = f * E_{\text{binder}} + (1 - f) * E_{\text{active}} \quad (5.4)$$

$$E_{\text{ink,low}} = \frac{1}{\left(\frac{f}{E_{\text{binder}}} + \frac{(1-f)}{E_{\text{active}}}\right)} \quad (5.5)$$

$$\rho_{\text{ink,high}} = f * \rho_{\text{binder}} + (1 - f) * \rho_{\text{active}} \quad (5.6)$$

* Value has been approximated.

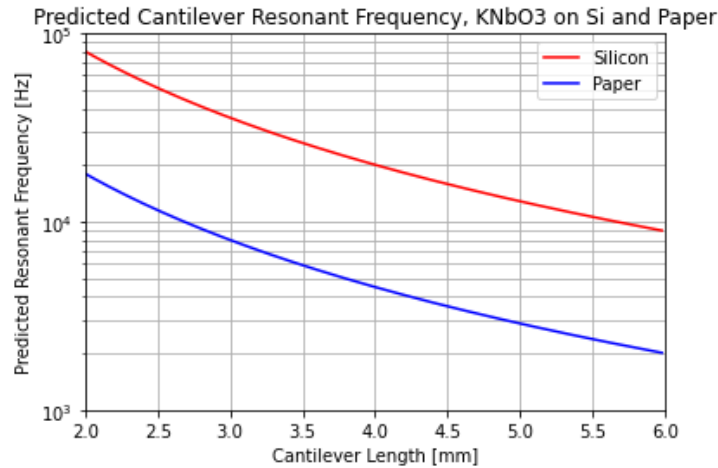
$$\rho_{ink,low} = \frac{1}{\left(\frac{f}{\rho_{binder}} + \frac{(1-f)}{\rho_{active}}\right)} \quad (5.7)$$

Table 5.3 Variables associated with the material property approximation model described in equations (5.3) through (5.7).

	Property	Variable	Units	Values
Binder (Ethyl cellulose)	Specific Mass	m_{binder}	g	11.5 [†]
	Density	ρ_{binder}	g/cm ³	1.05 [‡]
	Young's Modulus	E_{binder}	GPa	2 [‡]
	Specific Volume	V_{binder}	cm ³	10.97 [*]
Active material (KNbO ₃)	Specific Mass	m_{act}	g	88.5 [†]
	Density	ρ_{act}	g/cm ³	4.37 [‡]
	Young's Modulus	E_{act}	GPa	240 – 250 [‡]
	Specific Volume	V_{act}	cm ³	20.25 [*]
Ink, estimated	Filler Ratio	f	[-]	0.35 [*]
	Density	$\rho_{ink,range}$	g/cm ³	2.1 – 3.2 [*]
	Young's Modulus	$E_{ink,range}$	GPa	5.6 – 156.4 [*]

5.1.2.2.2 Finalized cantilever geometries

The finalized predictive model is represented in Figure 5.3 showing the correlation between cantilever length and expected resonance frequency for devices fabricated on both paper and silicon substrates. Based on this model, device dimensions were selected that would allow for the fabrication of cantilevers on both silicon and paper substrates of the same dimensions that resonate in the target range of 10⁴–10⁵ Hz (permitting high-quality characterization with available instrumentation). All designed cantilevers had a width of 700 μm, thickness of 200–250 μm, and lengths of 3.1, 4.1, or 5.1 mm (summarized in Table 5.4).

**Figure 5.3** Predicted resonance frequency of the cantilevers as a function of length for both substrate materials (Si and paper).**Table 5.4** Target dimension values for all components in the cantilever devices.

Property	Variable	Units	Substrate (Silicon)	Substrate (Paper)	Piezoelectric (KNbO ₃)	Electrodes (Gold)
Thickness	h_i	μm	247	200 – 230	8.4 – 11.2	0.11
Length	L_i	mm	3.1, 4.1, 5.1		3.0, 4.0, 5.0	2.9, 3.9, 4.9
Width	w_i	mm	0.7	0.7	0.5	0.3

†† Defined by Ink parameters.

‡ Value from literature.

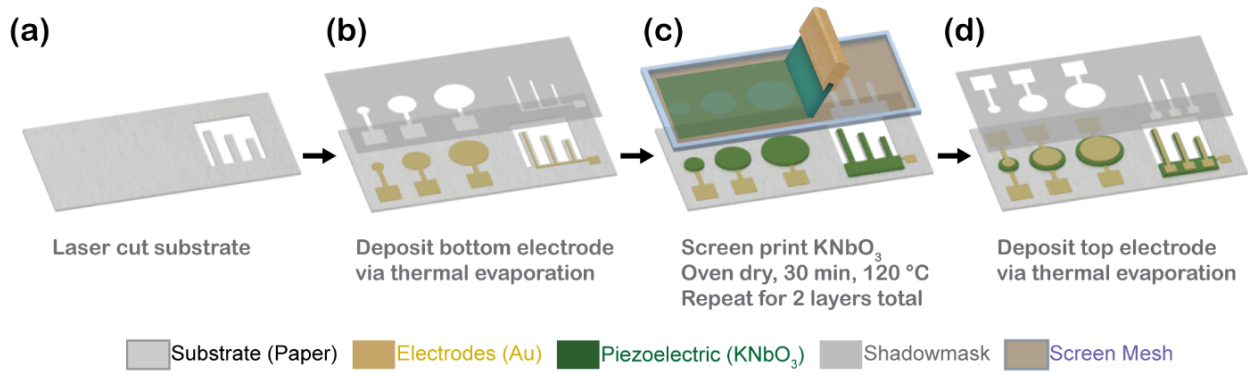


Figure 5.4 Full process flow diagram for piezoelectric device fabrication including (a) precutting the substrate for cantilever devices using laser cutting, (b) deposition of the Au bottom electrode via thermal evaporation, (c) screen printing of the KNbO₃ ink repeated once, with a 30 min oven drying step at 120 °C after each layer, and (d) deposition of the Au top electrode via thermal evaporation.

5.1.3 Fabrication

The full fabrication process for both circular capacitor and cantilever devices is depicted in Figure 5.4, for the structures made on paper substrates.

Specialty printing paper designed for use with printed electronics was utilized as a substrate due to its low surface roughness (empirically measured to be 3.2 μm) and robust thermal properties (stable up to 200 °C) relative to other biodegradable substrates (ArjoWiggins PowerCoat XD 200, approximately 200 μm thickness). The selected material additionally had no extra surface coatings, and thus exhibited consistent properties on both sides of the paper. The film density was empirically measured to be 1.027 g/cm³, matching well with the reported value of 1.02 g/cm³.

For the samples on paper, cantilever shapes were first laser cut directly from the substrate (Figure 5.4(a)) via laser cutting using a Trotec Speedy 300 laser cutter (60 W) to match the dimensions of a silicon substrate, enabling a consistent process across all samples. Next, Cr/Au bottom electrodes (10/100 nm thick) were deposited via thermal evaporation (Figure 5.4(b)) through a stainless steel shadowmask (125 μm thickness, Beta-Layout, GmbH). No pretreatments were required on paper substrates prior to electrode deposition. For all samples, both the bottom and top electrodes consisted of a 10 nm Cr adhesion layer followed consecutively by a 100 nm layer of Au.

For the silicon reference samples, standard microprocessing techniques were utilized instead. Substrates utilized were silicon wafers (100 mmØ, 525 μm thickness, p-type, resistivity 0.1–100 Ω/cm²) with a surface coating consisting of 500 nm wet thermal silicon oxide. Prior to electrode desposition, Silicon substrates were pretreated using an O₂ plasma cleaned (Diener ATTO, 100% Power, 10 min). Bottom electrodes were then deposited for circular capacitor structures using the same process as for the samples on paper substrates.

For exclusively the cantilever samples processed on silicon, the process for bottom electrode deposition and cantilever release deviated slightly. First, the bottom electrode was patterned in a cleanroom using a lift-off process to the same thickness as used for the paper substrate samples. Once complete, the cantilever structures were partially etched from the top using deep reactive ion etching (DRIE) and then released fully by mechanically thinning the wafer from the backside, reducing the thickness of the wafer from 525 to 247 μm in the process. Once the cantilevers were released and the gold bottom electrodes were deposited on both substrate materials, the process became the same as that for the other samples for the remaining fabrication steps.

Screen printing was next employed for deposition of the prepared KN ink. To this end, a manual screen printer was utilized, with a maintained substrate–mesh gap of 2 mm. Mesh fabrication was provided by Serilith AG using polymer mesh (PME 120-30Y) and steel mesh (SD 40/25) materials. The piezoelectric KNbO₃ ink was printed on all substrate and device iterations in 2 layers, with a 30 min drying step at 120 °C in an oven after printing each layer (Figure 5.4(c)). Printing two layers of piezoelectric significantly improved the device yield because the increased layer thickness compensated for the initial surface roughness of the paper substrate, thereby reducing spurious shorting across electrodes. Once the printing of the piezoelectric layer was complete, top gold electrodes were deposited on all samples via thermal evaporation using the same process as for the bottom electrodes (Figure 5.4(d)).

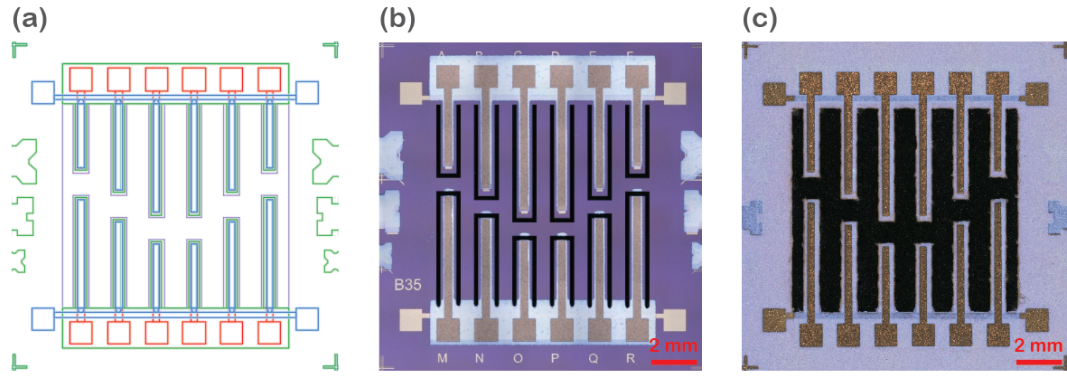


Figure 5.5 Top-down view of cantilever device designs showing (a) CAD design, compared to fully fabricated devices on (b) silicon and (c) paper.

Figure 5.5 shows a comparison of the initially designed cantilever samples in top-down view (a), as compared to the fully fabricated devices on (b) silicon and (c) paper substrates, showing consistent cantilever dimensions despite the minor differences in device design required by the different manufacturing methods.

5.2 Results and Discussion

5.2.1 Ink and printed layer properties

Prior to electrical characterization, the physical properties of the ink and printed layer were next evaluated. A summary of the ink and device parameters is shown in Table 5.5. The average KNbO₃ particle diameter after grinding was 160 ± 80 nm (Figure 5.2(c)). The KN printed layer density was empirically determined to be 3.2 ± 0.1 g/cm³, closely matching the predicted value of 3.2 g/cm³ (Figure 5.6(a,b)). This was evaluated by screen printing films of KN ink onto a set of silicon substrates with known film surface area between 4 and 64 mm². The differential substrate mass (before and after printing) determined the mass of KN ink deposited, and confocal microscopy was used to determine printed layer volume, the correlation of which was used to extract the printed layer density. The ink viscosity was 6.14 Pa.s at a shear rate of 100 s⁻¹ as measured under ambient conditions using a TA Instruments DHR-2 Rotational Rheometer (Figure 5.6(c)). Ink adhesion was consistent across substrate materials, with an ASTM F1842–15 rating of 4B–5B, showing good adhesion to the substrates (Figure 5.6(d)).

The initial surface roughness of the silicon and paper substrates was 2.3 ± 0.5 μm for paper and <5 nm for silicon. Figure 5.2(d) shows a representative edge profile of printed layers on both paper and silicon substrates; Figure 5.2(b) shows an SEM image of the KNbO₃ layer in the cross-section as printed on silicon. The KN layer thickness of printed devices was 11.2 ± 0.2 μm for capacitor structures on paper, and was 10.7 ± 0.2 μm for samples on silicon, scaling well relative to the single-layer thickness of 5.5 μm. The RMS surface roughness of the printed layers was 1.1 ± 0.3 μm for the structures on paper and 0.4 ± 0.1 μm on silicon, resulting predominantly from the greater initial surface roughness of the paper substrate. Layer thickness and surface roughness were characterized using an Ambios XP-2 profilometer.

Table 5.5 Key parameters of printed piezoelectric devices relative to reference values.

Property	Variable	Units	Value on Silicon	Value on Paper	Lit. Value (Bulk)	Ref.
Density	ρ_{KN}	g/cm ³	3.2 ± 0.1	—	4.4	277
Adhesion	—	[—]	4B–5B	4B–5B	—	
Layer Thickness	h_{KN}	μm	10.7 ± 0.16	11.2 ± 0.15	—	
Surface Roughness	$r_{q,KN}$	μm	0.4 ± 0.1	1.1 ± 0.3	—	
Relative Permittivity	ϵ_r	[—]	29.5 ± 0.2	29.3 ± 0.1	35.1	278
Dielectric Loss (@ 100 kHz)	$\tan(\delta)$	[—]	0.14	0.08	—	
Piezoelectric Coefficient	$d_{33,eff}$	pC/N	10.0 ± 1.7	13.6 ± 2.8	60–110	250

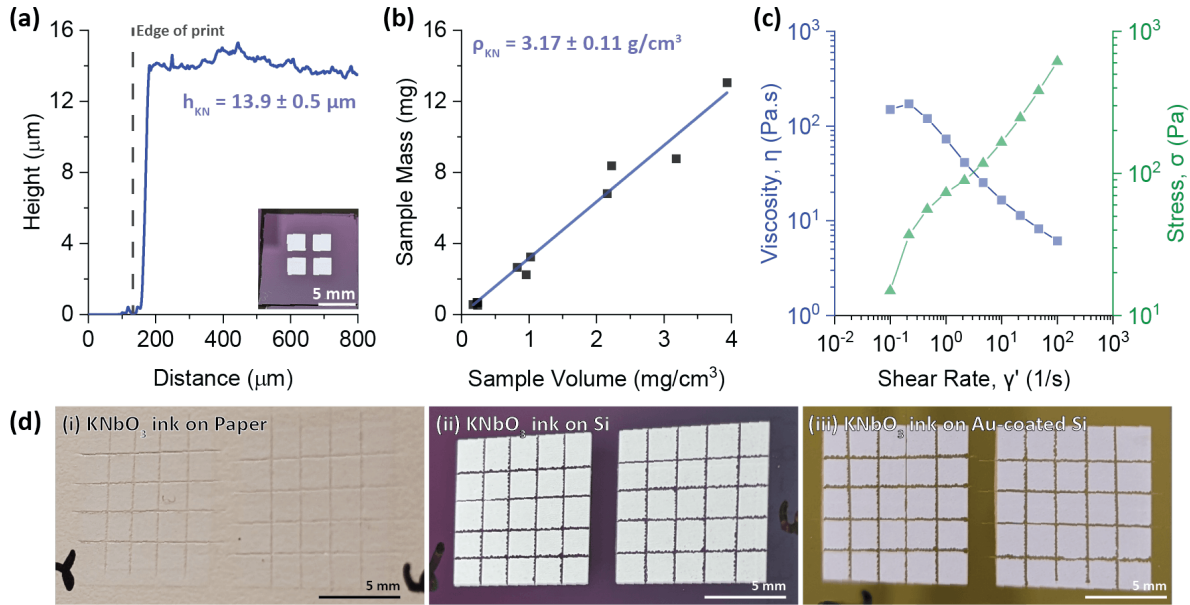


Figure 5.6 Characterization of ink and printed layer properties showing (a) sample profilometry of test samples used for KN ink density calculations, with inset showing one of the test structures as printed on a silicon wafer, (b) sample mass as a function of printed layer volume used in determining KN printed layer density, (c) rheology characteristics of ink in ambient conditions, and (d) Results of adhesion testing on (i) paper, (ii) silicon, and (iii) Gold-coated silicon, showing no major difference in adhesion based on substrate material according to ASTM F1842-15 protocol.

For the purposes of this work, the mechanical properties of devices were not rigorously studied, but future work could be conducted to assess the Young's modulus of the printed film and study device performance under various bending or shearing conditions.

With regards to the fabrication process, printing was conducted on a wafer-sized area of 100 x 100 mm², with a device failure rate of <10% in all cases (defined by the number of damaged or shorted devices upon completion of the fabrication process). This finding demonstrated the robustness of the process, despite the tight alignment tolerance of 100 μm for cantilever devices. The smallest printed features were 250 μm in width with a standard deviation of 15 μm (approximately 5%). This result matched well with the recent limits to line resolution in screen printing applications, which are generally 50–100 μm.⁷

5.2.2 Dielectric properties

Impedance data was collected using the circular capacitor structures on both paper and silicon substrates (circular capacitor devices with a surface area of 5 mm² are shown in Figure 5.7(a)). Impedance spectroscopy was used to characterize the dielectric properties of the as-fabricated capacitors in the range of 10³–10⁶ Hz. Figure 5.7(b) shows a comparison of capacitance versus the device surface area for samples on both paper and silicon substrates, with the calculated relative permittivity values annotated for samples on the two substrates relative to bulk reference values. The dielectric properties were measured using a Digilent Discovery 2 all-in-one test and measurement device and an Agilent 4294A impedance analyzer.

The relative permittivity was calculated at 100 kHz to reduce the influence of ambient humidity on measurements. The calculated relative permittivity of KN capacitors on paper was $\epsilon_{r,paper} = 29.3 \pm 0.1$ relative to those on silicon $\epsilon_{r,si} = 29.5 \pm 0.2$, showing agreement across substrates, supporting the argument that substrate material did not significantly influence dielectric behavior. Both values were below the bulk relative permittivity, $\epsilon_{r,Bulk} = 35.1$, due to the presence of ethyl cellulose ($\epsilon_{r,EC} \approx 2.8 - 3.9$) in the composited ink layer.²⁷⁹ Exemplary impedance spectra showing absolute impedance and phase data for circular capacitors with a surface area of 10 mm² on both silicon and paper substrates are shown in Figure 5.7(c) and (d). The impedance spectra for these devices deviated from ideal capacitor behavior, indicating that there was some electrical leakage present in the capacitor system. This was further verified by calculating the dielectric loss tangent, $\tan(\delta)$, of both device types, which was found to be 0.14 for devices printed on silicon and 0.08 for devices on paper substrates, deviating from the expected values for conventionally processed ceramics that are in the range of 0.1 – 0.2. Further work would be required to diagnose and improve on this leakage behavior.

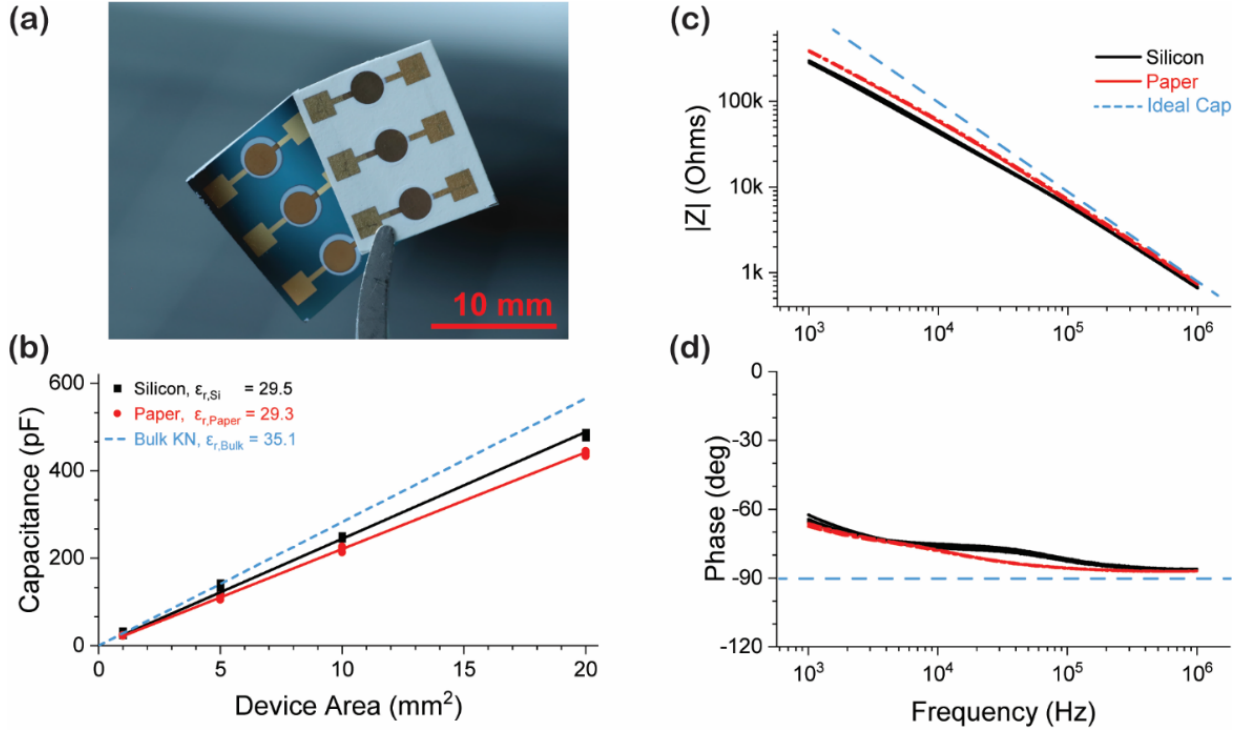


Figure 5.7 Dielectric characteristics of capacitor devices including (a) close-up image of the printed circular capacitor structures, showing those with surface areas of 5 mm². (b) Capacitance versus device area trends for capacitors on both substrates annotated with noted relative permittivities, as calculated at 100 kHz, with comparison to bulk KN behavior. (c) Impedance and (d) phase spectra of characteristic printed piezoelectric cantilevers on both silicon and paper substrates with comparison to an ideal capacitor of the same parameters.

5.2.3 Poling optimization and piezoelectric properties

The piezoelectric response, as both $d_{33,eff}$ and $d_{31,eff}$, was optimized as a function of the poling field and soak time to determine the ideal poling parameters. The direct piezoelectric effect was used to determine $d_{33,eff}$ values via the Berlincourt technique (see Section 8.2.1 of the Appendix for details of the setup and methodology used); the indirect piezoelectric effect was evaluated using Laser Doppler vibrometry (LDV) to further support those measurements (PolyTec MSV-400 microscope scanning vibrometer utilizing a VD-06 velocity decoder). The results of this optimization study are detailed in Figure 5.8, wherein trends are normalized to the maximum measured values for each test and substrate. The indirect piezoelectric effect was used to determine $d_{31,eff}$ from cantilever devices in resonance using LDV, as detailed below (and expanded upon in Appendix Section 8.2.2).

The optimization according to the applied poling field (Figure 5.8(b, d)) showed that poling saturation was attained at applied fields of 20 V/ μ m and higher, after which the measured piezoelectric response was within 20% of the maximum. A similar trend was found for poling time optimization (Figure 5.8(c,e)). After 0.5 minutes of poling, the measured $d_{33,eff}$ and $d_{31,eff}$ values were within 20% of the maximum measured value. From this, it was determined that ideal poling conditions occurred at poling fields between 20 and 40 V/ μ m and poling times greater than 0.5 min. For further studies, 30 V/ μ m and 5 min were selected to mitigate the risks of dielectric breakdown and reduce the poling duration.

In terms of absolute measurements, the average piezoelectric coefficient for samples printed on paper substrates was $d_{33,eff,paper} = 13.6 \pm 2.8$ pC/N as compared to those printed on silicon, $d_{33,eff,Si} = 10.0 \pm 1.7$ pC/N (Figure 5.1(d)). The highest attained $d_{33,eff}$ was 18.4 pC/N on paper substrates and 13.3 pC/N on silicon substrates. The variance in piezoelectric response was most likely attributed to interactions of the piezoelectric layer with the two different substrates, with more clamping in samples on stiff silicon substrates as opposed to the paper substrates. Poling optimization trends were validated using LDV measurements. With the highest reported value for bulk KN of $d_{33,bulk} = 107$ pC/N, the measured values were found to be more than sufficient when considering the adjustments required for these low temperature and printed devices.

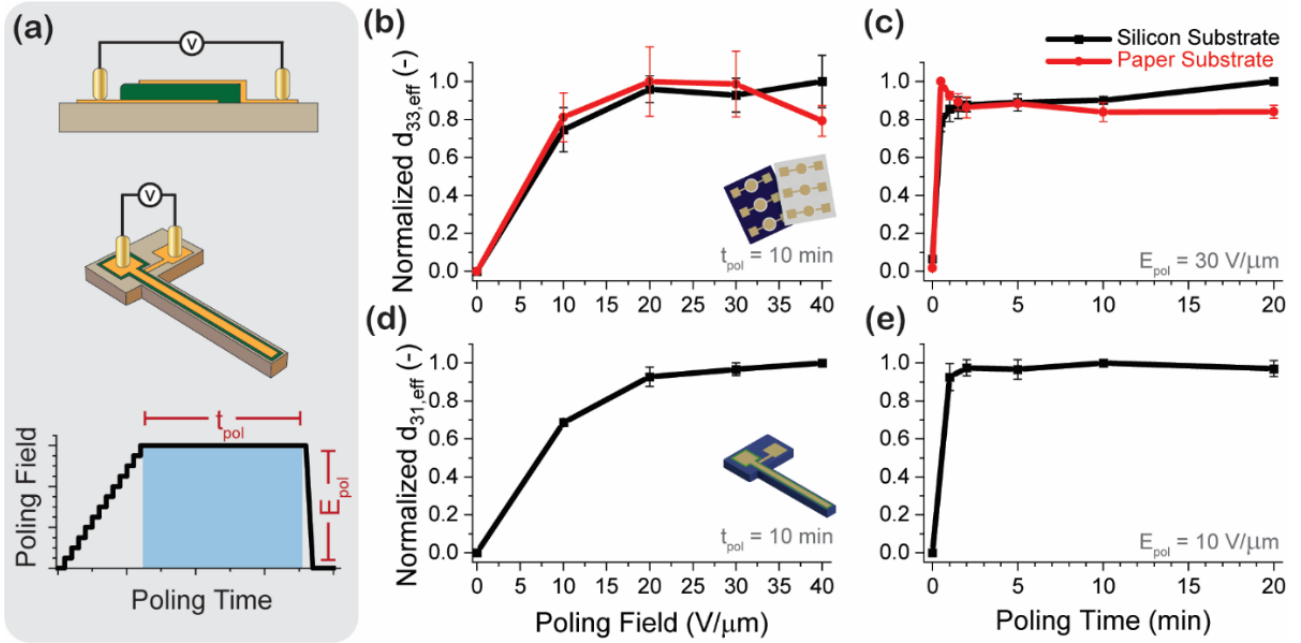


Figure 5.8 Optimization of the poling parameters for piezoelectric coefficients $d_{33,eff}$ and $d_{31,eff}$. All values are reported as the normalized piezoelectric response. (a) Schematic of devices used for poling optimization and applied poling ramp. (b) Optimization of $d_{33,eff}$ as a function of poling field as measured from printed circular capacitor devices via the Berlincourt method. (c) Optimization of $d_{33,eff}$ as a function of poling time as measured from printed circular capacitor devices via laser Doppler vibrometry. (d) Optimization of $d_{31,eff}$ as a function of poling field as measured from printed cantilever devices via laser Doppler vibrometry. (e) Optimization of $d_{31,eff}$ as a function of poling time as measured from printed cantilever devices via Laser Doppler Vibrometry.

Devices were poled at room temperature via direct (contact) poling across the deposited electrodes using a programmable high voltage power supply (Figure 5.8(a)). The applied electric fields utilized in this poling optimization were 0, 10, 20, 30, or 40 $V/\mu m$ with ramp steps equivalent to 1 $V/\mu m$ every 5 seconds, and the poling times were 0, 0.5, 1, 2, 5, 10, or 20 min. The maximum applied electric field was limited to 40 $V/\mu m$ due to dielectric breakdown.

We further aimed to characterize the piezoelectric coefficient transversal to the electric field, i.e., $d_{31,eff}$. To do so, we characterized the out-of-plane movements of cantilever beams (consisting of Si or paper, metal electrodes, and printed KN) using LDV to quantify the displacement around the first out-of-plane mode of each cantilever. As depicted in Figure 5.9(a), the empirical resonance frequencies of the fabricated devices matched well with the predicted values as modelled in the design phase. The small perturbations were attributed to deviations in design configurations during fabrication, along with small variances in the printed layer properties.

Cantilever devices on both substrates were then poled under a set of applied electric fields and poling times (following the values mentioned previously). In actuating each cantilever with a signal of known amplitude (1–5 V_{pp}), the vertical displacement at the cantilever tip was collected over the frequency range surrounding resonance. Thanks to a Lorentzian fit, it was possible to decouple the amplification due to the quality factor from the actual piezoelectric efficiency, and thus, $d_{31,eff}$ was extracted (refer to Section 8.2.2 of the Appendix for further details on the analysis methodology). Figure 5.9(b) and (c) show two typical results on Si and paper cantilevers, respectively. We note the wider peak of the paper sample, which we attributed to the large material losses that can be found with paper substrates relative to silicon. This finding was true for all poling conditions and cantilever lengths, with an average quality factor of cantilevers on silicon of 330 ± 110 and on paper of 25 ± 1 .

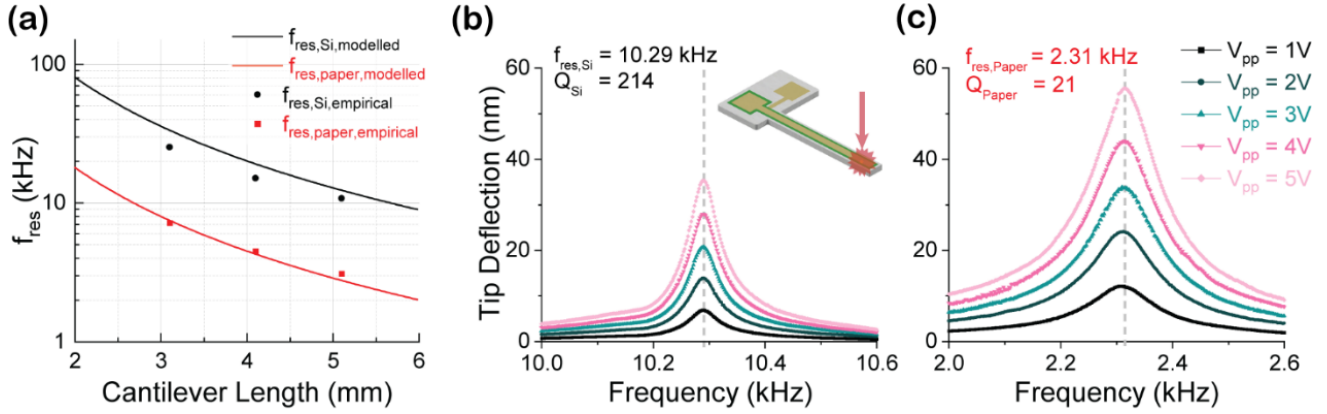


Figure 5.9 Characterization of cantilever devices including (a) modelled and empirical values of cantilever resonance frequencies on both silicon and paper substrates. (b) Silicon and (c) paper cantilever tip displacements at resonance as functions of frequency and actuating voltage, with annotated resonant frequencies and quality factors for samples processed and poled under the same conditions.

These measurements showed that the dependence of the cantilever actuation efficiency (proportional to $d_{31,eff}$) on the poling conditions followed the same trend as that for $d_{33,eff}$. However, the actual extracted values of $d_{31,eff}$ did not correspond to what was expected from the $d_{33,eff}$ values. For samples on silicon, $d_{31,eff,Si}$ was 0.11 ± 0.03 pC/N, while on paper, $d_{31,eff,Paper}$ was 0.12 ± 0.02 pC/N. This result constituted a difference approaching three orders of magnitude between $d_{33,eff}$ and $d_{31,eff}$ on both substrates. We believe that these low $d_{31,eff}$ values stem from suboptimal adhesion between the KN printed layer and the underlying materials. To generate out-of-plane movement in a cantilever structure, the piezoelectric layer must generate a bending moment. To do so, the expansion of the piezoelectric layer must be conveyed to the rest of the structure, for which a significant shear stress must be generated. If the adhesion was not large enough to sustain said stress, the quantification of $d_{31,eff}$ with the described method was flawed; however, qualitative conclusions on the dependence on poling conditions could still be drawn. This result requires further study into the mechanical properties of the layer before enhancements could be made.

5.3 Summary and conclusions

A process was realized to manufacture eco-friendly printed piezoelectric devices at low temperatures, enabling their integration with temperature-sensitive substrates and targeting the development of fully green printed piezoelectrics. A screen-printable ink was developed for printing potassium niobate powder, and then devices were designed and manufactured to characterize this ink and evaluate its applicability as a printed piezoelectric material. Devices were printed with high reproducibility on both silicon and paper substrates at a maximum processing temperature of 120 °C. The average measured piezoelectric coefficient for samples printed on paper substrates was $d_{33,eff,paper} = 13.6 \pm 2.8$ pC/N, with the largest measured value of 18.4 pC/N on paper substrates. The piezoelectric behavior of the devices showed a reduction relative to bulk coefficients for KN; however, the response was still of a value applicable for integration into devices, and further studies could be conducted to optimize ink composition towards this end. Future works would aim to further develop this process on two axes. First, ink properties would be tuned to improve transverse piezoelectric behavior. Additionally, this process would be fully integrated with printed biodegradable conductors to produce fully solution-processed, green piezoelectric devices.

Chapter 6 Integration of screen-printed KNbO_3 with degradable printed electrodes and integration into demonstrator devices

This chapter describes the process development taken for the integration of degradable printed electrodes with the screen-printable KNbO_3 printing process developed in previous sections of this work, as well as the parameters evaluated for best performance and realization of practical device demonstrations. The content of this chapter is based off of a research article currently under review for publication in *Advanced Materials Technologies*.

The manufacture of fully printed piezoelectric devices comprised entirely of degradable materials remains a significant challenge, as discussed previously in Section 2.4, and acts as an obstacle in the development of higher complexity sustainable printed electronics.¹¹⁵ The development of fully printed devices requires optimization of printable ink formulations, deposition processes, and post-treatment methods to achieve the desired functionalities while minimally influencing the adjacent device materials (e.g., substrates or other functional materials) or compromising the performance of the target material.^{115,121,124,280,281}

In this study, we present a novel approach to the fabrication of fully additively manufactured and green piezoelectric devices on paper. We look to integrate the established printed KNbO_3 process with printed degradable conductors in the form of carbon- or zinc-based inks. We further exploited the potential of the developed technology by fabricating sensing and actuating devices. While carbon inks have been the standard for many biodegradable electronics applications, their poor conductivity makes them non-ideal for widespread industrial use.^{282,283} Conversely, zinc-based conductive layers show remarkably better electrical performance relative to carbon, but in order to produce long-lifetime conductive layers, a multi-step hybrid sintering process should be implemented (as recently described by Fumeaux).⁴⁵ This combined electrochemical and photonic sintering procedure makes process integration into multi-material printed devices significantly more challenging. However, both zinc and carbon based printed conductive layers show great promise for integration into eco-friendly fully printed piezoelectric devices.

We look to evaluate the viability of an integrated printing process for piezoelectric devices using either electrode material, and assess the challenges and device characteristics achievable with either material. We evaluate the physical, dielectric, and piezoelectric properties of the devices, with focus on the influence of the two electrode materials on device performance. We also demonstrate the integration of these devices into sensing and actuating applications in the form of touch sensors and acoustic speakers, highlighting their potential for use in sustainable microsystems by taking advantage of both the direct and inverse piezoelectric capabilities of the printed devices. Figure 6.1 provides an overview of this work.

6.1 Materials, methods, and manufacturing

All devices fabricated for primary assessment followed a consistent fabrication procedure, with variance only in the processing of the electrode materials, as depicted in Figure 6.1(a). These devices were based on a parallel plate capacitor architecture with effective surface areas of 5, 10, 20, 30, and 60 mm^2 (Figure 6.1(d)). A stepped sandwich configuration, modified slight from that used previously, was selected to avoid any potential step-coverage related issues

coming from the printed bottom electrode layers. Carbon layers were printed using a commercial ink, while the zinc and piezoelectric KN inks were mixed in-house according to previously established recipes (see Section 6.1.3 Materials and methods for details).

6.1.1 Fabrication process overview

The following process was implemented for the fabrication of fully printed piezoelectric devices. First, bottom electrodes were deposited onto a paper substrate. For carbon and zinc inks, electrodes were screen printed onto the substrate. Carbon electrodes were dried in ambient conditions for 12 hours. Zinc electrodes were cured using the hybrid sintering process developed by Fumeaux, which will be discussed in the following paragraphs.⁴⁵ For the reference samples, a 10/100 nm Cr/Au layer was deposited via thermal evaporation, following previous work on this system.²⁶⁷

Once the bottom electrodes were deposited and cured, the piezoelectric film was screen-printed onto all devices. Each layer of KN ink was dried for 30 min at 120 °C in an oven. To ensure a sufficiently high yield of viable devices, six layers of KN were printed for a total KN film thickness of approximately 30 μm , thereby preventing shorts between the electrodes.

Finally, top electrodes were deposited following the same processes used for the bottom electrodes, resulting in piezoelectric capacitor devices with either both electrodes composed of carbon-based conductors (“carbon electrode”) or both composed of zinc-based conductors (“zinc electrode”). All parameters were maintained for the top electrode processing with the exception of the sintering parameters for the zinc printed layers.

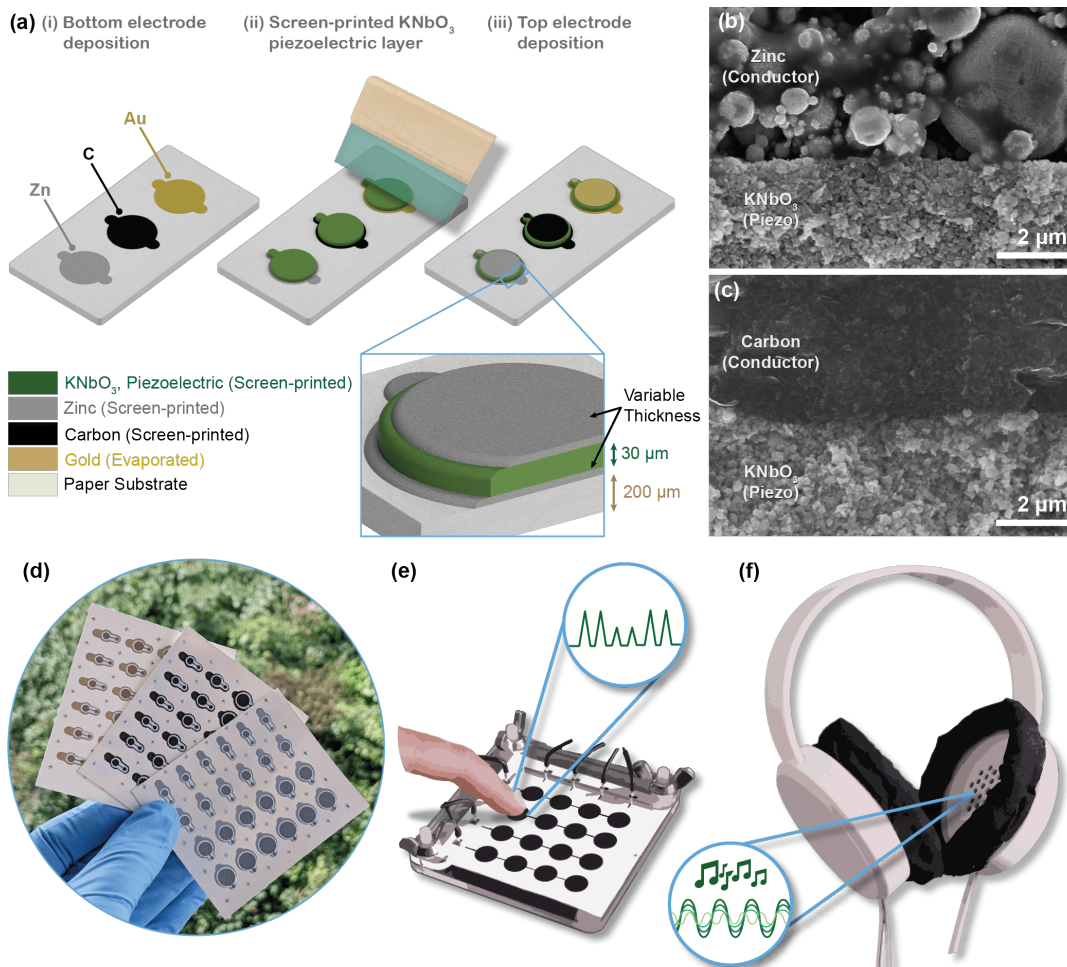


Figure 6.1 Overview of work on fully printed piezoelectric devices including (a) simplified process diagram showing the electrode materials under evaluation, printed zinc or carbon, as compared to conventional evaporated gold electrodes. The piezoelectric has been colored green for visibility. SEM image of the (b) zinc-KN and (c) carbon-KN interfaces. (d) Photographic image showing as-printed devices of varying electrode materials and capacitor sizes. (e) Stylized drawing of the fabricated degradable touch sensor grid demonstrator detailed in this work. (f) Stylized drawing of the fabricated degradable headphone demonstrator detailed in this work.

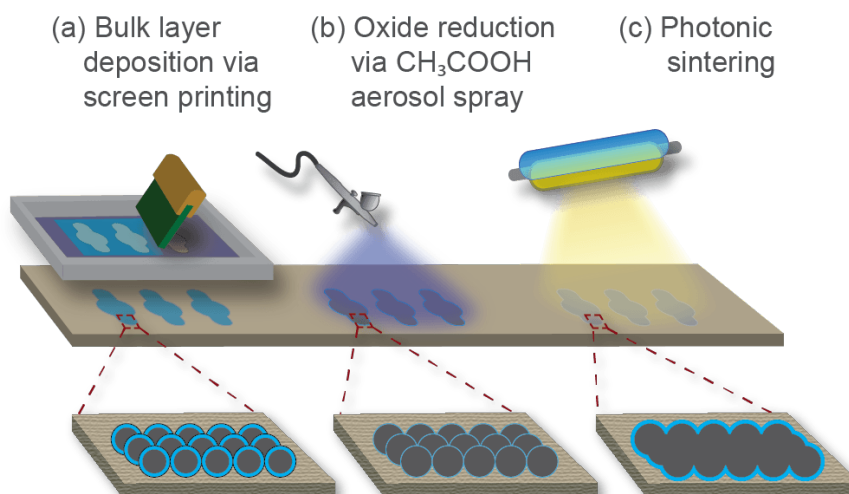


Figure 6.2 Zinc post-printing process schematic including (a) screen printing of the zinc layer, (b) removal of native oxides via aerosolized acetic acid spray, and (c) photonic sintering of the layer post-oxide removal.

6.1.2 Sintering of printed zinc films

Prior work by Fumeaux has established a two-step treatment process for producing conductive layers of printed zinc that is compatible with paper substrates (described schematically in Figure 6.2).⁴⁵ First, aerosolized acetic acid is used to reduce the native oxide layer on the zinc particles, then photonic sintering is used to agglomerate the zinc particles before re-oxidation can occur. As the efficacy of photonic sintering is dependent on the thermal properties of the device stack being exposed, sintering parameters must be determined separately for the top and bottom zinc electrode layers. A protocol consisting of three 6550 mJ/cm² pulses of 30 ms duration at a pulse frequency of 0.1 Hz was developed for screen printed zinc electrodes on paper substrates, directly applicable for the bottom electrode zinc layers in this work. As such, it remains to determine effective sintering parameters for the top electrode zinc layer, as the thermal characteristics of the system changes from that of the bottom electrode with the addition of further device layers. Critically, the sintering parameters for the top electrode layer must produce conductive layers of zinc, but not compromise the integrity of the stack below.

With all other conditions fixed, the pulse energy and the number of pulses imparted on the devices was varied. Figure 6.3 photographically shows the effects of varying these parameters on the device stack. A combination of visual inspection and electrode conductivity evaluation was used to identify ideal sintering parameters. From this, it was determined that one pulse of 7550 mJ/cm² was ideal with regards to sintering of top electrode zinc for this process.⁴⁵

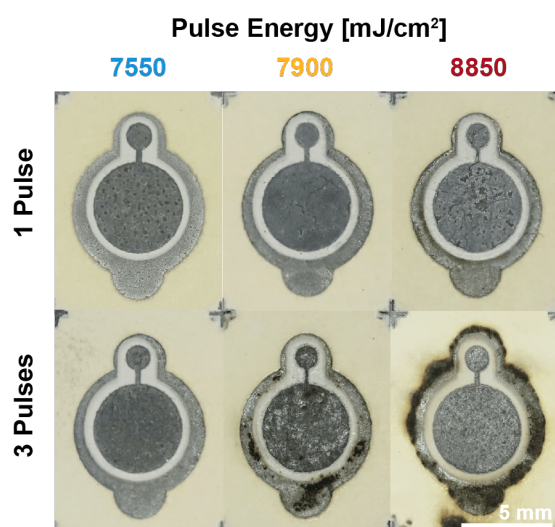


Figure 6.3 Zinc post-printing sintering process development. Photographic depiction of the influence of photonic sintering parameter on the printed layer stack, as used for the determination of ideal process parameters.

6.1.3 Materials and methods

6.1.3.1 Materials

All printed piezoelectric devices were fabricated on ArjoWiggins PowerCoat XD 200 screen printing paper (200 μm thickness, 219 g/m^2). For samples used in SEM imaging, samples were printed on glass wafers (Borofloat 33, 100 mm \varnothing , 500 μm thickness, Siebert Wafer GmbH).

The Cr/Au (10/100 nm) gold reference electrodes were thermally evaporated using a Leybold L560 thermal evaporator using shadow masks fabricated from 200 μm thick stainless steel by Beta-Layout GmbH. The carbon ink utilized was BareConductive Electric Paint (SKU-0216)—a water based, screen printable carbon ink utilizing natural resin as the adhesive ingredient. The zinc conductive ink was prepared using following components: Zn powder (CAS 7440-66-6, US Research Nanomaterials Ink., 500 nm average diameter, 99.9% (metal basis)), polyvinylpyrrolidone (CAS 9003-39-8, Merck, MW=360K), and pentanol (CAS 71-41-0, Merck, ReagentPlus, $\geq 99\%$).

The piezoelectric ink was prepared using the following components: KNbO₃ powder (99.999% purity, Alfa Aesar), ethyl cellulose, and pentanol. All component materials are recognized as non-toxic, with potential for sustainable production.^{20,233,284,285}

6.1.3.2 Preparation of Zn-based ink

The ink ingredients were mixed in a weight ratio of 25:1:5 Zn:PVP:pentanol. The ink was homogenized with a planetary mixer (Thinky ARE-250) at 300 rpm for 30 min. Three stainless steel mixing balls of 8 mm \varnothing were used as mixing media. The ink was stored at 4 $^{\circ}\text{C}$ in a well-sealed container. Prior to printing, the ink was re-homogenized at 500 rpm for 10 minutes in the planetary mixed and printed once at ambient temperature.

6.1.3.3 Preparation of KNbO₃-based ink

Prior to ink manufacture, the KN powder was ground in order to reduce average particle diameter and improve the homogeneity of the particle sizing, following the procedure previously described (Section 5.1.1).

The ground KN powder was then mixed with ethyl cellulose and pentanol in a proportional ratio of 58:7.5:35 wt% KN:EC:pentanol. Ink mixing was conducted in the planetary mixer using 5 g of 5 mm \varnothing Al₂O₃ spherical milling media (Retsch). Mixing was conducted at 700 rpm in 30 min intervals to reduce solvent evaporation due to system heating. The total duration of mixing was 2 hours. To adjust for the solvent lost due to heating, slight additions of pentanol were required to attain the targeted ink viscosity. Once mixed, ink was stored at 5 $^{\circ}\text{C}$ in a well-sealed container. No re-homogenization was required for this ink prior to printing.

6.1.3.4 Manufacturing

Paper substrates were pre-cut via laser cutting using a Trotec Speedy 300 (60 W) laser cutter to a consistent size with engraved alignment marks to ensure a consistent process across all samples. No pre-treatments were required on paper substrates prior to further processing. For the samples printed on glass, the substrates were pre-treated using an O₂ plasma cleaned (Diener ATTO, 100% Power, 10 min). All paper substrates were clamped to a stiff polyoxymethylene carrier plate before initial printing to reduce substrate warping through successive processing steps.

A manual screen printer was used for printing all inks (carbon, zinc, and KN). Mesh fabrication was provided by Serilith AG using polymer and steel mesh materials. Carbon ink layers were dried for 12 hours under ambient conditions. Zinc layers were dried for 30 min under ambient conditions prior to the post-printing treatment process detailed below. The KN ink layers were dried in a Memmert UF110plus oven at 120 $^{\circ}\text{C}$ for 30 min after each layer, for a total of 6 layers.

Post-printing treatment of zinc electrodes was conducted following Fumeaux, and consisted of the following two phases.⁴⁵ The first phase consisted of chemical reduction of the ZnO passivation layer on individual Zn particles. Dilute acetic acid (CAS 64-19-7, Merck, 1M CH₃COOH, diluted to 10 vol% in deionized water) was spray-coated on the screen-printed Zn electrodes using an aerosolizing airbrush (Harder & Steenbeck, 0.2 mm nozzle) supplied by nitrogen gas (2 bar) at a distance of approximately 10 cm from the sample surface. Each pass of spray was followed by a 5 min drying period on a hot plate at 50 $^{\circ}\text{C}$. This spray-coating/drying cycle was repeated a total of 10 times. This process was conducted

entirely under a fume hood. Once this phase was complete, samples were immediately transferred to the second phase of processing.

The second phase involved photonic sintering to melt the now-reduced Zn particles and produce a cohesive bulk layer of conductive zinc. Samples were first placed in an anaerobic environment, using a custom chamber adapted for the Novacentrix PulseForge 1200 photonic sintering instrument, to reduce the potential for Zn re-oxidation. The sealed chamber was purged with nitrogen for a minimum of 30 seconds prior to sintering. The photonic sintering treatment comprised pulse energies ranging from 6550 to 9900 mJ/cm² with between 1 and 3 pulses delivered. All recipes using in process optimization constrained pulse duration to 30 ms, with a pulse frequency of 0.1 Hz. Final recipes involved 3 pulses at 6550 mJ/cm² for the bottom electrode zinc layer, and 1 pulse of 7550 mJ/cm² for the top electrode zinc layer.

6.2 Influence of electrode material on device properties

6.2.1 Physical characteristics

The final completed devices were first evaluated for their physical properties. Profilometry was used to evaluate the surface roughness and thickness of each printed layer using an Ambios XP-2 profilometer. Representative profilometry data is shown in Figure 6.4 for devices printed on paper substrates with (i) zinc and (ii) carbon electrodes. As the high initial surface roughness of the paper substrates (2–3 μm) made measurement of individual layer thicknesses challenging, measurements were confirmed by comparison to samples printed on glass substrates (average roughness <5 nm). All values reported in the following discussion were measured for samples printed on paper substrates.

The bottom electrode layers were measured to be 18.5 ± 1.4 μm for zinc electrodes and 3.4 ± 2.8 μm for carbon bottom electrodes. The surface roughness values are comparable to that of the paper substrates, which was calculated to be 2.3 μm. The KN piezoelectric layer thickness was 29.2 ± 2.3 μm when printed on zinc electrodes, and 23.9 ± 2.0 μm when printed on carbon electrodes. The top electrodes had average thicknesses of 31.9 ± 5.2 μm and 3.4 ± 1.4 μm for the zinc and carbon layers respectively. This information is summarized along with other characteristic device parameters in Table 6.1.

Table 6.1 Comparison of piezoelectric device characteristics based on electrode material.

Property	Variable	Units	Zinc electroded	Carbon electroded	Gold electroded
Eco-friendliness	—	[—]	Biodegradable	Biodegradable	Inert
Rel. material cost	—	[—]	Cheap	Cheap	Expensive
Deposition method	—	[—]	Screen Printing	Screen Printing	Thermal Evaporation
Electrode conductivity [*]	σ	S/m	5×10^6	98 ± 21	4.55×10^7
Bottom electrode thickness [†]	h_{BE}	μm	18.5 ± 1.4	3.4 ± 2.8	~ 0.1
Piezoelectric layer thickness [†]	h_{KN}	μm	29.2 ± 2.3	23.9 ± 2.0	27.6 ± 1.3
Top electrode thickness [†]	h_{TE}	μm	31.9 ± 5.2	3.4 ± 1.4	~ 0.1
Relative permittivity	$\epsilon_{r,eff}$	[—]	14.6 ± 0.6	23.1 ± 0.1	22.3 ± 0.8
Piezoelectric coefficient (max.)	$d_{33,eff,max}$	pC/N	5.1 ± 0.8	4.6 ± 0.2	11.6 ± 0.8

^{*} Conductivity for gold taken as the conductivity of bulk gold.²⁸⁶ Conductivity of zinc as reported by Fumeaux.

[†] All layer thicknesses as reported when measured on paper substrates. Standard deviations represent calculated average surface roughness values. Gold electrode layer thicknesses assumed to be 0.1 μm based on thermal evaporation process parameters.

Overall, the thickness of the piezoelectric layer was found to be highly consistent regardless of electrode material, with each successive print deposition adding approximately 4–5 μm of KN, resulting in a final layer thickness 20–30 μm after 6 depositions. The printed carbon layers were significantly thinner than the zinc layers, and showed consistent thickness between the top and bottom electrode layers. The thicknesses of the top and bottom zinc electrodes showed larger deviation, with the top electrodes being, on average, over 70% thicker than the bottom electrodes. Additionally, the average surface roughness of the zinc top electrodes was more than twice that of the bottom electrodes. This change in electrode layer thickness and surface roughness are attributed to the variance in sintering parameters implemented between the top and bottom zinc electrodes.

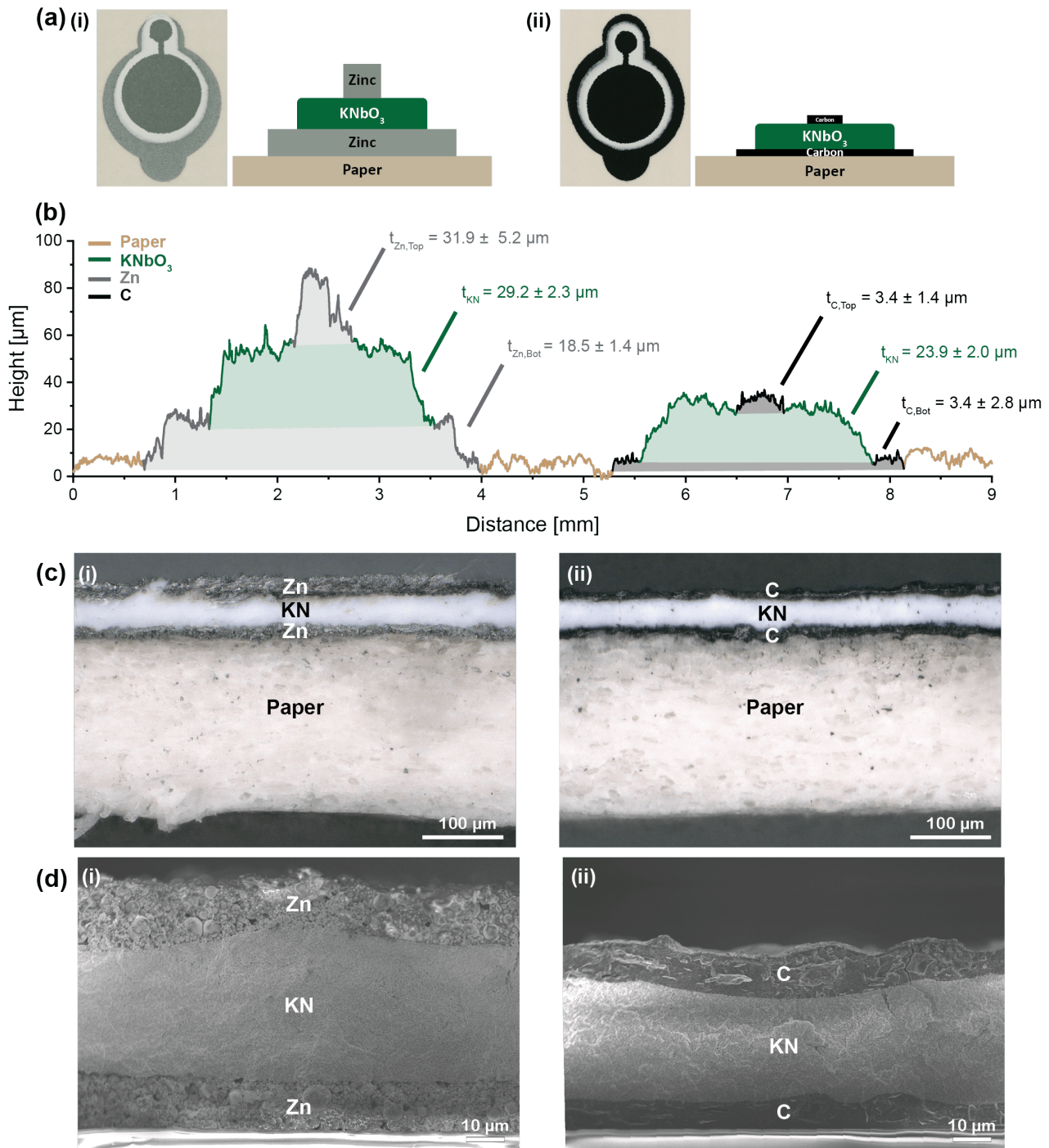


Figure 6.4 Physical characteristics of the fabricated devices. (a) Schematic diagrams and device photos for printed capacitor devices with (i) zinc and (ii) carbon electrodes. (b) Surface profiles of the full device stacks for both zinc and carbon electrode devices, as measured on paper substrates. Profiles have been color coded to show approximate locations of the three device layers. (c) Optical microscope images of devices cross section with (i) zinc and (ii) carbon electrodes, showing also the paper substrates and KN piezoelectric layers. (d) SEM cross-sectional images of capacitor devices made with (i) zinc and (ii) carbon electrode materials, as imaged on glass substrates.

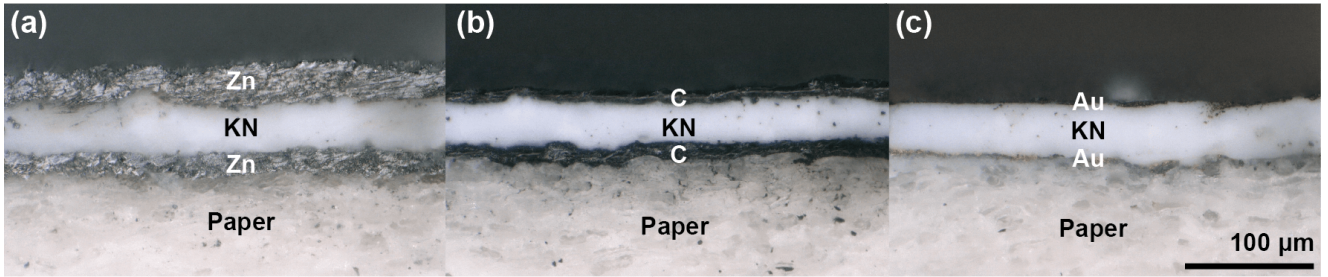


Figure 6.5 Optical images of each device type in cross-section with (a) zinc electrodes, (b) carbon electrodes, and (c) gold electrodes.

To further evaluate the morphological characteristics of these devices, optical and scanning electron microscopy (SEM) were utilized to inspect the interfaces between layers on each type of device. Ink properties were analysed using a Keyence VHX Digital Microscope Series optical microscope, a JEOL JSM-7500TFE scanning electron microscope. Optical microscopy images of the samples as printed on paper substrates are shown in Figure 6.5 as well as Figure 6.4(c). The images show consistent layer thickness for all printed components, and support the profilometry measurements indicating the increased thickness of the zinc electrode layers as compared to the carbon electrodes.

Due to the nature of the cellulose fibers in paper, cross-sectional imaging of samples on paper was limited to optical observation, and thus, the SEM images below portray samples printed on glass substrates, not on paper substrates. As a result, the characteristics of the zinc top electrodes in this image may not fully represent the samples on paper, as the sintering parameters were not optimized for samples printed on glass substrates. Scanning electron microscopy of samples in cross-section are depicted in Figure 6.4(d) for samples with (i) zinc and (ii) carbon electrodes, showing the full device stacks as printed on glass substrates. Figure 6.1(b) and (c) depict the KN-electrode interfaces in greater detail (as do Figure 6.5 and Figure 6.6).

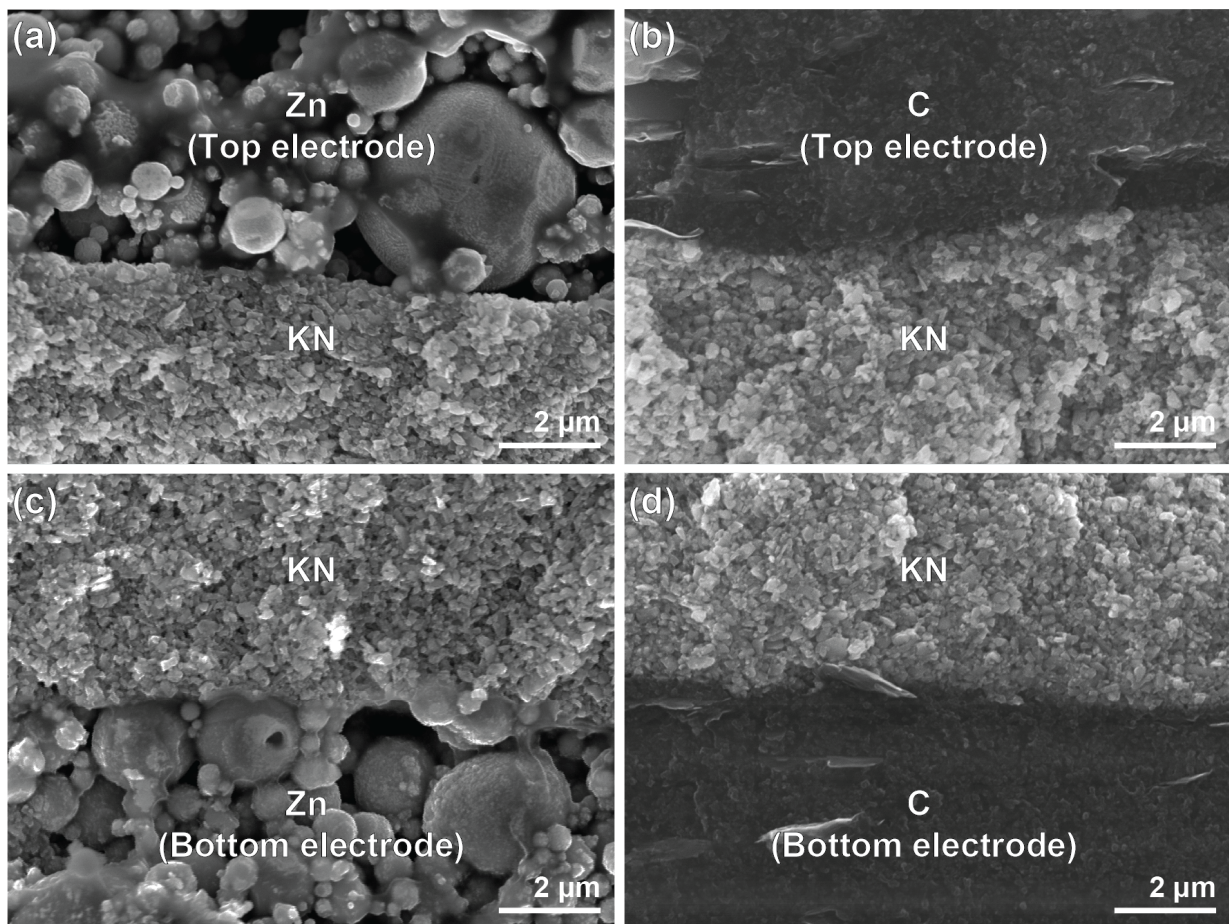


Figure 6.6 SEM images showing the KN-electrode interfaces including those between the KN piezoelectric layer and the (a) zinc top electrode, (b) carbon top electrode, (c) zinc bottom electrode, and (d) carbon bottom electrode. All images were taken of samples printed on glass substrates.

Inspection of the KN-top electrode interface shows excellent conformation for samples with carbon electrodes, however the interface for samples with zinc electrodes is less consistent, as the spherical nature of the zinc particles in combination with their variable size (ranging from 0.1–5 μm), results in a less consistent interfacial area. Further observation indicates that the top electrode zinc particulate near to the Zn-KN interface (deeper into the sample) may not have been fully sintered in the post-printing treatment process. This is most likely attributed to the directional nature of the photonic sintering step, which imparts the greatest energy on the exterior, exposed surface of the zinc layer before diffusing through to the lower portions of the layer. As previously discussed, the photonic sintering parameters were limited to mitigate the damaging effects of this high energy pulse on the lower layers of the device, it is possible that the identified parameters were sufficient to sinter the exposed surface of the top zinc electrode, but not the lower parts. To establish the validity of this hypothesis, and to evaluate the significance of its effects on the printed devices, further studies must be conducted, with more attention paid to this Zn-KN interface.

6.2.2 Dielectric and piezoelectric characteristics

The simple parallel plate capacitor design used in this investigation facilitated the evaluation of the dielectric characteristics of the devices, including the determination of the effective relative permittivity for the piezoelectric layers according to a parallel plate capacitor assumption as follows Equation (2.3).

Impedance and phase spectra were taken in the range of 1 kHz to 1 MHz at 1 V for samples with effective surface areas ranging between 5 and 30 mm^2 for all device types. Figure 6.7(a) and (b) show these spectra for samples of area 10 mm^2 of all types. The impedance spectra for these devices deviated from ideal capacitor behavior, indicating that there was some electrical leakage present in the capacitor system in all cases. From these spectra, the device permittivity was calculated, using capacitance data extracted at 100 kHz (selected in lieu of the conventional 1 kHz parameter to reduce the influence of ambient humidity on the hygroscopic KN layer at lower frequencies). In Figure 6.7(c), we compare the capacitance measured versus the capacitor area, with annotations of the calculated relative permittivity of the devices as calculated from this information.

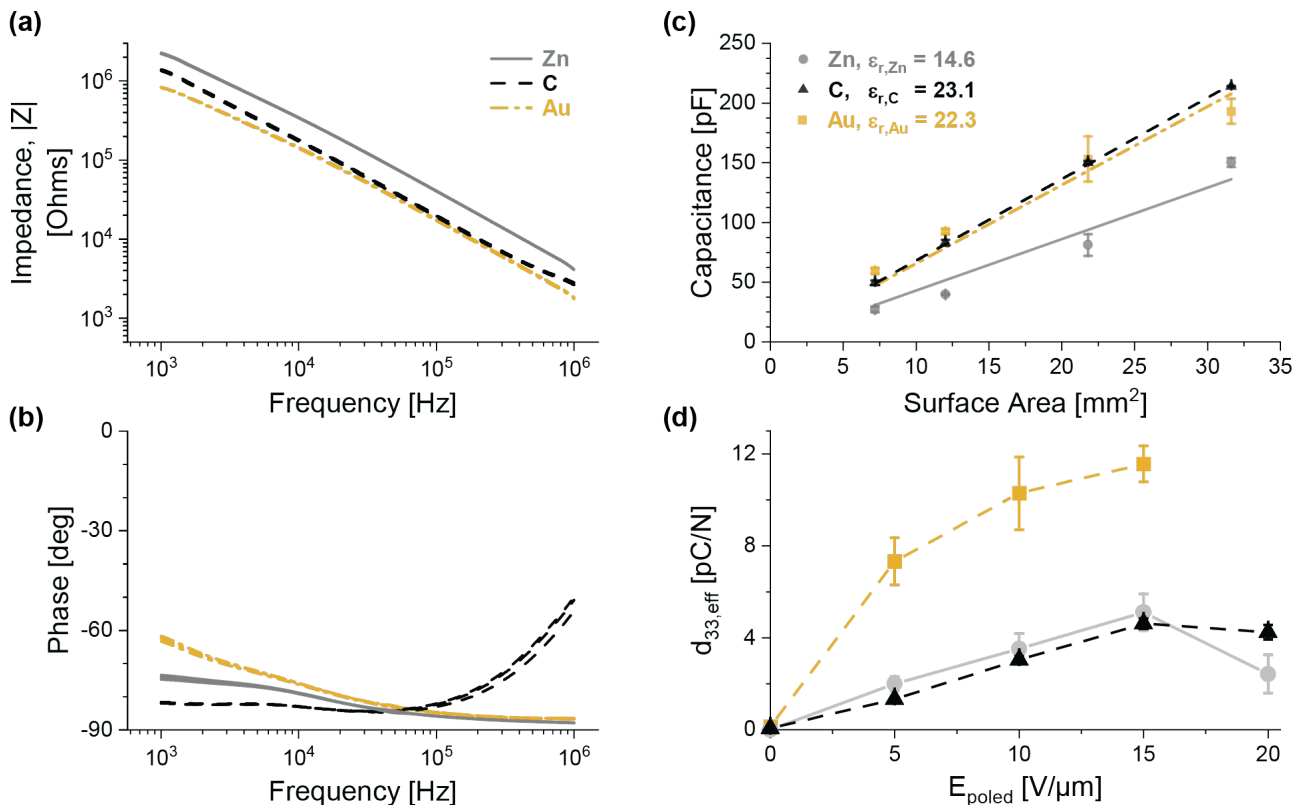


Figure 6.7 Electrical behavior of piezoelectric devices. (a) Impedance and (b) Phase spectra for devices fabricated with the varying electrode materials. (c) Device capacitance as a function of capacitor surface area, with annotated effective relative permittivities. (d) Piezoelectric coefficient, $d_{33,eff}$, as a function of applied field at poling.

The samples with gold and carbon electrodes show nice agreement, with relative permittivity values of 22.3 ± 0.8 and 23.1 ± 0.1 respectively. However, the calculated value for the relative permittivity of the zinc electrode samples was notably calculated as just 14.6 ± 0.6 , despite all samples being fabricated with close attention to consistent processing of the piezoelectric layers (both in terms of material used and layer thickness). The variance represents a reduction of approximately 37% in devices with zinc electrodes when compared to devices with gold or carbon electrodes. This could most likely be attributed to either a reduced electrode surface area for the zinc samples, as evidenced by the inconsistent interface between the KN and Zn layers in the cross-sectional images (Figure 6.4(d)), or to incomplete reduction of the oxide layer in the zinc top electrode, resulting in a double layer capacitor where the stack is comprised of Zn-ZnO_x-KN-Zn layers. As both steps of the zinc sintering process necessarily affect the top, exposed surface of the printed Zn layer before progressing through the interior. Hence, while the external surface of the top electrode is conductive, it is possible that the acid does not permeate sufficiently through to reduce the passivation layer on the particulate near the Zn-KN interface, or more likely, that the energy imparted during photonic process was only sufficient to sinter the top few microns of the printed electrode layer and not the full depth of it. Either condition, or a combination thereof, would result in a mixed device stack with a Zn-ZnO_x-KN-Zn mixed stack instead of the assumed Zn-KN-Zn device intended. Further studies are necessary to diagnose the source of this atypical behavior and resolve the discrepancy. This could be achieved through thinner Zn printed films or the introduction of reducing agents in the zinc ink itself.

Following dielectric analysis, the printed capacitors were poled to attain a piezoelectric response via direct (contact) poling following the procedure described in Section 4.1.3. All samples were instead poled in ambient conditions. The applied poling field was varied in the range from 0–20 V/ μm , as a means of evaluating the influence of electrode layers on the effective piezoelectric coefficient of the resulting devices, $d_{33,eff}$, when poled in ambient conditions. In line with the results of previous investigations (Section 5.2.3) on low temperature contact poling, the poling duration was fixed for all samples to be 5 min.²⁶⁷

The results of this study are depicted graphically in Figure 6.7(d). The magnitude of the piezoelectric response ($d_{33,eff}$) for the reference samples with gold electrodes match well with prior studies on this piezoelectric, with a maximum of 11.6 ± 0.8 pC/N when poled at 15 V/ μm (compared to 13.6 ± 2.8 pC/N reported previously).²⁶⁷ Samples with gold electrodes were not evaluated for piezoelectric coefficients when poled at 20 V/ μm due to breakdown events resulting in damage to the electrodes. A maximum piezoelectric response was obtained for samples with zinc or carbon electrodes when poled with an applied field of 15 V/ μm , where the average effective piezoelectric coefficient was 5.1 ± 0.8 pC/N for zinc electrode devices and 4.6 ± 0.2 pC/N for carbon electrode devices.

The significant reduction in effective piezoelectric response for samples with the printed electrodes may potentially be explained by the presence of the thick electrode layers themselves. That is to say, the presence of significantly thick electrodes of either Zn or C may mechanically constrain the transducer stack, thereby limiting its displacement and thus reducing the observed piezoelectric coefficient. Future works should evaluate the source of this reduced performance, and look to mitigate the effects. This could be achieved, for example, through thinner electrode layers, or modifying the recipe used in the electrode inks, to adjust the stiffness of the resulting printed layer.

6.3 Degradation Studies

With device performance characterization complete, we next look to evaluate the degradation of the printed devices. As a full degradation study to ISO standard 20200 is out of the scope of this work, we elected instead to make a preliminary investigation into device disintegration as a proof-of-concept degradation study upon which more in-depth experiments can be conducted in the future.

To study this, three test conditions were identified to replicate expected environments in which devices might be degraded at the end of their functional life, and 3 to 5 printed capacitive devices of both electrode types were placed into each environment. In the first, samples were placed in deionized water. The second, in commercial potting soil. The third test condition was household compost. As the degradation rate in soil and water were expected to be slow under ambient conditions, samples in these test conditions samples were instead heated to a constant 60 °C for the duration of the study.

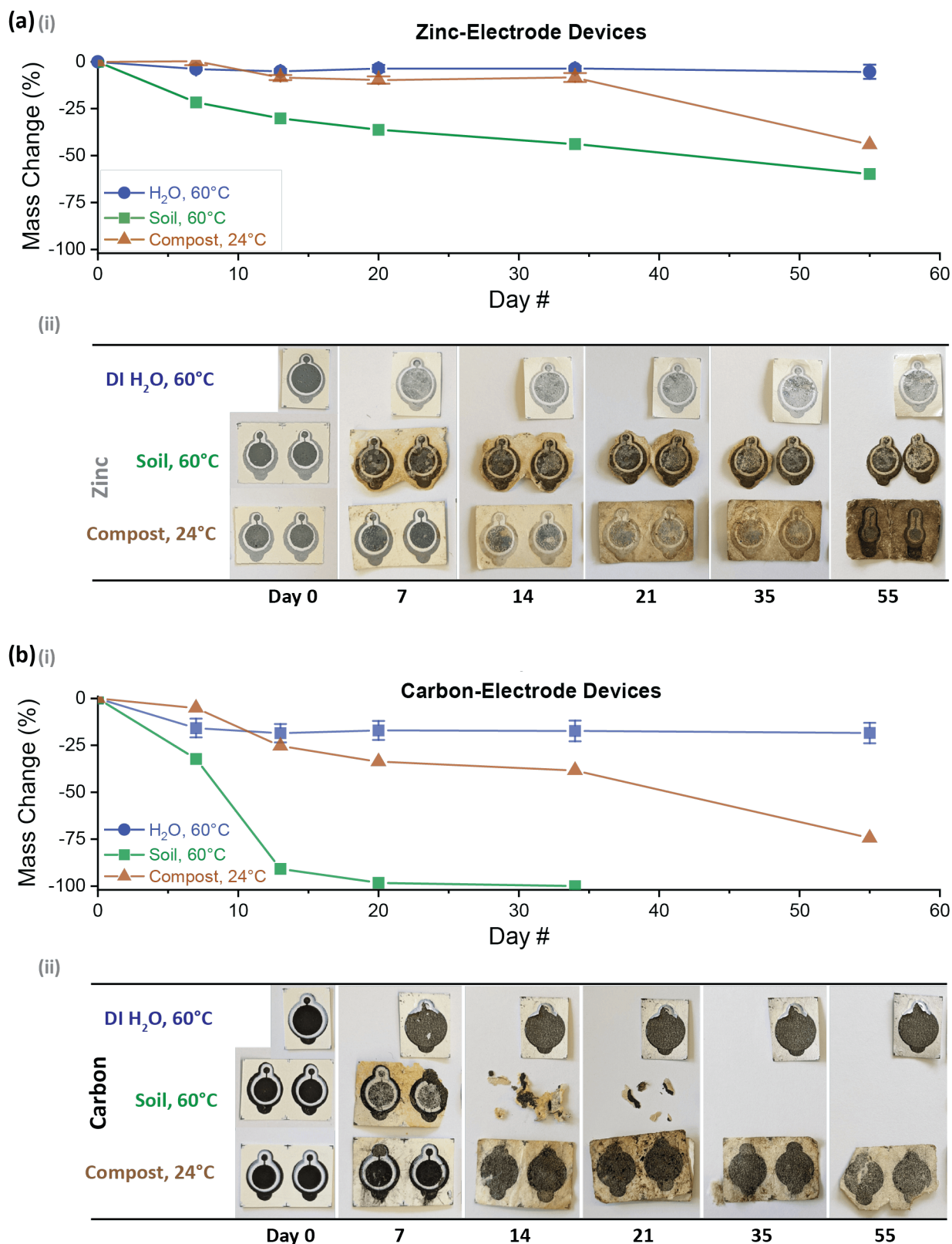


Figure 6.8 Degradation studies showing sample degradation under three different conditions for (a) zinc- and (b) carbon-electrode devices on paper. In (i), the rate of mass loss over time is tracked for samples in each condition, and in (ii) degradation is shown visually for each sample type.

Samples were placed into each degradation condition in isolated containers. At timepoints of 1–3 weeks, samples were then removed from the environments, rinsed with DI water, and dried in an oven at 80 °C for 3 hours before measurement of sample mass and imaging. Once complete, samples were returned to degradation environments in the same conditions. This process is continued for a period of 55 days.

In Figure 6.8, we depict the degradation of samples with (a) zinc or (b) carbon electrodes over time, and in each of the three degradation conditions. The average sample change in mass is depicted for each of the conditions in subfigures (i), and in subfigures (ii) sample degradation is shown visually in the associated photos. The rate of degradation of both zinc and carbon electrode devices was similar in the 60 °C water environment. After 55 days, only 5% of the mass of zinc samples was lost on average, and for carbon-electrode samples, 18% was lost. The larger value for carbon samples was attributed to the water-soluble carbon ink. After 55 days in compost at ambient conditions, approximately 44% of mass was lost for zinc samples, and for carbon-electrode samples this was 74% mass lost on average. The layers of the paper substrates were observed to readily delaminate from each other in this condition for devices of either electrode type after several weeks, increasing available surface area for degradation processes after that time. Finally, the mass loss of samples in soil after 55 days was 55% for zinc samples. After 34 days in soil at 60 °C all carbon samples were fully disintegrated and thus further degradation could not be studied. It was hypothesized that the slight acidity of the soil aided in disintegration of the substrates, as is well established for cellulose fiber-based materials. For the samples with zinc electrodes, the paper substrates were observed to have nearly fully disintegrated and the sintered zinc electrodes are degrading at a slower rate than the carbon electrodes. Even so, visual inspection confirms that the electrodes continue to degrade over time, and electrode resistance measurements show no conductivity of any device (carbon or zinc, in any environment) after 55 days of degradation.

This serves as a successful proof-of-concept that the materials involved in these devices will disintegrate at End-of-Life in simulated environmental conditions, paving the way for more in-depth studies of degradation mechanisms in the future.

6.4 Sensing Demonstration: Force Sensor

As a means of demonstrating the practical application of this technology platform for sensing applications, we have used the described process to manufacture fully green paper-based force sensor grids, with devices made using both zinc and carbon electrodes.

The fabrication of these devices follows the same procedure as aforementioned, using an altered device design to produce a matrix of piezoelectric capacitors in a 4x4 grid pattern. The active area of each device was selected as 50 mm², intended to match the approximate size of a human fingertip as would be appropriate for future touch sensing applications. Figure 6.9(a) depicts a schematic of this design, and Figure 6.9(b) shows a photograph of a fully realized sensor, as fabricated with carbon electrodes.

Individual capacitors were poled using a poling field of 15 V/μm and a soak duration of 5 min, following the poling conditions determined previously to maximize the piezoelectric response of the samples (see Figure 6.7(d)). The piezoelectric coefficient ($d_{33,eff}$) of each sample was measured using the Berlincourt method prior to force sensor characterization as a form of comparison. The measured piezoelectric coefficient for the devices studied was 6.0 ± 0.3 pC/N for samples with Zn electrodes, and 4.6 ± 0.2 pC/N for samples with carbon electrodes.

Figure 6.9(c) depicts a schematic of the measurement setup used in this evaluation. The vertical translation stage of an Instron 3340 Single Column Universal Testing System was used to compress the device as the applied force and voltage response were recorded using an in-line Futek 2519-50N force sensor and an Agilent 34410A multimeter. Compressions were implemented following a force-controlled triangular waveform with a 10 s compression and release cycle followed by a 5 s pause step at 0 N. Repetitions are made for sample compression from 5–20 N with an actuation frequency of 0.1 Hz. The parallel resistance of the devices was measured at 20 Hz using an Agilent E4980A Precision LCR meter. Figure 6.9(d) shows the resulting data, with the measured force (i) and voltage (ii) plotted as a function of time for samples with zinc or carbon electrodes. The resulting measurements show a clear trend with increasing applied force producing an appropriately increasing voltage measurement under controlled measurement conditions. More detailed examples of device actuation are shown in Figure 6.10 below.

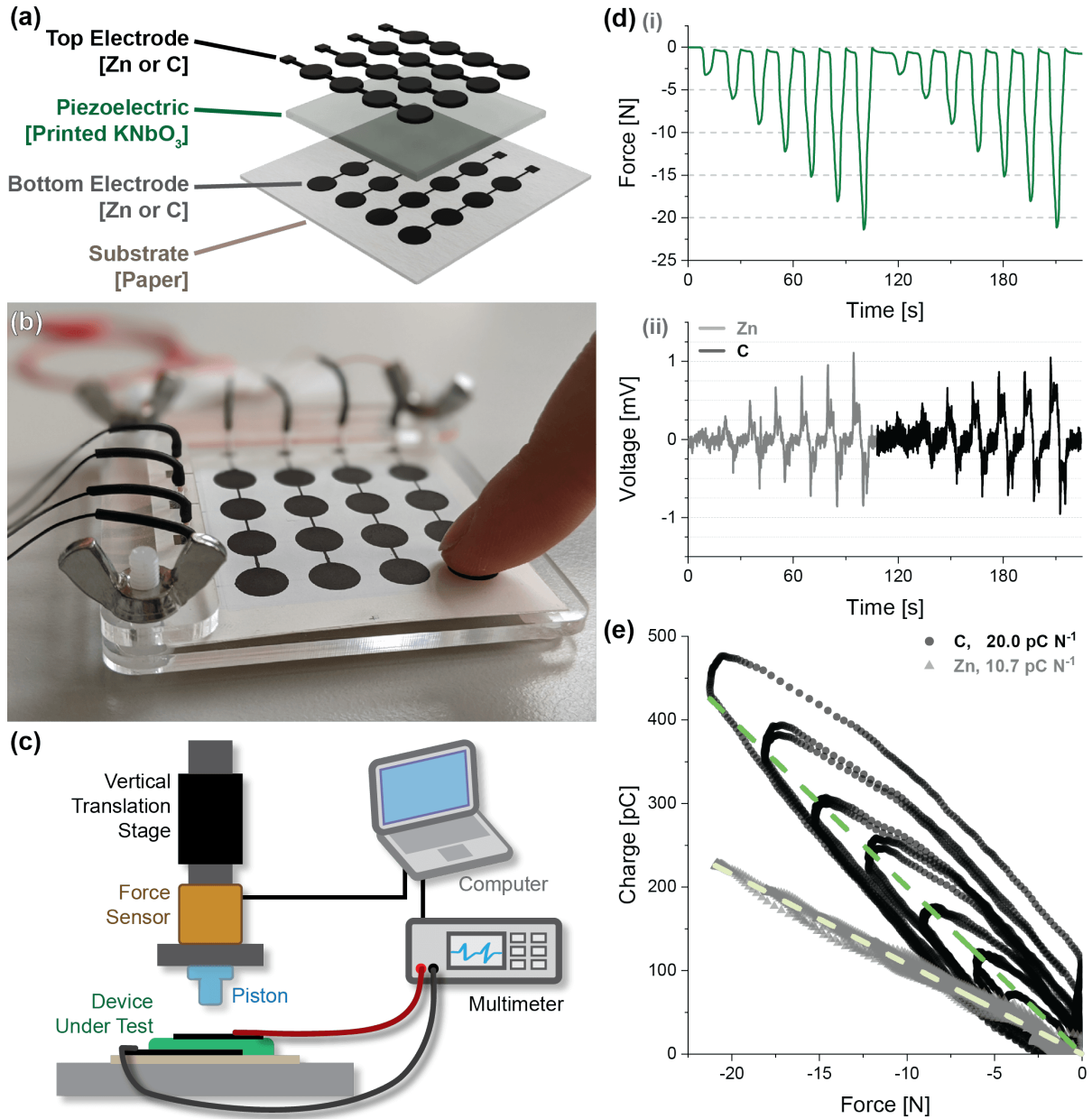


Figure 6.9 Fabrication and characterization of a fully printed degradable force sensor grid. (a) Schematic depicting the design components. (b) Photograph of the realized device, as fabricated using carbon electrodes. (c) Schematic of the test setup for response characterization. (d)(i) Force and (ii) voltage data collected during the measurement, showing the response of both sample types as the maximum applied force is increased. (e) Charge as a function of applied force depicted for capacitor devices with zinc or carbon electrodes, with annotated device responsivities.

The impedance of the devices and the input impedance of the voltmeter were next used to correlate the measured voltage with the corresponding charge according to Equation (6.1) below and the responsivity of the devices was calculated through a correlation of the charge measured as a function of force applied (see Figure 6.9(e)).

$$q = \frac{1}{Z_L} \int v dt \quad (6.1)$$

From this study, the responsivity of the device with zinc electrodes was calculated as 10.5 pC/N while the responsivity of the device with carbon electrodes was 20.0 pC/N. The change in responsivity despite seemingly equivalent voltage response (as observed in Figure 6.9(d)) results from the load impedance (Z_L) of the two devices, with the zinc electrode device having a parallel resistance nearly double that of the carbon electrode sample (7 M Ω as opposed to 5.4 M Ω).

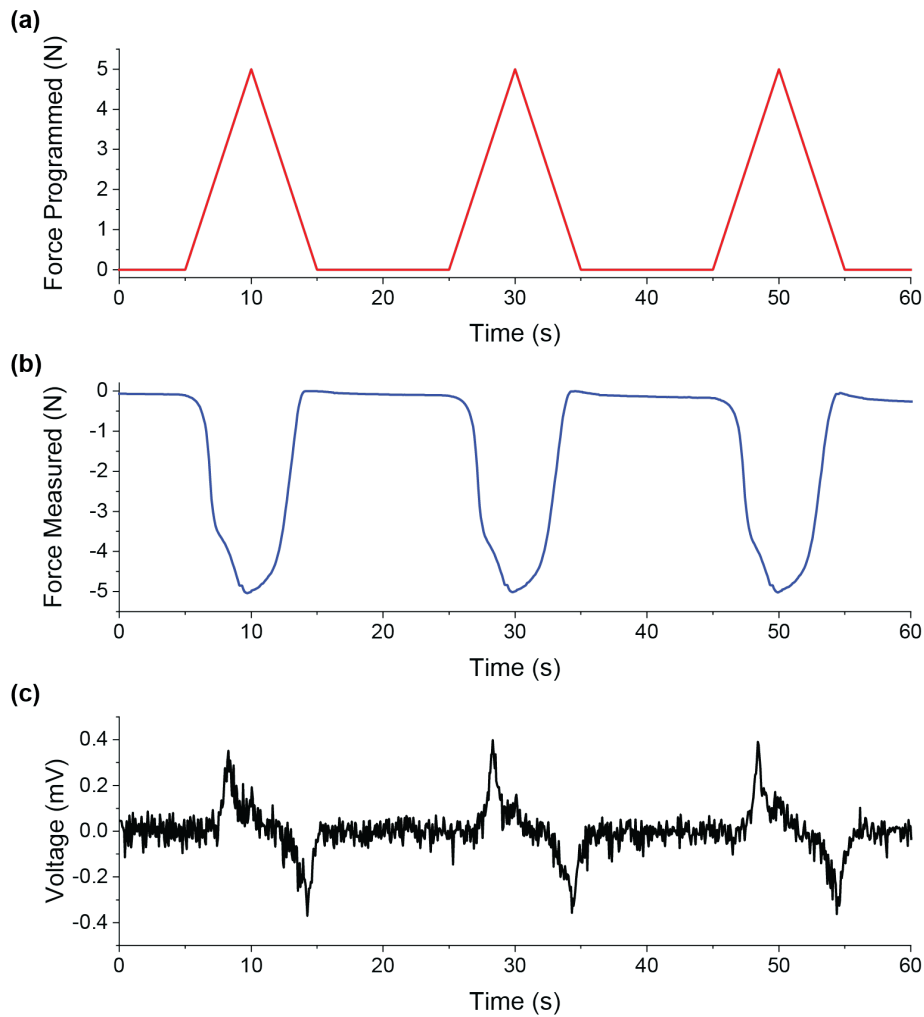


Figure 6.10 Example data showing details of the force sensor measurements. (a) Programmed compressive force waveform. (b) Actual force applied to sample. (c) Output voltage data from sample (zinc electrodes, in this example).

Figure 6.9(e) shows the clear presence of hysteresis in the carbon electrode samples, as evidenced by the varied sample response as the applied force is cycled. This might be caused by the performance characteristics of the carbon ink, as some piezoresistive may be present in the carbon electrode films. Such a theory is supported by the lack of hysteresis in the zinc-electroded devices as well as literature precedent of the piezoresistive effect in carbon inks.²⁸⁷ Further studies should be conducted to assess the source of this hysteresis to improve device performance through its reduction. With device responsivities determined, a matrix of such devices could be utilized to determine force applied by measuring the output voltage from a practical implementation.

Future improvements of these systems will look to improve the signal of these force sensors, and work to correct any signal distortions caused by conflating factors such as sample heating or variations in ambient humidity conditions.

6.5 Actuating Demonstration: Acoustic Speaker

By exploiting the inverse piezoelectric effect, we demonstrate the potential for this technology in an actuating application through the development of a printed green speaker. While prior works have demonstrated the potential for printed piezoelectrics in acoustic applications, none have yet realized a fully degradable piezoelectric speaker, much less one with such adaptability as provided by printed electronics.^{288–291} We elected to demonstrate this through the development of a speaker driver, which was even further implemented into degradable pair of personal headphones (Figure 6.11(a)).

All components including all adhesives, all contact wires, the headphone body, and the ear cushions were made from eco-friendly materials. The piezoelectric buzzer was comprised of the previously fabricated printed capacitor structures, integrated onto a cardboard backing plate, and sealed below a paper membrane (implemented to improve acoustic coupling). These buzzers were then evaluated for their acoustic response before being integrated into the 3D printed headphone body. A more detailed depiction of the assembly process can be found in Figure 6.12 (actuators) and Figure 6.13 (headphones).

Cardboard backing (550 g/m^2), was laser cut to form the backing plate and membrane support rings for use in piezoelectric buzzers. The piezoelectric devices were then adhered to the backing plate using non-toxic polyvinyl acetate (PVA) adhesive. Electrical interconnects are then made between devices using the carbon ink via stencil printing. Ink drying occurred under ambient conditions for 30 min. The tissue membrane (20 g/m^2) was tensioned across a frame and adhered to the membrane support rings using the PVA adhesive. The membrane was then attached to the backing plate with the same adhesive and allowed to cure in ambient conditions for a minimum of 1 hour. The headphone chassis was 3D printed from non-toxic polylactic acid (PLA) filament using a Raise3D E2 dual-extruder FDM Printer. The 3D model was adapted from a design produced by Shannon Ley. The earphone cushions were hand-sewn using cotton fabric and natural cotton stuffing. Cushions were attached via natural cotton yarn in lieu of adhesive (to allow for removal).

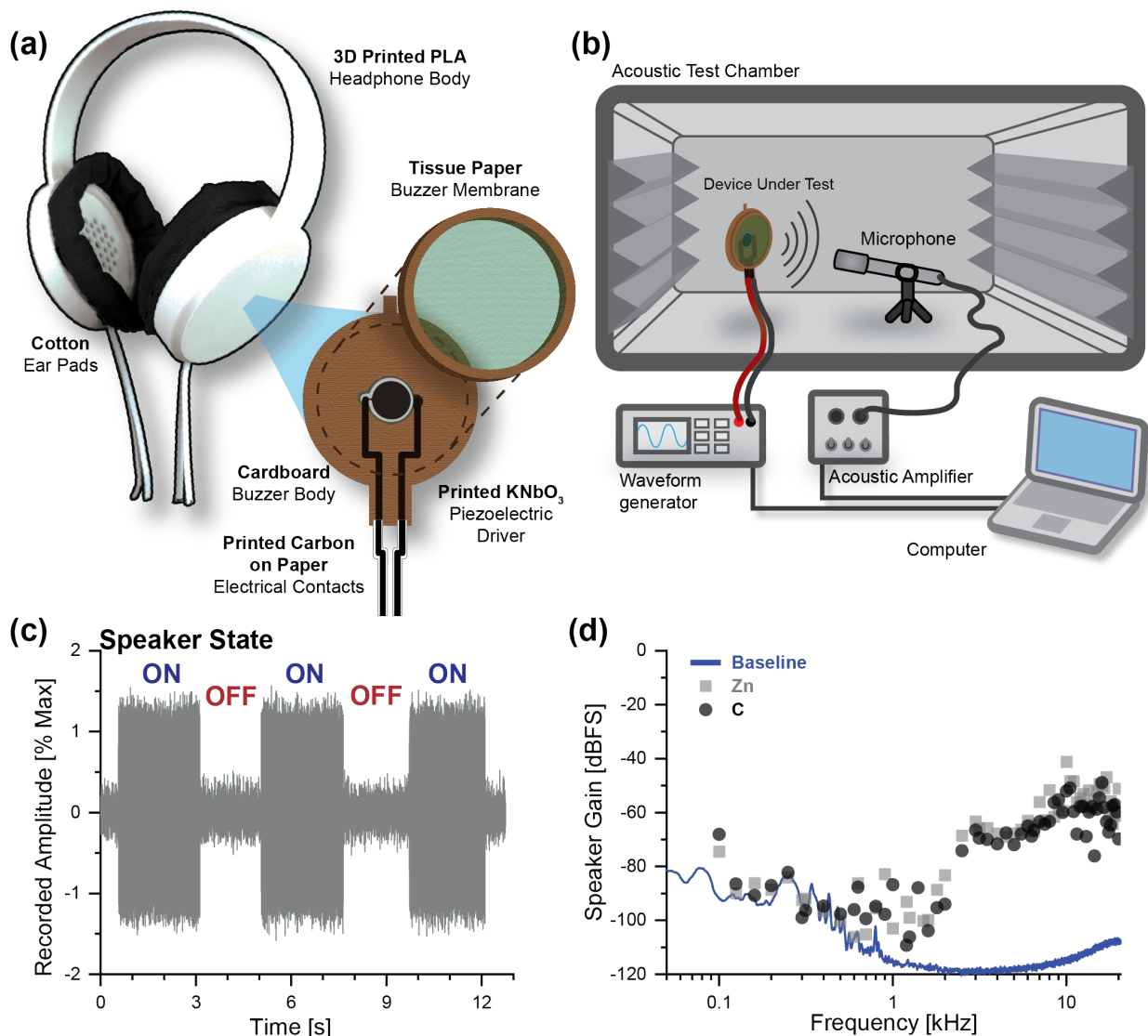


Figure 6.11 Fully degradable headphones demonstration. a) A schematic showing the final headphones, including the 3D printed chassis as well as the screen printed, green acoustic driver. b) A schematic of the test environment used to evaluate speaker response. c) Recorded signal amplitude as the speaker is cycled on and off, when actuated at 10 kHz. d) Acoustic periodogram showing response of speakers as a function of frequency relative to the ambient baseline noise level.

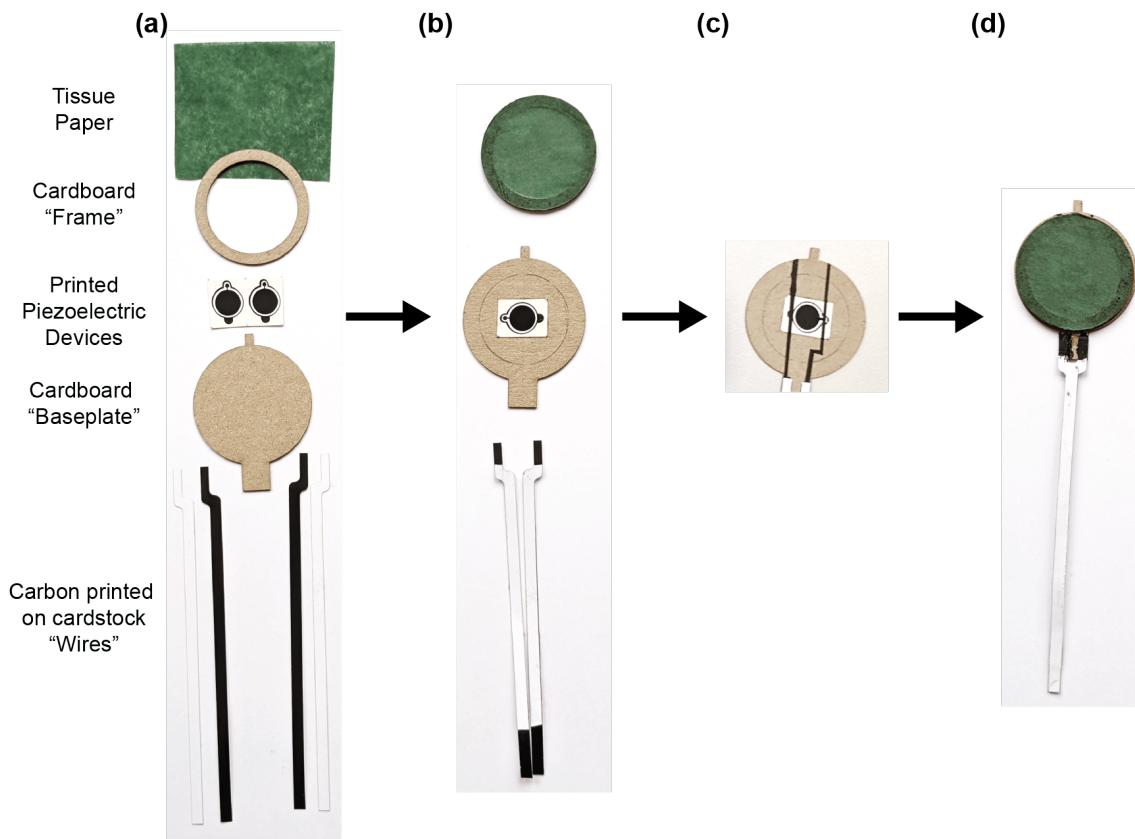


Figure 6.12 Assembly of degradable piezoelectric buzzers showing the four phases of fabrication. (a) Materials preparation. (b) Subcomponent assembly. (c) Printing of contact traces. (d) Final assembly.

In Figure 6.11(a), we depict the fully assembled headphones, with an inset describing the buzzer inside the device. Speaker characterization was conducted using a Sennheiser MKH 416-P48U3 microphone via a Steinberg UR mk II USB Audio Interface. Speaker drivers were actuated using a Digilent Analog Discovery 2 via the waveform generator functionality, with a set signal amplitude of 5 V. All audio data was recorded via Audacity with a sampling rate of 44.1 kHz and processed in Origin. Laser Doppler vibrometry was conducted using a Polytec MSV-400 microscope scanning vibrometer utilizing a VD-06 velocity decoder.

To produce the periodogram data for each speaker, the following process was implemented. First, the samples were installed in the acoustic test chamber, at a distance of 10 mm from the recording microphone. With the chamber sealed, the ambient noise was recorded for a duration of 30 s to establish the environmental baseline noise level for the test. Next, the speaker was actuated at a discrete frequency between 0.1–20 kHz, and the resulting audio recorded for a duration of 30 s. This process was repeated for a set of frequencies selected using a conventional A-weighting table. Each audio file was trimmed to be precisely 10 s in duration, and an FFT was taken of each. The speaker gain at each set test frequency could then be extracted from the corresponding FFT, and compared to the ambient baseline to establish the performance of the speaker.

Figure 6.11(b) shows a schematic depiction of the acoustic test chamber utilized to evaluate the response, including the mounted buzzer, recording microphone, and periphery electronics used to conduct testing. Figure 6.11(c) shows the recorded audio waveform as the speaker is cycled between an On and Off state of actuation at 10 kHz. The increase in response as the speaker is turned on is qualitatively significant.

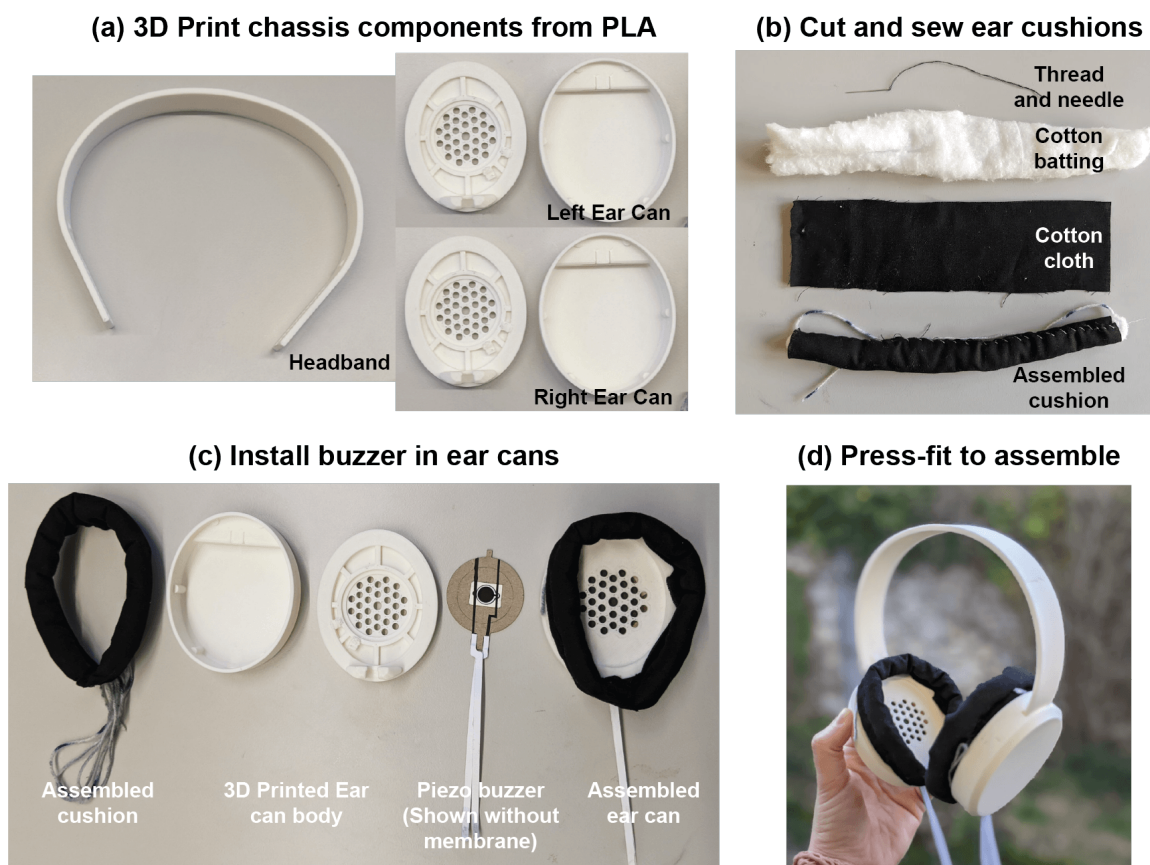


Figure 6.13 Assembly of degradable headphones showing the four steps to assembly. (a) 3D printing of headphone chassis. (b) Preparation of headphone cushions. (c) Installation of piezoelectric buzzer into ear cans. (d) Final assembly via press-fitting.

As a means of further quantifying the response of speakers, the relative sound amplitude at set discrete frequencies was measured and compared to the ambient noise floor of the testing environment. The resulting periodogram is plotted in Figure 6.11(d). Though the speaker response for both zinc electrode and carbon electrode buzzers was difficult to evaluate in the frequency range below 1 kHz, both types of devices showed a significant gain in the range from 2–20 kHz, being around 40–60 dB above the baseline in this frequency range. The periodogram further depicts a reasonably flat response in this frequency range, as is traditionally desirable for acoustic applications. Figure 6.14 includes Laser Doppler Vibrometry data depicting the displacement of the buzzer membranes over the range from 0.1–20 kHz. This sound level amplitude is comparable to the 30 dB reported by Kim for their ElectroActive Paper speakers (fabricated from bulk processing of piezoelectric cellulose), one of the few examples of paper-based piezoelectric speakers reported to date.^{189,290} In the only other reported instance of a green piezoelectric used in speaker applications, the same team reported on chitin film-based speakers with amplitudes of approximately 60 dB under similar operating conditions.¹⁹¹ Yet none of these works utilize fully green components for their electrode materials.

The simple architecture of this demonstrator shows great promise for degradable acoustic devices. Further optimization of both the printed piezoelectric capacitor shape as well as the housing design could provide significant improvements in acoustic performance. Future works will look to evaluating the progress that could be made to increase the speaker gain, particularly in the low frequency range, as well as evaluate methods to improve device efficiency at low actuation voltages to be compatible with conventional sound systems. In this sense, the adaptability and flexibility of a fully printed piezoelectric platform opens the door to novel architectures for piezoelectric drivers, a deviation from the current conventional drives which are constrained to simple disk shapes not optimized for all acoustic applications.

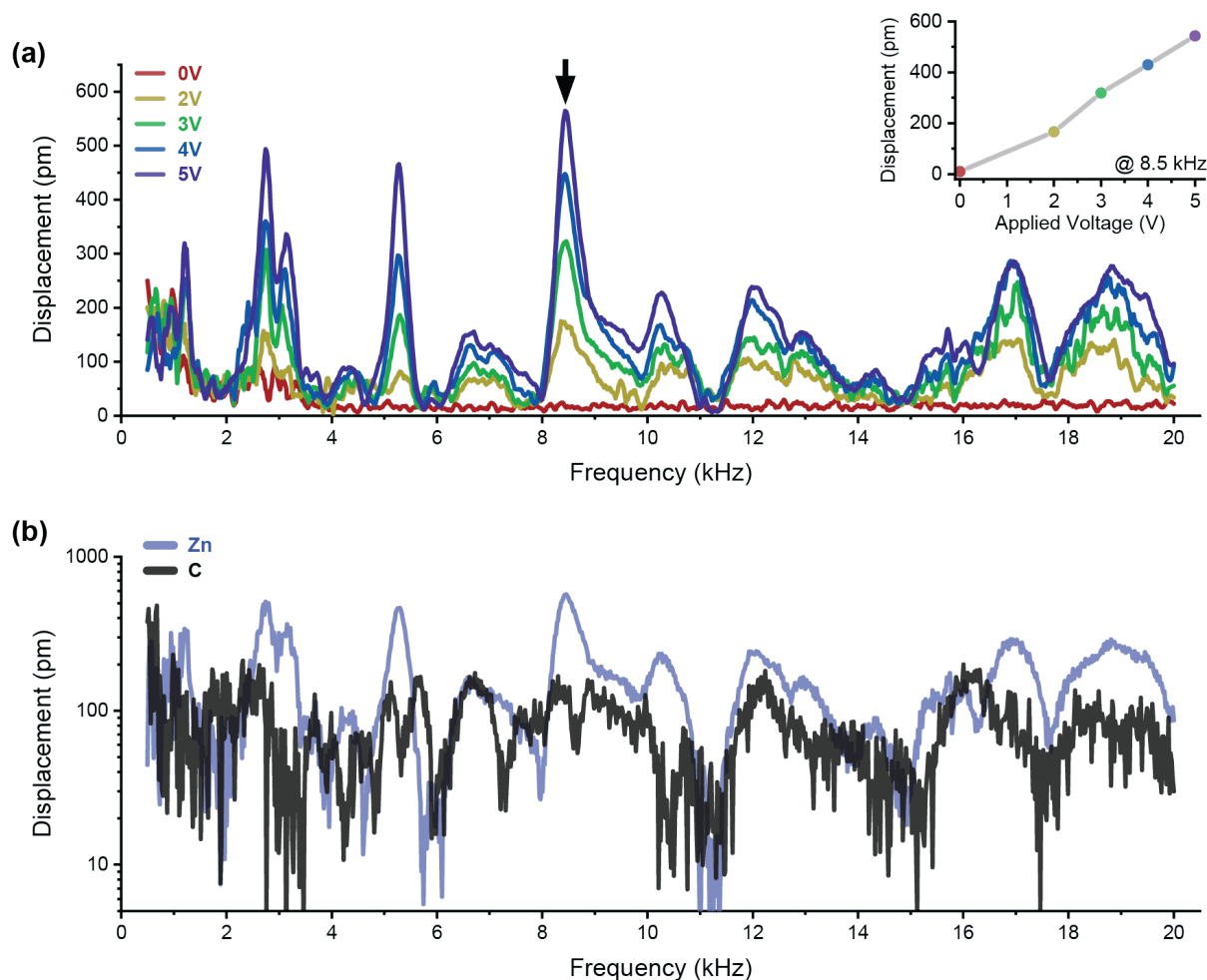


Figure 6.14 Displacement of a speaker membranes as measured using Laser Doppler Vibrometry in the auditory frequency range. (a) As a function of frequency and actuating voltage for a sample with zinc electrodes. Inset shows membrane displacement as a function of actuating voltage at 8.5 kHz. (b) With comparison between speakers using zinc or carbon electrode materials, when actuated at 5 V. The effective active area of all measured speakers was 150 mm².

6.6 Summary and conclusions

In this work, a process was developed to manufacture the first ever instances of fully printed degradable piezoelectric microsystems, through the integration of printed degradable conductors with a printed piezoelectric layer comprised of potassium niobate, KNbO₃, processed at low temperature on paper substrates. The process was established for two different degradable conductive inks, one utilizing carbon, and another utilizing zinc as the primary conductive components, and involved adapting the different printed layers to realize fully printed piezoelectric devices. The optimized process achieved a high fabrication yield of homogeneous devices, with printed active surface areas as large as 60 mm². Device characterization and analysis showed the viability of both zinc and carbon printed layers for use as degradable electrodes in KN based piezoelectric systems. Piezoelectric performance with the printed electrode was optimized for each type of device as a function of poling field, achieving effective piezoelectric coefficients of 5.1 ± 0.8 pC/N with zinc electrodes and 4.6 ± 0.2 pC/N with carbon electrodes. Preliminary degradation studies showed promising results for both zinc and carbon electrode devices, with samples in compost losing nearly 50% of device mass in less than 2 months, and more than 70% of mass lost when degraded in soil at 60 °C in the same time period.

This investigation culminated with the manufacture of two types demonstrator devices, one each to highlight the sensing and actuating potential of the technology through the direct and inverse piezoelectric effect respectively. A matrix of force sensors was fabricated using both zinc and carbon electrode materials, and the response of each determined in the typical force range for touch sensing applications. Taking advantage of the actuating capability of the printed piezoelectric

devices, we have demonstrated the first-ever acoustic speaker system fully made of degradable materials, including both the piezoelectric sound driver as well as an eco-friendly 3D printed headphone casing. Speaker drivers comprised of printed KN piezoelectric capacitors using either zinc or carbon electrodes in paper housings were evaluated for their acoustic performance in the auditory range of 50 Hz–20 kHz. Drivers with both electrode types showed peak performance in the range from 2–20 kHz, showing a relative gain of 40 dB above the ambient noise level, and with an open door for improved performance as designs are optimized for acoustic applications. Future developments would aim to improve the piezoelectric performance of the printed devices, as well as integrate this technology into more advanced forms of printed MEMS devices. This work paves the way for future implementation of such processes towards higher complexity and more sustainable piezoelectric devices and systems.

Chapter 7 Conclusions and outlook

The goal of this thesis was developing greener technologies for piezoelectric microsystems, working towards the reduction of harmful electronic waste. This was achieved through the utilization of eco-friendly materials and the integration of those materials with more sustainable additive manufacturing processes.

To this end, this thesis explored the field of printed green piezoelectric microsystems, covering various aspects from ink formulation to device fabrication and characterization. The research undertaken in this study has worked to advance our understanding of the capabilities and potential applications of such systems. By developing a non-toxic KNbO_3 -based ink screen printable at low temperatures, this thesis demonstrates the feasibility of printing eco-friendly piezoelectric materials, opening up alternative avenues for fabricating piezoelectric devices on degradable substrates. By integrating this process with printed conductive layers composed of carbon or zinc, entirely printed degradable piezoelectric devices are realized for the first time. This work closes with demonstrations of device functionality by fabricating both sensing and actuating piezoelectric devices in the form of a force sensing touch pad matrix and an acoustic driver that was then integrated into an entirely green headset.

7.1 Summary and conclusions

With each step of the development process, this thesis focused on addressing the challenges presented in the introduction of this work. Herein, the works and advancements of each phase are summarized along with the achievements made towards the end goal.

7.1.1 Materials selection

In the early stages of this thesis, materials for use in both the end-goal fully printed devices as well as in the piezoelectric ink are identified. Paper was selected as the degradable substrate material due to its comparatively high thermal limit of approximately $150\text{ }^\circ\text{C}$, and zinc- and carbon-based inks were identified as promising candidates for printed degradable electrode materials. By selecting these materials early in the process, their limitations could be considered during the development of a piezoelectric ink. This thesis also identifies green or sustainable binding agents for use in ink development, with preferred ingredients including PVP or ethyl cellulose binders and water or pentanol solvents.

Next, several potential piezoelectric functional materials identified in literature as showing promise for this application were evaluated for use in printing processes. Feasibility studies on degradable piezoelectric materials were conducted before turning the focus to non-toxic perovskites as an alternative.

This work found that rochelle salt and ammonium dihydrogen phosphate were too unstable for use in practical applications, and their inconsistent crystallization behavior introduced huge challenges with regards to reproducible printing processes. Though zinc oxide was printable, particle orientation during deposition was an immense challenge. Initial studies proposed some pathways towards resolving this issue through dielectrophoresis or using specially fabricated nanoflakes, but were not continued during this thesis. Following this, a screen-printable ink using hydroxyapatite as the functional material was developed, but crystallinity analysis proved the material was not in a piezoelectric phase of matter, and thus this pathway was not continued.

The focus turned to a non-toxic perovskite, potassium niobate (KNbO_3). Before diving deeply into KN process development, barium titanate (BaTiO_3) was used as a proxy material to confirm the viability of fabricating screen-printing

devices on degradable substrates as well as to demonstrate the feasibility of poling printed devices at low temperatures. Both validation experiments proved successful, with a measureable piezoelectric response achieved for BaTiO₃ samples printed on paper substrates that had been poled in ambient conditions.

The chapter ends with initial development of a stencil-printable KN ink. Solvent and binder materials for use with KN were down-selected, and then ball milling processes utilize to reduce the particle size of the source powder, enhancing the stability of the ink. This thesis confirms the potential of this ink by fabricating capacitive devices using the ink as the functional dielectric layer. Through powder diffraction, the piezoelectric nature of the KN powder used in this ink is confirmed. With this series of proof-of-concept investigations conducted, KN was selected as the piezoelectric material for further development, using ethyl cellulose and pentanol as the binding agent and solvent respectively.

7.1.2 Printing process development and performance improvement

In the next phase of development, this thesis further develops the ink initially established in the previous section, working to improve both the print quality and repeatability as well as the electric characteristics of capacitive devices fabricated with the ink.

To begin, the three primary manufacturing phases for device manufacture are described: KN powder preparation, ink mixing, and device fabrication. This work next details a validation experiment, fabricating and characterizing a series of capacitive devices to serve as a reference for further developments. In this benchmark, devices stencil printed in glass substrates exhibited a piezoelectric coefficient as high as 2.0 pC/N in layers 20 ± 10 μm thick.

This benchmark was followed first with a series of investigations focusing on printing performance, looking to improve process repeatability and device yield. By studying the influence of KN particle size and the associated grinding parameters, where dramatic advances in layer quality were made by improving the homogeneity of the powder used in ink preparation. The printing process was then transferred from stencil- to screen-printing, through which the printed thickness was reduced from 20 μm to just 6 μm per layer, with a reduction in average surface roughness and the potential to print multiple layers for added adaptability of device thickness. Next, the influence of ink composition on print quality and layer adhesion is studied, establishing a limit to the quantity of binding agent that can be incorporated into printed layers before mechanical failure of layers due to residual stresses during drying.

In the next series of studies, this thesis evaluates the influence of various parameters on device dielectric behavior. In studying the influence of KN layer drying temperature on dielectric behavior, a minor improvement in dielectric behavior yet a dramatic reduction in manufacturing time is found when layers are dried at 120 °C for 30 min as opposed to a 12 hour ambient drying condition. Device performance variance due to the influence of electrode parameters is explored, finding minimal influence from electrode material or layer thickness, but significant variance resulting from the device pre-treatment with oxygen plasma prior to top electrode deposition.

In the last round of investigations, this thesis looks into several process parameters for their influence on piezoelectric performance, focusing primarily on the properties of the KN source powder used in the inks. First, the influence of post-grinding annealing on KN powder crystallinity is investigated, where an improvement in powder crystallinity after 4.5 hours of annealing at 625 °C is found. Following this, device performance based on KN source material is studied, looking into how material supplier, purity, and particle size impact dielectric and piezoelectric characteristics. In this work, it was found that 99.999% purity powder supplied by Alfa Aesar, ground and annealed using the developed processes, produced the highest piezoelectric performance of the materials studied. Finally, the effects of grinding parameters such as milling media material and amount of solvent used during grinding on the piezoelectric performance of the resulting devices are assessed, where improvement was found when with using ZrO₂ media as opposed to stainless steel media, and when using 2 mL of IPA per gram of KN as opposed to 3 mL.

In comparison with the devices benchmarked at the beginning of this chapter, the finalized devices can be printed in layers of 6 μm with high reproducibility and device yields >90%. These devices have a measured piezoelectric response ($d_{33,eff}$) as high as 12.4 pC/N when screen-printed on silicon substrates, as compared to the 2.0 pC/N achieved with the benchmark samples, showing remarkable improvements through the course of this development process. With these improvements

in processing and performance, it was determined that further device integration onto degradable substrates could be implemented.

7.1.3 Low temperature processes on degradable substrates

The next phase of work in this thesis involved the integration of the KN ink and printing process developed above onto degradable paper substrates, with a focus on evaluating device performance and characteristics when fabricated on paper as compared to more conventional silicon substrates.

This section begins with a discussion of device design for two forms of devices: circular capacitive structures comparable to those utilized in the previous chapter, as well as more complex cantilever structures intended for characterizing the transverse piezoelectric coefficient, $d_{31,eff}$, for samples on both silicon and paper. This is followed with a discussion of the fabrication process for both device architectures on the two substrate materials.

With devices fabricated, the properties of the utilized ink are characterized, including particle size distribution, ink rheology, and printed layer properties such as film density, thickness, and surface roughness. Printed layers on paper and silicon were comparable in thickness, $11.2 \pm 0.2 \mu\text{m}$ for structures on paper and $10.7 \pm 0.2 \mu\text{m}$ for samples on silicon, however surface roughness of the layers on paper was significantly higher than that for layers on silicon ($1.1 \pm 0.3 \mu\text{m}$ on paper, $0.4 \pm 0.1 \mu\text{m}$ on silicon), to be expected as the initial roughness of the paper was also greater. In characterizing the dielectric properties of the devices, good agreement is again found across different substrates, with the relative permittivity of samples on paper and silicon substrates determined as 29.3 ± 0.1 and 29.5 ± 0.2 respectively.

With regards to piezoelectric response, a thorough investigation was conducted to assess the influence of poling parameters on piezoelectric response. It was found that poling times > 0.5 min were sufficient to achieve $>80\%$ of the maximum value, and applied poling fields of $20\text{--}30 \text{ V}/\mu\text{m}$ exhibited the largest piezoelectric response. The transverse piezoelectric coefficient, $d_{31,eff}$, determined from this evaluation were significantly lower than expected for samples on either substrate, and further studies are needed to diagnose the source of this behavior.

The study ends with a comparison of the longitudinal piezoelectric coefficient, $d_{33,eff}$, for samples on either substrate. The average piezoelectric coefficient for samples printed on paper substrates was $d_{33,eff,paper} = 13.6 \pm 2.8 \text{ pC/N}$ as compared to those printed on silicon, $d_{33,eff,Si} = 10.0 \pm 1.7 \text{ pC/N}$. The highest attained $d_{33,eff,max}$ was 18.4 pC/N on paper substrates and 13.3 pC/N on silicon substrates.

7.1.4 Integration of screen-printed KNbO_3 with printed degradable electrodes and integration into demonstrator devices

In the culminating section of this thesis, the previously developed KNbO_3 process printed on degradable substrates is transitioned to an entirely printed process by substituting the thermally evaporated gold electrodes for screen printed zinc or carbon electrodes, achieving the stated goal of this thesis.

The section begins with initial process development studies. After identifying issues related to device configuration that cause shorting across the electrodes, an alternative device layout is prepared to circumvent the issue. Next, the processes used to manufacture fully printed devices are elaborated, detailing the preparation of KN and Zn inks, and any post-processing steps required for the device layers. Here, the two-step Zn film sintering process and its challenges are discussed, then optimized to achieve conductive Zn layers without compromising the functionality of other device components. The finalized process developed was highly reproducible for printed capacitor devices with functional areas as large as 60 mm^2 .

Following fabrication, device characteristics were analyzed and the influence of electrode material on device performance was assessed, studying how printed electrodes composed of carbon or zinc printed layers as compared to thermally evaporated gold electrodes that had been used up to this point. It was found that the measured relative permittivity of the zinc-electroded devices deviated from the measured values for carbon- or gold-electroded devices by nearly 40%, potentially due to incomplete sintering of the Zn top electrode.

Piezoelectric characterization found the gold-electrode devices to have piezoelectric coefficients, $d_{33,eff}$, as large as 11.6 ± 0.8 pC/N, while the zinc- and carbon-electrode devices had maximum coefficients of 5.1 ± 0.8 and 4.6 ± 0.2 pC/N respectively. It was hypothesized that this reduction in effective piezoelectric coefficient is due to clamping from the printed electrodes that is not observed with the significantly thinner evaporated gold electrodes. Preliminary degradation studies showed promising results for both zinc and carbon electrode devices, with samples in compost losing nearly 50% of device mass in less than 2 months, and more than 70% of mass lost when degraded in soil at 60 °C in the same time period.

With process development and characterization completed, the final portion of this thesis involved the implementation of the manufacturing process to develop demonstrator devices aimed to showcase the applicability of the technology in real world applications. To this end, two forms of demonstrators were designed and fabricated: a force sensing touchpad, and an acoustic actuator. Both demonstrators were composed entirely from degradable and green materials, and verified their functionality through standard characterization mechanisms. To date, this marks the first example of fully printed eco-friendly piezoelectric devices for practical applications.

7.2 Outlook

With the establishment of this highly reproducible fabrication process for eco-friendly fully printed piezoelectric devices, one could imagine a broad range of future works, focused on the various aspects of the development process. This includes materials development, novel printing or dipole orientation methods, ink optimization for piezoelectric response, as well as development and characterization of more complex piezoelectric devices and studying their degradation mechanisms.

Piezoelectric materials and manufacturing. Further development of materials and manufacturing can come in many forms. In a logical next step, the KN printing process can be transitioned to KNN, which is expected to have a greater piezoelectric response than KN. The degradation of KN (and KNN) must be empirically evaluated, and full life-cycle analyses conducted on all device component materials. Studying the whole lifecycles of perovskite materials can help identify viable alternates for KN and improve overall device sustainability. Alternatively, naturally occurring perovskite materials such as CaTiO_3 or MgSiO_3 could be used in place of KN for even greener piezoelectric devices.

Further research into printing processes for the initially screened degradable piezoelectric materials could involve the development of novel manufacturing methods for oriented printing of these materials to achieve a measurable piezoelectric response in the deposited layers. In developing low-temperature compatible methods for dipole orientation of printed piezoelectrics, the library of viable green materials would increase greatly.

On a more challenging front, future work could focus on the development of degradable piezoelectric materials themselves, focusing on achieving large piezoelectric response using first principles theory. By studying the mechanisms of materials degradation as well as the material properties that induce a large piezoelectric response, one could realize a material that exhibits both properties in a predictable manner.

KN process improvement. In the development and optimization of a printing process for potassium niobate, a wide range of factors influencing print quality and device performance were evaluated. In doing so, several pathways were identified for further process improvement. One could imagine an in-depth study of ink composition, looking to optimize piezoelectric response based on component materials and their proportions. Associated with this would be a study of the KN material used for ink preparation: studying optimum particle size, purity, and dopant chemicals for maximum piezoelectric response. More in-depth studies could be conducted to assess the influence of printed electrodes on effective piezoelectric response, and identify (or develop) other degradable printed conductors to improve this. Along with this, further work could be done to modify electrode ink formulation to reduce the detrimental clamping effects through improved mechanical behavior or thinner conductive layers.

Alternative work could focus on improving the transverse piezoelectric response of printed KN films, as these initial studies found this characteristic to be significantly lower than expected values based on longitudinal piezoelectric

coefficients. This would involve first diagnosing the reduced response, then studying methods to compensate for this. For example, one could look to improve the piezoelectric response of printed layers through post-processing methods. A ceramic sintering method compatible with degradable substrates could dramatically improve piezoelectric response of printed layers. This could be realized through chemical or photonic sintering, perhaps with some modification of the ink component materials for sintering temperature adjustment.

In another direction, works could focus on process transfer to other printing methods such as inkjet or 3D printing, to expand the toolkit with which green piezoelectric devices can be fabricated. With a low temperature process, transferring the process to other green substrates, such as PLA or silk, is possible. Taking advantage of the mechanical properties of such substrates permits a wider variety of device applications. In another direction, a more universal process could be developed to accommodate for the diversity of substrate materials.

From a practical perspective, studies could be conducted to establish the lifetime of functional devices through degradation studies. Indeed, even the development of a standard testing protocol for degradable electronics has yet to be developed. This concept could be further developed with the implementation of encapsulation layers, which could be used to tune device lifetime for use in a wider range of applications. Encapsulation would have the further benefit of reducing the effects of environmental conditions (e.g., humidity, soil chemistry, etc.) on device performance, and optimizing the encapsulation material and properties for stable performance will be critical for widespread use of such degradable technologies. Printed films of ethyl cellulose and beeswax have shown promise for this application in other degradable electronics, and could be implemented here as well. One could imagine engineering a device with a specific functional lifetime by tuning the encapsulation thickness appropriately.

Device development. The successful fabrication of fully printed piezoelectric devices on paper substrates opens the door for a wide range of future studies towards realizing more intricate green electronics. Stemming from the demonstrated sensing and actuating devices, more complex devices and systems could be realized. Resonating sensors could be developed for use in such applications as gas or biological sensing, either using the previously developed cantilever architectures or designing more specialized structures based on intended use case. Alternatively, one could imagine the addition of a degradable communications block for wireless data transfer, entirely fabricated on a cardboard package, for smart shipping applications. The realm of higher complexity printed degradable devices is broad, and has huge potential for further improvement with the addition of degradable printed piezoelectrics into the toolbox.

From a different angle, one could work to scale up these fabrication methods, and quantitatively evaluate the impact of this manufacturing process on the environment. In doing so, sources of material waste, high energy consumption, or toxic chemical usage can be identified and mitigated for a product that is green in every aspect.

7.3 Closing remarks

In this work, this thesis has realized the first ever fully printed eco-friendly piezoelectric device on paper substrates. This began with materials selection, followed by ink development and process improvements. With robust printing methods, the process was transferred onto degradable paper substrates. Finally, printed degradable electrodes were integrated with the process to manufacture demonstrator devices entirely made from green components for degradable piezoelectric applications.

This work continued iteratively through these successive process steps with the primary goal ever in mind: the development of greener technologies as alternatives for environmentally harmful forms of electronic waste. This work has not only contributed to the body of knowledge in this emerging field but also paved the way for the development of innovative, sustainable, and eco-friendly electronic devices that can be integrated into our daily lives. It is strongly believed that, while there is still a long road ahead to reach this goal, the body of work described in this thesis will serve as a stepping stone down the correct path for future researchers to follow.

Chapter 8 Appendix

8.1 Appendix A: Library of Green Materials

Table 8.1 Summary table of green materials, including those reported in literature to be degradable, bioresorbable, transient, or otherwise green, with notes regarding common applications and degradation mechanisms. Fields in yellow annotated with an asterisk (*) indicate that this claim is disputed. Empty fields indicate that the status is unknown.

Material	Mat'l class	Substrate	Insulator	Conductor	Semiconductor	Piezoelectric	Degradable	Bio-compatible	Bio-resorbable	Printing precedent	Degradation method(s)	Ref
Actin	Polymer / Organic					y	y	y	y	y	Enzymatic, Hydrolysis	90
ADP (NH ₄ PO ₄)	Polymer / Organic					y	y			n	Hydrolysis	108
Al ₂ O ₃	Inorganic	y	y				y*	y		y	Inert, Acid-soluble	9,21,222,292
Albumin (egg whites)	Polymer / Organic	y					y	y	y		Enzymatic	27,293
Alginate	Polymer / Organic		y				y	y				21
AlN	Inorganic				y	y		y		n		58,61-63
Anthraquinones	Polymer / Organic				y		y					27
AZ31B Mg alloy	Inorganic			y			y					32
BaTiO ₃	Perovskite					y		y		y		58
BaTiO ₃ Composites	Composite					y	y*	y		y		154,294-296
BNT ((Bi,Na)TiO ₃)	Perovskite					y		y				58
BZT-BCT	Perovskite					y		y				58
Caffeine	Polymer / Organic	y					y	y	y	y	Enzymatic	27,297,298
Calcium Phosphates	Inorganic		y				y	y	y*			17
Caramelized glucose	Polymer / Organic	y					y	y	y			27,297
Carbon nanotubes (CNTs)	Polymer / Organic			y			y*	n	n	y		
CaTiO ₃	Perovskite					y		y		n		73
Cellulose	Polymer / Organic	y				y	y	y	y*	y	Enzymatic (certain bacteria)	99,189,228,299
Cellulose nanofibril paper	Polymer / Organic	y					y				Enzymatic (certain bacteria)	15
Chitin	Polymer / Organic					y	y				Enzymatic, Hydrolysis	95,191
Chitosan	Polymer / Organic			y		y	y	y	y		Enzymatic	27,297,300
Clarifoil™ (Cellulose Diacetate + others)	Polymer / Organic	y					y				Enzymatic (certain bacteria)	
Collagen (ex: bone, tendon)	Polymer / Organic	y				y	y	y	y	y	Enzymatic	58,68,88,89
Collagen-Hydroxyapatite	Composite					y	y	y				88
cPPA	Polymer / Organic	y					y				Acid-soluble	15
DDFTTF (5,5'-bis-(7-dodecyl-9H-fluoren-2-yl)-2,2'-bithiophene)	Polymer / Organic				y		y					27,297
Dibutyl sebacate (C ₁₈ H ₃₄ O ₄)	Polymer / Organic						y				Several. See reference	
DNA	Polymer / Organic					y	y	y	y	y	Enzymatic, Hydrolysis	68,80
DNA - adenine	Polymer / Organic	y				y	y	y	y	y	Enzymatic, Hydrolysis	27,80,297
DNA - guanine	Polymer / Organic	y				y	y	y	y	y	Enzymatic, Hydrolysis	27,80,297
Ecoflex™ (Corn starch+PLA)	Polymer / Organic	y					y					27,297
Elastin	Polymer / Organic					y	y	y	y	y	Enzymatic, Hydrolysis	90
Fibrin	Polymer / Organic					y	y			y	Enzymatic, Hydrolysis	95
GaN	Inorganic				y	y	n	y		n		58
Gelatin	Polymer / Organic	y					y	y	y	y		27,297,301,302
Germanium, Ge	Inorganic				y		y	y	y	y	Hydrolysis	16
Glucose	Polymer / Organic	y					y	y	y			27,297

Material	Mat'l class	Substrate	Insulator	Conductor	Semiconductor	Piezoelectric	Degradable	Bio-compatible	Bio-resorbable	Printing precedent	Degradation method(s)	Ref
Glycine	Polymer / Organic					y	y	y		y	Enzymatic, Hydrolysis	58
Gold, Au	Inorganic			y			y [†]	y	n	y	Inert	39,222
Graphene	Polymer / Organic			y		y	y	y	y	y		58,227,303
Hydroxyapatites (ex: bone)	Inorganic	y				y	y	y		y		68,89
Indanthrene brilliant orange RF	Polymer / Organic				y		y	y				27,297
Indanthrene yellow G	Polymer / Organic				y		y	y				27,297
Indigo (organic)	Polymer / Organic				y		y	y [†]				27,297
Iron, Fe	Inorganic			y			y [†]	y	y	y	Hydrolysis	32
KN (KNbO ₃)	Perovskite					y	Non-toxic	y		n		16,53,58,61,62
KNN ((K,Na)NbO ₃)	Perovskite					y	Non-toxic	y		y		295
KNN-PDMS	Composite					y	n	y		y		27,297
Lactose	Polymer / Organic	y					y	y	y			304
Leather	Polymer / Organic	y					y					58
LiNbO ₃	Perovskite					y		y				14
Liquid crystal polymers (LCs)	Polymer / Organic		y				n	y	n			32
Lithium Iodate (LiIO ₃)	Inorganic					y	y				Hydrolysis	15
Magnesium, Mg	Inorganic			y			y	y	y	y	Hydrolysis	73
MBTT / cPPA	Polymer / Organic	y					y				Acid-soluble	32
MEH-PPV (poly[2-methoxy-5-(2-ethyl-hexyloxy)-1,4-phenylene vinylene])	Polymer / Organic			y				y		y		90
Melanin	Polymer / Organic			y			y	y	y			17
Methyl cellulose	Polymer / Organic	y					y	y	y		Enzymatic	305
MgO	Inorganic		y				y	y			Hydrolysis	222
MgSiO ₃	Perovskite					y		y				95,99
Molybdenum, Mo	Inorganic			y			y	y	y	y	Hydrolysis	17,98
Myosin	Polymer / Organic					y	y	y	y	y	Enzymatic, Hydrolysis	17,27
Na-CMC (Sodium carboxymethyl cellulose)	Polymer / Organic	y					y	y	y		Hydrolysis	14,307,308
Natural rubber latex (cis-1,4-polyisoprene + others)	Polymer / Organic	y					y				Enzymatic (certain bacteria)	93,99,309
Ni-Ti Alloys	Inorganic			y			n [†]	y	n [†]			15,17,80,910
Nylons (Polyamides)	Polymer / Organic	y					y				Enzymatic (certain bacteria)	8,99,227,310
P4HB (Poly-4-hydroxybutyrate)	Polymer / Organic		y				y	y	y		Hydrolysis	93,309
PAni (Polyaniline)	Polymer / Organic			y			y	y	y	y		310,311
Parylene-C (Poly(dichloro-p-xylylene))	Polymer / Organic		y			y	n [†]	y	n [†]			14,103
PBS (Polybutylene succinate)	Polymer / Organic	y					y				Enzymatic (certain bacteria), Hydrolysis	102,312
PCL (Polycaprolactone)	Polymer / Organic	y					y	y	y	y	Enzymatic (certain bacteria), Hydrolysis	310,311
PCL-BS (Poly ε-caprolactone butylene succinate)	Polymer / Organic	y					y				Hydrolysis	17,299
PDLLA (Poly(DL-lactic acid))	Polymer / Organic	y					y	y	y			103,222
PDMS (Polydimethylsiloxane)	Polymer / Organic		y				n	y	n	y [†]		17,80,313,314
PDMS (void-containing)	Polymer / Organic					y	n [†]	y				21
PDO (Polydioxanone)	Polymer / Organic		y				y	y	y			27,297,313,315
PDPP-PD	Polymer / Organic				y		y				Acid-soluble	316,317
PE (Polyethylene)	Polymer / Organic	y					n [†]	y			Enzymatic (certain bacteria)	
PEDOT (Poly(3,4-ethylenedioxythiophene))	Polymer / Organic			y			n [†]	y		y	Hydrolysis	
PEDOT-HA (Hyaluronic acid doped PEDOT)	Polymer / Organic			y			n [†]	y				
PEDOT:PSS (Poly(3,4-ethylenedioxythiophene):poly(styrene sulfonate))	Polymer / Organic			y	y		n [†]	y		y		
PEF (Poly(ethylene furanoate))	Polymer / Organic		y									

Material	Mat'l class	Substrate	Insulator	Conductor	Semiconductor	Piezoelectric	Degradable	Bio-compatible	Bio-resorbable	Printing precedent	Degradation method(s)	Ref
PEG (Poly(ethylene glycol))	Polymer / Organic		y				y	y [†]	y [†]	y		80
PEG-DT (Polyethylene glycol + desaminotyrosyl-tyrosine) composite	Polymer / Organic		y					y				14
Pentacene	Polymer / Organic				y		y					
Perylene bisimides	Polymer / Organic				y		y					27,297
Perylene diimide	Polymer / Organic				y		y	y [†]				27,297
PES (Polyethylene succinate)	Polymer / Organic		y				y				Enzymatic (certain bacteria)	99
PET (Polyethylene terephthalate)	Polymer / Organic	y					y [†]	y	n		Enzymatic (certain bacteria)	222
PETS (Polyethylene terephthalate succinate)	Polymer / Organic	y					y				Hydrolysis	93,309
PGA (Poly-glycolic acid)	Polymer / Organic	y					y	y	y		Hydrolysis	98,227
PGS (Poly(glycerol-sebacate))	Polymer / Organic		y					y			PBS-Soluble	14
PHB (Poly-β-hydroxybutyrate)	Polymer / Organic					y	y	y	y		Enzymatic, Hydrolysis	95,97-100
PHBHHx (3-hydroxybutyrate and 3-hydroxyhexanoate Copolymer)	Polymer / Organic		y				y	y	y			17,98
PHBV (Poly(3-hydroxybutyrate-co-3-hydroxyvalerate))	Polymer / Organic	y					y	y	y		Enzymatic (certain bacteria), Hydrolysis	17,98,99
PHO (Poly3-hydroxyoctanoate)	Polymer / Organic		y				y	y	y			17,98
PI (Polyimide)	Polymer / Organic		y				n	y	n	y		14,103,318
PLA (Poly(lactic acid))	Polymer / Organic	y					y	y	y	y	Enzymatic (certain bacteria), Hydrolysis	15,17,98,9,9,228
PLGA (Poly(lactic-co-glycolic acid))	Polymer / Organic	y					y	y	y	y	Hydrolysis, Some solvents	14,15,17,8,0,98,228,3,19
PLLA (Poly(L-lactic acid))	Polymer / Organic	y				y	y	y	y		Hydrolysis	58,93-95,98,310,320
PLLA-PPy	Polymer / Organic			y			y					310
PMMA (Poly(methyl methacrylate))	Polymer / Organic	y					y [†]			y	Enzymatic (certain bacteria)	
PMN-PT (Pb(Mg,Nb)O ₃ -PbTiO ₃)	Perovskite					y		n				58
PNTs (peptide nanotubes)	Polymer / Organic					y	y	y		y	Hydrolysis	58,78,321
POC (Poly(1,8-octanediol-co-citrate))	Polymer / Organic	y					y				PBS-Soluble	15
POE (Polyorthoester)	Polymer / Organic		y				y	y	y			310,311
Poly(thiophene)s	Polymer / Organic			y			y [†]	y				27,297
POMaC (poly(octamethylene maleate (anhydride) citrate))	Polymer / Organic	y	y									
PP (Polypropylene) (Void-containing)	Polymer / Organic					y		y				102,222
PPA (Poly-(phthalaldehyde))	Polymer / Organic	y					n [†]				Acid-soluble	15
PPF (Poly(propylene fumarate))	Polymer / Organic		y				y	y	y		Clay-catalyzed	98,322
PPy (Poly(pyrrole))	Polymer / Organic			y			n [†]	y	n	y	Enzymatic, Hydrolysis	17,27,297,323,324
Prestin	Polymer / Organic					y	y	y	y		Enzymatic, Hydrolysis	90
PTFE (Polytetrafluoroethylene)	Polymer / Organic	y					y [†]	y	n			222
PU (Polyurethane)	Polymer / Organic	y					n [†]					13
PVA (Polyvinyl alcohol)	Polymer / Organic	y					y [†]	y	y	y	Enzymatic, Hydrolysis	17,229,230
PVDF (Polyvinylidene fluoride)	Polymer / Organic	y				y	n	y	n			58,102,103
PVDF-TrFE (poly(vinylidene fluoride-co-trifluoroethylene))	Polymer / Organic					y				y		58,95,104,105
PVP (Polyvinylpyrrolidone)	Polymer / Organic	y				y	y	y	y	y	Enzymatic (certain bacteria), Hydrolysis	15,17,80,3,15
PZN-PT (Pb(Zr,Nb)O ₃ -PbTiO ₃)	Perovskite					y		n				58
PZT (Pb(Zr,Ti)O ₃)	Perovskite					y	n	n	n	y		58,61,62,76

Material	Mat'l class	Substrate	Insulator	Conductor	Semiconductor	Piezoelectric	Degradable	Bio-compatible	Bio-resorbable	Printing precedent	Degradation method(s)	Ref
Quartz, SiO ₂	Inorganic	y	y			y	y	y*			Hydrolysis	58,68
Rice paper	Polymer / Organic	y					y	y	y			227
Rochelle Salt (NaK ₂ C ₄ H ₄ O ₆ ·4H ₂ O)	Polymer / Organic					y	y	y	y	y	Hydrolysis	74,325
RS Composites	Composite					y	y					184,186
Shellac	Polymer / Organic	y					y	y				27
Si ₃ N ₄	Inorganic	y	y				y	y	y	y	Hydrolysis	15-17
SiGe	Inorganic				y		y*	y	y		Hydrolysis	16,221
Silicon, Si	Inorganic	y			y		y	y	y	y	Hydrolysis	16,17,227,326
Silicone (Polysiloxanes)	Polymer / Organic		y				n	y	n			14
Silk	Polymer / Organic	y	y			y	y	y	y	y	Enzymatic, Hydrolysis	17,27,58,86
Silver, Ag	Inorganic			y			n*	n*		y	Hydrolysis	39,222
SiO ₂	Inorganic	y	y				y	y	y	y	Hydrolysis	15,21
Stainless Steel 316L	Inorganic			y				y				222
Starch (amylose)	Polymer / Organic	y				y	y				Enzymatic	95
Sucrose	Polymer / Organic					y	y	y	y		Enzymatic, Hydrolysis	68,81
Sugar-based epoxy	Polymer / Organic	y					y					17
Titanium, Ti (commercially pure)	Inorganic			y			y	y	n			222
Topaz	Inorganic					y	y					68
Tourmaline	Inorganic					y	y					68
Tungsten, W	Inorganic			y			y	y	y	y	Hydrolysis	32
Tyrian purple (6,6'-dibromoindigo)	Polymer / Organic				y		y					27,297
UHMWPE (Ultra-high-molecular-weight polyethylene)	Polymer / Organic	y					n	y	n			
Vinyl	Polymer / Organic	y					y					230
Zinc, Zn	Inorganic			y			y	y	y	y	Hydrolysis	32
ZnO	Inorganic				y	y	y	y	y	y	Hydrolysis	16,58,64,65
ZnO Composites	Composite				y	y		y				171,295,327
ZrO ₂	Inorganic		y				y*	y		y	Inert, Acid-soluble	9,103,222
α-keratin (ex: hair, nails, etc)	Polymer / Organic					y	y	y	y		Enzymatic, Hydrolysis	58
β-carotene	Polymer / Organic				y		y					27,297

8.2 Appendix B: Characterization methods

8.2.1 Piezoelectric characterization: Berlincourt method

8.2.1.1 Derivation of effective longitudinal piezoelectric coefficient using Berlincourt method

We assume that the force applied to the reference piezoelectric (ref) and the device under test (DUT) in the z-direction is equivalent.

$$F_{appl,DUT} = F_{appl,Ref} = F_{appl,3} \quad (8.1)$$

We also know that for each piezoelectric device (ref and DUT), the basic response follows

$$D_3 = d_{33} * \sigma_3 \quad (8.2)$$

And the stress can be formulated as

$$\sigma_3 = \frac{F_{appl,3}}{A} \quad (8.3)$$

Making the relationship

$$D_3 = d_{33} * \left(\frac{F_{appl,3}}{A} \right) \quad (8.4)$$

Which can be re-interpreted to find the charge produced during actuation:

$$D_3 * A = d_{33} * F_{appl,3} = Q_{free} \quad (8.5)$$

By placing known capacitors in parallel with each piezoelectric device, we can convert from charge to voltage, which can be measured with an oscilloscope

$$C = \frac{Q_{free}}{V} \quad (8.6)$$

We can thus relate the measured voltage to the applied force for each device according to

$$V = d_{33} \left(\frac{F_{appl,3}}{C} \right) \quad (8.7)$$

We specify that the capacitors used for each device are equivalent:

$$C_{DUT} = C_{Ref} = C \quad (8.8)$$

Which, with the equivalent force assumption in Equation (8.1) allows us to relate the output of the two piezoelectric devices as

$$\frac{F_{appl}}{C} = \frac{V_{DUT}}{d_{33,DUT}} = \frac{V_{ref}}{d_{33,ref}} \quad (8.9)$$

And, since the piezoelectric coefficient of the reference piezo is known,

$$d_{33,DUT} = d_{33,ref} * \frac{V_{DUT}}{V_{ref}} \quad (8.10)$$

Table 8.2 Variables used in derivation of Berlincourt method piezoelectric coefficient $d_{33,eff}$ calculation.

VARIABLE	UNITS	DESCRIPTION
D_3	C/m ²	Electric displacement field
d_{33}	C/N	Piezoelectric coefficient (longitudinal)
σ_3	N/m ²	Applied stress (z-direction)
$F_{appl,3}$	N	Applied force (z-direction)
Q_{free}	C	Free charge resulting from the piezoelectric effect
C	F	Capacitance of the capacitor in parallel with the DUT
V	V	Measured voltage across the capacitor

8.2.1.2 Berlincourt setup

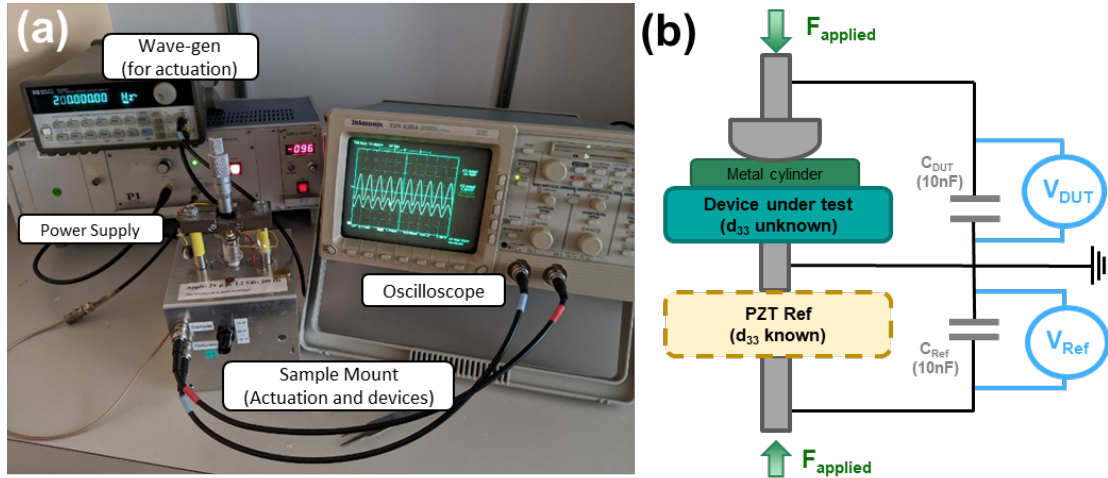


Figure 8.1 Visualization of the as-used Berlincourt meter showing (a) Annotated photograph of setup and (b) simplified schematic of circuitry.

Table 8.3 Equipment used for the in-house Berlincourt measurement

EQUIPMENT	MODEL	DESCRIPTION
Wavegen	Agilent Multimeter 33120A	Provides sinusoidal waveform for sample actuation. $f = 200$ Hz, $2 V_{pp}$, 1.2 V offset
Power Supply	PI Module E-120	Amplifies waveform fed to sample from wavegen
Oscilloscope	TDS 430A	Measured resulting voltage output from both the reference and test samples
Reference Piezo	N/A	Known PZT piezoelectric reference, $d_{33,ref} = 17.5$ pC/N

8.2.2 Cantilever characterization via Laser Doppler vibrometry

The LDV setup used for this thesis work is depicted in Figure 8.2 below. In this characterization method, a laser is pointed at the sample surface while the sample is actuated. The reflected light changes characteristic based on the movement of the sample, which is then converted into a voltage signal. By tuning the conversion sensitivity with different decoders, the sample displacement can be calculated to below 1 nm resolution.

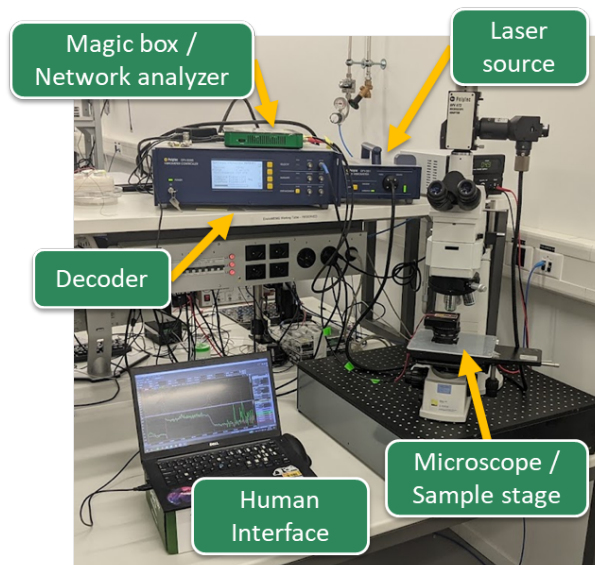


Figure 8.2 Annotated photograph of LDV setup.

For our implementation, a Polytec MSV system is used, with a Polytec OFV-5000 vibrometer controller, an OFV-551 fiber vibrometer, and an OFV 072 microscope adapter (lens magnification 10x). A Digilent Discovery Pro ADP-3450 serves as a waveform generator and network analyzer. Figure 8.3 below shows a general schematic of the signal processing implemented for this measurement.

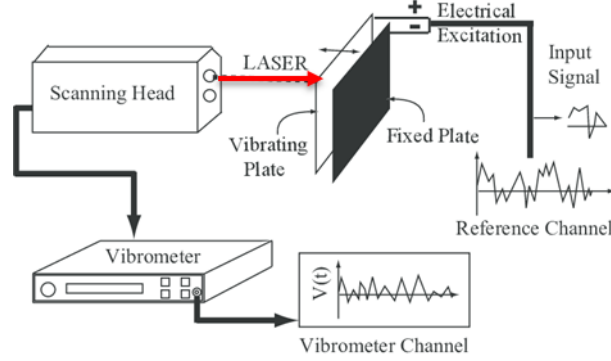


Figure 8.3 Schematic of LDV signal processing. Image reproduced from Venkatesh.³²⁸

We utilize a VD-06 decoder for measuring sample velocity, as it has a higher resolution than a simple displacement decoder. We then convert sample velocity to displacement according to (8.11):

$$d_{DUT}(\omega) = \frac{V_{LDV,decoded} * Range_{decoder}}{2\pi\omega} \quad (8.11)$$

For circular parallel-plate capacitor samples, this displacement can be correlated to the actuation voltage used for the measurement sweep to determine displacement as a function of voltage in a non-resonating frequency range and thus calculate an effective piezoelectric coefficient in pm/V. If the sample is not well clamped to the measurement stage, this value can be erroneous, particularly with low mechanical stiffness substrates such as paper or steel shim.

For samples of cantilever architecture, this measurement is used to calculate piezoelectric $d_{31,eff}$ coefficients, but the analysis method is more involved. This value can be determined from the sample at resonance, but its quality factor must be decoupled from the system to determine the coefficient accurately.

The sample is mounted in the LDV stage and strongly clamped in position. The laser is positioned at the tip of the cantilever. Next, the sample is actuated and the first resonance frequency is determined. Next, a series of high-resolution measurement sweeps are conducted within a 5 kHz range of the resonance, with varied actuation voltages.

Then, for each dataset, the sample velocity is converted to displacement, as before, and then the resonance peak data is fit to a Lorentzian function (Equation (8.12)) in order to decouple sample displacement from the quality factor such that the piezoelectric coefficient can be calculated. Relevant variables are defined in Table 8.4.

$$u_n(\omega) \approx \chi_n^A \left(\frac{d_{31} z_{offset} L^2}{t_{total}^3} \right) \left(\frac{w_{elec}}{w_{canti}} \right) \left(\frac{E_{piezo}}{E_{sub}} \right) \left(\frac{V}{1 - \left(\frac{\omega}{\omega_n} \right)^2 + j \frac{\omega}{\omega_n Q}} \right) \quad (8.12)$$

becomes

$$d_{31} \approx \left(\frac{t_{total}^3}{\chi_n^A z_{offset} L^2 Q} \right) \left(\frac{w_{canti}}{w_{elec}} \right) \left(\frac{E_{sub}}{E_{piezo}} \right) \left(\frac{u_n(\omega_n)}{V} \right) \quad (8.13)$$

with slope

$$slope = \frac{u_n(\omega_n)}{V} \quad (8.14)$$

Table 8.4 Variables used in derivation of LDV method piezoelectric coefficient $d_{31,eff}$ calculation.

Variable	Units	Description
u_n	m	Max deflection (this is the max amplitude for each respective sweep)
V	V	Actuation voltage
$\chi = 1.38$	[-]	Geometric factor for cantilever with full length electrodes
L	m	Length of the resonator
t_{total}	m	Thickness of the resonator
w_{canti}	m	Width of the resonator
w_{elec}	m	Width of the electrode
$z_{offset} = t_{total} - z_0$	m	Off-axis placement of the Piezo layer with respect to the neutral axis
$z_0 = \frac{\sum E_i t_i z_i}{\sum E_i t_i}$	m	Neutral axis (the plane in z with no longitudinal strain)
E_i	GPa	Youngs modulus of the material in layer i

8.2.3 Particle size analysis

Samples of an ink containing the ground or unground KN particulate are fabricated by screen printing onto a silicon substrate. The samples are then cleaved in liquid nitrogen to produce a clean cross-section. SEM images of the cross section are acquired, with clearly resolved particulate. Images were taken at several locations over the cross-section, then ImageJ software was used to sample the diameter of the particulate over several locations using the Intersection method. This is done by assigning randomly defined lines across an image and identifying the number of particulates occurring in that length of the cross section. This is repeated at least 50 times to achieve a distribution of particle sizes such that statistics can be completed with confidence. This entire process is repeated for both the ground and unground KN powders.

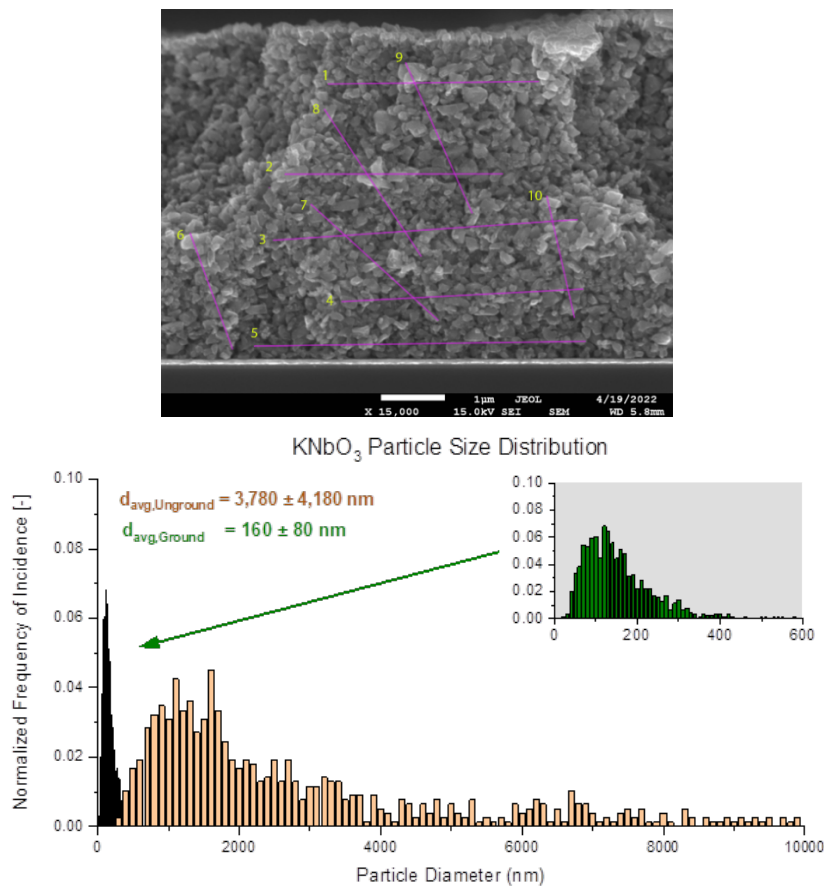


Figure 8.4 Particle size distribution analysis method including (a) An SEM micrograph of the printed KN layer post-grinding, with annotated lines used for particle sizing. (b) Particle size distribution for both the unground (orange) and ground (green) KNbO₃ particles.

8.3 Appendix C: Expanded literature review on commonly printed piezoelectric materials

8.3.1 Literature review on printing of common piezoelectric materials

Table 8.5 Expanded state of the art on 2D printed piezoelectrics, including information regarding printing method, substrate and electrode materials, processing temperatures, and piezoelectric response characterization. Abbreviations for printing methods include Screen Printing (SP); Digital Light Processing (DLP); Inkjet Printing (IJP); Electrohydrodynamic Jetting (EHD).

Author	Year	Piezo material	Print Method	Substrate (s)	Electrode (s)	$T_{max,Proc}$ (°C)	$d_{33,eff}$ (pm/V)	P_r ($\mu\text{C}/\text{cm}^2$)	E_c (kV/cm)	Notes	Ref
Monroe (This work)	2022	KNbO ₃	SP	Silicon, Paper	Au (Evap)	120	13	-	-		
Stojanovic	2004	BaTiO ₃	SP	Al ₂ O ₃	Ag-Pd	850	-	0.0107	0.00003		252
Wagiran	2005	BaTiO ₃	SP	Ceramic Glass	Ag (SP)	850	-	-	-	Values not reported	329
Chen	2022	BaTiO ₃	DLP	-	Ag (SP)	1300	146	-	-		265
Wang	2020	BaTiO ₃	SLP	-	Ag (SP)	1320	190	-	-		266
Sakai	2006	BaTiO ₃	IJP	ZrO ₂	Pt (SP)	1400 (Pt) 600 (BTO)	-	3.1	1.1		330
Almeida	2004	BaTiO ₃ - HA	SP	Al ₂ O ₃	Ag (SP)	850	-	-	-	Values not reported	331
Lim	2017	BaTiO ₃ -epoxy	IJP	PI	Ag (IJP)	250 (+NIR oven)	-	-	-	Assumed $d_{33} = 78 \text{ pC/N}$ from COMSOL	332
Nguyen	2022	BaTiO ₃ -PUA	SP	Steel	Ag (SP)	150 (+UV Cure)	1.31	-	-		148
Liu	2020	Bio _{0.5} Na _{0.5} TiO ₃	SP	MgO, Al ₂ O ₃	Pt (SP) / Au (SP)	1380 (Pt) 900 (BNT0)	80 / 50	10	35		256
Markham	2017	HA	SP	ITO	ITO (Film)	25	0.02	-	-		205
Korostynska	2011	HA	SP	Al	Al (Foil)	400	-	-	-	Values not reported	245
Silva	2005	HA	SP	Al ₂ O ₃	Ag (SP)	700	-	-	-	Values not reported	333
Badurova	2020	HA	SP	ITO	ITO (Film)	1200	0.03	-	-		334
Zhang	2010	KNBT	SP	Al ₂ O ₃	Pt (SP)	850	88	5-10	57.3		139
Levassort	2011	KNN	SP, Pad Printing	-	Au / Ag (Printed)	1000	-	-	-	Values not reported	335
Li	2012	KNN	SP	Glass	-	1100	133	20	9.1		258
Pavlic	2012	KNN	SP	Al ₂ O ₃	Pt (SP)	1100	-	-	-	Values not reported	336
Pavlic	2014	KNN	SP	Al ₂ O ₃	Pt (SP)	1100	44	-	-		337,338
Hansen	2009	KNN-LT	SP	Al ₂ O ₃	? (SP)	1000	86	-	-		339
Mercier	2017	KNN-Sr	SP	Al ₂ O ₃	Pt (SP)	1200	80	-	-		340,341
Hubler	2012	PVDF-TrFE	Flexographic	Paper	PEDOT:PSS (Flexographic)	130	-	-	-	Values not reported	342
Haque	2016	PVDF-TrFE	IJP	PI, PET	Ag (IJP)	140	-	-	-	Values not reported	104
Sekine	2016	PVDF-TrFE	IJP	PEN	Ag (IJP)	180	-	5	5		136
Goncalves	2019	PVDF-TrFE	SP	Glass	Ag (SP)	230	19	-	-		343
Glinsek	2022	PZT	IJP	Glass	ITO	700	-	4	-	Reported $e_{33}^* = 7.7 \text{ C/m}^2$	344
Glynn-Jones	2000	PZT	SP	Si	Pt (e-beam Evap) / Ag (SP)	750	101	-	-		143
Kok	2009	PZT	SP	Carbon paste (Sacrificial)	Ag-Pd (SP)	800	53	-	-		345
Chen	1995	PZT	SP	Si	Ti-Pt	850	38	2.5	40		346
Very	2013	PZT	SP	Al ₂ O ₃	Ag-Pd	850	0.15	-	-		347
Grall	2020	PZT	SP	Al ₂ O ₃	Au (SP)	900	-	-	-	Values not reported	144
Debeda	2015	PZT	SP	Al ₂ O ₃	Au (SP)	920	-	-	-	Values not reported	348
Zhu	2000	PZT	SP	Al ₂ O ₃	Ag-Pd	1030	41 (d_{31})	-	-		349
Torah	2004	PZT	SP	Al ₂ O ₃	Ag-Pd	750	33	-	-		253
Sivanandan	2008	PZT	SP	Al ₂ O ₃	Pt (SP)	1000	-	-	-	Reported $e_{31}^* = -4.00 \text{ C/m}^2$	268
Yildirim	2020	PZT-PDMS	SP (Blade cast)	Glass, PET	ITO	-	-	-	-	Values not reported	350
Garcia-Farrera	2019	ZnO	EHD	Si, PET	ITO (Sputtered)	25	23 ^(PFM)	-	-		151
Garcia	2021	ZnO	Gravure	PET	ITO	100	4	-	-	Printed seed layer only, ZnO layer via 16 hr CBD	244

8.3.2 Literature review on solution processed or printed ZnO

Table 8.6 Expanded state of the art regarding solution processed zinc oxide, as used for any application. Empty spaces indicate parameter was not provided.

SOURCE	Year	INK PARAMETERS							DRYING		CURING		Thickness (μm)
		Ink Type	ZnO Source	Solvent	Binders & additives	Mixing condition	Print Method	Substrate	t_{dry} (hrs)	T_{dry} ($^{\circ}\text{C}$)	T_{cure} (hrs)	T_{cure} ($^{\circ}\text{C}$)	
WU	2010	Sol-gel Precursor	Zn Acetate dihydrate (Fischer)	2-ethanolamine, isopropoxy ethanol				Si	(Hotplate)	200	(Oven)	450 – 600	
FLEISCHHAUER	2010	NP Suspension	ZnO (commercial)	Ammonia (aq) 7M			Spin coated	PEN				150	
PARK	2012	NP Suspension	ZnO Powder (Sigma 99.999%)	Ammonium hydroxide (aq) (99.9%)			Spin coated	Si			1	300	
UL HASAN	2012	Metal Salt Precursor	Zn nitrate hexahydrate + HMT	H_2O	XG383 Plastijet XG Varnish	Mixed for 3 h at 90°C , then dried and powder collected	Screen-printed	paper					
KIM	2018	Metal Salt Precursor	Zn nitrate + HMT	H_2O			Bath Deposition	PVDF	13 (Oven)	60			
KAR	2009	Metal Salt Precursor	Zn nitrate + HMT			Constant temp bath $60\text{--}90^{\circ}\text{C}$							
SCRYMGEOUR	2007	Metal Salt Precursor	Zn nitrate + HMT (hexamethylenetetramine)	H_2O					1 – 3				
TANG	2008	Metal Salt Precursor	Zn nitrate hexahydrate + Cetyltrimethylammonium bromide (CTAB) (Alfa)	H_2O		Mixed for up to 5min at $25, 50,$ or 100°C , quenched in icewater.							
LIANG	2009	Metal Salt Precursor	Zn nitrate hexahydrate + HMT (1:1)	H_2O , some NaOH for pH adjustment					1, 4, 8 (Oven)	95			
PATIL	2009	NP Suspension	ZnO Powder (AR99.99%)	Butyl Carbitol Acetate	ethyl cellulose, glass frit		Screen-printed	Alumina	1 (IR Lamp)		2 (Furnace)	700 – 900	20 – 22
FEKETE	2014	NP Suspension	ZnO Powder	Terpineol	ethyl cellulose		Screen-printed	FTO glass			Hotplate		0.6 – 2.4
SHOU	2017	NP Suspension	Zn powder (US Rsch Nanomats)	MeOH:Butyl Acetate (9:1)		20wt% Zn NPs in solvent	Dropcast	glass			Laser-sintered		
JUNG	2014	NP Suspension	ZnO NPs and Nanorods synthesized in house	Methanol			IJP	glass	0.25 (Hotplate)	80			
SHARMA	2017	NP Suspension	ZnO Powder (Sigma), milled in house	EtOH, EG			IJP	glass					
SHARMA	2017	NP Suspension	ZnO Powder (Sigma), milled in house	EtOH, EG	PAANA (surfactant)		IJP	glass			0.5 (Oven)	60, 100	
ZARGAR	2015	NP Suspension	ZnO Powder (99.999%)	EG	ZnCl_2		Screen-printed	glass	2	110	0.2 (Furnace)	550	1
CHACKRABARTI	2018	NP Suspension	ZnO Powder (99.999%)	EG	Anhydrous ZnCl_2	Mortar	Screen-printed	glass	2 (Hotplate)	110	0.2 (Furnace)	550	
PATIL	2010	NP Suspension	ZnO powder (in house)	butyl cellulose, butyl carbitol acetate, terpinol	ethyl cellulose		Screen-printed	glass			0.5	500	12 – 15
SRIVASTAVA	2011	NP Suspension	ZnO Powder (Ranbaxy 99%)	n-butyl acetate	ethyl cellulose, glass frit (5% total wt mixture)		Screen-printed	glass			4	500	
ISMAIL	2001	NP Suspension	ZnO powder		Polypropylene Glycol, paraffin, ZnCl_2		Screen-printed	glass	1	130	0.3 – 1.1	450 – 550	10
RUBIN	2017	NP Suspension	ZnO Powder (commercial, <100nm) 40wt%	EtOH	Hydroiropyl cellulose 10wt%		Screen-printed	Glass					
RUBIN	2017	NP Suspension	ZnO Powder (commercial, <100nm) 40wt%	EtOH	Hydroiropyl cellulose 15wt%		Screen-printed	Glass					
RUBIN	2017	NP Suspension	ZnO Powder (commercial, <100nm) 40wt%	EtOH	Hydroiropyl cellulose 5wt%		Screen-printed	Glass					
RUBIN	2017	NP Suspension	ZnO Powder (commercial, <100nm) 40wt%	H_2O	Carboxymethyl cellulose 5wt%		Screen-printed	Glass					
RUBIN	2017	NP Suspension	ZnO Powder (commercial, <100nm) 50wt%	H_2O	Carboxymethyl cellulose 3wt%		Screen-printed	Glass					
FABER	2009	NP Suspension	ZnO NPs suspended in MTBE (SusTech Darmstadt)				Spin coated	glass	0.1 (Ambient)	50			
RUBIN	2017	NP Suspension	ZnO Powder (commercial, <100nm particles) 40wt%	EtOH, Toluene	ethyl cellulose		Screen-printed	Glass, office paper					
RUBIN	2017	NP Suspension	ZnO Powder (commercial, <100nm particles) 50wt%	EtOH	Hydroiropyl cellulose 5wt%		Screen-printed	Glass, office paper					
RUBIN	2017	NP Suspension	ZnO Powder (commercial, <100nm particles) 40wt%	H_2O	Carboxymethyl cellulose 3wt%		Screen-printed	Glass, office paper, FS2, Tracing paper	0.25	25, 60, 120			
AZEEZ	2015	NP Suspension	ZnO nanorods (in house using Zn Nitrate process)		PVA		Screen-printed	glass, Si, SiO_2	0.5 (Ambient)	120	1 (Furnace)	500	
LIU	2012	NP Suspension	ZnO NPs (made in house)	Methanol, PGMEA	n-butylamine, polyester (both dispersants)		IJP	ITO glass	2	180	1 (Anaerobic)	200	

FENG	2019	NP Suspension	Zn μ Ps (Shanghai Naiou Nanotech co.)	EtOH	PVP (1300K)	20wt% PVP in EA, with Zn NPs, 25:4 by wt (Zn:PVP)	Screen-printed	Na-CMC, PLGA, Cellulose Acetate, PVA	30 (Ambient)				
LIM	2014	NP Suspension	ZnO Nanorods (in house using modified ZnAc process)	H ₂ O		see publication	Spin, IJP	Si		1 (Aerobic)	150	0.15	
OMEROVIC	2019	NP Suspension	ZnO Powder (Alfa 99+%)	H ₂ O, propylene glycol, n-propanol	gum arabic, solperse, Byk-028 (antifoaming agent)		IJP	Si, PI, PET, paper	2	100			
SUGANTHI	2018	NP Suspension	ZnO NPs in house precipitation	EG		Sonic bath 6h, 0.5-4 vol% ZnO	Direct Writer		0.5	60			
SHARMA	2017	NP Suspension	ZnO Powder (Sigma), milled in house	EtOH, Glycerol									
SHARMA	2017	NP Suspension	ZnO Powder (Sigma), milled in house	EtOH, H ₂ O	PAANa (surfactant)								
SHEN	2005	Sol-gel Precursor	Zn Acetate dihydrate	EtOH, glycerin	Ethylene glycol	ZnAc + EG at 120°C, 20min, cooled to solid, add EtOH + glycerin, filtered	IJP	Al ₂ O ₃ with gold IDEs	24 (Ambient)	24	4	500	
SCHNEIDER	2009	Sol-gel Precursor	Zn Oximate complexes	H ₂ O			Spin coated, IJP	glass, PET			2	150	
TRAN	2017	Sol-gel Precursor	Zn Acetate dihydrate (Sigma)	EtOH		Stirred 60°C, 1hr, filtered 0.22 μ m PTFE	IJP	PI	0.2 (Hotplate)	200	1 (Furnace)	400	
FLEISCHHA KER	2010	Sol-gel Precursor	ammine-hydroxo complex [Zn(NH ₃) _x](OH) ₂	H ₂ O, ammonia (aq)			Spin coated	Si				150	0.015
WANG	2006	Sol-gel Precursor	Zn Acetate dihydrate	IPA, DEA, H ₂ O		Heated to 60°C for 30min, distilled 100°C for 2h	Spin coated	Si	0.2	300 – 450	0.5	550 – 800	0.5
RAMADAN	2018	Sol-gel Precursor	Zn Acetate dihydrate (Sigma)	EtOH			Spin coated	Si	(Thermal, MW Plasma)				
LAURENTI	2014	Sol-gel Precursor	Zn Acetate dihydrate (Sigma)	H ₂ O, EtOH(1:1)		Stirred at RT 1hr, 350 rpm, sonic'd 30min		Si, FTO glass	0.4	350			
KWON	2013	Sol-gel Precursor	Zinc Acetate (5mM)	Ethanol			IJP	Si, glass	0.4 (Hotplate)	200 – 350			
ONG	2007	Sol-gel Precursor	Zn Acetate dihydrate	MEA, anhydrous 2-methoxy-ethanol			Spin coated	Si, glass, ATO/ITO/glass				300 – 600	0.04
LIANG	2009	Sol-gel Precursor	Zn Acetate dihydrate	MEA, anhydrous 2-methoxy-ethanol (2:1 MEA:ZnAc)			IJP	Si, glass, ITO glass	0.2 (Hotplate)	180	1	300, 450	
LIANG	2013	Sol-gel Precursor	Zn Acetate dihydrate	MEA, anhydrous 2-methoxy-ethanol		maintain 2:1 ratio of solvents to each other	IJP		0.2 (Hotplate)	180	1	300	
CHUNG	2012		Zn nitrate hexahydrate				Spin coated	IRO/ PET	1 (Hotplate)	120			0.087
MEYERS	2008		Zn nitrate hexahydrate	IPA, Ammonia (aq), H ₂ O			IJP	Si	0.1–0.2 (Hotplate)	150 – 500			
MEYERS	2008		Hydrothermal Precursor				Spin coated	Si	0.1–0.2 (Hotplate)	150 – 500			
SINGH	2014		Hydrothermal Precursor				Spin coated	Si	(Hotplate)	150	5 (Hotplate)	450	

8.4 Appendix D: Expanded details on materials down-selection studies

8.4.1 Initial studies concerning Rochelle salt and ADP

The first two materials investigated for use as printable biodegradable piezoelectric materials were Rochelle Salt and ADP. As water soluble crystals, processing of these materials is initially straightforward: depositing saturated aqueous solutions of the materials and allowing them to dry initiates crystal precipitation onto the deposited substrate from the saturated solution. Initial work by Lemaire served as a jumping off point for producing RS and ADP inks.^{184,185,262}

A selection of biodegradable, water-soluble ink binders were obtained and ink formulations were mixed following Table 8.7.* Inks were initially drop cast on to PET, PI, glass, and paper substrates to evaluate the quality of the inks based on grown crystal size, coverage, and adhesion. It was found that consistent coverage and crystallization behavior were difficult to achieve on any substrate, with samples deposited in the same conditions showing highly variable crystallization behavior. Adhesion of RS inks to substrates was found to be extremely poor, regardless of binder type or amount, and the brittleness of the crystals made device lifetime and reliability low. Solutions containing ADP were found to crystallize at such a fast rate that the resulting layers were inhomogeneous and unreproducible. Further attempts to slow the crystallization process were unsuccessful.

Table 8.7 Tested ink formulations for green RS and ADP screen printing inks

Active Material	% Sat'd (in H ₂ O)	Binder Material	Binder wt%*
RS	90 – 100	None	0
RS	90	PVA	0.5 – 7
RS	90	PVP	0.5 – 7
RS	90	Gum Tragacanth	0.5 – 7
RS	90	Gelodiet	0.5 – 1
RS	90	Gelodiet + EA	1 (GD) + 0.8 (EA)
ADP	90 – 100	None	0
ADP	90	PVA	0.5 – 2
ADP	90	PVP	0.5 – 2

Annealing RS crystals to mitigate the inconsistent crystallization was evaluated next. The results showed that RS chemically decomposed at 36 °C (despite a nominal melting point of 76 °C), from which RS crystals could not reform due to different solubilities of the two component salts.³⁵¹ As such, annealing of printed RS crystal layers was found to be impractical.

The results of these investigations indicate that RS can be solution deposited in a facile manner, but has several serious drawbacks for device integration concerning stability and reliability. To produce consistent devices using RS would be quite challenging, while the low decomposition and Curie temperatures limit the potential applications for this material. It may provide a viable path forward, but would be extremely limited in application scope, with great hurdles to overcome in the development of reproducible processes. As such, this material was dismissed from further study at this point.

8.4.2 Initial studies concerning ZnO

As discussed previously, ZnO has already been the focus of much work in photovoltaic and piezoelectric applications, and there is an enormous body of work on the printing of ZnO, with multiple inks commercially available for inkjet printing applications. Initial evaluation of ZnO included assessing the printability of ZnO inks made with fully green components and initial assessment of methods to orient ZnO NPs onto substrates.

* Weight percent of binder is reported as the weight percent relative to the amount of piezoelectric material, not total weight of the ink solution.

8.4.2.1 Initial screen printing of ZnO

Initial ZnO screen printing inks were formulated according to the recipes in Table 8.8, with a narrowed selection of biodegradable binders.

Table 8.8 Tested ink formulations for green ZnO screen printing inks.

Active Material	ZnO NP wt% (in H ₂ O)	Binder Material	Binder wt%*
ZnO	15	None	0
ZnO	15	PVA	0.5 – 2
ZnO	15	PVP	0.5 – 2
ZnO	10	PVP	0.5 – 20

Initial screening showed that ZnO-based screen printable inks can be successfully developed using entirely degradable components. To start, aqueous dispersions of ZnO nanoparticles (NPs) (CAS 1314-13-2, 20 wt% in H₂O, 50–80 nm ϕ , 99.99%, Nanoshel-UK Ltd.) was mixed with PVA or PVP binders such that binder content was 2–10 wt% relative to ZnO content, which was 10–15 wt% of the total ink mass. It was found that inks with 10 wt% ZnO and 5–10 wt% PVP produced high quality films, with a layer thickness of 12 ± 2 μ m when stencil printed through 27 μ m thick PET stencils and dried at room temperature. Inks were stable for up to 3 weeks before particle agglomeration caused significant change in print quality. These inks can be printed onto glass, polyimide, and paper substrates with reasonably good adhesion.

8.4.2.2 Feasibility study: Orientation of ZnO nanoparticles

In addition to the development of a printable ZnO ink, it is critical to establish a method by which the ZnO particulate can be oriented, as this is necessary to produce a permanent dipole in the material and thus a piezoelectric response. As a non-ferroelectric material, the dipole orientation must be established during layer deposition.

Orientation of ZnO particles has been achieved in several ways; template assisted nanoparticle growth is fairly common, as is tape casting of nanoparticle solutions.^{67,213,352–356} From one approach, oriented systems can be deposited through the formation of particles that have a natural preference for positioning themselves in a given direction due to geometry (for example, plate- or flake-shaped particles, like a coin, will preferentially lie on the larger material face over the edge).^{264,357–359} From another, dielectrophoresis has also been used to orient individual ZnO NWs in solution, but has yet to be implemented in larger scale processes.^{360–362} These two processes (oriented particle synthesis and dielectrophoresis-assisted deposition) were evaluated for viability in this investigation.

Towards particle synthesis, shape directed nanoflake (NF) synthesis is typically used. Therein, a hydrothermal process is implemented using a ZnO precursor, zinc nitrate hexahydrate (Zn(NO₃)₂·6H₂O), with a shape directing agent, hexamethylenetetramine (HMTA, (CH₂)₆N₄), and involving a chemical bath at 90 °C for 3 hours. This technique is thus not compatible with biodegradable substrates, which typically have issues with extended submersion in aqueous solutions. Instead, Vabbina synthesized ZnO NFs that oriented themselves to lie flat on arbitrary substrates by utilizing a sonic probe to react the precursor solution (for 30 min instead of the 3 hour heated bath used conventionally), then dip coating substrates in the solution to produce a film of oriented ZnO NFs.²⁶⁴ This process showed great promise for integration into printed methods, but a feasibility study was first conducted.

Initially, the nanoflake synthesis process was verified by duplicating the described process successfully, before further feasibility evaluation for printing process integration. A precursor solution was initially prepared containing 0.02 M zinc nitrate hexahydrate and 0.02 M HMTA. Vabbina's process was duplicated and found to successfully produce ZnO NFs. Next, a process was established to assess if the process could be done in controllable locations via dropcasting. In 10 μ L aliquots, the precursor solution was dropcast on glass and PET substrates adhered to the interior bottom of glass beakers, which were then placed in a sonic bath for 30 min to initiate NF synthesis. This modified procedure was successful, with NF formation within the dropcast solution. Nanoflakes had the expected dimensions reported by Vabbina of several microns in diameter and 10s of nanometers thickness. The particles preferentially formed at the air-liquid-substrate interface, producing an approximately 40 μ m wide "coffee ring" of nanoflakes that were relatively well oriented towards the substrate. This confirmed the potential for low-temperature and aqueous bath-free synthesis of oriented ZnO particles.

While this process was successful in synthesizing oriented ZnO NFs in a potentially printable manner, the yield of particles and the thickness of the layers were both quite low, posing a challenge for use in scalable processes. Optimization would be necessary for this process to be viable.

As an alternative to oriented particle synthesis, we next evaluated the viability of incorporating dielectrophoresis (DEP) into the printing process as a means of aligning ZnO nanowires/nanorods directly on the substrate. Previous studies have shown this to be a successful method of piezoelectric texturing with KNN, BaTiO₃, and other materials.^{67,362–364} Figure 8.5 depicts one possible implementation of such a setup. In this system, the printed bottom electrode is used with an external top electrode brought close the substrate behind the printhead. An electric field is used to orient particles in the ink immediately after printing, but prior to the ink drying. Temperature control of the substrate or meshed top electrodes can be used to control drying behavior.

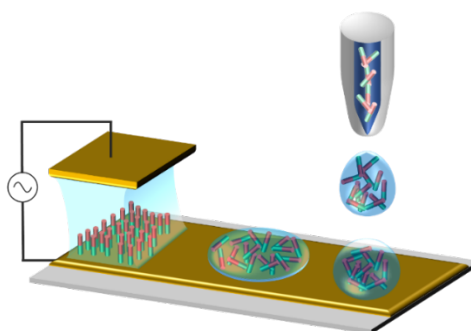


Figure 8.5 Schematic of a possible *in situ* texturing method for a printed piezoelectric material via dielectrophoresis. This schematic is not to scale.

Initial studies on DEP-based alignment of ZnO particles was conducted using conventionally microfabricated interdigitated electrodes of platinum deposited on polyimide substrates. The substrates were positioned on a flat surface and a 3 mm deep PMMA well was positioned around the active area. Low concentration (2–10 wt%) dispersions of ZnO particles in EtOH, H₂O, or IPA were drop cast into the wells in aliquots of 10, 20, and 100 μ L. Electric fields were applied across the two electrodes according to Deutz and Riaharfar, applying a sinusoidal waveform of 0.2–2 kHz with AC fields in the range of 2–10 V/ μ m.^{365,366}

From this initial study, several conclusions were quickly drawn. First, this process requires very low loading of active material (1–10 wt%) in a low viscosity solvent to facilitate movement of the particulate, but must also utilize solvents with low enough volatility to permit time for particle re-orientation, thus limiting the library of potential solvents applicable for this process. Further, the slow evaporation rate required by this process significantly extends the process duration. Finally, the low particulate loading results in extremely thin layers of particulate ($\ll 1 \mu$ m), and therefore any functional device would require many, many layers of this process in order to have appreciable piezoelectric properties. Thus, it was concluded that this process is impractical for implementation in the current study.

8.4.2.3 Final conclusions concerning zinc oxide

Initial screening shows that ZnO-based screen printable inks can be developed using entirely degradable components. These inks can be printed onto glass, polyimide, and paper substrates with reasonable adhesion. However, the as-printed inks were not oriented and thus exhibited no piezoelectric response.

Two feasibility studies were conducted to assess whether ZnO could be printed into an oriented layer. The first involved nanoflake synthesis for directed positioning. A process was made to screen print a precursor solution, then ultrasonically react the solution to synthesize ZnO nanoflakes. While flakes were successfully synthesized in a room temperature process, the yield of nanoflakes was deemed too low to reliably produce viable devices for practical applications. In the second feasibility study, dielectrophoresis was utilized to attempt layer orientation of a ZnO particle dispersion. The investigation showed some minor particle alignment, but the process was deemed impractical for the high-volume device applications for which this thesis is targeting.

Hence it was concluded that ZnO was not an ideal candidate for further study, but could be revisited if all other studies proved unsuccessful.

8.4.3 Initial studies concerning hydroxyapatite

8.4.3.1 Initial hydroxyapatite-based ink development

Inks of hydroxyapatite were formulated using aqueous HA nanoparticle (HA NP) dispersions with PVA and PVP binders. Ink compositions are summarized in Table 8.9. Initial tests involved drop casting and screen printing onto PET, PI, paper, and glass substrates to evaluate ink quality in terms of adhesion, homogeneity, and other physical properties. In initial testing, post-processing of the ink to burn off the binder and anneal the samples was not conducted, and the binder was left in the final layer.

Table 8.9 Tested ink formulations for hydroxyapatite-based screen-printing inks.

Active Material	HA NP wt% (in H ₂ O)	Binder Material	Binder wt%*
HA	25	None	0
HA	25	PVA	0.5 – 2
HA	25	PVP	0.5 – 15
HA	12.5	PVP	2 – 10
HA	8	PVP	5 – 10

Printed layer quality was significantly enhanced over several iterations of ink formula and process improvements, resulting in printed HA layers with minimal defects from cracking or microbubbles, as exemplified in Figure 8.6. HA was successfully screen printed on all tested substrates with these inks.

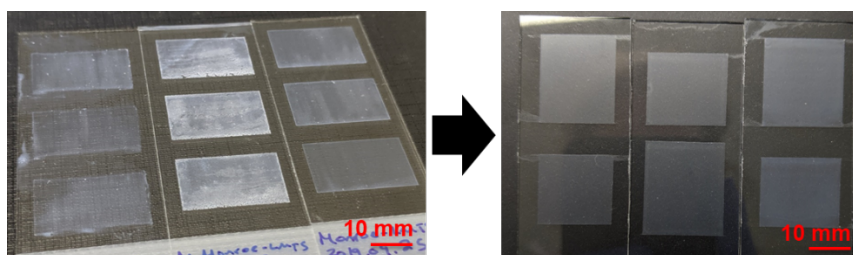


Figure 8.6 Quality improvement of screen-printed HA films after four generations of ink development.

In practical experimentation, hydroxyapatite was found to be reactive with many conventionally used conductive materials, (including Cu, Al, and many conductive inks commonly used for fast prototyping), limiting its applicability for use in green devices, as it is expected that HA printed layers will interact with degradable conductive layers in unfavorable ways. As a noble metal, gold is compatible with HA and thus was selected for initial tests of HA piezoresponse. To this end, stencil printed HA devices were fabricated using sputtered gold electrodes on glass, using a three-layer parallel plate capacitor architecture, as described in Figure 8.7 below. Single HA layers printed in this manner were typically 5–10 μm thick, with 20 nm of sputtered gold for each electrode. Resistance across these devices was $\geq 10 \text{ M}\Omega$, and thus the samples were deemed viable for further characterization.

8.4.3.2 Initial piezoelectric measurements of hydroxyapatite

Samples of HA screen printed on glass with sputtered Au electrodes were poled using a contact poling method, with parameters based off of the works of the Tofail group.^{205,206,367–370} Samples were heated to setpoints in the range 150–230 $^{\circ}\text{C}$, and a DC electric field of 10–20 $\text{V}/\mu\text{m}$ was applied across the electrodes for 1 hour. The samples were then allowed to passively cool to room temperature with the field applied. A Berlincourt meter (courtesy of the Damjanovic lab at EPFL) was used to evaluate the piezoelectric $d_{33,eff}$ coefficient of the samples. Despite the high sensitivity of the utilized equipment (sensitivity of $<0.2 \text{ pC/N}$), no piezoelectric response was observed in any of the HA samples evaluated. Discussions with D. Damjanovic regarding this result indicate that the large piezoelectric values reported by Lang (16 pC/N) may have been erroneous, as other have been unable to reproduce the same results in bulk HA samples.^{89,204}

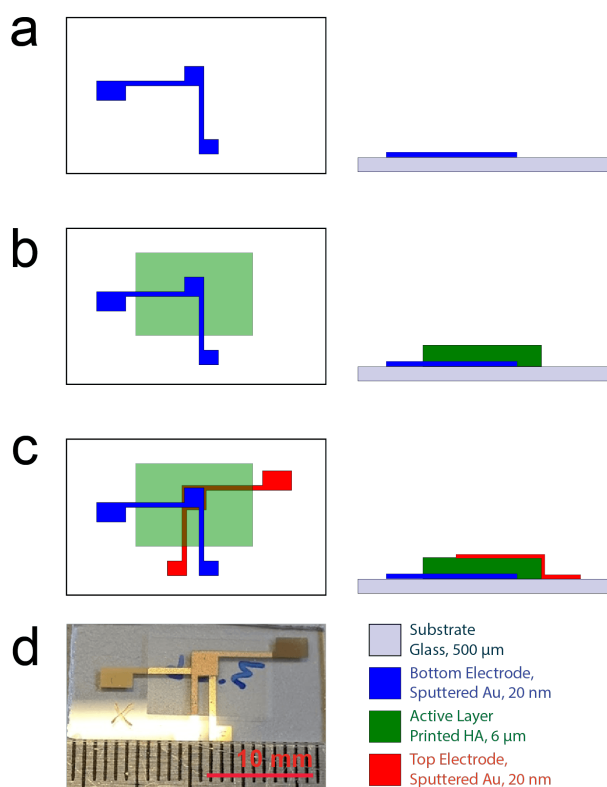


Figure 8.7 Simplified Process flow for HA device fabrication on glass substrate depicting both top-down (left) and cross-section (right) views of (a) Sputtered Au bottom electrode, (b) stencil printed HA active layer, (c) Sputtered Au top electrode, and (d) Photo of an as-fabricated sample (surface area of 4mm²).

8.4.3.3 Further ink development of hydroxyapatite

To confirm these results, the work done by Markham et al was replicated, producing a screen printable ink with a recipe significantly deviating from the previous work reported herein by increasing the loading of active material in the ink from <20 wt% to nearly 50 wt%, and thus increasing the viscosity of the ink. A planetary ball mill was used to mix an ink consisting of 49.1 wt% HA, 3.4 wt% polyvinyl butyral, and 47.5 wt% Diethylene glycol monobutyl ether (DEGMBE), as reported by Markham.²⁰⁵

Devices were printed via stencil printing, with sputtered gold electrodes following the device configuration depicted in Figure 8.7. Confocal microscopy was utilized to determine printed layer thickness. Figure 8.8 depicts one such printed layer. The printed layers had an average thickness of $140 \pm 69 \mu\text{m}$ and an average surface roughness of $5.71 \mu\text{m}$.

Capacitor devices were fabricated using this ink, with sputtered gold (10 nm thickness) implemented as top and bottom electrodes. Devices fabricated has surface areas of 1, 4, and 9 mm². Impedance spectroscopy was then used to investigate the dielectric characteristics of the devices. Of note, it was observed that the HA capacitive devices showed a significant sensitivity to ambient humidity conditions, nonideal for stable device functions. Further work on this system would necessitate the implementation of encapsulation layers.

These samples were next evaluated for their piezoelectric properties. Devices were poled at 30, 100, 200, or 230 °C for a duration of 30 or 60 min using a programmable high voltage power supply to apply a DC field of 3.125 V/ μm across the electrodes. The Berlincourt method was then used to determine the effective piezoelectric coefficient, $d_{33,eff}$, of the HA devices using an in-house measurement setup developed by D. Damjanovic of EPFL-IMX-DD, with a minimum resolution of 0.04 pC/N. No sample produced a measurable piezoelectric response, regardless of poling conditions utilized.

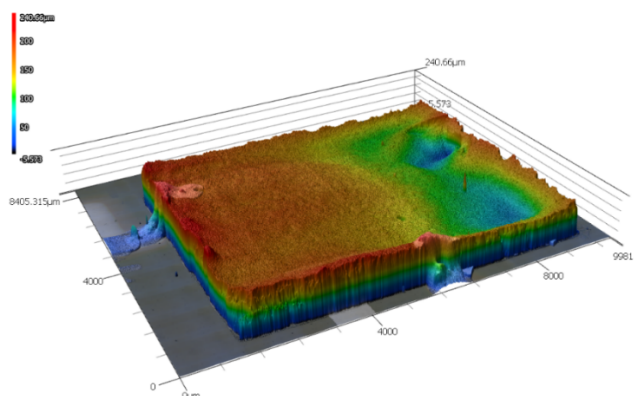


Figure 8.8 Thickness measurement for screen printed hydroxyapatite layers as measured using confocal microscopy.

8.4.3.4 Structural analysis of hydroxyapatite

Following the poor device performance of printed hydroxyapatite films, the piezoelectric nature of the material was called into question. Several studies have found conflicting results regarding the crystal structure of stoichiometric hydroxyapatite.^{204,366,371} Thus, powder diffraction was performed on the HA powder utilized in the inks discussed previously to determine its crystalline nature. The source material was stoichiometric hydroxyapatite powder provided by CamBioceramics ($\geq 99\%$ pure, $D_{50} = 32 \mu\text{m}$). The resulting spectra are depicted in Figure 8.9 below, in red. The crystal structure was determined to be hexagonal, with space group $P6_3/m$. As this is a centrosymmetric phase, it is therefore not a piezoelectric phase of matter. A second sample was then assessed after calcining the source material at 850°C for 2.5 hours followed by a passive cooling to ambient temperature over 15 hours, intended to verify the crystalline nature was not affected by any processing. This analysis resulted in excellent agreement with the uncalcined HA powder, as shown in Figure 8.9, in blue. From this it was concluded that stoichiometric hydroxyapatite remains in a centrosymmetric phase and thus cannot show piezoelectric behavior.

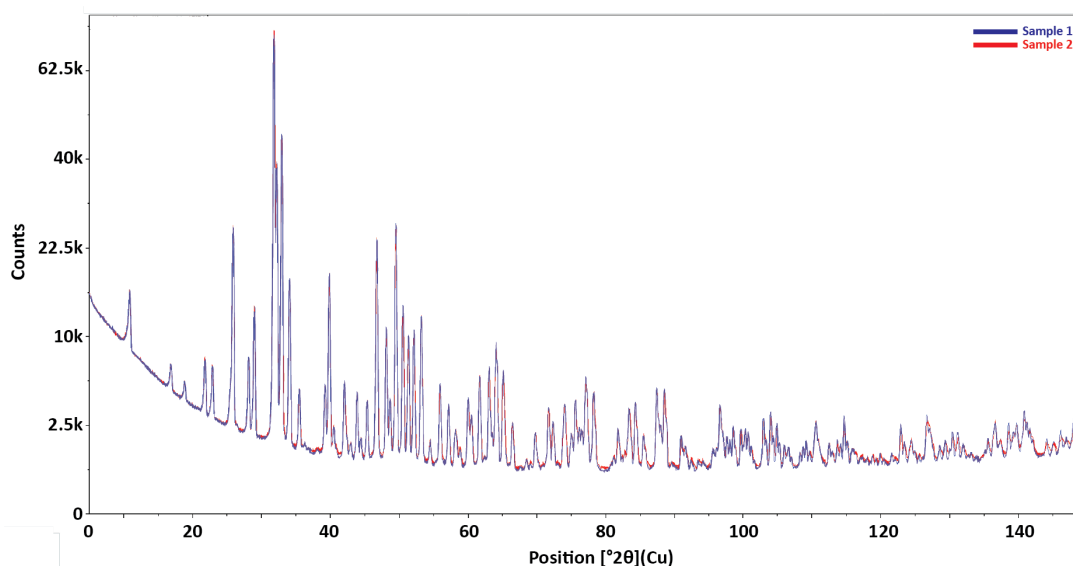


Figure 8.9 Powder diffraction spectra for two samples of hydroxyapatite analyzed, showing good agreement, and indicating a hexagonal crystal system, $P6_3/m$.

8.4.3.5 Final conclusions concerning hydroxyapatite

Hydroxyapatite has been reported by multiple groups to present piezoelectric properties, and its biodegradable and sustainable nature make it a promising material for printed electronics applications. Through successive iterations, inks were developed for stencil printing of hydroxyapatite layers. Samples were electrically poled, but no piezoelectric response was verified from the experimental samples. Further investigations of material properties via powder diffraction showed the stoichiometric source powder was centrosymmetric and could not be piezoelectric as a result. This, combined with the material incompatibilities of HA with most degradable conductor candidates in consideration indicates that this

material is not an ideal candidate for further study at this time, and was dismissed. It should be noted, however, that the humidity sensitivity of the printed layers implies great potential for HA in other sensing applications.

8.4.4 Process validation with barium titanate

Prior to the validation experiment detailed in Section 3.3.1, the printing process for BT inks was implemented on non-degradable substrates. This was done to verify the ink composition used, as well as to confirm the poling process on more thermally robust substrates prior to transfer onto paper.

Towards this, a screen-printable BaTiO_3 ink was prepared with the same binding agent and solvent as the proposed KN ink (ethyl cellulose and pentanol) using a BT screen printing recipe previously established by Stojanovic.²⁵² The refined recipe was: 70 wt% BT, 10 wt% EC, and 20 wt% pentanol. The ink was mixed in a planetary mixer at 1000 rpm for a duration of 5 min prior to printing.

The BT ink was stencil printed onto a stainless-steel foil substrate (acting also as a bottom electrode) through a stencil composed of 125 μm thick PET. The layer was dried in ambient conditions for 3 hours, then a top electrode was stencil printed on the BT layer to produce a parallel-plate capacitor structure. The top electrode was composed of a commercial carbon-based screen-printable ink (BareConductive Electric Paint). The resulting devices had an active area of approximately 64 mm^2 and an active layer thickness of approximately 60 μm based on confocal microscopy measurements. Figure 8.10(a-c) depict the architecture and physical characteristics of these devices.

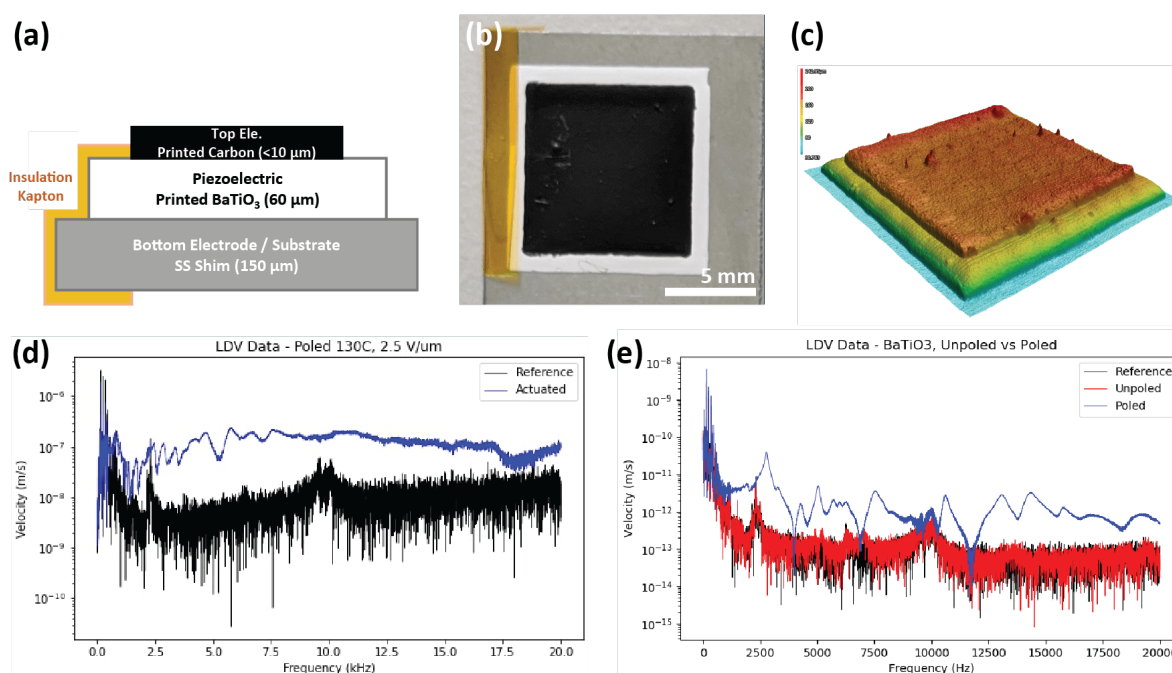


Figure 8.10 Initial Stencil printed BT device details showing physical details as (a) schematic of the device, (b) photograph of an as-fabricated device, (c) confocal microscopy scan showing the thickness of the BT and Carbon layers (Magnified 10x for visualization). LDV data showing sample velocity as a function of actuating frequency resulting from piezoelectric response when actuated at 10 V for samples poled at (d) 135 °C and 2.5 V/ μm , and (e) 25 °C and 5 V/ μm . Velocity measured at the center of the sample.

Laser Doppler vibrometry was then used to evaluate the piezoelectric response of the BT devices after poling. Figure 8.10(d) depicts the results of one such measurement, from a BT device screen printed onto SS shim with carbon top electrode. The actuated sample shows clear displacement in this frequency range, indicating that the sample is indeed piezoelectric after poling at the Curie temperature, confirming the fundamental aspects of the poling process are indeed functional for use with printed ferroelectric layers.

In the next phase of process validation, the poling process was repeated for the same configuration of BT samples on SS substrates, but without the heating step. Instead, these samples were poled under ambient conditions of approximately 25 °C. Laser doppler vibrometry was again used to evaluate the piezoelectric response of the BT devices both before and after poling. Figure 8.10(e) depicts the results of one such measurement, from a BT device comparable to that used for

the Curie temperature poling tests. The sample response prior to poling matches well with the reference response of the sample with no actuation, indicating no significant piezoelectric response in unpoled printed layers. The post-poling actuated sample shows significant displacement above the reference, indicating that the sample is indeed piezoelectric. The large number of resonance peaks is attributed to poor clamping of the flexible SS substrate. Regardless, this simple test verified that poling of the printed BT layer at room temperature was successful. This series of investigations provided proof-of-concept verification that screen-printed perovskite ferroelectrics can be poled under ambient conditions and produce a measurable piezoelectric response.

In Section 3.3.1, we discuss the continuation of this study, with a transfer of the process onto paper substrates.

8.4.5 Initial studies concerning potassium niobate

No reports were found in literature of additively manufactured potassium niobate layers. As such, the establishment of a basic ink was necessary before further studies could be implemented. Initial solvent and binder materials were selected following the result of work on ZnO and HA, with solvents of H₂O, IPA, and EtOH as primary solvent options, while polyvinylpyrrolidone (PVP), ethyl cellulose (EC), and gum tragacanth (GT) were selected as potential binding agents. While KN has no literature precedent for printing processes, corollaries could be made from work where similar perovskite materials were printed. From this, several additional solvents were selected for evaluation, namely Diethylene glycol monobutyl ether (DEGMBE) and pentanol. The body of literature for printing potassium sodium niobate ((K,Na)NbO₃), a sister material to KN, proposes ethyl cellulose or PVA as binding agents for typical processes. The evaluated KN inks are summarized in Table 8.10 below.

Table 8.10 Ink compositions tested for potassium niobate-based screen-printing inks.

Active Material	Solvent Material	Binder Material	KN wt%	Binder wt% (rel. KN)
KN	H ₂ O	None	5 – 10	0
KN	H ₂ O	PVP (36k)	5 – 10	2 – 10
KN	H ₂ O	PVP (400k)	10	10
KN	H ₂ O	GT	10	5
KN	IPA	PVP (36k)	10	10
KN	EtOH	PVP (36k)	10	10
KN	DEGMBE	PVP (36k)	10	10
KN	Pentanol	PVP (36k)	10	10
KN	DEGMBE	PVB	10 – 40	5 – 10
KN	IPA	EC	10	10
KN	EtOH	EC	10	10
KN	Pentanol	EC	10 – 70	5 – 20

For initial testing, inks were manually mixed in small batches of 10 mL and stencil printed onto glass substrates through masks of 125 μm thick PET. Evaluation was conducted based on several parameters: stability of the ink, roughness of the printed layer, and adhesion of the printed layer to the substrate.

As the most environmentally friendly solvent, a range of inks were manufactured first using water as the carrier fluid. However, despite a range of tested parameters, the polar nature of the fluid resulted in agglomeration of KN particular in the ink, and thus all H₂O-based KN inks were found to be insufficiently stable for quality printing processes without significant modification.

In the second phase of evaluation, the binder and KN parameters were fixed to be either 10 wt% PVP (36K) and 10 wt% KN, or 10 wt% EC and 10 wt% KN with varied solvents, as a means to assess the various solvents for use with KN. From this study, IPA and EtOH were found to be poorly suited to use with KN, as the volatility of these solvents resulted in printed layers with high residual stress that would result in cracking or delamination. DEGMBE and Pentanol, however,

produced relatively stable inks and layers of significantly higher quality. These initial inks were found to be stable for as long as one week prior to significant sedimentation (as compared to <24 hours for inks containing IPA as the solvent).

Though both DEGMBE and pentanol solvents proved promising during this initial process evaluation, pentanol was selected for further investigation due to its decreased reactivity and reduced toxicity as compared to DEGMBE. Ethyl cellulose and PVP binding agents both proved promising as well, but EC was selected for continuation of the work as its insolubility in water make EC-based printed layers less sensitive to changes in ambient humidity.

The result of this ink development investigation is a screen printable KN-based ink, comprised of 10 wt% KN and 10 wt% EC in a pentanol solvent. This ink was determined to be sufficient proof-of-concept for the printability of potassium niobate, but improvements were deemed necessary before full devices could be fabricated with the ink. In particular, the large KN particulate size as identified as a source of both ink instability due to sedimentation as well as printed layer roughness and cracking. Improvements on this challenge will be discussed in the following section.

8.4.5.1 Refinement of KN ink composition

Following verification that capacitive devices could be produced from the ink discussed in this section, a final phase of refinement was conducted to improve the quality of the printed device layers. In this phase of KN ink development, pentanol based KN inks were evaluated with varying the loading of KN between 10 and 70 wt%. Significant improvements to ink quality were found for inks with KN loading between 40–50 wt%. Further improvements were found through transitioning from a manual to a mechanical mixing process in a planetary mixer. Finally, the KN loading was fixed to 50 wt% in pentanol and the loading of binder was varied from 5–20 wt%. From this study, it was found that binder content greater than approximately 10 wt% resulted in layer cracking and delamination, and that quality layers could be achieved with binder loading in the range of 5–10 wt% ethyl cellulose.

Through this ink development investigation, a screen printable KN-based ink was developed, comprised of 40–50 wt% KN and 5–10 wt% EC in a pentanol solvent. The resulting ink was found to be shelf-stable for several months under ambient conditions in a well sealed container and produce high quality films of 5–20 μm thickness.

8.5 Appendix E: Dielectric leakage studies

8.5.1 Electrode coverage and material

It was hypothesized that the thin top electrode (thermally evaporated Cr/Au, 10/100 nm) was not continuous across the relatively rough printed surface (see Figure 4.9, inset), resulting in a smaller effective device area than that specified in the initial design due to the disconnected layer segments, which could potentially allow ambient water to permeate the electrode layer. In a simple test for this discontinuity in top electrode, samples were fabricated with significantly thicker top electrodes (300–600 nm), and their dielectric behavior characterized. It was hypothesized that adding a thicker top electrode would re-connect the discontinuous components of the gold layer, and thus increase the effective area of the capacitors, however the samples with thicker top electrodes exhibited no significant change in dielectric behavior as compared to equivalent devices with the standard 100 nm of gold top electrode tested under the same conditions. Hence, it was concluded that the effective device area was unchanged with the additional material and therefore the electrode was likely continuous across the device.

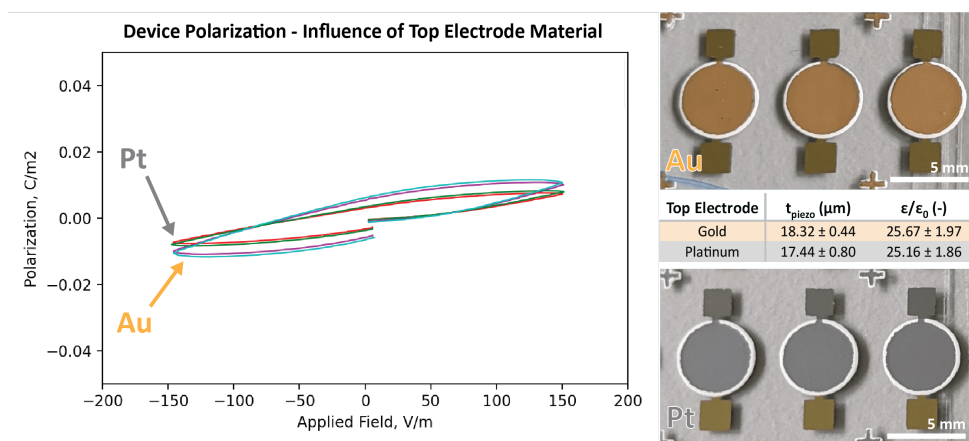


Figure 8.11 Evaluation of the influence of top electrode material on ferroelectric device performance.

Similar investigations were conducted to evaluate the potential impact the electrode material might have on device performance. All devices were fabricated simultaneously under the same processing conditions, with the only variance in the deposition of the top electrode, for which half of the devices received a gold top electrode and the other half platinum, both of which were thermally evaporated and approximately 100 nm in thickness.

Physical characteristics of all samples agreed between the two sample sets, confirming the consistent fabrication of the device layers. The thickness of the KN layer on the gold-electrode devices averaged $18.32 \pm 0.44 \mu\text{m}$ while that of the platinum-electrode devices was $17.44 \pm 0.80 \mu\text{m}$. Impedance spectroscopy also found consistent device behavior, with a calculated relative permittivity of the gold-electrode devices measuring 25.67 ± 1.97 and the platinum-electrode devices measuring 25.16 ± 1.86 . As a final confirmation, the ferroelectric behavior of the samples was characterized utilizing the Sawyer-Tower method to generate hysteretic P-E loops, as depicted in Figure 8.11. The two device types exhibited similar behavior, with only slight variance in the maximum polarization measured. With the consistency of the device fabrication validated, and the excellent agreement of device dielectric and ferroelectric behavior between the two device sets, it was concluded that the top electrode material (Au, Pt) did not have a significant influence on device performance. To maintain consistency for the following experiments, gold was selected as the standard electrode material until process integration with printed conductive electrode materials was implemented (to be discussed in Chapter 6). The effect of electrode material on device performance will be revisited in that chapter, where the influence of carbon or zinc-based printed electrodes will be evaluated as compared to thermally evaporated gold electrodes.

8.5.2 Humidity sensitivity of printed KN films

Early investigations of device capacitance noted that the as-fabricated devices showed a high sensitivity to changes in ambient humidity, with device capacitance changing by more than 50% depending on ambient conditions. As KNbO_3 is known to be highly hygroscopic, there was a concern that environmental changes of this manner would negatively affect device performance. To assess the significance of this, investigations were conducted to determine the change in sample capacitance as a function of ambient humidity in a controlled setting. Printed samples fabricated using the process

described above were installed in an Espec environmental chamber SH-661 and their capacitance was measured using an Agilent E4980A LCR meter, with a logging frequency of 0.1 Hz. The temperature of the chamber was held constant at 24.3 °C (replicating ambient conditions), and the relative humidity cycled between 35, 45, and 55%RH with a 30 min soak period at each condition, repeated 6 times. The resulting data is plotted in Figure 8.12(a). The samples exhibited a high degree of variance and drift over the course of the test, with a maximum change of over 250% from the initial capacitance value (measured at 20%RH).

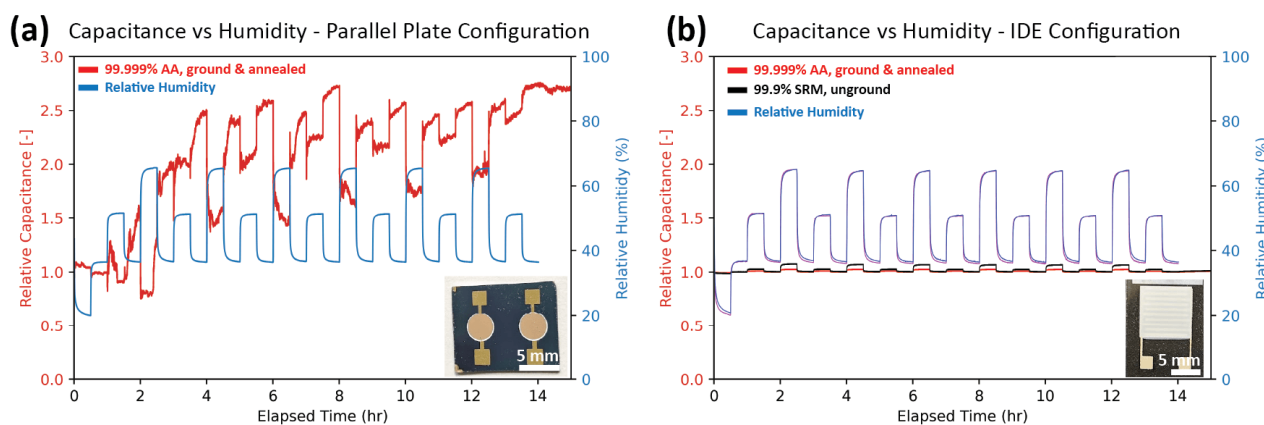


Figure 8.12 Influence of ambient humidity on KN device capacitance, showing response when evaluated using (a) a parallel plate device configuration and (b) an inter-digitated electrode configuration.

It was hypothesized that, in addition to the expected material response from adsorbed water changing the device capacitance, there may be changes to device layer thickness convoluting the resulting response. To decouple this issue, the investigation was repeated with devices instead fabricated using an inter-digitate electrode (IDE) configuration, with screen-printed silver electrodes covered by a stencil printed piezoelectric layer. With the planar electrodes, the inter-electrode distance was fixed, and the resulting device response reflected this changed as a dramatic reduction in capacitance drift (Figure 8.12(b)). This improved process was repeated with inks prepared using two different source powders, from which it was observed that the 99.9% purity SRM powder had a larger response to changed in humidity than the 99.999% purity AA powder (ground and annealed), but both inks showed a relatively low sensitivity to changes in humidity, with the capacitance of the IDE coated with 99.9% pure SRM ink increasing by just 7.5% when the relative humidity was increased to 55%RH. For the 99.999% AA ink, this was just 2.5% at 55%RH. Due to the lack of experimental control of these powders in terms of material purity and particle size, the difference in sensitivity could be attributed either to material properties or to a difference in exposed surface area resulting from the difference in particle size distribution. Future studies should introduce an encapsulation layer to reduce device performance variability to changing humidity levels.

References

1. Kuehr, R. E-waste seen from a global perspective. in *Waste Electrical and Electronic Equipment (WEEE) Handbook* 1–16 (Elsevier, 2019). doi:10.1016/B978-0-08-102158-3.00001-X.
2. Balde, C. & Forti, V. *The Global E-waste Monitor 2017: Quantities, Flows, and Resources*. vol. 35 (2015).
3. Schlupe, M. *et al. Recycling - from e-waste to resources*. (2009).
4. Iacopi, F. & McIntosh, M. Opportunities and perspectives for green chemistry in semiconductor technologies. *Green Chem.* **21**, 3250–3255 (2019).
5. Hu, S. C., Shiue, A., Chuang, H. C. & Xu, T. Life cycle assessment of high-technology buildings: Energy consumption and associated environmental impacts of wafer fabrication plants. *Energy Build.* **56**, 126–133 (2013).
6. Şengül, H., Theis, T. L. & Ghosh, S. Toward sustainable nanoproductions: An overview of nanomanufacturing methods. *J. Ind. Ecol.* **12**, 329–359 (2008).
7. Khan, S., Lorenzelli, L. & Dahiya, R. S. Technologies for Printing Sensors and Electronics Over Large Flexible Substrates: A Review. *IEEE Sens. J.* **15**, 3164–3185 (2015).
8. Lau, G. & Shrestha, M. Ink-Jet Printing of Micro-Electro-Mechanical Systems (MEMS). *Micromachines* **8**, 194 (2017).
9. Calvert, P. Inkjet Printing for Materials and Devices. *Chem. Mater.* **13**, 3299–3305 (2001).
10. Oxford English Dictionary. green, adj., sense III.13.b. (2023).
11. Le Borgne, B. *et al.* Eco-Friendly Materials for Daily-Life Inexpensive Printed Passive Devices: Towards ‘Do-it-yourself’ Electronics. *Electronics* **8**, 699 (2019).
12. Irimia-Vladu, M. ‘Green’ electronics: Biodegradable and biocompatible materials and devices for sustainable future. *Chem. Soc. Rev.* **43**, 588–610 (2014).
13. Tan, M. J. *et al.* Biodegradable electronics: cornerstone for sustainable electronics and transient applications. *J. Mater. Chem. C* **4**, 5531–5558 (2016).
14. Chen, Y. *Transient electronics: Materials, mechanics, and applications*. (Iowa State University, 2018).
15. Fu, K. K., Wang, Z., Dai, J., Carter, M. & Hu, L. Transient Electronics: Materials and Devices. *Chem. Mater.* **28**, 3527–3539 (2016).
16. Jung, Y. H., Zhang, H., Gong, S. & Ma, Z. High-performance green semiconductor devices: Materials, designs, and fabrication. *Semicond. Sci. Technol.* **32**, (2017).
17. Yu, X., Shou, W., Mahajan, B. K., Huang, X. & Pan, H. Materials, Processes, and Facile Manufacturing for Bioresorbable Electronics: A Review. *Adv. Mater.* **30**, 1–27 (2018).
18. Bioplastics, E. *EN 13432 Certified Bioplastics Performance in Industrial Composting*. (2015).
19. Klemchuk, P. P. Degradable plastics: A critical review. *Polym. Degrad. Stab.* **27**, 183–202 (1990).
20. Beguin, P. & Aubert, J.-P. The Biological degradation of Cellulose. *FEMS Microbiol. Rev.* **13**, 25–58 (1994).
21. Feig, V. R., Tran, H. & Bao, Z. Biodegradable Polymeric Materials in Degradable Electronic Devices. *ACS Cent. Sci.* **4**, 337–348 (2018).
22. Uva, A., Lin, A., Babi, J. & Tran, H. Bioderived and degradable polymers for transient electronics. *J. Chem. Technol. Biotechnol.* **97**, 801–809 (2022).
23. Li, J., Long, Y., Yang, F. & Wang, X. Degradable piezoelectric biomaterials for wearable and implantable bioelectronics. *Curr. Opin. Solid State Mater. Sci.* 100806 (2020) doi:10.1016/j.cossms.2020.100806.
24. Morsada, Z., Hossain, M. M., Islam, M. T., Mobin, M. A. & Saha, S. Recent progress in biodegradable and bioresorbable materials: From passive implants to active electronics. *Appl. Mater. Today* **25**, (2021).
25. Ashammakhi, N. *et al.* Biodegradable Implantable Sensors: Materials Design, Fabrication, and Applications. *Adv. Funct. Mater.* **31**, (2021).
26. Cenci, M. P. *et al.* Eco-Friendly Electronics—A Comprehensive Review. *Adv. Mater. Technol.* **2001263**, 1–34 (2021).
27. Irimia-Vladu, M., Głowacki, E. D., Voss, G., Bauer, S. & Sariciftci, N. S. Green and biodegradable electronics. *Mater. Today* **15**, 340–346 (2012).
28. ASTM. *ASTM D5510-94: Standard Practice for Heat Aging of Oxidatively Degradable Plastics*. (1994).
29. Huang, X. *et al.* Biodegradable Materials for Multilayer Transient Printed Circuit Boards. *Adv. Mater.* **26**, 7371–7377 (2014).
30. Lambert, S. & Wagner, M. Environmental performance of bio-based and biodegradable plastics: the road ahead. *Chem. Soc. Rev.* **46**, 6855–6871 (2017).
31. Wen, D. L. *et al.* Recent progress in silk fibroin-based flexible electronics. *Microsyst. Nanoeng.* **7**, (2021).
32. Yin, L. *et al.* Dissolvable Metals for Transient Electronics. *Adv. Funct. Mater.* **24**, 645–658 (2014).
33. Mahajan, B. K. *et al.* Aerosol printing and photonic sintering of bioresorbable zinc nanoparticle ink for transient electronics manufacturing. *Sci. China Inf. Sci.* **61**, 1–10 (2018).

34. Li, J. *et al.* Anhydride-Assisted Spontaneous Room Temperature Sintering of Printed Bioresorbable Electronics. *Adv. Funct. Mater.* **1905024**, 1905024 (2019).
35. Kamyshny, A. & Magdassi, S. Conductive nanomaterials for printed electronics. *Small* **10**, 3515–3535 (2014).
36. Feng, S., Tian, Z., Wang, J., Cao, S. & Kong, D. Laser Sintering of Zn Microparticles and Its Application in Printable Biodegradable Electronics. *Printable Electron.* **1800693**, 1–7 (2019).
37. Shou, W. *et al.* Low-Cost Manufacturing of Bioresorbable Conductors by Evaporation–Condensation-Mediated Laser Printing and Sintering of Zn Nanoparticles. *Adv. Mater.* **29**, 1–7 (2017).
38. Perelaer, J. *et al.* Printed electronics: the challenges involved in printing devices, interconnects, and contacts based on inorganic materials. *J. Mater. Chem.* **20**, 8446–8453 (2010).
39. Raut, N. C. & Al-Shamery, K. Inkjet printing metals on flexible materials for plastic and paper electronics. *J. Mater. Chem. C* **6**, 1618–1641 (2018).
40. Hwang, H. J., Chung, W. H. & Kim, H. S. In-situ monitoring of flash-light sintering of copper nanoparticle ink for printed electronics. *Nanotechnology* **23**, (2012).
41. Liu, J., Ji, H., Wang, S. & Li, M. The low temperature exothermic sintering of formic acid treated Cu nanoparticles for conductive ink. *J. Mater. Sci. Mater. Electron.* **27**, 13280–13287 (2016).
42. Karunakaran, R., Orgies, S., Tamayol, A., Bobaru, F. & Sealy, M. P. Additive manufacturing of magnesium alloys. *Bioact. Mater.* **5**, 44–54 (2020).
43. Telang, V. S. *et al.* Harnessing additive manufacturing for magnesium-based metallic bioimplants: Recent advances and future perspectives. *Curr. Opin. Biomed. Eng.* **17**, 100264 (2021).
44. Kwon, J. *et al.* Digitally patterned resistive micro heater as a platform for zinc oxide nanowire based micro sensor. *Appl. Surf. Sci.* **447**, 1–7 (2018).
45. Fumeaux, N. & Briand, D. Zinc hybrid sintering for printed transient sensors and wireless electronics. *Npj Flex. Electron.* **7**, 14 (2023).
46. Banerjee, S., Bairagi, S. & Wazed Ali, S. A critical review on lead-free hybrid materials for next generation piezoelectric energy harvesting and conversion. *Ceram. Int.* **47**, 16402–16421 (2021).
47. Priya, S. *et al.* A Review on Piezoelectric Energy Harvesting: Materials, Methods, and Circuits. *Energy Harvest. Syst.* **4**, 3–39 (2017).
48. Aksel, E. & Jones, J. L. Advances in Lead-Free Piezoelectric Materials for Sensors and Actuators. *Sensors* **10**, 1935–1954 (2010).
49. Wu, H., Murti, B. T., Singh, J., Yang, P. & Tsai, M. Prospects of Metal-Free Perovskites for Piezoelectric Applications. *Adv. Sci.* **9**, 2104703 (2022).
50. He, H. *et al.* Advances in lead-free pyroelectric materials: A comprehensive review. *J. Mater. Chem. C* **8**, 1494–1516 (2020).
51. Shibata, K., Wang, R., Tou, T. & Koruza, J. Applications of lead-free piezoelectric materials. *MRS Bull.* **43**, 612–616 (2018).
52. Wei, H. *et al.* An overview of lead-free piezoelectric materials and devices. *J. Mater. Chem. C* **6**, 12446–12467 (2018).
53. Safari, A. & Abazari, M. Lead-free piezoelectric ceramics and thin films. *IEEE Trans. Ultrason. Ferroelectr. Freq. Control* **57**, 2165–2176 (2010).
54. Zhang, N., Zheng, T. & Wu, J. Lead-Free (K,Na)NbO₃-Based Materials: Preparation Techniques and Piezoelectricity. *ACS Omega* **5**, 3099–3107 (2020).
55. Rödel, J. *et al.* Perspective on the Development of Lead-free Piezoceramics. *J. Am. Ceram. Soc.* **92**, 1153–1177 (2009).
56. Panda, P. K. Review: Environmental friendly lead-free piezoelectric materials. *J. Mater. Sci.* **44**, 5049–5062 (2009).
57. Panda, P. K. & Sahoo, B. PZT to lead free piezo ceramics: A review. *Ferroelectrics* **474**, 128–143 (2015).
58. Chorsi, M. T. *et al.* Piezoelectric Biomaterials for Sensors and Actuators. *Adv. Mater.* **31**, 1802084 (2019).
59. Iacomini, A. *et al.* Processing Optimization and Toxicological Evaluation of “Lead-Free” Piezoceramics: A KNN-Based Case Study. *Materials* **14**, 4337 (2021).
60. Jewett, S. A., Makowski, M. S., Andrews, B., Manfra, M. J. & Ivanisevic, A. Gallium nitride is biocompatible and non-toxic before and after functionalization with peptides. *Acta Biomater.* **8**, 728–733 (2012).
61. Murali, P. Recent Progress in Materials Issues for Piezoelectric MEMS. *J. Am. Ceram. Soc.* **91**, 1385–1396 (2008).
62. Petroni, S. *et al.* Aluminum Nitride piezo-MEMS on polyimide flexible substrates. *Microelectron. Eng.* **88**, 2372–2375 (2011).
63. Berg, N. G., Paskova, T. & Ivanisevic, A. Tuning the biocompatibility of aluminum nitride. *Mater. Lett.* **189**, 1–4 (2017).
64. Zhang, Y., Nayak, T. R., Hong, H. & Cai, W. Biomedical Applications of Zinc Oxide Nanomaterials. *Curr. Mol. Med.* **13**, 1633–1645 (2013).
65. Peng, X. *et al.* Perovskite and Organic Solar Cells Fabricated by Inkjet Printing: Progress and Prospects. *Adv. Funct. Mater.* **27**, (2017).
66. Krishnan, B. & Nampoory, V. P. N. Screen printed nanosized ZnO thick film. *Bull. Mater. Sci.* **28**, 239–242 (2005).

67. Garcia-Farrera, B. & Velasquez-Garcia, L. F. Room Temperature Direct Writing of Ultrathin Zinc Oxide Piezoelectric Films Via Near-Field Electrohydrodynamic Jetting for High-Frequency Flexible Electronics. in *2019 20th International Conference on Solid-State Sensors, Actuators and Microsystems & Eurosensors XXXIII (TRANSDUCERS & EUROSENSORS XXXIII)* 1651–1654 (IEEE, 2019). doi:10.1109/TRANSDUCERS.2019.8808776.
68. Manbachi, A. & Cobbold, R. S. C. Development and application of piezoelectric materials for ultrasound generation and detection. *Ultrasound* **19**, 187–196 (2011).
69. Jung, J. *et al.* Review of piezoelectric micromachined ultrasonic transducers and their applications. *J. Micromechanics Microengineering* **27**, (2017).
70. Smirnov, A. *et al.* Progress and challenges of 3D-printing technologies in the manufacturing of piezoceramics. *Ceram. Int.* **47**, 10478–10511 (2021).
71. Chen, C. *et al.* Additive Manufacturing of Piezoelectric Materials. *Adv. Funct. Mater.* **30**, 1–29 (2020).
72. Leontsev, S. O. & Eitel, R. E. Progress in engineering high strain lead-free piezoelectric ceramics. *Sci. Technol. Adv. Mater.* **11**, (2010).
73. Uetsuji, Y. *et al.* Biocompatibility Evaluation of Piezoelectric Materials through Cytotoxicity Test. *J. Soc. Mater. Sci. Jpn.* **57**, 899–904 (2008).
74. Tressler, J. F., Alkoy, S. & Newnham, R. E. Piezoelectric Sensors and Sensor Materials. *J. Electroceramics* **2**, 257–272 (1998).
75. Acosta, M. *et al.* BaTiO₃-based piezoelectrics: Fundamentals, current status, and perspectives. *Appl. Phys. Rev.* **4**, (2017).
76. Cui, H. *et al.* Three Dimensional printing of piezoelectric materials with designed anisotropy and directional response. *Nat. Mater.* (2019) doi:10.1038/s41563-018-0268-1.
77. Smith, G. L. *et al.* PZT-based piezoelectric MEMS technology. *J. Am. Ceram. Soc.* **95**, 1777–1792 (2012).
78. Safaryan, S. *et al.* Diphenylalanine-Based Microribbons for Piezoelectric Applications via Inkjet Printing. *Appl. Mater. Interfaces* **10**, 10543–10551 (2018).
79. Zorlutuna, P. *et al.* Microfabricated Biomaterials for Engineering 3D Tissues. *Adv. Mater.* **24**, 1782–1804 (2012).
80. Gans, B. D., Duineveld, P. C. & Schubert, U. S. Inkjet Printing of Polymers: State of the Art and Future Developments. *Adv. Mater.* **16**, 203–213 (2004).
81. Curie, J. & Curie, P. Développement par compression de l'électricité polaire dans les cristaux hémihédres à faces inclinées. *Bull. Société Minéralogique Fr.* **3**, 90–93 (1880).
82. Chen, S. *et al.* Biodegradable Elastomers and Gels for Elastic Electronics. *Adv. Sci.* **9**, 1–27 (2022).
83. Cheng, Y. *et al.* Rheology of edible food inks from 2D/3D/4D printing, and its role in future 5D/6D printing. *Food Hydrocoll.* **132**, 107855 (2022).
84. Ali, M., Bathaei, M. J., Istif, E., Karimi, S. N. H. & Beker, L. Biodegradable Piezoelectric Polymers: Recent Advancements in Materials and Applications. *Adv. Healthc. Mater.* 2300318 (2023) doi:10.1002/adhm.202300318.
85. Kimura, T. Processing of textured piezoelectric and dielectric perovskite-structured ceramics by the reactive-templated grain growth method. in *Handbook of Advanced Dielectric, Piezoelectric and Ferroelectric Materials* 799–817 (CRC Press, 2008). doi:10.1201/9781439832882.ch26.
86. Tao, H. *et al.* Inkjet Printing of Regenerated Silk Fibroin: From Printable Forms to Printable Functions. *Adv. Mater.* **27**, 4273–4279 (2015).
87. Kaczmarek, H., Królikowski, B., Klimiec, E., Chylińska, M. & Bajer, D. Advances in the study of piezoelectric polymers. *Russ. Chem. Rev.* **88**, 749–774 (2019).
88. Silva, C. C. *et al.* Collagen-hydroxyapatite films: piezoelectric properties. *Mater. Sci. Eng. B* **86**, 210–218 (2001).
89. Lang, S. B. *et al.* Pyroelectric, piezoelectric, and photoeffects in hydroxyapatite thin films on silicon. *Appl. Phys. Lett.* **98**, 123703 (2011).
90. Chen-Glasser, M., Li, P., Ryu, J. & Hong, S. Piezoelectric Materials for Medical Applications. in *Piezoelectricity - Organic and Inorganic Materials and Applications* (2018).
91. Ghosh, S. K., Park, J., Na, S., Kim, M. P. & Ko, H. A Fully Biodegradable Ferroelectric Skin Sensor from Edible Porcine Skin Gelatine. *Adv. Sci.* **2005010**, 1–11 (2021).
92. Lay, R., Deijis, G. S. & Malmström, J. The intrinsic piezoelectric properties of materials - a review with a focus on biological materials. *RSC Adv.* **11**, 30657–30673 (2021).
93. Fuse, N. *et al.* Partial Discharge Degradation of Several Biodegradable Polymers. *Electr. Eng. Jpn.* **168**, 459–466 (2009).
94. Ando, M., Kawamura, H., Kageyama, K. & Tajitsu, Y. Film sensor device fabricated by a piezoelectric poly(L-lactic acid) film. *Jpn. J. Appl. Phys.* **51**, (2012).
95. Ribeiro, C., Sencadas, V., Correia, D. M. & Lanceros-méndez, S. Piezoelectric polymers as biomaterials for tissue engineering applications. *Colloids Surf. B Biointerfaces* **136**, 46–55 (2015).
96. Karanth, D., Puleo, D., Dawson, D., Holliday, L. S. & Sharab, L. Characterization of 3D printed biodegradable piezoelectric scaffolds for bone regeneration. *Clin. Exp. Dent. Res.* **9**, 398–408 (2023).

97. Sun, Q. *et al.* Functional biomaterials towards flexible electronics and sensors. *Biosens. Bioelectron.* **119**, 237–251 (2018).
98. Rezwani, K., Chen, Q. Z., Blaker, J. J. & Roberto, A. Biodegradable and bioactive porous polymer/inorganic composite scaffolds for bone tissue engineering. *Biomaterials* **27**, 3413–3431 (2006).
99. Emadian, S. M., Onay, T. T. & Demirel, B. Biodegradation of bioplastics in natural environments. *Waste Manag.* **59**, 526–536 (2017).
100. Holmes, P. A. Applications of PHB - a Microbially Produced Biodegradable Thermoplastic. *Phys. Technol.* **16**, (1985).
101. Habib, M., Lantgios, I. & Hornbostel, K. A review of ceramic, polymer and composite piezoelectric materials. *J. Phys. Appl. Phys.* **55**, 423002 (2022).
102. Ramadan, K. S., Sameoto, D. & Evoy, S. A review of piezoelectric polymers as functional materials for electromechanical transducers. *Smart Mater. Struct.* **23**, (2014).
103. Rim, Y. S., Bae, S., Chen, H., Marco, N. D. & Yang, Y. Recent Progress in Materials and Devices toward Printable and Flexible Sensors. *Adv. Mater.* **28**, 4415–4440 (2016).
104. Haque, R. I. *et al.* Inkjet printing of high molecular weight PVDF-TrFE for flexible electronics. *Flex. Print. Electron.* **1**, 015001 (2016).
105. Thuau, D., Kallitsis, K., Dos Santos, F. D. & Hadziioannou, G. All inkjet-printed piezoelectric electronic devices: energy generators, sensors and actuators. *J. Mater. Chem. C* **5**, 9963–9966 (2017).
106. Valasek, J. Piezoelectric and allied phenomena in Rochelle Salt. *Phys. Rev.* **17**, 475–481 (1921).
107. Horia, V. A. Second-order transition in Rochelle-salt saturated solutions. *Phys. Rev. A* **45**, (1992).
108. Milek, M. & Neuberger, J. T. Ammonium Dihydrogen Phosphate (ADP). in *Linear Electrooptic Modular Materials* 23–24 (1972).
109. Tichý, J., Erhart, J., Kittinger, E. & Přivratská, J. *Fundamentals of Piezoelectric Sensorics. Fundamentals of Piezoelectric Sensorics* (2010). doi:10.1007/978-3-540-68427-5.
110. Gautschi, G. *Piezoelectric Sensorics*. (Springer Berlin Heidelberg, 2002). doi:10.1007/978-3-662-04732-3.
111. Nissen, N. F. WEEE Ch 16 - ErP – the European directive on ecodesign. in *Waste Electrical and Electronic Equipment (WEEE) Handbook* 423–441 (2019). doi:10.1016/b978-0-08-102158-3.00016-1.
112. Aleeva, Y. & Pignataro, B. Recent advances in upscalable wet methods and ink formulations for printed electronics. *J. Mater. Chem. C* **2**, 6436–6453 (2014).
113. Sreenilayam, S. P., Ahad, I. U., Nicolosi, V., Acinas Garzon, V. & Brabazon, D. Advanced materials of printed wearables for physiological parameter monitoring. *Mater. Today xxx*, (2019).
114. Wu, W. Inorganic nanomaterials for printed electronics: A review. *Nanoscale* **9**, 7342–7372 (2017).
115. Li, J. *et al.* Micro and nano materials and processing techniques for printed biodegradable electronics. *Mater. Today Nano* **18**, 100201 (2022).
116. Garlapati, S. K. *et al.* Printed Electronics Based on Inorganic Semiconductors: From Processes and Materials to Devices. *Adv. Mater.* **30**, 1707600 (2018).
117. ASTM F1842-15: Standard Test Method for Determining Ink or Coating Adhesion on Flexible Substrates for a Membrane Switch or Printed Electronic Device. doi:10.1520/F1842-15.
118. Mancinelli, A. Deep-UV approaches and printing of indium zinc oxide thin-film transistors targeting their processing on thermosensitive substrates.
119. Derby, B. Inkjet printing ceramics: From drops to solid. *J. Eur. Ceram. Soc.* **31**, 2543–2550 (2011).
120. Derby, B. Inkjet Printing of Functional and Structural Materials: Fluid Property Requirements, Feature Stability, and Resolution. *Annu. Rev. Mater. Res.* **40**, 395–414 (2010).
121. Zhang, Y. *et al.* Ink formulation, scalable applications and challenging perspectives of screen printing for emerging printed microelectronics. *J. Energy Chem.* **63**, 498–513 (2021).
122. Suresh, R. R. *et al.* Fabrication of screen-printed electrodes: opportunities and challenges. *J. Mater. Sci.* **56**, 8951–9006 (2021).
123. Zavanelli, N. & Yeo, W.-H. Advances in Screen Printing of Conductive Nanomaterials for Stretchable Electronics. *ACS Omega* **6**, 9344–9351 (2021).
124. Somalu, M. ., Muchtar, A., Daud, W. R. W. & Brandon, N. P. Screen-printing inks for the fabrication of solid oxide fuel cell films: A review. *Renew. Sustain. Energy Rev.* **75**, 426–439 (2017).
125. Lee, D. H. & Derby, B. Preparation of PZT suspensions for direct ink jet printing. *J. Eur. Ceram. Soc.* **24**, 1069–1072 (2004).
126. Anand, K. & Varghese, S. Role of surfactants on the stability of nano-zinc oxide dispersions. *Part. Sci. Technol.* **35**, 67–70 (2017).
127. Huang, Q. & Zhu, Y. Printing Conductive Nanomaterials for Flexible and Stretchable Electronics: A Review of Materials, Processes, and Applications. *Adv. Mater. Technol.* **4**, 1–41 (2019).

128. Jung, M., Ji, S. G., Kim, G. & Seok, S. I. Perovskite precursor solution chemistry: From fundamentals to photovoltaic applications. *Chem. Soc. Rev.* **48**, 2011–2038 (2019).
129. Chilibon, I. & Marat-Mendes, J. N. Ferroelectric ceramics by sol–gel methods and applications: a review. *J. Sol-Gel Sci. Technol.* **64**, 571–611 (2012).
130. Kim, D. W. *et al.* Rapid curing of solution-processed zinc oxide films by pulse-light annealing for thin-film transistor applications. *Electron. Mater. Lett.* **11**, 82–87 (2015).
131. Zhang, Y. & Chen, D. *Multilayer Integrated Film Bulk Acoustic Resonators. Multilayer Integrated Film Bulk Acoustic Resonators* (2013). doi:10.1007/978-3-642-31776-7_9.
132. Cernea, M., Andronescu, E., Radu, R., Fochi, F. & Galassi, C. Sol-gel synthesis and characterization of BaTiO₃-doped (Bi_{0.5}Na_{0.5})TiO₃ piezoelectric ceramics. *J. Alloys Compd.* **490**, 690–694 (2010).
133. Praveen, J. P. *et al.* Effect of poling process on piezoelectric properties of sol-gel derived BZT-BCT ceramics. *J. Eur. Ceram. Soc.* **35**, 1785–1798 (2015).
134. Almasri, A., Ounaies, Z., Kim, Y. S. & Grunlan, J. Characterization of Solution-Processed Double-Walled Carbon Nanotube Poly(vinylidene fluoride) Nanocomposites. *Macromol. Mater. Eng.* **293**, 123–131 (2008).
135. Wang, M., Wang, J., Chen, W., Cui, Y. & Wang, L. Effect of preheating and annealing temperatures on quality characteristics of ZnO thin film prepared by sol-gel method. *Mater. Chem. Phys.* **97**, 219–225 (2006).
136. Sekine, T. *et al.* Fully printed and flexible ferroelectric capacitors based on a ferroelectric polymer for pressure detection. *Jpn. J. Appl. Phys.* **55**, 10TA18 (2016).
137. Zirkl, M. *et al.* An All-Printed Ferroelectric Active Matrix Sensor Network Based on Only Five Functional Materials Forming a Touchless Control Interface. *Adv. Mater.* **23**, 2069–2074 (2011).
138. Jagers, R. M. Is Polyvinylidene difluoride (PVDF) film biocompatible in the Murine Cochlea? (Wright State University Follow, 2015).
139. Zhang, H., Jiang, S., Xiao, J. & Kajiyoshi, K. Low temperature preparation and electrical properties of sodium-potassium bismuth titanate lead-free piezoelectric thick films by screen printing. *J. Eur. Ceram. Soc.* **30**, 3157–3165 (2010).
140. Burns, S. R. & Dolgos, M. R. Sizing up (K_{1-x}Na_x)NbO₃ films: a review of synthesis routes, properties & applications. *New J. Chem.* **45**, 7408–7436 (2021).
141. Trung, D. T. & Fisher, J. G. Controlled-Atmosphere Sintering of KNbO₃. *Appl. Sci.* **10**, 2131 (2020).
142. Wu, J., Xiao, D. & Zhu, J. Potassium–sodium niobate lead-free piezoelectric ceramics: recent advances and perspectives. *J. Mater. Sci. Mater. Electron.* **26**, 9297–9308 (2015).
143. Glynne-Jones, P., Beeby, S. P., Dargie, P., Papakostas, T. & White, N. M. An investigation into the effect of modified firing profiles on the piezoelectric properties of thick-film PZT layers on silicon. *Meas. Sci. Technol.* **11**, 526–531 (2000).
144. Grall, S., Santawitee, O., Dufour, I., Aubry, V. & Debéda, H. New corn-based sacrificial layer for MEMS based on screen-printed PZT ceramics. *Sens. Actuators Phys.* **304**, 111826 (2020).
145. Ma, N., Zhang, B.-P., Yang, W.-G. & Guo, D. Phase structure and nano-domain in high performance of BaTiO₃ piezoelectric ceramics. *J. Eur. Ceram. Soc.* **32**, 1059–1066 (2012).
146. Kim, H. T. & Han, Y. H. Sintering of nanocrystalline BaTiO₃. *Ceram. Int.* **30**, 1719–1723 (2004).
147. Gao, J., Xue, D., Liu, W., Zhou, C. & Ren, X. Recent Progress on BaTiO₃-Based Piezoelectric Ceramics for Actuator Applications. *Actuators* **6**, 24 (2017).
148. Nguyen, V.-C. *et al.* Printing smart coating of piezoelectric composite for application in condition monitoring of bearings. *Mater. Des.* **215**, 110529 (2022).
149. Khan, S., Dang, W., Lorenzelli, L. & Dahiya, R. Flexible Pressure Sensors Based on Screen-Printed P(VDF-TrFE) and P(VDF-TrFE)/MWCNTs. *IEEE Trans. Semicond. Manuf.* **28**, 486–493 (2015).
150. Mazaheri, M., Zahedi, A. M. & Sadrnezhad, S. K. Two-step sintering of nanocrystalline ZnO compacts: Effect of temperature on densification and grain growth. *J. Am. Ceram. Soc.* **91**, 56–63 (2008).
151. García-Farrera, B. & Velásquez-García, L. F. Ultrathin Ceramic Piezoelectric Films via Room-Temperature Electro Spray Deposition of ZnO Nanoparticles for Printed GHz Devices. *ACS Appl. Mater. Interfaces* **11**, 29167–29176 (2019).
152. Gao, X. *et al.* Piezoelectric Actuators and Motors: Materials, Designs, and Applications. *Adv. Mater. Technol.* **5**, 1900716 (2020).
153. Ando, A. & Kimura, M. Resonator Characteristics of Bismuth Layer Structured Ferroelectric Materials. in *Lead-Free Piezoelectrics* 373–403 (Springer New York, 2012). doi:10.1007/978-1-4419-9598-8_13.
154. Dalle Vache, S. *et al.* The effect of processing conditions on the morphology, thermomechanical, dielectric, and piezoelectric properties of P(VDF-TrFE)/BaTiO₃ composites. *J. Mater. Sci.* **47**, 4763–4774 (2012).
155. Trolier-McKinstry, S. & Murali, P. Thin film piezoelectrics for MEMS. *J. Electroceramics* **12**, 7–17 (2004).
156. Fu, Y. Q. *et al.* Advances in piezoelectric thin films for acoustic biosensors, acoustofluidics, and lab-on-chip applications. *Prog. Mater. Sci.* **89**, 31–91 (2017).

157. Eom, C. B. & Trolier-McKinstry, S. Thin-film piezoelectric MEMS. *MRS Bull.* **37**, 1007–1017 (2012).
158. Khan, A., Abas, Z., Kim, H. S. & Oh, I. Piezoelectric thin films: an integrated review of transducers and energy harvesting. *Smart Mater. Struct.* **25**, (2016).
159. Bukowski, T. J. *et al.* Piezoelectric properties of sol-gel derived ZnO thin films. *Integr. Ferroelectr.* **17**, 339–347 (1997).
160. Akmal, M. H. M. *et al.* Optimizing the processing conditions of sodium potassium niobate thin films prepared by sol-gel spin coating technique. *Ceram. Int.* **44**, 317–325 (2018).
161. Kobayashi, T., Tsauro, J., Ichiki, M. & Maeda, R. Fabrication and performance of a flat piezoelectric cantilever obtained using a sol-gel derived PZT thick film deposited on a SOI wafer. *Smart Mater. Struct.* **15**, (2006).
162. Messing, G. L. *et al.* Templated Grain Growth of Textured Piezoelectric Ceramics. *Crit. Rev. Solid State Mater. Sci.* **29**, 45–96 (2004).
163. Wang, C. *et al.* High Performance Flexible Piezocomposites Based on a Particle Alignment Strategy. *Eur. J. Inorg. Chem.* **2020**, 770–772 (2020).
164. Sarkar, P. & Nicholson, P. S. Electrophoretic Deposition (EPD): Mechanisms, Kinetics, and Application to Ceramics. *J. Am. Ceram. Soc.* **79**, 1987–2002 (1996).
165. Khanbareh, H., Van Der Zwaag, S. & Groen, W. A. Effect of dielectrophoretic structuring on piezoelectric and pyroelectric properties of lead titanate-epoxy composites. *Smart Mater. Struct.* **23**, (2014).
166. Kohli, M. & Murali, P. Poling of ferroelectric thin films. *Ferroelectrics* **225**, 155–162 (1999).
167. Kounga, A. B., Granzow, T., Aulbach, E., Hinterstein, M. & Rödel, J. High-temperature poling of ferroelectrics. *J. Appl. Phys.* **104**, (2008).
168. Kamel, T. M. & de With, G. Poling of hard ferroelectric PZT ceramics. *J. Eur. Ceram. Soc.* **28**, 1827–1838 (2008).
169. Wada, S., Seike, A. & Tsurumi, T. Poling Treatment and Piezoelectric Properties of Potassium Niobate Ferroelectric Single Crystals. *Jpn. J. Appl. Phys.* **40**, 5690–5697 (2001).
170. Cholleti, E. R. A Review on 3D printing of piezoelectric materials. *IOP Conf. Ser. Mater. Sci. Eng.* **455**, (2018).
171. Gullapalli, H. *et al.* Flexible Piezoelectric ZnO-Paper Nanocomposite Strain Sensor. *Small* **6**, 1641–1646 (2010).
172. Mun, S. *et al.* Enhanced electromechanical behavior of cellulose film by zinc oxide nanocoating and its vibration energy harvesting. *Acta Mater.* **114**, 1–6 (2016).
173. Ko, H.-U., Kim, H. C., Kim, J. W., Zhai, L. & Kim, J. Fabrication Method Study of ZnO Nanocoated Cellulose Film and Its Piezoelectric Property. *Materials* **10**, 611 (2017).
174. Costa, S. V., Gonçalves, A. S., Zaguete, M. A., Mazon, T. & Nogueira, A. F. ZnO nanostructures directly grown on paper and bacterial cellulose substrates without any surface modification layer. *Chem. Commun.* **49**, 8096–8098 (2013).
175. Wang, Y. *et al.* A Paper-Based Piezoelectric Accelerometer. *Micromachines* **9**, (2018).
176. Song, P., Wang, Y. & Liu, X. Flexible physical sensors made from paper substrates integrated with zinc oxide nanostructures. *Flex. Print. Electron.* **2**, (2017).
177. Kim, K.-H., Lee, K. Y., Seo, J.-S., Kumar, B. & Kim, S.-W. Paper-Based Piezoelectric Nanogenerators with High Thermal Stability. *Small* **7**, 2577–2580 (2011).
178. Zhu, G., Yang, R., Wang, S. & Wang, Z. L. Flexible high-output nanogenerator based on lateral ZnO nanowire array. *Nano Lett.* **10**, 3151–3155 (2010).
179. Dagdeviren, C. *et al.* Transient, biocompatible electronics and energy harvesters based on ZnO. *Small* **9**, 3398–3404 (2013).
180. Kim, K. N. *et al.* Silk fibroin-based biodegradable piezoelectric composite nanogenerators using lead-free ferroelectric nanoparticles. *Nano Energy* **14**, 87–94 (2015).
181. Maiti, S. *et al.* Bio-waste onion skin as an innovative nature-driven piezoelectric material with high energy conversion efficiency. *Nano Energy* **42**, 282–293 (2017).
182. Curry, E. J. *et al.* Biodegradable Piezoelectric Force Sensor. *Proc. Natl. Acad. Sci.* **115**, 909–914 (2018).
183. Lemaire, E., Briand, D., Haque, R. I., Atli, A. & Monroe, M. M. Green Piezoelectric Transducers Based on Transfer and Printing of Piezoelectric Inks. in vol. 1 99–100 (2019).
184. Lemaire, E., Moser, R., Borsa, C. J., Shea, H. & Danick, B. Green paper-based piezoelectric material for sensors and actuators. in *Procedia Engineering* vol. 120 360–363 (Elsevier B.V., 2015).
185. Lemaire, E., Moser, R., Borsa, C. J. & Danick, B. Green paper-based piezoelectronics for sensors and actuators. *Sens. Actuators Phys.* **244**, 285–291 (2016).
186. Lemaire, E., Ayela, C. & Atli, A. Eco-friendly materials for large area piezoelectronics: self-oriented Rochelle salt in wood. *Smart Mater. Struct.* **27**, (2018).
187. Kim, J. *et al.* Paper Actuators Made with Cellulose and Hybrid Materials. *Sensors* **10**, 1473–1485 (2010).
188. Rajala, S. *et al.* Cellulose Nanofibril Film as a Piezoelectric Sensor Material. *Appl. Mater. Interfaces* **8**, 15607–15614 (2016).
189. Kim, J. H., Yun, S., Kim, J. H. & Kim, J. Fabrication of Piezoelectric Cellulose Paper and Audio Application. *J. Bionic Eng.* **6**, 18–21 (2009).

190. Ba, Y., Bao, J., Song, R., Zhu, C. & Zhang, X. Printing Paper-like Piezoelectric Energy Harvesters based on Natural Cellulose Nanofibrils. in *Transducers 2019* vol. 1 1451–1454 (2019).
191. Kim, K. *et al.* Biodegradable, electro-active chitin nanofiber films for flexible piezoelectric transducers. *Nano Energy* **48**, 275–283 (2018).
192. Karan, S. K. *et al.* A new insight towards eggshell membrane as high energy conversion efficient bio-piezoelectric energy harvester. *Mater. Today Energy* **9**, 114–125 (2018).
193. Karan, S. K. *et al.* Nature driven spider silk as high energy conversion efficient bio-piezoelectric nanogenerator. *Nano Energy* **49**, 655–666 (2018).
194. Karan, S. K. *et al.* Designing high energy conversion efficient bio-inspired vitamin assisted single-structured based self-powered piezoelectric/wind/acoustic multi-energy harvester with remarkable power density. *Nano Energy* **59**, 169–183 (2019).
195. Shin, D. M., Hong, S. W. & Hwang, Y. H. Recent advances in organic piezoelectric biomaterials for energy and biomedical applications. *Nanomaterials* **10**, (2020).
196. Yuan, H., Lei, T., Qin, Y., He, J. H. & Yang, R. Design and application of piezoelectric biomaterials. *J. Phys. Appl. Phys.* **51**, (2019).
197. Curry, E. J. *et al.* Biodegradable Piezoelectric Force Sensor. *PNAS* 1–6 (2017) doi:10.1073/pnas.1710874115.
198. Curry, E. J. *et al.* Biodegradable nanofiber-based piezoelectric transducer. *PNAS* **117**, 214–220 (2020).
199. DeBari, M. K., Keyser, M. N., Bai, M. A. & Abbott, R. D. 3D printing with silk: considerations and applications. *Connect. Tissue Res.* **61**, 163–173 (2020).
200. Karim, M. N., Afroj, S., Rigout, M., Yeates, S. G. & Carr, C. Towards UV-curable inkjet printing of biodegradable poly (lactic acid) fabrics. *J. Mater. Sci.* **50**, 4576–4585 (2015).
201. Rodriguez, M. J. *et al.* 3D freeform printing of silk fibroin. *Acta Biomater.* **71**, 379–387 (2018).
202. Nocera, A. D., Comín, R., Salvatierra, N. A. & Cid, M. P. Development of 3D printed fibrillar collagen scaffold for tissue engineering. *Biomed. Microdevices* **20**, 26 (2018).
203. Goldmann, T. & Gonzalez, J. S. DNA-printing: utilization of a standard inkjet printer for the transfer of nucleic acids to solid supports. *J. Biochem. Biophys. Methods* **42**, 105–110 (2000).
204. Lang, S. B. *et al.* Ferroelectric Polarization in Nanocrystalline Hydroxyapatite Thin Films on Silicon. *Nat. Sci. Rep.* (2013) doi:10.1038/srep02215.
205. Markham, S. K., Stapleton, A., Haq, E. U., Kowal, K. & Tofail, S. A. M. Piezoelectricity in screen-printed hydroxyapatite thick films. *Ferroelectrics* **509**, 99–104 (2017).
206. Markham, S. K. Electrical Properties of Hydroxyapatite Thick Films. (University of Limerick).
207. Schneider, J. J. *et al.* Zinc oxide derived from single source precursor chemistry under chimie douce conditions: Formation pathway, defect chemistry and possible applications in thin film printing. *J. Mater. Chem.* **19**, 1449–1457 (2009).
208. Laurenti, M., Verna, A., Fontana, M., Quaglio, M. & Porro, S. Selective growth of ZnO nanowires on substrates patterned by photolithography and inkjet printing. *Appl. Phys. A* **117**, 901–907 (2014).
209. Khalil, A. S. G. *et al.* Stable aqueous dispersions of ZnO nanoparticles for ink-jet printed gas sensors. in *INEC 2010 - 2010 3rd International Nanoelectronics Conference, Proceedings* 440–441 (2010). doi:10.1109/INEC.2010.5424503.
210. Rudež, R., Pavlič, J. & Bernik, S. Preparation and influence of highly concentrated screen-printing inks on the development and characteristics of thick-film varistors. *J. Eur. Ceram. Soc.* **35**, 3013–3023 (2015).
211. Gebauer, J. S., Mackert, V., Ognjanović, S. & Winterer, M. Tailoring metal oxide nanoparticle dispersions for inkjet printing. *J. Colloid Interface Sci.* **526**, 400–409 (2018).
212. Wei, Y., Zhan, Z., Du, H. & Tran, V.-T. Influence of annealing to the defect of inkjet-printed ZnO thin film. in *Proceedings of SPIE* 46 (2018). doi:10.1117/12.2286856.
213. Liang, Y. N. *et al.* Effects of the morphology of inkjet printed zinc oxide (ZnO) on thin film transistor performance and seeded ZnO nanorod growth. *Thin Solid Films* **544**, 509–514 (2013).
214. Chung, S. Y. *et al.* All-Solution-Processed Flexible Thin Film Piezoelectric Nanogenerator. *Adv. Mater.* **24**, 6022–6027 (2012).
215. Saadon, R. & Abdul Azeez, O. Chemical route to synthesis hierarchical ZnO thick films for sensor application. *Energy Procedia* **50**, 445–453 (2014).
216. Ul Hasan, K., Nur, O. & Willander, M. Screen printed ZnO ultraviolet photoconductive sensor on pencil drawn circuitry over paper. *Appl. Phys. Lett.* **100**, 98–101 (2012).
217. Patil, A. V. *et al.* Study of Microstructural Parameters of Screen Printed ZnO. *Sens. Transducers* **117**, 62–70 (2010).
218. Winarski, D. J. *et al.* Photoconductive ZnO Films Printed on Flexible Substrates by Inkjet and Aerosol Jet Techniques. *J. Electron. Mater.* **47**, 949–954 (2018).

219. Sánchez, J. G. *et al.* Impact of inkjet printed ZnO electron transport layer on the characteristics of polymer solar cells. *RSC Adv.* **8**, 13094–13102 (2018).
220. Lemaire, E., Borsari, C. J. & Danick, B. Green piezoelectric for autonomous smart textile. in *PowerMEMS 2015* vol. 660 (2015).
221. Kang, S. K. *et al.* Biodegradable Thin Metal Foils and Spin-On Glass Materials for Transient Electronics. *Adv. Funct. Mater.* **25**, 1789–1797 (2015).
222. ASTM. Overview of Biomaterials and Their Use in Medical Devices. in *Handbook of Materials for Medical Devices* (2003).
223. Liaw, D.-J. *et al.* Advanced polyimide materials: Syntheses, physical properties and applications. *Prog. Polym. Sci.* **37**, 907–974 (2012).
224. Chisca, S., Sava, I., Musteata, V.-E. & Bruma, M. Dielectric and conduction properties of polyimide films. in *CAS 2011 Proceedings (2011 International Semiconductor Conference)* 253–256 (IEEE, 2011). doi:10.1109/SMICND.2011.6095784.
225. Tortorich, R., Shamkhalichenar, H. & Choi, J.-W. Inkjet-Printed and Paper-Based Electrochemical Sensors. *Appl. Sci.* **8**, 288 (2018).
226. Zhu, B. *et al.* Silk Fibroin for Flexible Electronic Devices. *Adv. Mater.* **28**, 4250–4265 (2016).
227. Hwang, S. W. *et al.* High-performance biodegradable/transient electronics on biodegradable polymers. *Adv. Mater.* **26**, 3905–3911 (2014).
228. Chang, J. K. *et al.* Materials and processing approaches for foundry-compatible transient electronics. *Proc. Natl. Acad. Sci.* **114**, E5522–E5529 (2017).
229. Uddin, M. J., Middya, T. R. & Chaudhuri, B. K. Room temperature ferroelectric effect and enhanced dielectric permittivity in Rochelle salt/PVA percolative composite films. *Curr. Appl. Phys.* **13**, 461–466 (2013).
230. Amann, M. & Minge, O. Biodegradability of Poly(vinyl acetate) and Related Polymers. *Adv. Polym. Sci.* **245**, 137–172 (2012).
231. Vatanpour, V. *et al.* Cellulose acetate in fabrication of polymeric membranes: A review. *Chemosphere* **295**, 133914 (2022).
232. Fischer, S. *et al.* Properties and Applications of Cellulose Acetate. *Macromol. Symp.* **262**, 89–96 (2008).
233. Tseng, H.-C. Production of Pentanol in Metabolically Engineered *Escherichia coli*. *Massachusetts Institute of Technology* (2011).
234. Chamberlain, M., DeLap, R. A. & Stacy, C. L. Weathering of Ethylcellulose Plastic - Extent of Various Types of Degradation. *Ind. Eng. Chem.* **48**, 1209–1211 (1956).
235. Bampidis, V. *et al.* Safety and efficacy of ethyl cellulose for all animal species. *EFSA J.* **18**, (2020).
236. Jaffe, H. von R. Polymorphism of Rochelle Salt. *Phys. Rev.* **51**, 43–47 (1937).
237. Andrusyk, A. Piezoelectric Effect in Rochelle Salt. in *Ferroelectrics - Physical Effects* (2011).
238. dos Santos, A. O. *et al.* Rochelle salt piezoelectric coefficients obtained by x-ray multiple diffraction. *J. Phys. Condens. Matter* **13**, (2001).
239. Kalisz, L., Fugiel, B. & Ziolo, J. Dielectric Relaxation in Rochelle Salt in Non-Parallel Electric Fields. *Solid State Commun.* **89**, 393–395 (1994).
240. Mason, W. P. The Elastic, Piezoelectric, and Dielectric Constants of Potassium Dihydrogen Phosphate and Ammonium Dihydrogen Phosphate. *Phys. Rev.* **69**, 829–839 (1946).
241. Lian, Y. *et al.* The rapid growth of ADP single crystal. *CrystEngComm* **18**, 7530–7536 (2016).
242. Xu, D., Xiong, X., Yang, L., Zhang, Z. & Wang, X. Determination of the Solubility of Ammonium Dihydrogen Phosphate in Water-Ethanol System at Different Temperatures from 283.2 to 343.2 K. *J. Chem. Eng. Data* **61**, 78–82 (2016).
243. Neelagantaprasad, B., Jegatheesan, A., Sadeeshkumar, C., Jayanalina, T. & Ravi, B. Optical, Thermal, and Mechanical Properties of Mono Ammonium Phosphate (MAP) Single Crystal. *Coromandal J. Sci.* **2**, 20–24 (2013).
244. Garcia, A. J. L. *et al.* Low-Temperature Growth of ZnO Nanowires from Gravure-Printed ZnO Nanoparticle Seed Layers for Flexible Piezoelectric Devices. *Nanomaterials* **11**, 1430 (2021).
245. Korostynska, O., Gigilashvili, G., Gandhi, A. A. & Tofail, S. A. M. High temperature induced pyroelectricity in screen-printed Hydroxyapatite thick films. in *14th International Symposium on Electrets* 141–142 (IEEE, 2011). doi:10.1109/ISE.2011.6085022.
246. Dolhen, M. *et al.* Sodium potassium niobate (K_{0.5}Na_{0.5}NbO₃, KNN) thick films by electrophoretic deposition. *RSC Adv.* **5**, 4698–4706 (2015).
247. Politova, E. D. *et al.* Structure, ferroelectric and piezoelectric properties of KNN-based perovskite ceramics. *Ferroelectrics* **538**, 45–51 (2019).
248. Zhengfa, L., Yongxiang, L. & Jiwei, Z. Grain growth and piezoelectric property of KNN-based lead-free ceramics. *Curr. Appl. Phys.* **11**, S2–S13 (2011).
249. Birol, H., Damjanovic, D. & Setter, N. Preparation and Characterization of KNbO₃ Ceramics. *J. Am. Ceram. Soc.* **88**, 1754–1759 (2005).
250. Kim, D. H. *et al.* Influence of sintering conditions on piezoelectric properties of KNbO₃ ceramics. *J. Eur. Ceram. Soc.* **34**, 4193–4200 (2014).

251. Ganeshkumar, R., Sopiha, K. V., Wu, P., Cheah, C. W. & Zhao, R. Ferroelectric KNbO₃ nanofibers: synthesis, characterization and their application as a humidity nanosensor. *Nanotechnology* **27**, 395607 (2016).
252. Stojanovic, B. D., Foschini, C. R., Pejovic, V. Z., Pavlovic, V. B. & Varela, J. A. Electrical properties of screen printed BaTiO₃ thick films. *J. Eur. Ceram. Soc.* **24**, 1467–1471 (2004).
253. Torah, R. N., Beeby, S. P. & White, N. M. Improving the piezoelectric properties of thick-film PZT: The influence of paste composition, powder milling process and electrode material. *Sens. Actuators Phys.* **110**, 378–384 (2004).
254. Huang, L. *et al.* Piezoelectric-AlN resonators at two-dimensional flexural modes for the density and viscosity decoupled determination of liquids. *Microsyst. Nanoeng.* **8**, (2022).
255. Martin, F., Murali, P., Dubois, M.-A. & Pezous, A. Thickness dependence of the properties of highly c-axis textured AlN thin films. *J. Vac. Sci. Technol. Vac. Surf. Films* **22**, 361–365 (2004).
256. Liu, L., Karaki, T., Fujii, T. & Sakai, Y. Effect of substrate material to the properties of screen-printed lead free (Bi_{0.5}Na_{0.5})TiO₃-based thick films. *Jpn. J. Appl. Phys.* **59**, 0–6 (2020).
257. Dulina, I. O., Umerova, S. O. & Ragulya, A. V. Barium Titanate Thin Films Obtained by Screen Printing Technology. in *Proceedings of the International Conference Nanomaterials: Applications and Properties* vol. 2 3–5 (2013).
258. Li, Y., Hui, C., Wu, M., Li, Y. & Wang, Y. Textured (K_{0.5}Na_{0.5})NbO₃ ceramics prepared by screen-printing multilayer grain growth technique. *Ceram. Int.* **38**, S283–S286 (2012).
259. Polonini, H. C. *et al.* Size-dependent ecotoxicity of barium titanate particles: the case of *Chlorella vulgaris* green algae. *Ecotoxicology* **24**, 938–948 (2015).
260. Polonini, H. C. *et al.* Ecotoxicological studies of micro- and nanosized barium titanate on aquatic photosynthetic microorganisms. *Aquat. Toxicol.* **154**, 58–70 (2014).
261. Ahamed, M., Akhtar, M. J., Khan, M. A. M., Alhadlaq, H. A. & Alshamsan, A. Barium Titanate (BaTiO₃) Nanoparticles Exert Cytotoxicity through Oxidative Stress in Human Lung Carcinoma (A549) Cells. *Nanomaterials* **10**, 2309 (2020).
262. Lemaire, E. & Danick, B. *Solution processed green piezoelectric paper.* (2017).
263. Vabbina, P. K. *et al.* Controlled synthesis of single-crystalline ZnO nanoflakes on arbitrary substrates at ambient conditions. *Part. Part. Syst. Charact.* **31**, 190–194 (2014).
264. Vabbina, P. K. *et al.* Synthesis of crystalline ZnO nanostructures on arbitrary substrates at ambient conditions. *Nanoepitaxy Mater. Devices III* **8106**, 81060H (2011).
265. Chen, X. *et al.* Effect of the particle size on the performance of BaTiO₃ piezoelectric ceramics produced by additive manufacturing. *Ceram. Int.* **48**, 1285–1292 (2022).
266. Wang, W. *et al.* Fabrication of piezoelectric nano-ceramics via stereolithography of low viscous and non-aqueous suspensions. *J. Eur. Ceram. Soc.* **40**, 682–688 (2020).
267. Monroe, M. M., Villanueva, L. G. & Briand, D. Low-temperature processing of screen-printed piezoelectric KNbO₃ with integration onto biodegradable paper substrates. *Microsyst. Nanoeng.* **9**, 19 (2023).
268. Sivanandan, K., Achuthan, A. T., Kumar, V. & Kanno, I. Fabrication and transverse piezoelectric characteristics of PZT thick-film actuators on alumina substrates. *Sens. Actuators Phys.* **148**, 134–137 (2008).
269. Ghayour, H. & Abdollahi, M. A brief review of the effect of grain size variation on the electrical properties of BaTiO₃-based ceramics. *Powder Technol.* **292**, 84–93 (2016).
270. Sun, S. *et al.* Structural origin of size effect on piezoelectric performance of Pb(Zr,Ti)O₃. *Ceram. Int.* **47**, 5256–5264 (2021).
271. Ge, H., Huang, Y., Hou, Y., Xiao, H. & Zhu, M. Size dependence of the polarization and dielectric properties of KNbO₃ nanoparticles. *RSC Adv* **4**, 23344–23350 (2014).
272. Yang, W. *et al.* A Study on the Relationship Between Grain Size and Electrical Properties in (K,Na)NbO₃-Based Lead-Free Piezoelectric Ceramics. *Adv. Electron. Mater.* **5**, 1900570 (2019).
273. Hu, X., Li, D., Gao, Y., Mu, L. & Zhou, Q. Knowledge gaps between nanotoxicological research and nanomaterial safety. *Environ. Int.* **94**, 8–23 (2016).
274. Jain, A., Ranjan, S., Dasgupta, N. & Ramalingam, C. Nanomaterials in food and agriculture: An overview on their safety concerns and regulatory issues. *Crit. Rev. Food Sci. Nutr.* **58**, 297–317 (2018).
275. Kabir, E., Kumar, V., Kim, K.-H., Yip, A. C. K. & Sohn, J. R. Environmental impacts of nanomaterials. *J. Environ. Manage.* **225**, 261–271 (2018).
276. Uchino, K. Manufacturing Methods for Piezoelectric Ceramic Materials. in *Advanced Piezoelectric Materials* 385–421 (Elsevier Ltd., 2017). doi:10.1016/b978-0-08-102135-4.00010-2.
277. de Jong, M., Chen, W., Geerlings, H., Asta, M. & Persson, K. A. A database to enable discovery and design of piezoelectric materials. *Sci. Data* **2**, 150053 (2015).
278. Petousis, I. *et al.* Data Descriptor: High-throughput screening of inorganic compounds for the discovery of novel dielectric and optical materials. *Sci. Data* **4**, 1–12 (2017).
279. Koch, W. Properties and Uses of Ethylcellulose. *Ind. Eng. Chem.* **29**, (1937).

280. Mitra, K. Y., Willert, A., Chandru, R., Baumann, R. R. & Zichner, R. Inkjet Printing of Bioresorbable Materials for Manufacturing Transient Microelectronic Devices. *Adv. Eng. Mater.* **22**, (2020).
281. Chang, J., Ge, T. & Sanchez-Sinencio, E. Challenges of printed electronics on flexible substrates. *Midwest Symp. Circuits Syst.* 582–585 (2012) doi:10.1109/MWSCAS.2012.6292087.
282. Poulin, A., Aeby, X., Siqueira, G. & Nyström, G. Versatile carbon-loaded shellac ink for disposable printed electronics. *Sci. Rep.* **11**, 1–9 (2021).
283. O'Mahony, C., Haq, E. U., Sillien, C. & Tofail, S. A. M. Rheological Issues in Carbon-Based Inks for Additive Manufacturing. *Micromachines* **10**, 99 (2019).
284. Agrawal, A. M., Manek, R. V., Kolling, W. M. & Neau, S. H. Studies on the interaction of water with ethylcellulose: Effect of polymer particle size. *AAPS PharmSciTech* **4**, (2003).
285. Cann, A. F. & Liao, J. C. Pentanol isomer synthesis in engineered microorganisms. *Appl. Microbiol. Biotechnol.* **85**, 893–899 (2010).
286. *CRC Handbook of Chemistry and Physics*. (CRC Press, 2016). doi:10.1201/9781315380476.
287. Kang, K., Park, J., Kim, K. & Yu, K. J. Recent developments of emerging inorganic, metal and carbon-based nanomaterials for pressure sensors and their healthcare monitoring applications. *Nano Res.* **14**, 3096–3111 (2021).
288. Han, J., Saravanapavanantham, M., Chua, M. R., Lang, J. H. & Bulović, V. A versatile acoustically active surface based on piezoelectric microstructures. *Microsyst. Nanoeng.* **8**, (2022).
289. Mitra, K. Y. *et al.* Fully Inkjet-Printed Thin-Film Transistor Array Manufactured on Paper Substrate for Cheap Electronic Applications. *Adv. Electron. Mater.* **3**, 1700275 (2017).
290. Kim, J., Yun, G. Y., Kim, J. H., Lee, J. & Kim, J. H. Piezoelectric electro-active paper (EAPap) speaker. *J. Mech. Sci. Technol.* **25**, 2763–2768 (2011).
291. Gao, R. *et al.* A study on (K, Na) NbO₃ based multilayer piezoelectric ceramics micro speaker. *Smart Mater. Struct.* **23**, (2014).
292. Ainsley, C., Reis, N. & Derby, B. Freeform fabrication by controlled droplet deposition of powder filled melts. *J. Mater. Sci.* **37**, 3155–3161 (2002).
293. Zekic, A. A., Mitrovic, M. M., Elezovic-Hadzic, S. M. & Malivuk, D. A. Long-Time Growth Rate Changes of Sodium Chlorate, Potassium Dihydrogen Phosphate, and Rochelle Salt Crystals Independent of Growth Conditions. *Ind. Eng. Chem. Res.* **50**, 8726–8733 (2011).
294. Mahadeva, S. K., Walus, K. & Stoeber, B. Fabrication and Testing of Piezoelectric Hybrid Paper for MEMS Applications. in *MEMS 2014* 620–623 (2014).
295. Dagdeviren, C. *et al.* Recent progress in flexible and stretchable piezoelectric devices for mechanical energy harvesting, sensing and actuation. *Extreme Mech. Lett.* **9**, 269–281 (2016).
296. Morvan, J., Buyuktanir, E., West, J. L. & Jáklí, A. Highly piezoelectric biocompatible and soft composite fibers. *Appl. Phys. Lett.* **100**, 3–7 (2012).
297. Irimia-Vladu, M. *et al.* Biocompatible and biodegradable materials for organic field-effect transistors. *Adv. Funct. Mater.* **20**, 4069–4076 (2010).
298. Scoutaris, N., Ross, S. & Douroumis, D. Current Trends on Medical and Pharmaceutical Applications of Inkjet Printing Technology. *Pharm. Res.* **33**, 1799–1816 (2016).
299. Lei, T. *et al.* Biocompatible and totally disintegrable semiconducting polymer for ultrathin and ultralightweight transient electronics. *Proc. Natl. Acad. Sci.* **114**, 5107–5112 (2017).
300. Rodrigues, S., Dionísio, M., López, C. R. & Grenha, A. Functional Biomaterials Biocompatibility of Chitosan Carriers with Application in Drug Delivery. *J. Funct. Biomater.* **3**, 615–641 (2012).
301. Maddaus, A. *et al.* Design and fabrication of bio-hybrid materials using inkjet printing. *Biointerphases* **11**, (2016).
302. Chen, M., Tan, J., Lian, Y. & Liu, D. Preparation of Gelatin coated hydroxyapatite nanorods and the stability of its aqueous colloidal. *Appl. Surf. Sci.* **254**, 2730–2735 (2008).
303. Kong, D., Le, L. T., Li, Y., Zunino, J. L. & Lee, W. Temperature-Dependent Electrical Properties of Graphene Inkjet-Printed on Flexible Materials. *Langmuir* **28**, 13467–13472 (2012).
304. Kim, D. *et al.* Silicon electronics on silk as a path to bioresorbable, implantable devices. *Appl. Phys. Lett.* **95**, (2009).
305. Alaman, J., Alicante, R., Pena, J. I. & Sanchez-Somolinos, C. Inkjet Printing of Functional Materials for Optical and Photonic Applications. *Materials* **9**, (2016).
306. Borah, R., Ingavle, G. C., Sandeman, S. R., Kumar, A. & Mikhalovsky, S. Electrically conductive MEH-PPV:PCL electrospun nano fibres for electrical stimulation of rat PC12 pheochromocytoma cells. *Biomater. Sci.* **6**, 2342–2359 (2018).
307. Sappati, K. K. & Bhadra, S. Piezoelectric Polymer and Paper Substrates: A Review. *Sensors* **18**, (2018).
308. Kim, J. Y., Cheng, A. & Tai, Y. Parylene-C as a Piezoelectric Material. in *2011 IEEE 24th International Conference on Micro Electro Mechanical Systems* 473–476 (IEEE, 2011). doi:10.1109/MEMSYS.2011.5734464.

309. Hirai, N. *et al.* Effects of Water Temperature on Degradation of Several Biodegradable Polymers Immersed in Water. in *2005 International Symposium on Electrical Insulating Materials* 771–774 (2005).
310. Boutry, C. M. Biodegradable passive resonant circuits for wireless implant applications. (ETH Zurich, 2012).
311. Middleton, J. C. & Tipton, A. J. Synthetic biodegradable polymers as orthopedic devices. *Biomaterials* **21**, 2335–2346 (2000).
312. Reulmann, M. B. *et al.* Polymers, Biodegradable. in *Ullmann's Encyclopedia of Industrial Chemistry, Vol. 29* 265–294 (2012). doi:10.1002/14356007.n21.
313. Yang, M., Zhang, Y., Zhang, H. & Li, Z. Characterization of PEDOT:PSS as a Biocompatible Conductive Material. in *10th IEEE International Conference on Nano/Micro Engineered and Molecular Systems* 149–151 (IEEE, 2015). doi:10.1109/NEMS.2015.7147397.
314. Asplund, M. *et al.* Toxicity evaluation of PEDOT/biomolecular composites intended for neural communication electrodes. *Biomed. Mater.* **4**, (2009).
315. Yin, Z., Huang, Y., Bu, N., Wang, X. & Xiong, Y. Inkjet printing for flexible electronics: Materials, processes and equipments. *Chin. Sci. Bull.* **55**, 3383–3407 (2010).
316. Sun, J. *et al.* Sustainable and biodegradable wood sponge piezoelectric nanogenerator for sensing and energy harvesting applications. *ACS Nano* **14**, 14665–14674 (2020).
317. Rosenboom, J.-G., Hohl, D. K., Fleckinstein, P., Storti, G. & Morbidelli, M. Bottle-grade polyethylene furanoate from ring-opening polymerisation of cyclic oligomers. *Nat. Commun.* **9**, (2018).
318. Zhang, F. *et al.* Inkjet printing of polyimide insulators for the 3D printing of dielectric materials for microelectronic applications. *J. Appl. Polym. Sci.* (2016) doi:10.1002/app.43361.
319. Mattana, G., Briand, D., Murette, A., Vásquez Quintero, A. & De Rooij, N. F. Polylactic acid as a biodegradable material for all-solution-processed organic electronic devices. *Org. Electron.* **17**, 77–86 (2015).
320. Bettinger, C. J. Materials Advances for Next-Generation Ingestible Electronic Medical Devices. *Trends Biotechnol.* **33**, 575–585 (2015).
321. Ciofani, G. & Menciassi, A. *Piezoelectric Nanomaterials for Biomedical Applications.* (2012).
322. Wang, S., Lu, L. & Yaszemski, M. J. Bone Tissue-Engineering Material Poly(propylene fumarate): Correlation between Molecular Weight, Chain Dimensions, and Physical Properties. *Biomacromolecules* **7**, 1976–1982 (2006).
323. Wang, X. *et al.* Evaluation of biocompatibility of polypyrrole in vitro and in vivo. *J. Biomed. Mater. Res. A* **68**, 411–422 (2003).
324. Balint, R., Cassidy, N. J. & Cartmell, S. H. Conductive polymers: Towards a smart biomaterial for tissue engineering. *Acta Biomater.* **10**, 2341–2353 (2014).
325. Valasek, J. Piezoelectric Activity of Rochelle Salt Under Various Conditions. *Phys. Rev.* **19**, 478–491 (1922).
326. Kang, S. kyun *et al.* Dissolution Chemistry and Biocompatibility of Silicon- and Germanium-Based Semiconductors for Transient Electronics. *Appl. Mater. Interfaces* **7**, 9297–9305 (2015).
327. Kutlakova, K. M., Tokarsky, J. & Peikertová, P. Functional and eco-friendly nanocomposite kaolinite/ZnO with high photocatalytic activity. *Appl. Catal. B Environ.* **162**, 392–400 (2015).
328. Venkatesh, K. P. & Pratap, R. Capturing higher modes of vibration of micromachined resonators. *J. Phys. Conf. Ser.* **181**, 012079 (2009).
329. Wagiran, R. *et al.* Characterization of screen printed BaTiO₃ thick film humidity sensor. *Int J Eng. Techn* **2**, 22–26 (2005).
330. Sakai, Y., Futakuchi, T. & Adachi, M. Preparation of BaTiO₃ Thick Films by Inkjet Printing on Oxygen-Plasma-Modified Substrates. *Jpn. J. Appl. Phys.* **45**, 7247–7251 (2006).
331. Almeida, A. F. L. *et al.* Optical and electrical properties of barium titanate-hydroxyapatite composite screen-printed thick films. *Solid State Sci.* **6**, 267–278 (2004).
332. Lim, J. *et al.* All-inkjet-printed flexible piezoelectric generator made of solvent evaporation assisted BaTiO₃ hybrid material. *Nano Energy* **41**, 337–343 (2017).
333. Silva, C. C. *et al.* Hydroxyapatite screen-printed thick films: optical and electrical properties. *Mater. Chem. Phys.* **92**, 260–268 (2005).
334. Badurova, K. *et al.* Piezoelectricity in Sr doped thick films of hydroxyapatite. *IEEE Trans. Dielectr. Electr. Insul.* **27**, 1409–1414 (2020).
335. Levassort, F. *et al.* High frequency single element transducer based on pad-printed lead-free piezoelectric thick films. in *2011 IEEE International Ultrasonics Symposium* 848–851 (IEEE, 2011). doi:10.1109/ULTSYM.2011.0207.
336. Pavlič, J., Kosec, M., Holc, J. & Rojac, T. K_{0.5}Na_{0.5}NbO₃ thick films: preparation and properties. (2012).
337. Pavlič, J., Malič, B. & Rojac, T. Small Reduction of the Piezoelectric d₃₃ Response in Potassium Sodium Niobate Thick Films. *J. Am. Ceram. Soc.* **97**, 1497–1503 (2014).

338. Pavlič, J., Malič, B. & Rojac, T. Microstructural, structural, dielectric and piezoelectric properties of potassium sodium niobate thick films. *J. Eur. Ceram. Soc.* **34**, 285–295 (2014).
339. Hansen, K., Astafiev, K. & Zawada, T. Lead-free piezoelectric thick films based on potassium sodium niobate solutions. *Proc. - IEEE Ultrason. Symp.* 1738–1741 (2009) doi:10.1109/ULTSYM.2009.5441677.
340. Mercier, H., Kuscer, D. & Levassort, F. Processing and sintering of sodium-potassium niobate-based thick films. *J. Microelectron. Electron. Compon. Mater.* **47**, 179–185 (2017).
341. Mercier, H. *et al.* Electrophoretic deposition and properties of strontium-doped sodium potassium niobate thick films. *J. Eur. Ceram. Soc.* **37**, 5305–5313 (2017).
342. Hübler, A. C. *et al.* Fully mass printed loudspeakers on paper. *Org. Electron.* **13**, 2290–2295 (2012).
343. Gonçalves, S. *et al.* Environmentally Friendly Printable Piezoelectric Inks and Their Application in the Development of All-Printed Touch Screens. *ACS Appl. Electron. Mater.* **1**, 1678–1687 (2019).
344. Glinsek, S. *et al.* Inkjet-Printed Piezoelectric Thin Films for Transparent Haptics. *Adv. Mater. Technol.* **7**, 2200147 (2022).
345. Kok, S.-L., White, N. M. & Harris, N. R. Fabrication and characterization of free-standing thick-film piezoelectric cantilevers for energy harvesting. *Meas. Sci. Technol.* **20**, 124010 (2009).
346. Chen, H. D., Udayakumar, K. R., Cross, L. E., Bernstein, J. J. & Niles, L. C. Dielectric, ferroelectric, and piezoelectric properties of lead zirconate titanate thick films on silicon substrates. *J. Appl. Phys.* **77**, 3349–3353 (1995).
347. Very, F. *et al.* Piezoelectric thick film sensors: Fabrication and characterization. in *2013 Joint IEEE International Symposium on Applications of Ferroelectric and Workshop on Piezoresponse Force Microscopy (ISAF/PFM)* 287–290 (IEEE, 2013). doi:10.1109/ISAF.2013.6748690.
348. Debéda, H., Clément, P., Llobet, E. & Lucat, C. One-step firing for electroded PZT thick films applied to MEMS. *Smart Mater. Struct.* **24**, (2015).
349. Zhu, W., Yao, K. & Zhang, Z. Design and fabrication of a novel piezoelectric multilayer actuator by thick-film screen printing technology. *Sens. Actuators Phys.* **86**, 149–153 (2000).
350. Yildirim, A. *et al.* Roll-to-Roll Production of Novel Large-Area Piezoelectric Films for Transparent, Flexible, and Wearable Fabric Loudspeakers. *Adv. Mater. Technol.* **5**, 2000296 (2020).
351. Lowry, H. H. & Morgan, S. O. The vapor pressures of rochelle salt, the hydrates of sodium and potassium tartrates and their saturated solutions. *J. Am. Chem. Soc.* **46**, 2192–2196 (1924).
352. Vernieuwe, K., Feys, J., Cuypers, D. & De Buysser, K. Ink-Jet Printing of Aqueous Inks for Single-Layer Deposition of Al-Doped ZnO Thin Films. *J. Am. Ceram. Soc.* **99**, 1353–1359 (2016).
353. Wang, H., Yu, J., Liu, H. & Xu, X. Low temperature, rapid and controllable growth of highly crystalline ZnO nanostructures via a diluent hydrolytic process and its application to transparent super-wetting films. *CrystEngComm* **20**, 7602–7609 (2018).
354. Kitsomboonloha, R., Morris, S. J. S., Rong, X. & Subramanian, V. Femtoliter-scale patterning by high-speed, highly scaled inverse gravure printing. *Langmuir* **28**, 16711–16723 (2012).
355. Hsu, J. W. P. *et al.* Spatial organization of ZnO nanorods on surfaces via organic templating. in *Proceedings of SPIE* vol. 5592 (2005).
356. Chackrabarti, S., Hafiz, A. K. & Zargar, R. A. A Comprehensive Review of Properties of Screen-Printed Pure and Doped ZnO and CdO Thick Films. *Curr. Altern. Energy* **2**, 42–71 (2018).
357. Vabbina, P. K. Sonochemical Synthesis of Zinc Oxide Nanostructures for Sensing and Energy Harvesting. *FIU Electronic Theses and Dissertations* (2016). doi:10.25148/etd.FIDC000787.
358. Jung, S. H. *et al.* Sonochemical preparation of shape-selective ZnO nanostructures - SI. *Cryst. Growth Des.* **8**, 265–269 (2008).
359. Song, X. X. *et al.* Facile and Rapid Preparation of ZnO Nanomaterials with Different Morphologies and Superficial Structures for Enhanced Ethanol-Sensing Performances. *J. Inorg. Organomet. Polym. Mater.* **29**, 33–40 (2019).
360. Zhang, X. *et al.* Enhancing dielectric and piezoelectric properties of micro-ZnO/PDMS composite-based dielectrophoresis. *Mater. Des.* **192**, 108783 (2020).
361. Tao, Q., Liu, L. & Li, G. Selective manipulation of ZnO nanowires by controlled dielectrophoretic force. *Proc. IEEE Conf. Nanotechnol.* 1106–1109 (2011) doi:10.1109/NANO.2011.6144483.
362. Choi, K., Choi, W., Yu, C. & Park, Y. T. Enhanced Piezoelectric Behavior of PVDF Nanocomposite by AC Dielectrophoresis Alignment of ZnO Nanowires. *J. Nanomater.* **2017**, 1–5 (2017).
363. Martinez-Duarte, R. Microfabrication technologies in dielectrophoresis applications-A review. *Electrophoresis* **33**, 3110–3132 (2012).
364. van den Ende, D. A. *et al.* Dielectrophoretically structured piezoelectric composites with high aspect ratio piezoelectric particles inclusions. *J. Appl. Phys.* **111**, 124107 (2012).

365. Deutz, D. B. *et al.* Flexible Piezoelectric Touch Sensor by Alignment of Lead-Free Alkaline Niobate Microcubes in PDMS. *Adv. Funct. Mater.* **27**, 1–7 (2017).
366. Riahifar, R. *et al.* Sorting ZnO particles of different shapes with low frequency AC electric fields. *Mater. Lett.* **65**, 632–635 (2011).
367. Lang, S. B. Review of ferroelectric hydroxyapatite and its application to biomedicine. *Phase Transit.* **89**, 678–694 (2016).
368. Tofail, S. A. M. & Bauer, J. Electrically Polarized Biomaterials. *Adv. Mater.* **28**, 5470–5484 (2016).
369. Tofail, S. A. M. *et al.* Direct and ultrasonic measurements of macroscopic piezoelectricity in sintered hydroxyapatite. *J. Appl. Phys.* **105**, 064103 (2009).
370. Gandhi, A. A., Wojtas, M., Lang, S. B., Kholkin, A. L. & Tofail, S. A. M. Piezoelectricity in Poled Hydroxyapatite Ceramics. *J. Am. Ceram. Soc.* **97**, 2867–2872 (2014).
371. Fihri, A., Len, C., Varma, R. S. & Solhy, A. Hydroxyapatite: A review of syntheses, structure and applications in heterogeneous catalysis. *Coord. Chem. Rev.* **347**, 48–76 (2017).

Curriculum Vitae

MORGAN MONROE

NEUCHÂTEL, SWITZERLAND

+41 79 701 26 62

MORGANMONROE@BERKELEY.EDU

LANGUAGES: ENGLISH (NATIVE) | FRENCH (B2-C1) | SPANISH (A2) | GERMAN (A1)

EDUCATION

École Polytechnique Fédérale de Lausanne (EPFL), Switzerland 02/2019 – 10/2023

Sc.D. in Microtechnology

- Advisors: Danick Briand & L. Guillermo Villanueva
- Thesis Title: “Printed degradable piezoelectric microsystems: From ink formulation to device fabrication and characterization”

University of California at Berkeley, Berkeley, CA, USA 08/2011 – 05/2016

M.S. in Materials Science and Engineering Class of 2016

- Advisor: Joel Ager
- Thesis Title: “Membraneless laminar flow cell for electrocatalytic CO₂ reduction with liquid product separation”

B.S. in Chemical Engineering / Materials Science and Engineering Class of 2015

EMPLOYMENT HISTORY

Doctoral Assistant 02/2019 – 09/2023

Soft Transducers Lab (LMTS), École Polytechnique Fédérale de Lausanne (EPFL) – Neuchâtel, NE, CH

- Developed, manufactured, and characterized degradable, fully printed piezoelectric microsystems
- Optimized novel low-temperature process for screen-printed KNbO₃ piezoelectrics compatible with biodegradable substrates, including device design and ink formulation
- Designed, iterated on, and characterized first-ever fully degradable acoustic headphones
- Established and implemented novel lab organization and safety protocols
- Supervised several Masters student projects on degradable and printable electronics
- Served as a teaching assistant, with over 300 hrs teaching (Static Mechanics 2) both in person and online
- Conducted numerous science communication and outreach activities

Associate R&D Engineer 09/2016 – 05/2018

Modern Electron, LLC – Bellevue, WA, USA

- Improved process consistency and internal product yield by more than 50% via extensive reliability testing and in-depth device post-mortem in collaboration with nanofabrication engineering team
- Developed highly automated high throughput dielectric breakdown test setup
- Designed, built, and executed alkali-gas selective ultra-high vacuum pressure gauge and measurement system for utilization in low work function/surface chemistry experiments

Masters Thesis 08/2015 – 08/2016

Ager Group, Joint Center for Artificial Photosynthesis and SinBeRISE – Berkeley, CA, USA

- Thesis Title: “Membraneless laminar flow cell for electrocatalytic CO₂ reduction with liquid product separation”
- Computationally modeled and empirically verified novel device for electrochemical solar fuel production

Battery Test Engineering Intern 05/2015 – 08/2015

General Motors – Warren, MI, USA

- Verified and validated computational model for 1D thermal propagation in automotive battery modules

- Designed and implemented experimental apparatus for thermal abuse testing of Lithium ion battery cells in an anaerobic environment for analysis of decomposed electrolyte composition

Process Engineering and Research Intern**05/2014 – 08/2014***Imprint Energy – Oakland, CA, USA*

- Implemented novel system to assess failure rates in flexible, printed ZincPoly® batteries
- Refined production process to increase production yield by more than 30% with greater consistency
- Investigated issues relating polymeric packaging materials to decreased longevity

Undergraduate Research Intern**01/2012 – 05/2014***Bokor Group, Center for Energy Efficient Electronics – Berkeley, CA, USA*

- Analyzed the magnetostrictive properties of Terfenol-D for computing memory applications

Undergraduate Research Intern**07/2013 – 09/2013***Ionescu Group, Nanoelectronic Devices Laboratory, EPFL – Lausanne, VD, CH*

- Characterized the electrical properties of and diagnosed reliability issues in curved cantilever NEMS relays for use in logic applications

Independent Research**08/2009 – 01/2011**

- Conducted an assessment of indented reverse-pyramidal arrays on the ordering of catalytic nucleation points for the production of aligned-growth ZnO nanowires
- Investigated effectiveness of copper/gold alloy catalysts for the synthesis of ZnO nanowires via CVD

PROFESSIONAL QUALIFICATIONS AND SKILLS

Interpersonal

- Strong teamwork and leadership skills
- Excellent presentation and communication skills (English)
- Experienced in hiring: job description writing, technical and behavioral interviewing

Computational

- **Advanced:** AutoCAD, Python, LabVIEW, Origin, Illustrator
- **Intermediate:** MATLAB, COMSOL

Technical

- Advanced experience in additive manufacturing technologies, particularly functional ink development and printing process optimization
- Advanced experience in experimental design and lab setup, including high throughput setups, test automation, drafting SOPs, and developing safety protocols
- Experience in ISO 5 (US Class 100) clean room procedures and techniques including photolithography, chemical vapor deposition (CVD) growth techniques, plasma sputtering
- Advanced experience with SEM and EDS (>300 hrs); proficient with AFM and GC analysis
- Experience with MOKE Magnetometry, EIS, potentiometry

ACTIVITIES AND AWARDS

EPFL Medical First Responder, Microcity Campus**06/2020 – Present***EPFL – Neuchâtel, NE, CH*

- Medical first responder, Certified for BLS-AED-SRC (IAS1&2)
- Acted as a medical first responder for building of >200 people, working in an 8-person team
- Performed regular trainings for Basic Life Support and Advanced Trauma Life Support, with specialty focus on chemical and electrical related incidents

Modern Electron Safety Committee, Founder**09/2016 – 05/2018***Modern Electron, LLC – Bellevue, WA, USA*

- Wrote company-wide safety protocols and garnered full buy-in from entire company
- Developed and implemented workplace inspection procedures and improved worksite safety through direct action

Design Challenge Winning Team**02/2016 – 06/2016***Imprint Energy Collider at UC Berkeley – Berkeley, CA, USA*

- Completed an in-depth analysis of IoT and wearable electronic device technologies to evaluate their energy demand needs from the standpoint of a battery developer or manufacturer
- Developed and designed a standardized flexible battery product datasheet aimed to provide product designers accurate and consistent information and facilitate fair evaluation of competitive products

Social Chair and Webmaster**09/2013 – 05/2015***Materials Science and Engineering Association (MSEA) – Berkeley, CA, USA*

- Improved interaction between officers and members via social media
- Developed and implemented new social activities to enhance member relations and increase networking opportunities

PUBLICATIONS, CONFERENCES, AND TALKS

- **Monroe, M.M.**, Fumeaux, N., Villanueva, L.G. & Briand, D. (2023). Additively manufactured degradable piezoelectric microsystems for sensing and actuating. *Adv. Mat. Tech.*
 - Submitted 11 May 2023, Under revision (as of July 21, 2023)
- **Monroe, M.M.**, Villanueva, L.G., & Briand, D. (2023). Printed biodegradable piezoelectric microsystems: From ink formulation to device fabrication and characterization. *EPFL EDM Research Day 2023.*
 - Invited Speaker
- **Monroe, M.M.**, Villanueva, L.G. & Briand, D. (2023). Low-temperature processing of screen-printed piezoelectric KNbO₃ with integration onto biodegradable paper substrates. *Microsystems & Nanoengineering* **9**, 19 (2023). <https://doi.org/10.1038/s41378-023-00489-0>
 - Featured Article, May 2023
- **Monroe, M.M.**, O’Conner, E., Villanueva, L.G., & Briand, D. (2021). Screen-Printed Low Temperature BaTiO₃ Piezoelectrics for Integration on Eco-Friendly Substrates. *International Workshop on Piezoelectric Materials and Applications in Actuators, IWPMA 2021.*
- Lemaire, E., Haque, R.I., **Monroe, M.M.**, Briand, D., & Atli, A. (2019). Green piezoelectric transducers based on transfer and printing of piezoelectric salts. *International Workshop on Piezoelectric Materials and Applications in Actuators, IWPMA 2019.*
- **Monroe, M.M.**, Koch, A.T., Lingley, A.R., Mankin, M.N., Pan, T.S., & Sun, Y. (2017). Dielectric Surface Breakdown in Sub-100 nm Metal-Insulator-Metal Fins with Exposed SiO_x and Si₃N₄ Sidewalls. *2017 6th International Workshop on Mechanisms of Vacuum Arcs, MeVArc 2017.*
- Lu, H.I., Sun, Y., Lingley, A.R., Koch, A.T., Clark, S.E., **Monroe, M.M.**, Kannan, A., Gorski, R., Mankin, M.N., & Pan, T.S. (2017). Mitigation of space charge via nanoscale grids. *2017 30th International Vacuum Nanoelectronics Conference, IVNC 2017*, 174–175. <https://doi.org/10.1109/IVNC.2017.8051596>
- **Monroe, M. M.**, Lobaccaro, P., Lum, Y., & Ager, J. W. (2017). Membraneless laminar flow cell for electrocatalytic CO₂ reduction with liquid product separation. *Journal of Physics D: Applied Physics*, **50**(15), 154006. <https://doi.org/10.1088/1361-6463/aa6359>
- Lambson, B., Gu, Z., **Monroe, M.M.**, Dhuey, S., Scholl, A., & Bokor, J. (2013). Concave nanomagnets: investigation of anisotropy properties and applications to nanomagnetic logic. *Applied Physics A*, **111**(2), 413–421. <https://doi.org/10.1007/s00339-013-7654-y>